

(NASA-CR-165346) ADVANCED GAS TURBINE (AGT)
POWERTRAIN SYSTEM Semiannual Technical
Summary Report (Detroit Diesel Allison,
Indianapolis, Ind.) - 111 p HC-A06/MF A01
CSCL 21E G3/37 00716

N 83-11497

Unclass

DOE/NASA/0168-81/2
NASA CR-165346
DDA EDR 10578

ADVANCED GAS TURBINE (AGT) POWERTRAIN SYSTEM DEVELOPMENT

Second Semi-annual Report

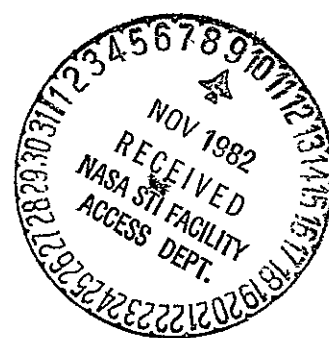
For work performed from July 1, 1980-December 31, 1980

Detroit Diesel Allison
Division of General Motors Corporation
Indianapolis, Indiana 46206

July 1981

Prepared for
National Aeronautics and Space Administration
Lewis Research Center
Cleveland, Ohio 44135
Contract DEN 3-168

For
U.S. DEPARTMENT OF ENERGY
Conservation and Solar Energy
Office of Transportation Programs



NOTICE

This report was prepared to document work sponsored by the United States Government. Neither the United States nor its agent, the United States Department of Energy, nor any Federal employees, nor any of their contractors, subcontractors or their employees makes any warranty, express or implied, or assumes any legal liability or responsibility for the accuracy, completeness, or usefulness of any information, apparatus, product or process disclosed, or represents that its use would not infringe privately owned rights.

FOREWORD

This report presents a technical summary of the Detroit Diesel Allison (DDA) project to develop an automotive gas turbine powertrain system under NASA Contract DEN 3-168 (Department of Energy funding). It covers the 6-month period July 1980 through December 1980.

The basic objective of this project is to develop and demonstrate, by May 1985, an advanced automotive gas turbine powertrain system that will, when installed in a 1985 Pontiac Phoenix vehicle of 1360 kg (3000 lbm) inertia weight, achieve a fuel economy of 18 km/L (42.5 mpg), meet or exceed the 1985 emission requirements, and have alternate fuel capability.

Several General Motors Divisions and other companies are major contributors to this effort. They are: Pontiac Motor Division—vehicle, Delco Electronics Division—electronic control, Delco Remy Division—starter/boost motor, Harrison Radiator Division and Corning Glass Works—regenerator, Hydra-matic Division—transmission, The Carborundum Company and GTE—ceramics.

The DDA Program Manager for the AGT 100 is H. E. (Gene) Helms; design effort is directed by James Williams; materials effort is directed by Dr. Peter Heitman and project effort is directed by Richard Johnson. The Pontiac effort is headed by James Kaufeld, and the Delco Electronics work is managed by Robert Kordes. The NASA AGT 100 Project Manager is Paul T. Kerwin and Assistant Project Manager is James Calogeras.

DOE/NASA/0168-81/2
NASA CR-165346
DDA EDR 10578

ADVANCED GAS TURBINE (AGT) POWERTRAIN SYSTEM DEVELOPMENT

**Second Semi-annual Report
For work performed from July 1, 1980-December 31, 1980**

**Detroit Diesel Allison
Division of General Motors Corporation
Indianapolis, Indiana 46206**

July 1981

Prepared for
National Aeronautics and Space Administration
Lewis Research Center
Cleveland, Ohio 44135
Contract DEN 3-168

**For
U.S. DEPARTMENT OF ENERGY
Conservation and Solar Energy
Office of Transportation Programs**

TABLE OF CONTENTS

Title	Page
Foreword	II
Summary	1
Introduction	3
I. Vehicle System Development	5
1.1 Vehicle Design	5
II. Engine Powertrain Development	7
2.1 Reference Powertrain Design	7
2.2 Mod I	10
III. Compressor Development	11
3.1 Compressor Aero	11
3.2 Compressor Mechanical Development	12
IV. Gasifier Turbine Development	17
4.1 Gasifier Turbine Aerodynamic Development	17
4.2 Gasifier Turbine Mechanical Development	21
4.3 Ceramic Gasifier Turbine Rotor	25
V. Power Turbine Development	27
5.1 Power Turbine Aerodynamic Development	27
5.2 Power Turbine Mechanical Development	36
VI. Combustor Development	37
6.1 RPD	37
6.2 Mod I	38
VII. Regenerator Development	41
7.1 RPD	41
7.2 Mod 1	47
VIII. Engine Subsystems	51
8.1 Block/Insulation	51
8.2 Gearbox And Power Transfer	52
8.3 Starter/Boost System	52
IX. Materials Development	53
9.1 Materials Development—DDA Design Support	53
9.2 Suppliers Effort—Unique Work	55
9.3 Suppliers Effort—Common Work Summary	66
X. Controls	69
10.1 Delco Electronics	69
10.2 Detroit Diesel Allison	69
XI. Transmission Development	73
11.1 DDA Transmission Activity	73
XII. Supportive Manufacturing, Cost and Marketability	75
12.1 Manufacturing Feasibility—Pontiac Motor Division	75
12.2 Cost Analysis—Pontiac Motor Division	75
References	77
Terms & Definitions	78
Appendix—Carborundum Common Work	80

LIST OF ILLUSTRATIONS

Figure	Title	Page
1	Schedule	4
2	AGT 100 Gas Turbine Powered Pontiac Phoenix	5
3	Engine Exhaust Flange to Exhaust Duct	6
4	Vehicle Heating System	6
5	Initial RPD Engine Arrangement	8
6	AGT 100 General Arrangement	9
7	AGT 100 Heat Rejection	10
8	AGT 100 BU 1 Impeller and Diffuser	12
9	AGT 100 BU 1 Partially Assembled Compressor Rig	12
10	AGT 100 BU 1 Compressor Rig	12
11	Compressor Rig Stabilization, 70% speed—BU 1	13
12	Initial Performance Data	13
13	Model for Gasifier Shroud Deflection	14
14	Compressor Module	14
15	AGT 100 Gasifier Rotor Damper	15
16	Gasifier Thrust Bearing Temperature and Heat Transfer	15
17	Finite Element Model of the Area Surrounding the Gasifier Bearing	15
18	Power Loss Analysis—Bearing Positions	16
19	Measured HP Loss #2 Bearing	16
20	AGT 100 Bearing Loss (Predicted)	16
21	Mod I Gasifier Turbine Flow Path	17
22	Efficiency Goal—RPD and Mod 1 Gasifier Turbine with Inlet Scroll	18
23	Mod I Gasifier Vane Design	19
24	Mod I Vane Velocity Distribution	19
25	Mod I Gasifier Rotor Mean Velocity Distribution—Idle	20
26	Mod I Gasifier Rotor Mean Velocity Distribution—48 km/h (30 mph)	20
27	Mod I Gasifier Rotor Mean Velocity Distribution—80 km/h (50 mph)	20
28	Mod I Gasifier Rotor Mean Velocity Distribution—Maximum Power	20
29	Damaged Turbine Rig Module Hardware	21
30	Test Rig Vane and Rotor Assembly	21
31	Assembly of Gasifier Turbine Rig	21
32	Water Brake Installation	22
33	AGT 100 Ceramic Gasifier Turbine Inner Backplate Contour Plot of Temperature—Maximum Power	22
34	AGT 100 Ceramic Gasifier Turbine Outer Backplate Contour Plot of Temperature—Maximum Power	23
35	AGT 100 Ceramic Gasifier Turbine Outer Backplate Contour Plot of Temperature—Maximum Power	23
36	AGT 100 Ceramic Gasifier Turbine Scroll Contour Plot of Temperature—Maximum Power	24
37	AGT 100 Ceramic Gasifier Turbine Scroll Contour Plot of Temperature—Maximum Power	24
38	AGT 100 Ceramic Gasifier Turbine Guide Vanes Contour Plot of Temperature—Maximum Power	25
39	3-D Finite Element Model of Gasifier Turbine	25
40	AGT 100 Cold Start to Max Transient	26
41	Ceramic Gasifier Turbine Max. Principal Stress Distribution	26
42	Required Material Strength for Sintered Silicon Carbide Gasifier Turbine at Maximum Transient Operating Condition	26
43	Mod I Power Turbine Flow Path	27
44	Efficiency Goal—RPD and Mod 1 Power Turbine Without Inlet Scroll	29
45	Mod I Power Turbine Vane Design	29
46	Mod I Power Turbine Vane Velocity Distribution	30
47	Mod I Power Turbine Rotor Mean Velocity Distribution—Idle	30
48	Mod I Power Turbine Rotor Mean Velocity Distribution—48 km/h (30 mph)	30
49	Mod I Power Turbine Rotor Mean Velocity Distribution—80 km/h (50 mph)	30

Figure	Title	Page
50	Mod I Power Turbine Rotor Mean Velocity Distribution—Max Power (565)	31
51	Interturbine Duct and Scroll Test Rig Setup	31
52	Test Rig Instrumentation	31
53	Traverse Mechanism and Plexiglass Backplate	32
54	Interturbine Duct Wall Static Pressures	32
55	Scroll Wall Pressure Coefficient	33
56	Circumferential Total Pressure Traverses	33
57	Region of Depressed Total Pressure	34
58	Scroll Flow Splitter	35
59	Variation in Circumferential Traverse with Swirl at Vane Mid Span	35
60	Swirl Effect of Vane Feed	36
61	AGT 100 Mod I Metal Power Turbine Scroll Computer Model Simulation	36
62	AGT 100 Combustor Steady-State 96 km/h (60 mph) Temperature Profiles	37
63	AGT 100 Combustor Thermal Gradient and Stress Overview	37
64	Effect of Variable Geometry Position Accuracy on Emissions	38
65	AGT 100 Mod I Combustor	38
66	AGT 100 Mod I Pilot Assembly	38
67	AGT 100 Combustor Rig—Top View	39
68	AGT 100 Combustor Rig—Exhaust Instrumentation	39
69	AGT 100 RPD Initial Regenerator Generator Arrangement	41
70	Revised RPD Regenerator Preliminary Design	42
71	Transient Cycle Parameters for Idle to Full Power	43
72	Comparison of Disk Temperature Distribution for Uniform and Severely Distorted Flow Conditions	44
73	Estimated Temperatures of Disk/Ring Gear Elastomer Joint	44
74	Regenerator Disk Finite Element Stress Model	45
75	Cross Section of Regenerator Seal Cross-Arm at Hub (Initial AGT 100 Configuration)	46
76	Summary of Temperatures Calculated for the Regenerator Cross-Arm (Negative Side) Mid-Span	46
77	Summary of Temperatures for the Regenerator Rim Seal-Hot Side	46
78	Regenerator Cross-Arm Metal Leaf Seal Temperature at 48km/h (30 mph)	46
79	Inboard Regenerator Seal Finite Element Model	47
80	Regenerator Hot Test Rig—Working Section	48
81	Seal Leaf Leakage Test Rig	49
82	Model of Block and Associated Components	51
83	Etched Polished Surface of Hot Pressed Mullite	53
84	Elemental Analysis of Impurities in Hot Pressed Mullite	54
85	X-ray Diffraction Pattern of Mullite With Secondary Phases Present	56
86	Fracture Surface Showing SiO_2 Failure Source	56
87	Fracture Surface Showing TiO_2 Failure Source	57
88	Green Machined Isopressed RBSiC Gasifier Rotor After Siliconization	57
89	Thixotropically Cast RBSiC Rotor With Shaft Extension Attached and Siliconized	57
90	Green Transfer Molded RBSiC Gasifier Rotors, New Mix Composition	59
91	Solid One-Piece Injection Molded Sintered Alpha SiC Gasifier Rotor	60
92	One-Piece Barrel Plaster Mold for Combustor Body	61
93	Green Slip-Cast Alpha SiC Combustor Made from One-Piece Mold	61
94	One-Piece Barrel Plaster Mold for Combustor Body Without Cross Bars	61
95	Green Slip-Cast Alpha SiC Combustor Without Air Intake Slots	61
96	Sintered Alpha SiC Slip-Cast Combustor	62
97	Wood Gasifier Turbine Outer Backplate Model	62
98	Epoxy Gasifier Turbine Outer Backplate Pattern for Making Slip-Cast Molds	62
99	Plaster Slip-Casting Mold for the Outer Gasifier Backplate	63
100	Sintered Alpha Slip-Cast Gasifier Rotor Scroll Backplate With Thick Tab and Vane Pocket Regions	63
101	Gasifier Scroll Slip-Casting Pattern	63
102	Epoxy Mold Castings Made from the Original Wood Gasifier Scroll Slip-Casting Pattern	63

Figure	Title	Page
103	Plaster Mold for Slip-Casting Gasifier Scroll	64
104	Green Slip-Cast Alpha SiC Gasifier Scroll	64
105	Sintered Alpha SiC Slip-Cast Gasifier Rotor Scroll and Backplate	65
106	Isopressed Sintered Alpha SiC Combustor Dilution Ring, Finish Ground	65
107	Isopressed Sintered Alpha SiC Combustor Swirl Plate, Finish Ground	65
108	Isopressed Sintered Alpha SiC Combustor Flange, Finish Ground	65
109	Isopressed Sintered Alpha SiC Pilot Flame Tube, Finish Ground	66
110	Underspeed Control Modes.	70
111	Start Control Modes	71
112	Typical THM440-T4 Shift Pattern	73
113	AGT 100 with THM 440-T4 Powertrain Performance at Steady State	74
..		
	Appendix	
114	Strength Levels Achieved in Various Density Ranges for CVD Coated Bars	82
115	Microstructures and Failure Origins for Injection Molded SiC Specimen Used as Control in CVD Evaluation Studies	82
116	Coating Evaluation for MTC-Coated Specimens	83
117	Coating Evaluation for DCI-Coated Specimens	83
118	Coating Evaluation for RCI-Coated Specimens	84
119	San Fernando Laboratories CNTD-Coating Evaluations	84
120	Appearance of a $100 \mu\text{m}$ (.004 in.) Void Detected by Microfocus X-ray	85
121	Ultrasonic A- and C-Scans for 12.7 mm (0.50 in.) Thick Disk of Alpha SiC Containing Seeded 125-250 μm Voids. Longitudinal Wave Velocity, $V_e = 11.80 \times 10^3 \text{ m/s}$	86
122	Ultrasonic A- and C-Scans for 6.33 mm (0.25 in.) Thick Disk of Alpha SiC Containing Seeded 125-250 μm B_4C Inclusions. $V_e = 11.9 \times 10^3 \text{ m/s}$.	86
123	Ultrasonic C-Scan of Seeded Void Plate at 36MHz.	87
124	Ultrasonic C-Scan of Seeded Void Plate at 36 MHz With Transducer on the opposite face of the plate	87
125	Effect of Attenuation Selection Characteristics on the C-Scan Indications for Alpha Silicon Carbide Test Bar	88
126	RBSiC Bar 175	88
127	Region outside of the central area of the bar	89
128	Zone of transmission variation	89
129	100 MHz micrographs showing two low contrast flaws	89
130	Acoustic micrographs showing large high contrast	90
131	Flaw Features	90
132	Vane 184	91
133	Sample V2-3	92
134	Amplitude micrograph	93
135	Two circular structures found near tip of the airfoil	93
136	Area of the airfoil of Vane 321	93
137	Block Diagram of the Apparatus	94
138	Polished SiC Knoop Flaw #1	95
139	Polished SiC Knoop Flaw #18	95
140	Polished SiC Knoop Flaw #7	96
141	Unpolished SiC Surface (No Knoop Flaw)	96
142	High Temperature Strength Retention of Silicon Carbide Materials	97
143	Static Stress Rupture Plots for Compression Molded Reaction Bonded SiC (a) at 1000°C (1832°F) and (b) at 1200°C (2192°F) in Air in 4-Point Bend	98
144	Creep Curves at 1200°C (2192°F) for Fine Grain Reaction Sintered SiC in Air in 4-Point Bend	99
145	Creep Rate Data at 1200°C (2192°F) for Fine Grain Reaction Sintered SiC	99
146	Thermal Diffusivity Measurements for (a) Sintered Alpha SiC and (b) Reaction Bonded Silicon Carbide	99

LIST OF TABLES

Table	Title	Page
I	AGT 100 Driving Cycle Fuel Economy Sensitivities	7
II	Phoenix Weight Summary	10
III	Summary of Compressor Rig Instrumentation	11
IV	AGT 100 Static Structure Deflections	12
V	Mod I and RPD Gasifier Turbine Parameters for Various Engine Operating Points	18
VI	Mod I and RPD Power Turbine Parameters for Various Engine Operating Points	28
VII	Interturbine Duct Test Conditions	32
VIII	Steady State Regenerator Operating Conditions	43
IX	Stress/Strength Comparisons	43
X	Loss in Tangential MOR	49
XI	Total Heat Rejection of RPD Engine	52
XII	Mullite Strength Summary	55
XIII	4-Point Bend Test Results of Thixotropic Cast RBSiC	58
XIV	Rotor Mix Identities	59
XV	Strength of SiC Components	64
Appendix		
XVI	Effect of Chemistry on Strength of Hot Pressed Alpha Silicon Carbide	80
XVII	Strength Evaluation of CVD-Coated Alpha SiC Bars	80
XVIII	Results of "Hipping" Plates of Pre-Sintered Alpha Silicon Carbide	81
XIX	Detection of Defects in Seeded Disks of Sintered Alpha SiC by Microfocus X-ray	85
XX	Flaw Location—Seeded Disks	91
XXI	Carborundum Flaw Locations	92
XXII	Flaw Definitions	92
XXIII	Defective Types and Distributions in Flexural Strength Specimens	97
XXIV	Distribution of Failure Origins	97
XXV	Distribution of Failure Origins	97

Figure	Title	Page
103	Plaster Mold for Slip-Casting Gasifier Scroll.	64,
104	Green Slip-Cast Alpha SiC Gasifier Scroll	64
105	Sintered Alpha SiC Slip-Cast Gasifier Rotor Scroll and Backplate	65
106	Isopressed Sintered Alpha SiC-Combustor Dilution Ring, Finish Ground	65
107	Isopressed Sintered Alpha SiC Combustor Swirl Plate, Finish Ground	65
108	Isopressed Sintered Alpha SiC Combustor Flange, Finish Ground	65
109	Isopressed Sintered Alpha SiC Pilot Flame Tube, Finish Ground	66
110	Underspeed Control Modes	70
111	Start Control Modes	71
112	Typical THM440-T4 Shift Pattern	73
113	AGT 100 with THM 440-T4. Powertrain Performance at Steady State	74
Appendix		
114	Strength Levels Achieved in Various Density Ranges for CVD Coated Bars	82
115	Microstructures and Failure Origins for 'Injection Molded' SiC Specimen Used as Control in CVD Evaluation Studies	82
116	Coating Evaluation for MTC-Coated Specimens	83
117	Coating Evaluation for DCI-Coated Specimens	83
118	Coating Evaluation for RCI-Coated Specimens	84
119	San Fernando Laboratories CNTD-Coating Evaluations	84
120	Appearance of a $100 \mu\text{m}$ (.004 in.) Void 'Detected' by Microfocus X-ray	85
121	Ultrasonic A- and C-Scans for 12.7 mm (0.50 in.) Thick Disk of Alpha SiC Containing Seeded 125-250 μm Voids. Longitudinal Wave Velocity, $V_e = 11.80 \times 10^3 \text{ m/s}$.	86
122	Ultrasonic A- and C-Scans for 6.33 mm (0.25 in.) Thick Disk of Alpha SiC Containing Seeded 125-250 μm B_4C Inclusions. $V_e = 11.9 \times 10^3 \text{ m/s}$.	86
123	Ultrasonic C-Scan of Seeded Void Plate at 36MHz	87
124	Ultrasonic C-Scan of Seeded Void Plate at 36 MHz With Transducer on the opposite face of the plate.	87
125	Effect of Attenuation Selection Characteristics on the C-Scan Indications for Alpha Silicon Carbide Test Bar	88
126	RBSiC Bar 175	88
127	Region outside of the central area of the bar	89
128	Zone of transmission variation	89
129	100 MHz micrographs showing two low contrast flaws	89
130	Acoustic micrographs showing large high contrast	90
131	Flaw Features	90
132	Vane 184	91
133	Sample V2-3	92
134	Amplitude micrograph	93
135	Two circular structures found near tip of the airfoil	93
136	Area of the airfoil of Vane 321	93
137	Block Diagram of the Apparatus	94
138	Polished SiC Knoop Flaw #1	95
139	Polished SiC Knoop Flaw #18	95
140	Polished SiC Knoop Flaw #7	96
141	Unpolished SiC Surface (No Knoop Flaw)	96
142	High Temperature Strength Retention of Silicon Carbide Materials	97
143	Static Stress Rupture Plots for Compression Molded Reaction Bonded SiC (a) at 1000°C (1832°F) and (b) at 1200°C (2192°F) in Air in 4-Point Bend	98
144	Creep Curves at 1200°C (2192°F) for Fine Grain Reaction Sintered SiC in Air in 4-Point Bend	99
145	Creep Rate Data at 1200°C (2192°F) for Fine Grain Reaction Sintered SiC	99
146	Thermal Diffusivity Measurements for (a) Sintered Alpha SiC and (b) Reaction Bonded Silicon Carbide	99

LIST OF TABLES

Table	Title	Page
I	AGT 100 Driving Cycle Fuel Economy Sensitivities	7
II	Phoenix Weight Summary	10
III	Summary of Compressor Rig Instrumentation	11
IV	AGT 100 Static Structure Deflections	12
V	Mod I and RPD Gasifier Turbine Parameters for Various Engine Operating Points	18
VI	Mod I and RPD Power Turbine Parameters for Various Engine Operating Points	28
VII	Interturbine Duct Test Conditions	32
VIII	Steady State Regenerator Operating Conditions	43
IX	Stress/Strength Comparisons	43
X	Loss in Tangential MOR	49
XI	Total Heat Rejection of RPD Engine	52
XII	Mullite Strength Summary	55
XIII	4-Point Bend Test Results of Thixotropic Cast RBSiC	58
XIV	Rotor Mix Identities	59
XV	Strength of SiC Components	64
Appendix		
XVI	Effect of Chemistry on Strength of Hot Pressed Alpha Silicon Carbide	80
XVII	Strength Evaluation of CVD-Coated Alpha SiC Bars	80
XVIII	Results of "Hipping" Plates of Pre-Sintered Alpha Silicon Carbide	81
XIX	Detection of Defects in Seeded Disks of Sintered Alpha SiC by Microfocus X-ray	85
XX	Flaw Location—Seeded Disks	91
XXI	Carborundum Flaw Locations	92
XXII	Flaw Definitions	92
XXIII	Defective Types and Distributions in Flexural Strength Specimens	97
XXIV	Distribution of Failure Origins	97
XXV	Distribution of Failure Origins	97

Summary

Detroit Diesel Allison (DDA), Division of General Motors Corporation, is conducting a 68 month Advanced Gas Turbine Powertrain System Development project under contract DEN 3-168 to NASA Lewis Research Center, sponsored with funds from the Department of Energy Office of Transportation Programs

The objective of the project is to develop an experimental powertrain system that demonstrates; (1) a combined cycle fuel economy of 17.9 km/L (42.5 mpg) using diesel fuel No. 2 in a 1984 Pontiac Phoenix of 1364 kg (3000 lbm) weight on a 15.5°C (59°F) day; (2) emission levels less than federal research standards; and (3) the ability to use a variety of fuels. It is intended that the technology demonstrated through this project could assist the automotive industry in making a go/no go decision leading to production engineering development of gas turbine powertrains.

While meeting the project objective, designs are constrained to, (1) achieve reliability and life in the turbine powertrain comparable to 1985 vehicles, (2) achieve initial and life cycle powertrain costs competitive with 1985 powertrains; (3) demonstrate vehicle acceleration suitable for safety and maneuverability, and (4) meet 1985 federal vehicle noise and safety standards

The Pontiac Phoenix 1984 X-body automobile with a Hydra-Matic four-speed transmission has been selected as the demonstration vehicle. A Delco Electronics control system, using a basic automotive electronic control introduced in early 1980's General Motors cars, will be modified to serve the turbine engine. Harrison Radiator Division will supply the regenerator system for the engine. The Corning Glass Company (regenerator disks and other parts), the Carborundum Company (most hot flow path parts) and the GTE Sylvania Company (ceramic rotors) will supply the ceramic components.

Key elements of the project are developing small, high-performance aerodynamic components as well as ceramic components to meet high temperature requirements. High emphasis is placed on these two development areas

This report covers the work for the time period July 1980 through December 1980. The major accomplishments for this period are given in the succeeding paragraphs

Vehicle System Development

The main effort at Pontiac continues to be to integrate the powertrain with the vehicle. Interference points were resolved this reporting period to allow a single air cleaner to be used, where previously there had been two, and to relocate the battery in the engine compartment from its former position in the trunk. A binary heater system concept was selected which used both engine and transmission heat to heat passenger compartment air

Reference Powertrain Design

The RPD Engine Design Review was held Sept. 30, 1981. The results of this review indicated some areas of concern—primarily cost and weight, but also including heat losses and bearing DN number. These concerns were addressed directly, and the conclusion was that a design

iteration would be beneficial to help achieve project goals

A more compact configuration is evolving from the design iteration. Significant changes include elimination of cast iron hardware, locating most gears, shafts, and cold section parts within the gearbox housing, and locating most hot section parts within a cylindrical envelope defined by the regenerator diameter. Approximately 50 significant parts have been eliminated and the engine weight estimate is 3% less than a comparable 6-cylinder spark ignition engine. The compact configuration allows the heat loss to be significantly reduced such that the RPD goal appears achievable

Compressor Development

The compressor rig was completed this period and a checkout run performed on the first impeller. This first test was without inlet guide vanes and clearances were set wide to prevent accidental rubbing. The impeller also had some geometrical deviations incurred during fabrication. Rig operation was free from problems and results were encouraging. Aero and mechanical data up to 80% design speed was obtained in over 15 hours of testing.

Gasifier Turbine Development

Development activity this period focused on the design of the Mod I turbine, fabrication of rig hardware, and rig installation and checkout. The Mod I rotor has a tip diameter of 112.52 mm (4.43 in) and a tip speed of 508 m/sec (1667 ft/sec). It has been designed with emphasis on low cost, low inertia, low exit Mach number, and high efficiency.

Rig fabrication and checkout continued this period up to the point where a bearing failure in a water brake dynamometer caused damage to the rig. The rig has been rebuilt. A calibration of the torquemeter has been accomplished in preparation for turbine testing early in January 1981.

Power Turbine Development

Activity this period concentrated on design of Mod I turbine, design and fabrication of the test rig and experimental evaluation of the interturbine duct/power turbine scroll assembly. The turbine was designed with objectives similar to the gasifier turbine—low cost, low inertia, low exit Mach number, and high efficiency. The rotor is slightly larger than the gasifier rotor 148.1 mm (5.83 in) and has a somewhat reduced tip speed, 422 m/sec (1384 ft/sec).

Design, layout, and detailing were completed for the basic rig, inlet scroll and exhaust duct. Fabrication of the rig is 1/3 complete, and hardware should be complete in March 1981

The interturbine duct and power turbine scroll configurations have undergone 150 hours of cold flow testing. Results have been very encouraging. Measured interturbine duct loss is 1.15% vs RPD design goal of 1.8%, and power turbine vane loss is less than RPD goal by a slight amount.

Combustor Development

Primary effort this period was in the areas of design and stress analysis of the RPD combustor, and initial testing of the Mod I combustor. The results of the thermal gradient

analysis of the RPD combustor show the maximum gradients occur eight seconds after the start of the transient cycle. Though the maximum transient stress is more than four times the steady state stress, the magnitude is quite low, 39.5 MPa (5.7 ksi), and the probability of failure is low, 1.7×10^{-8}

A study of the effect of burner variable geometry on emissions indicates greater sensitivity at low vehicle speeds (less than 48 km/h) and that the emissions can increase by a ratio of 1.5 to 2.0 for a 1.25 mm (0.050 in) misposition.

Mod I combustor testing was initiated this period. At a burner inlet temperature of 593°C (1100°F) ignition was accomplished without difficulty and the pilot was stable at less than 0.22 kg/h (0.5 lb/h) fuel flow.

Regenerator Development

Design analysis of the RPD regenerator system continued during this period, concentrating upon the disk/ring gear assembly and the hot and cold seals.

Disk thermal analyses were completed for four steady-state conditions and indicated the maximum elastomer temperature to be within material limits. It was also found that effectiveness and thermal gradients were relatively insensitive to engine power whereas pressure drop was influenced by engine power. The most significant parameter was radial flow distribution which could lower effectiveness several percentage points, and increase both temperature gradients and pressure drop.

A new wearface platform is being designed for the crossarm seal and development is underway to permit joining the wearface material to the platform.

Mod I hardware has been designed and long lead items ordered for testing early in 1981. The hot test rig and cold flow distribution rig will be completed at this time. The seal leaf leakage rig and regenerator core LCF simulation rig are both complete at this writing.

Secondary Systems

Block and insulation studies continued. A three-dimensional finite element model of all the structural elements was constructed. Heat loss studies identified high loss areas and the results of these studies helped define critical areas to be addressed in the design iteration.

Gearbox and power transfer work progressed to the point where detail drawings were being made.

A combination starter/boost motor is being supplied by Delco-Remy. The booster is directly coupled to the gasifier shaft and is used to improve acceleration characteristics from rest. The booster is energized for very brief periods—approximately one-second duration. A brush-lifting

mechanism is being utilized to reduce brush wear since the armature turns with the engine. Brush wear and the required lifting mechanism do not appear to be a problem.

Materials Development

DDA effort includes an aluminum impeller strength investigation. Castings have been received and samples are being prepared. If the samples are sound the study to determine effects of peening on LCF properties will continue.

Under Carborundum unique effort, work was directed toward fabricating rotors and stationary parts. Six techniques for making rotors were explored— injection molding, injection molding a bladed shell and filling, slip casting into shell molds, thixotropic casting, transfer molding, and ultrasonic machining green material. From these, two methods selected for further development were injection molding and transfer molding.

A variety of stationary parts have been made—primarily combustor items and gasifier scroll parts. These have been fabricated by slip casting, isostatic pressing, and injection molding, depending on the part geometry and physical requirements.

Controls Development

A control specification was prepared and design has started on selected items. Delco Electronics has developed environmental and electrical operating characteristics of the electronic control, as well as estimates of size and weight. DDA control effort has concentrated upon hardware definition and control mode definition. Hardware items included the electronic control, sensors, fuel system, actuators, and power transfer clutch control. Control mode studies were conducted for the electronic control, underspeed governor, start control, overspeed protection, and burner variable geometry.

Transmission Development

Transmission shift schedules have been developed using the Hydra-matic THM 440-T4 transmission with the AGT 100 engine. Optimization studies indicate that maximum fuel economy is achieved with only modifications to the 3-4 shift valve on the 440-T4 transmission.

Supportive Manufacturing, Cost, and Marketability

Pontiac continued the manufacturability and cost studies for the RPD. The costs of some of the parts were exceeding goals, and the desire to reduce overall costs helped lead to a design iteration. Preliminary review of the new design indicate cost concerns are being reduced greatly.

Introduction

This is one of a series of semi-annual reports documenting work performed on an Advanced Gas Turbine (AGT) powertrain system development project for automotive applications. The work is performed under NASA/DOE contract DEN3-168. The objective of the project is to develop an experimental powertrain system that demonstrates (1) a combined cycle fuel economy of 17.9 km/L (42.5 mpg) using diesel fuel No. 2 in a 1984 Pontiac Phoenix of 1364 kg (3000 lbm) weight on a 15.5°C (60°F) day, (2) emission levels less than federal standards, and (3) the ability to use a variety of fuels. It is intended that the technology demonstrated through this project would assist the automotive industry in making a go/no go decision regarding the production engineering development of gas turbine powertrains.

In meeting the project objective, the design is constrained to (1) achieve reliability and life comparable to conventional 1985 vehicles, (2) achieve initial and life cycle powertrain costs competitive with 1985 powertrains, (3) demonstrate vehicle acceleration suitable for safety and maneuverability, and (4) meet 1985 federal vehicle noise and safety standards.

A team concept is used in this project, with many of the team members being General Motors Divisions. Detroit Diesel Allison (DDA) is the prime contractor and team leader with responsibility for the overall powertrain and controls. Pontiac Motor Division (PMD) has vehicle responsibility. Delco Electronics will develop the electronic control, and Delco Remy will develop the starter/boost system for the engine. Hydra-matic Division will produce the four-speed automatic transmission that will be used with the engine, and Harrison Radiator Division (HRD) is involved in the regenerator design and fabrication. The primary non-GM groups on the team are Carborundum and Corning Glass Works who are involved in the ceramic effort.

Prior to this contract, DDA and PMD conducted a gas turbine powertrain concept study. In July 1979 the results of the concept study⁽¹⁾ were published by DDA. In this study several configurations had been evaluated and a two-shaft regenerative engine coupled with a conventional automatic transmission was recommended as providing the potential for meeting the established goals. Further results of the concept study were published in March 1980⁽²⁾ wherein the long-lead technology development tasks required to support the design and development of an Experimental Advanced Gas Turbine Powertrain were presented. Both these studies were funded through NASA contract DEN3-28.

The current project became effective October 1979. As shown in Figure 1 the program is 68 months long, and divided into two phases. Phase I is 45 months long and Phase II is 23 months. Establishing and maintaining a Reference Powertrain Design (RPD) is a continuing activity as is component development effort. In addition, two experimental powertrain versions will be designed, fabricated and tested. Mod I, the first, is the early version and is a stepping stone to Mod II, which is the final project version. Powertrain testing will be conducted on engine dynamometer as well as in vehicles.

The Reference Powertrain Design (RPD) is a preliminary engineering design of the powertrain system which has the best potential for meeting the goals and objectives of the project. The RPD can incorporate timely emerging technologies, and it will be updated as project activity progresses.

The RPD in this current program evolved from the earlier studies identified previously. The RPD is presented as a "concept" of a fully developed production powertrain. The Mod I and Mod II experimental engines should converge toward the RPD as this development project proceeds.

The main development challenges in the program are in building small, high-performance gas turbine components and developing ceramic components for the required high engine cycle temperatures that are price competitive and which can be produced in an automotive production environment. Because of the small size engine [0.35 kg/s (0.77 lbm/sec) airflow] extensive rig testing is planned for component development. A major ceramic component development program is being pursued, and the ultimate success of the engine depends heavily on the success of this activity.

This report is structured on a component basis (e.g., all work relating to the gasifier turbine rotor, including rig work and ceramic rotor development, is discussed as a part of the gasifier turbine section). Exceptions to this are functional areas that are not peculiar to any one major component. Engine subsystems cover structures, gearbox and power transfer, rotor bearings, shafts/seals, and secondary flow. There are separate sections for materials development and controls development.

The report treats the largest item, the vehicle, first, then the engine/powertrain, then the major components of the powertrain followed by the subsystems, materials, and controls. The transmission and manufacturing feasibility and cost efforts are treated last. Within each section the work discussed is identified as it pertains to the RPD, Mod I, or Mod II designs.

ORIGINAL PAGE
BLACK AND WHITE PHOTOGRAPH

AGT-100 POWERTRAIN DEVELOPMENT SCHEDULE

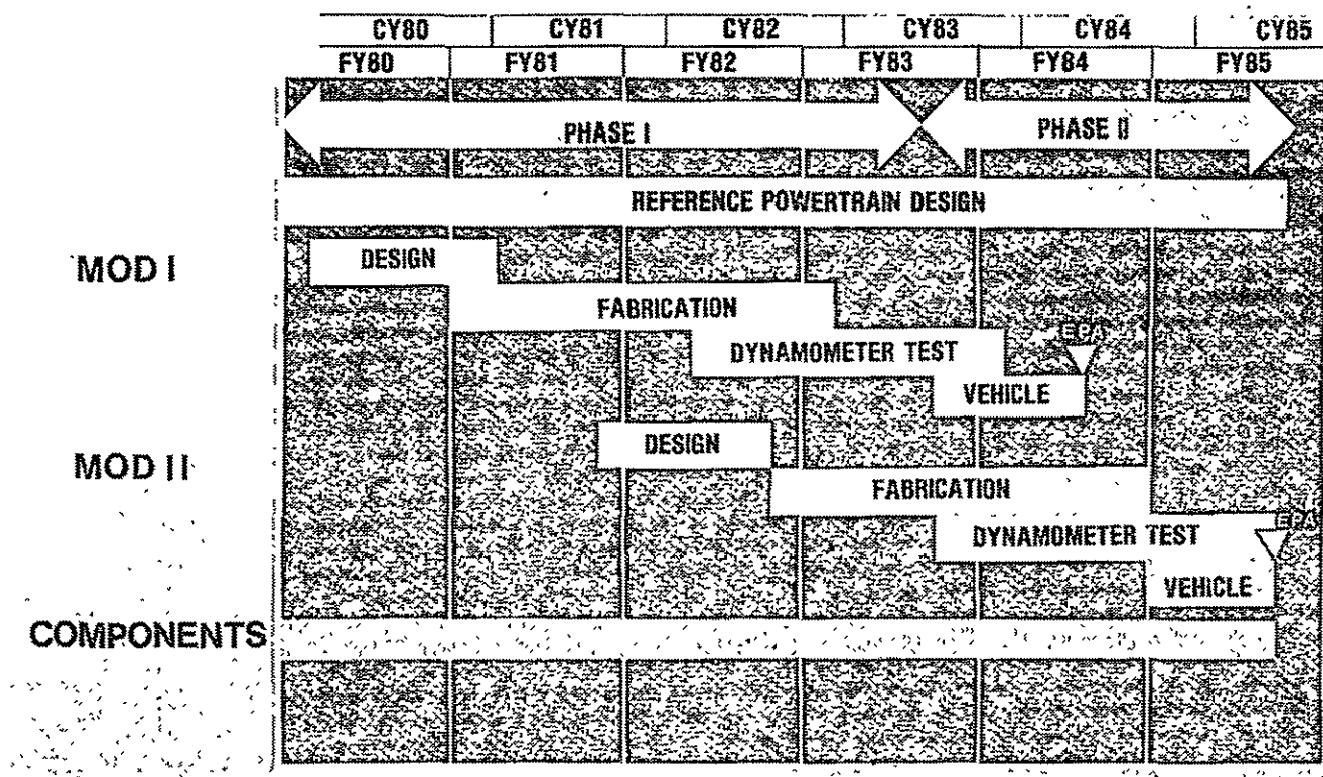


Figure 1 — Schedule

I. Vehicle System Development

1.1 Vehicle Design

The vehicle design work has continued at Pontiac with the goals of integrating the power train to vehicle components for minimum cost and minimum deviation from the baseline vehicle. The vehicle pictured in Figure 2 illustrates a standard arrangement of a single air cleaner mounted in the right front of the engine compartment allowing location of the battery in the left front.

Design iteration on installing a revised general arrangement engine was initiated. This arrangement will have lower production costs and less weight than the initial powertrain.

Exhaust System

The design of the exhaust system remains as reported in the first semi-annual report, but with additional detail of the engine to exhaust duct connection as shown in Figure 3. A cast connector has been designed to attach to the engine exhaust outlet with a spherical jointed intermediate connector between the connector and the exhaust duct. This system provides flexibility for installation with normal body to engine variations, and also provides a flexible joint to accommodate relative engine-to-body movement under operating conditions.

Engine Air Induction System

The induction system has been changed from the dual air cleaner design described in the first semi-annual report to a single air cleaner as shown in the vehicle pictured in Figure 2. This was accomplished by designing a two element single air cleaner which could take advantage of more of the available space in the fender skirt area, and by accepting a smaller filter area, 0.181 m^2 (281 in.²) vs 0.226 m^2 (350 in.²). This size filter will not affect engine operation, but will require more frequent changes than the baseline vehicle change frequency of 30,000 miles.

Battery Installation

The battery installation has been changed from the rear cargo area, as described in the first annual report, to the left front engine compartment area as shown in the vehicle pictured in Figure 2. This was made possible by eliminating the left front air cleaner and by reworking the fender skirt to allow placement of the battery further outboard than in production vehicles.

Vehicle Heating System

A vehicle heating system is proposed as shown in the schematic, Figure 4. This system utilizes the standard pro-

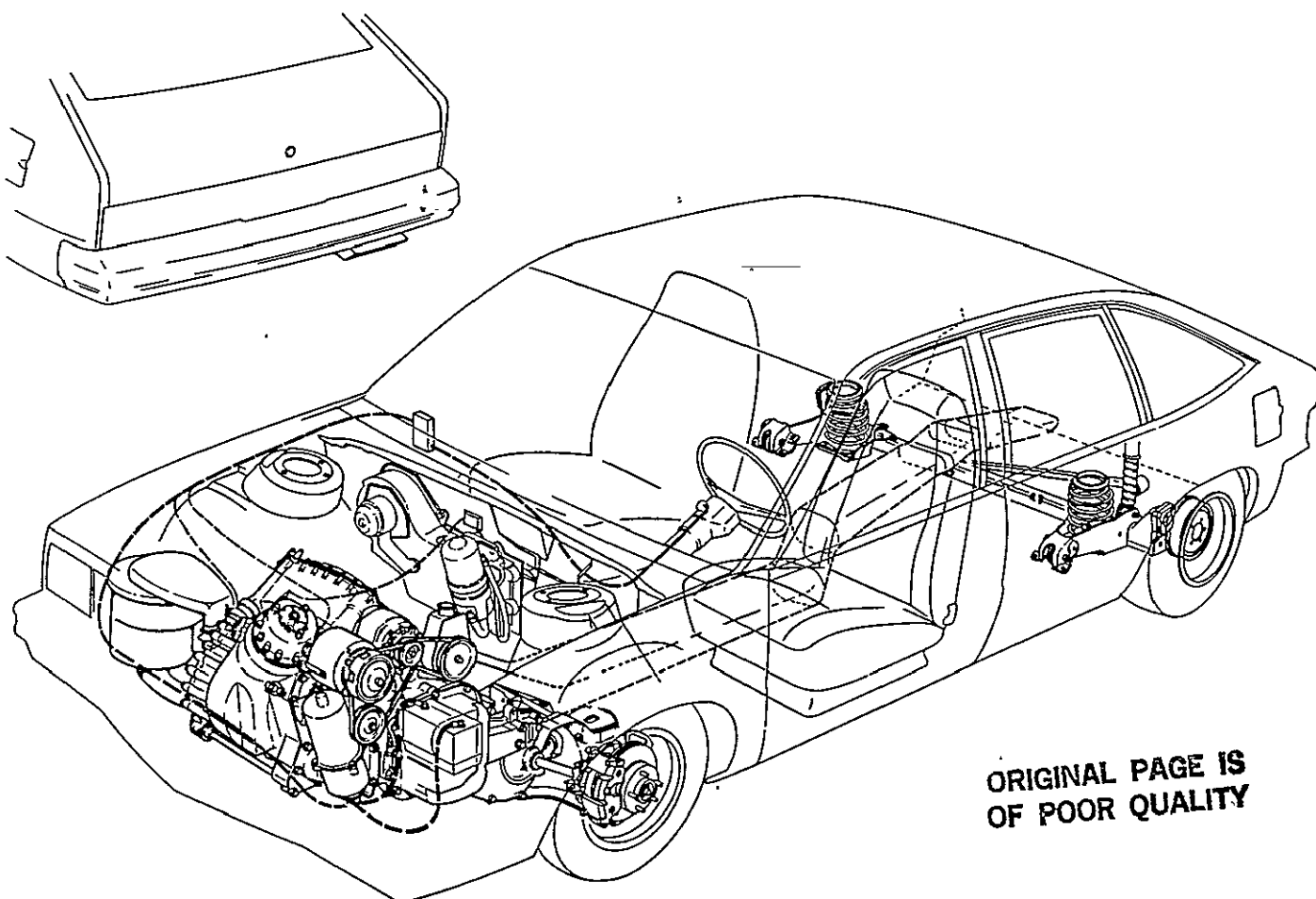


Figure 2 — AGT 100 Gas Turbine Powered Pontiac Phoenix

production heater core and air conditioning system, but also uses engine and transmission heat, via oil to water heat exchangers, to supply vehicle heat under moderately cold ambient conditions. Under more extreme cold conditions engine exhaust gas is used to supply supplemental heat to the water

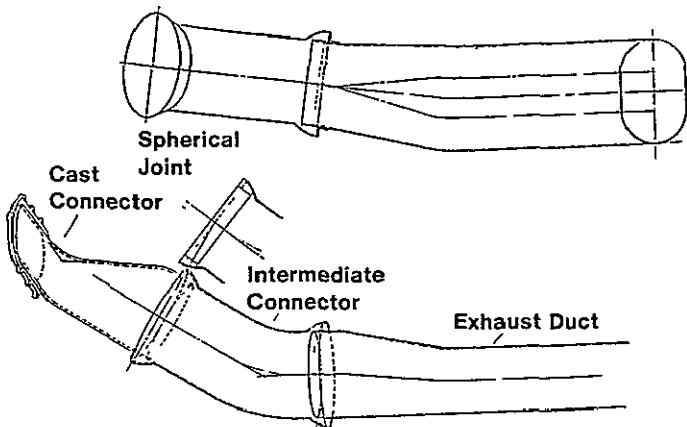


Figure 3 — Engine Exhaust Flange to Exhaust Duct

A radiator is incorporated in the system to use as a heat dump under hot ambient conditions for engine and transmission cooling.

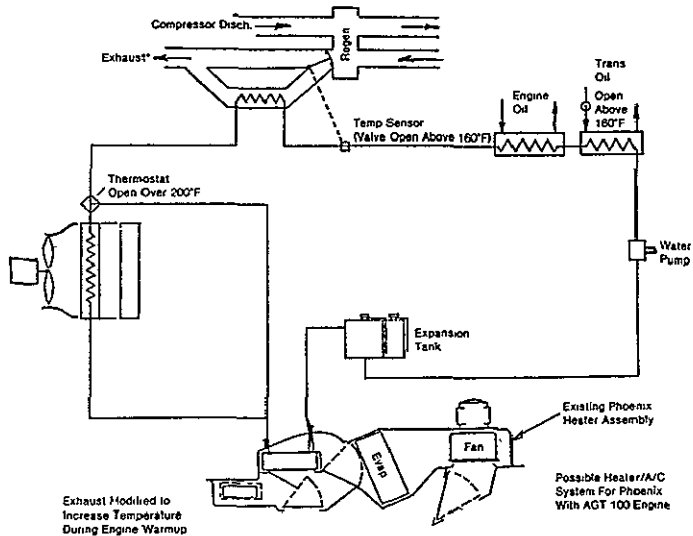


Figure 4 — Vehicle Heating System

ORIGINAL PAGE IS
OF POOR QUALITY

21-06771-51-1-1
V771210-1-1

II. Engine Powertrain Development

2.1 Reference Powertrain Design

General Arrangement (original)

The original AGT 100 General Arrangement (Figure 5) and its components were described in detail in the first semi-annual report CR-165178

The AGT 100 engine is a two-shaft, regenerative gas turbine that, when coupled to an existing production 4-speed automatic transmission, can be installed in any of the General Motors front wheel drive automobiles (X-body)

The engine operation can be summarized as follows: Inlet air passes through a conventional automotive air cleaner to the compressor. There it passes through variable inlet guide vanes (which can be used to change engine air flow) and then to an aluminum impeller where it is compressed. The compressed air passes from the impeller through a parallel-wall radial-vaned diffuser and is collected by an aluminum scroll. The compressor discharge air then passes through the high pressure side of a rotating ceramic regenerator disk where it is heated. From the regenerator it flows through a ceramic combustor

Fuel is mixed with the air and burned in the combustor to bring the temperature of the fuel/air mixture to 1288°C (2350°F). A variable geometry arrangement is used to control emissions over the operating range. The hot gases are collected by an inlet scroll where the vanes direct the flow to the gasifier turbine. Sufficient power is extracted at this point to meet the requirements of the compressor, oil pump, and power transfer clutch.

The discharge from the gasifier turbine is directed through an interturbine duct to another scroll and vane arrangement at the power turbine. The vanes direct the flow to the power turbine where the power for vehicle and accessory needs is extracted. The flow from the power turbine is through the low pressure side of the regenerator to the exhaust.

The power turbine drives a reduction gear train which lowers the output to a speed appropriate for the transmission, accessories, and power transfer clutch.

The rotors, vanes, backplates, and scrolls for both turbines are ceramic.

General Arrangement (iteration)

The initial RPD design review was completed by September 30, 1980 as scheduled. The results of this review, along with additional information, indicated some areas of concern. These were cost, weight, heat losses and bearing DN number.

The conclusion was that an iteration in the design would be beneficial in reaching the program objectives. This iteration has resulted in a rearrangement of the existing components into the engine shown in Figure 6. The view is looking aft from the front of the vehicle. Changes to the general arrangement are as follows:

1. The gasifier has been rotated 180° and relocated from the left side of the engine to the right side where the compressor and main shaft bearings are integrated into the gearbox.

2. The shafting, bearings, and bevel gears associated with the power transfer system have been eliminated. Only

straight or helical spur gears are now used, and all are contained within the gearbox with the exception of the regenerator pinion and gear

3. The block has been eliminated. The main engine structure is now the two aluminum gearbox castings which contain the main shaft bearings and the locating features for the turbine scrolls/shrouds.

4. The regenerator has been moved from its former position at the rear of the engine to the left end of the engine where it is connected to the gearbox by a cylindrical pressure vessel which contains the hot engine components

5. The bore of the mainshaft thrust bearings was reduced in the revised general arrangement. As a result, the reliability of the mainshaft bearings has been enhanced. In the redesign, approximately 51 parts have been eliminated. Among these are:

- 6 cast iron castings
- 4 aluminum castings
- 7 accessory bearings
- 4 bevel and 1 worm gear sets

This, plus ease of assembly and other cost reduction measures, improve significantly the cost assessment for the engine.

Performance

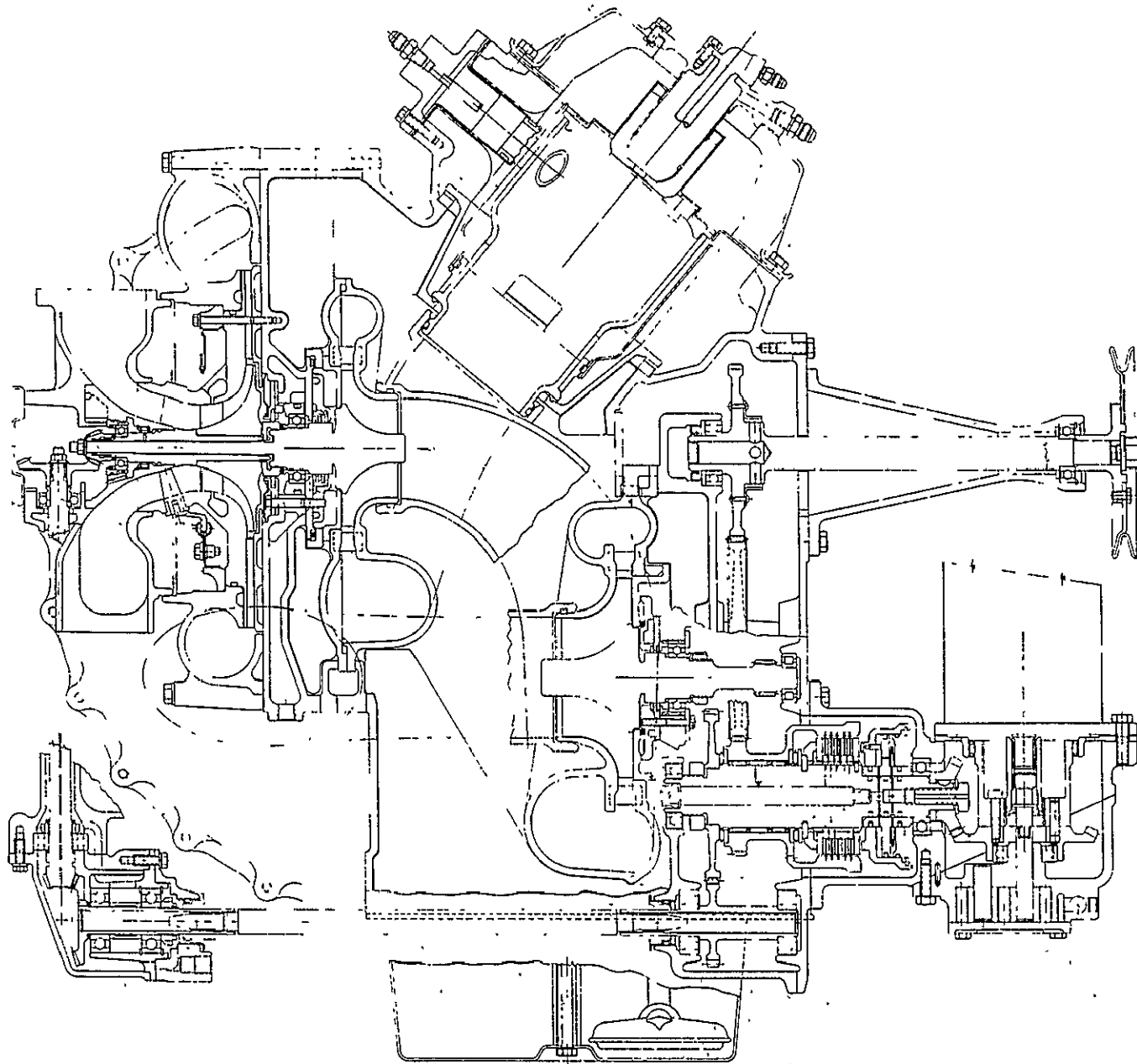
An integrated engine cycle/vehicle simulation computer program was developed. This program can be used to evaluate system performance through a prescribed schedule such as the Federal Driving Cycle. The program has component dynamic performance capability and will be used for control mode studies and to determine the effects of heat storage and volume dynamics on driving cycle fuel economy.

Driving cycle fuel economy engine sensitivity estimates were completed for the RPD engine and are shown in Table I. The parameters investigated included component efficiencies, ducting pressure drops, overboard and regenerator leakage, and mechanical losses.

Table I
AGT-100 Driving Cycle Fuel Economy Sensitivities

One Point Parameter Change at Max Power	Percent Change in Driving Cycle Fuel Economy
-1.0% compressor efficiency	-0.75%
-1.0% gasifier turbine efficiency	-0.45%
-1.0% power turbine efficiency	-0.40%
-1.0% regenerator effectiveness	-4.20%
+1.0% heat rejection	-0.95%
+1.0% overboard leakage	-0.65%
+1.0% regenerator leakage	-1.90%
+1.0% compressor inlet pressure loss	-0.15%
+1.0% compressor to gasifier turbine pressure loss	-0.95%
+1.0% gasifier turbine to power turbine pressure loss	-0.45%
+1.0% power turbine diffuser pressure loss	-0.2%
+.75 kw (+1.0 hp) gasifier accessory drive power	-3.00%
+75 kw (+1.0 hp) power turbine accessory drive power	-3.00%

ORIGINAL PAGE IS
OF POOR QUALITY



BASIC ENGINE SECTION

Figure 5 — Initial RPD Engine Arrangement

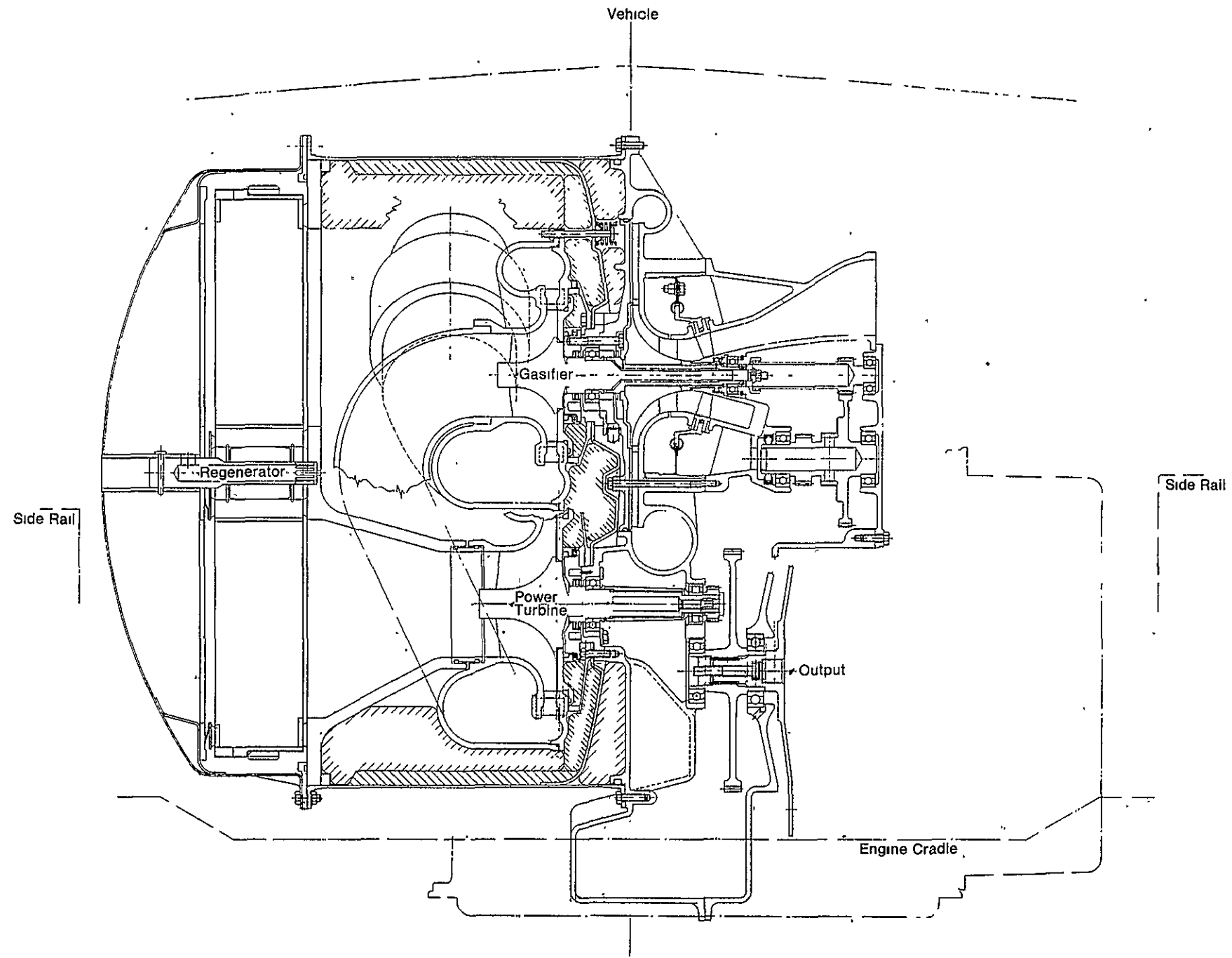


Figure 6 — AGT 100 General Arrangement

ORIGINAL PAGE IS
OF POOR QUALITY

100-100

Studies of various methods of vehicle heating and defrosting were made. These studies were necessary because the engine exhaust alone was insufficient to meet the minimum requirement at idle on a -18°C (0°F) day.

Several methods of supplementing or increasing the available exhaust heat were investigated:

- engine and transmission oil exhaust heat
- power turbine exhaust bleed
- combustor inlet bleed
- regenerator cold and/or hot side flow blockage
- mechanical power extraction to drive a supplemental system, i.e., alternator/resistance heater or air compressor.

The current plan is to supplement the engine exhaust heat with waste heat from the engine and transmission. The method will result in minimal loss to the engine cycle and therefore have little effect on vehicle fuel economy.

Weight

The revised engine general arrangement has reduced the vehicle weight, shown in Table II with the gas turbine option, to be slightly less than the baseline vehicle.

TABLE II
Phoenix Weight Summary
6 Cylinder Spark Ignition & AGT 100 Gas Turbine

	Baseline 6 Cyl. S.I.	AGT 100
Base Engine, kg (lbs)	141.4 (311)	137.3 (302)
+ Engine Dress Items	48.6 (107)	50.0 (110)
Dressed Engine	190.0 (418)	187.3 (412)
+ Transaxle	70.0 (154)	77.3 (170)
Powertrain Weight	260.0 (572)	264.5 (582)
+ Vehicle W/O Powertrain	998.2 (2196)	988.6 (2175)
Vehicle Curb Weight	1258.2 (2768)	1253.2 (2757)
+ 2 Person Allowance	136.4 (300)	136.4 (300)
Loaded Vehicle Weight	1394.5 (3068)	1389.5 (3057)

Heat Loss

The design approach to reduce heat loss was to:

1. Isolate the hot section and cold sections of the engine from each other.
2. Shield the end of the hot section with the hot side of the regenerator.
3. Minimize the "short circuits" where hot ceramic parts are cross keyed to metal structure.
4. Remove metal parts from the hot section—including the use of a lithium aluminum silicate (LAS) ceramic regenerator crossarm in lieu of a cast iron crossarm.
5. Provide room for adequate insulation; optimize the insulation for temperature capability and thermal conductivity for each location.

As a result of these changes, it is possible to attain the heat loss goal shown in Figure 7.

ORIGINAL PAGE IS
OF POOR QUALITY

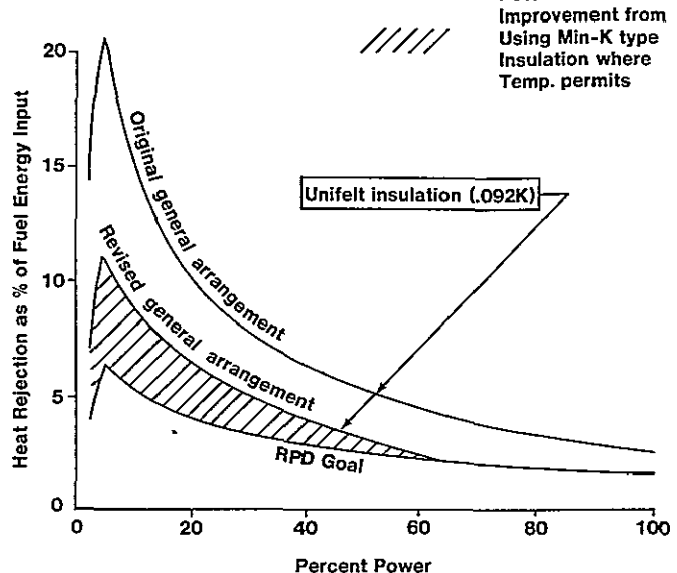


Figure 7 — AGT 100 Heat Rejection

Bearings

The use of air bearings was considered for the revised general arrangement, but conventional rolling element bearings were retained for the following reasons:

1. The ability to minimize radial running clearances on the turbines & compressor as a result of the lower bearing radial clearance.
2. The ability to minimize axial running clearances on the turbines and compressor by mounting the thrust bearing close to the aero components, thus minimizing the effects of operating deflections and temperatures.
3. Minimizing the development effort

The gains on component performance associated with tighter running clearances offset savings in mechanical losses from the incorporation of air bearings.

Results from analyses of soakback temperature of the gasifier thrust bearing shows a maximum temperature of 257°C (494°F) (see section 3.2). This represents the worst case for the initial general arrangement and is improved in the revised G A

2.2 Mod I

Design

The Mod I engine design is essentially the same as the RPD except in areas where technology advancements require demonstration before committing to engine hardware. These consist of most of the ceramic flow path components including the rotors.

Detail layouts currently underway for the new general arrangement include definition of both RPD, ceramic Mod I and the metal hot section components to be used until the ceramic components can be phased into the program.

III. Compressor Development

3.1 Compressor Aero

Design

The main effort was directed toward the fabrication of the test rig hardware, the assembly of the rig and the initial test. During fabrication, compressor hardware progress was monitored closely to expedite delivery and to minimize any deviations from design intent which might affect aerodynamic performance.

Actual surface finish was one important item monitored during fabrication. The "as machined" surface finish of flowpath hardware was evaluated visually and quantitatively (profilometer check). Where possible, the hardware was polished to provide improved surface finish.

In general the parts to be tested achieved reasonably good surface finish. Means of achieving these levels of surface finish in a production situation will be studied.

The first compressor built exhibited three major deviations from the "as designed" configuration. They were:

- (1) Inlet guide vanes (IGV's) were replaced with plugs
- (2) Initial impeller had several important hardware deviations, namely:
 - a) full blade leading edge cutback due to machining error
 - b) blunt leading edge resulting from blend operation
 - c) errant full blade-to-splitter spacing
- (3) Impeller-to-shroud clearances were set large to ensure parts safety on initial build

Replacement plugs maintained the inlet duct flowpath contour and provided a positive seal between the flowpath and the inducer bleed manifold. During subsequent testing, these plugs will be used in back-to-back testing of a compressor with and without IGV's to determine the effect of IGV wakes on compressor operation.

Detailed impeller inspection upon receipt from the vendor revealed two significant print deviations. The first was reduced throat area between the splitter and full blade which was traced, primarily, to excessive thickness near the splitter leading edge. This condition was corrected by hand blending of the splitter leading edges.

The second deviation was errant circumferential spacing of full blades and splitters. The full blades were within print limits. However, at the impeller exit, the splitters were displaced approximately $1/2^\circ$ toward the adjacent full blade pressure surface. This condition improved toward the splitter leading edge and was within print limits at this location.

A second impeller also was procured from the vendor. This impeller was inspected and proved to be superior to the first piece. Aerodynamic features of the new impeller were to print with the exception of the exit spacing. The spacing was improved compared to the first impeller. Maximum spacing errors between full blades and splitters near the exit were reduced to approximately $1/4^\circ$. The delivery date of this piece prevented its use in the first build.

Calculated changes in build-to-hot running clearances were slight, but actual rig characteristics had not been determined prior to this testing. Therefore, build clearances were set open to provide a margin for error.

Rub pins were included to provide documentation of minimum running clearances. These data will be used to safely reduce clearances in future builds.

The primary goal of the first build was to determine operational characteristics of the rig and impeller-to-cover running clearances.

The compressor rig included a full complement of instrumentation. The design and location of this instrumentation drew from past testing experience to improve reliability and provide for measurement accuracy. A summary of compressor rig instrumentation utilized in the first build of the AGT-100 compressor rig is shown in Table III.

TABLE III SUMMARY OF COMPRESSOR RIG INSTRUMENTATION

Station	Measurements			
	P _{static}	P _{total}	Total	Other
Inlet Plenum	4			4
Inlet Split Line	4 ⁽¹⁾	18 ⁽²⁾		
Shroud-Inlet to Exit		21		
Diffuser—L.E.			6	
—Throat	3			
—Exit	24		9	
Collector	12			
Bleed Manifold	3		4	
Compressor Exit	6	12	12	
Meas. Station				
Impeller Inlet, Knee, Exit				9 rub pin clearance probes

⁽¹⁾2 each inlet

⁽²⁾9 each inlet

Measurements from this instrumentation are required to provide input for use of DDA's jet/wake performance analysis model. Data reduction with this model will provide assessment of individual component performance and allow a subsequent comparison of this performance with other DDA designs.

A photograph of the first build impeller and instrumented diffuser are shown on Figure 8. Total pressure rakes at diffuser inlet and exit can be seen in the foreground of this picture. The partially assembled rig is illustrated by Figure 9. Shroud and collector instrumentation leads are apparent. The inlet can be seen just to the left of the basic rig. The completed rig is shown on Figure 10. This picture was taken from the bottom of the rig. Bifurcated features of the inlet, oil services and instrumentation leads are visible.

Rig installation in the test cell commenced in December and the first set of data obtained. Rig running gave the following accomplishments:

- Aero and mechanical data obtained up to 80% of design speed
- Rig vibration signatures were continuously monitored and frequency analyzed on line

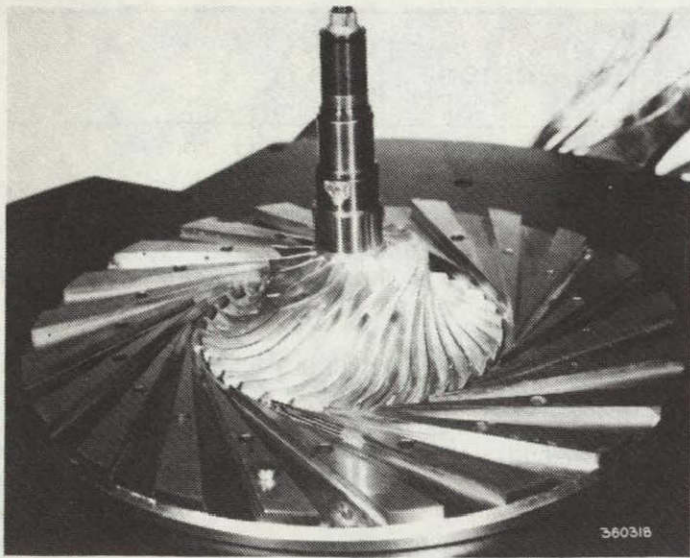


Figure 8 — AGT 100 BU 1 Impeller and Diffuser

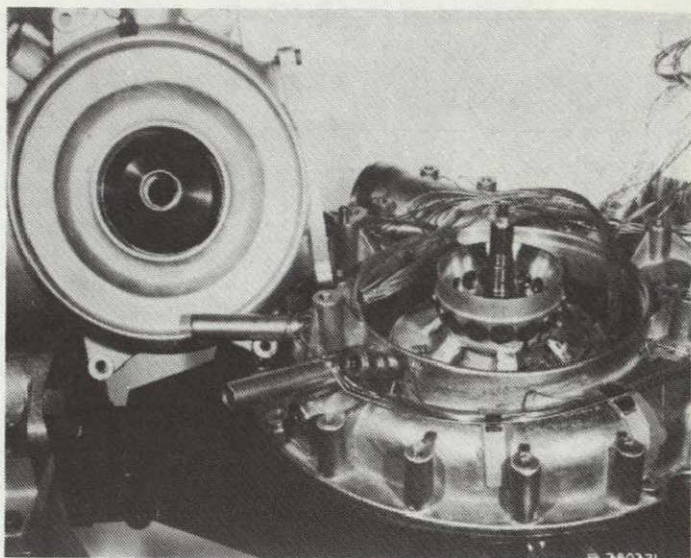


Figure 9 — AGT 100 BU 1 Partially Assembled Compressor Rig

**ORIGINAL PAGE
BLACK AND WHITE PHOTOGRAPH**

- Front isolator stiffness and damping characteristics were adjusted and the resulting effects on rig vibration levels were determined
- Rotor axial location was continuously monitored with a capacitance probe
- Four complete speed lines of aerodynamic data at 40, 50, 60 and 70% speed were obtained from choke to surge
- Aerodynamic instrumentation was checked and repaired, as necessary
- Inducer bleed flow rates were varied at each speed
- Thermal stabilization times were evaluated at each speed

Rig thermal stabilization was determined at each speed by setting off to a given back pressure and obtaining several data points in succession. Calculated efficiency was then plotted against time and stabilization was assumed when efficiency became constant. An example of this type of data is shown in Figure 11. This procedure was applied at each speed and, after stabilizing, the compressor was then loaded from choke to surge.

A performance map was generated up to 70% design speed. This initial performance data with nominal inducer bleed is shown on Figure 12. The remainder of the first build testing will be completed during the next reporting period. Data reduction from the completed first build will be used to formulate plans for the second build.

3.2 Compressor Mechanical Development

Design

To achieve the aerodynamic goals of the compressor it is necessary to predict and control the deflections between the impeller shroud and shroud cover. A finite element analysis of the compressor static structure was conducted to determine the static deflections.

The finite element model is shown in Figure 13. The deflections computed were from cold engine to stabilized 85° day maximum power conditions. The deflections of the

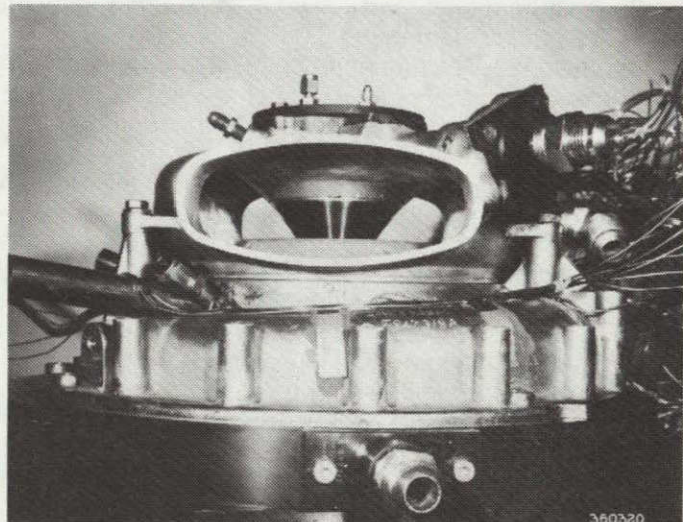


Figure 10 — AGT 100 BU 1 Compressor Rig

shroud are shown in Table IV, with axial deflections given relative to the rear thrust bearing.

The deflections computed are small. The radial (outward) deflection over the inducer is 0.0212 mm (0.0008

Node	Deflections (mm)	
	x	R
100	-0.0420	0.0090
105	-0.0370	0.0088
107	-0.0302	0.0096
114	-0.0209	0.0212
20	-0.0224	0.0353
31	-0.0373	0.1270
32	-0.0408	0.1364

Table IV — AGT 100 Static Structure Deflections

ORIGINAL PAGE IS
OF POOR QUALITY

AT 70% N/θ 0.5
VOLUME FLOW 40

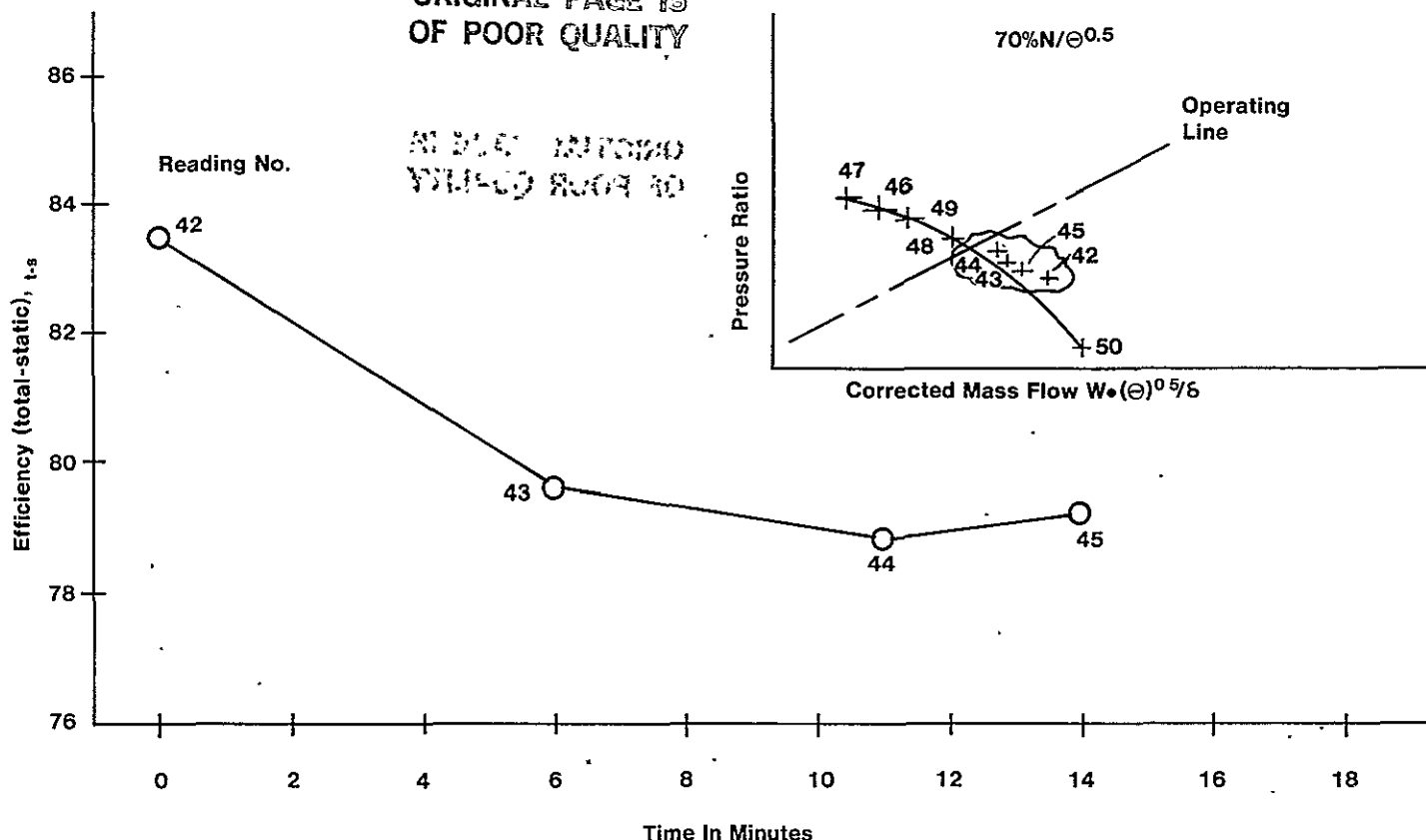


Figure 11 -- Compressor Rig Stabilization, 70% speed - BU 1

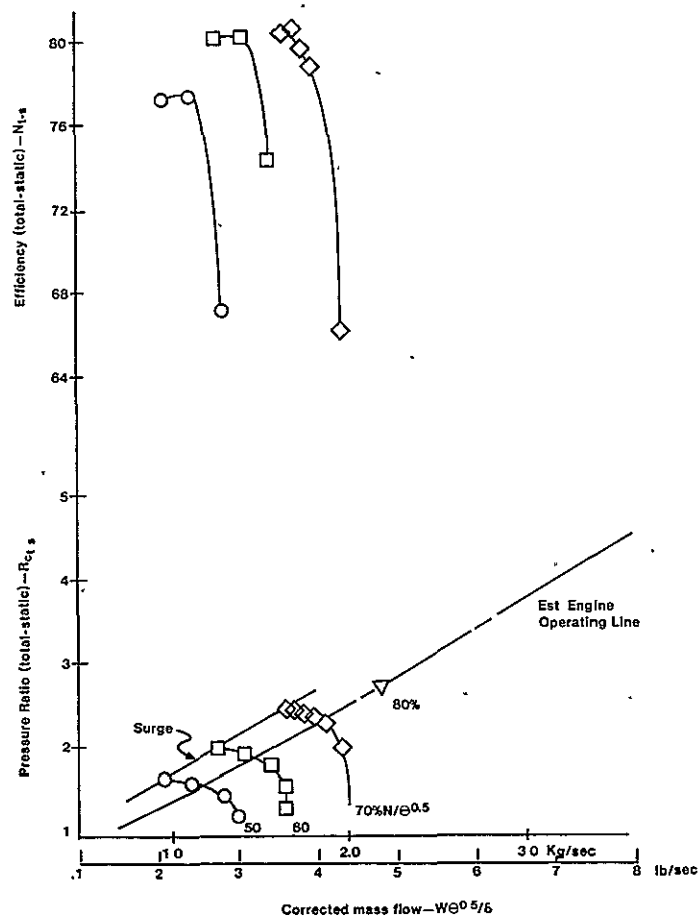


Figure 12 — Initial Performance Data

in.) while the axial deflection (forward) is 0.0373 mm (0.0015 in.). These deflections are a direct contribution to change in impeller clearance and are very acceptable levels.

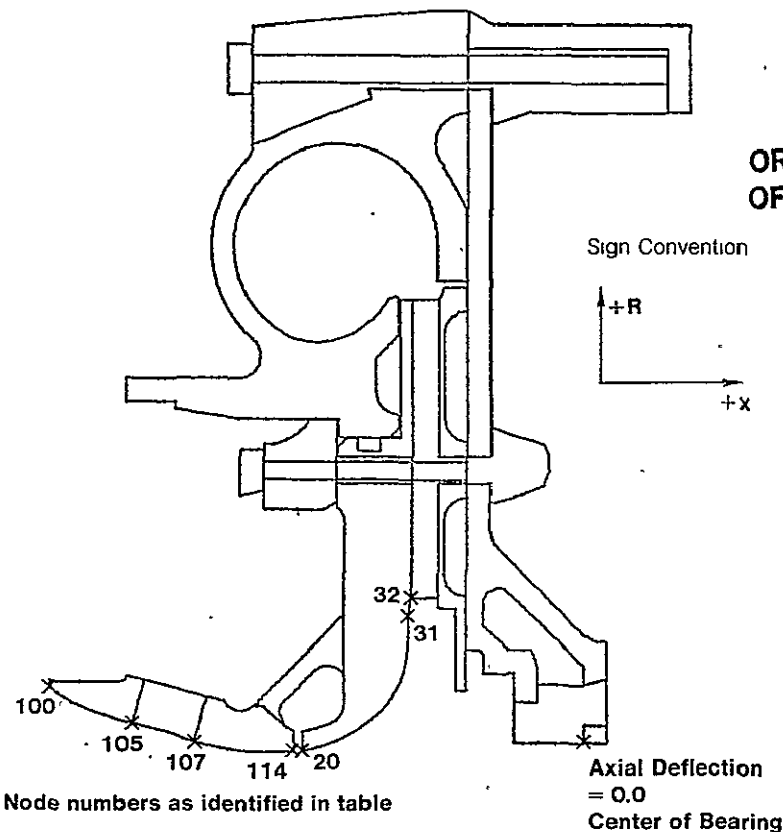
IMPELLER CONTAINMENT

One design objective of the AGT 100 program is to ensure containment of the compressor impeller should a burst occur. A study was conducted to analyze the capability of the compressor shroud and surrounding structure to absorb the energy if an impeller fails. To provide containment to 150 percent of impeller design speed, the compressor shroud wall thickness was tapered from compressor inlet to outlet as shown in Figure 14.

COMPRESSOR FRONT BEARING MASS ISOLATOR

The mass isolator is designed to minimize dynamic excitation from a source such as the bevel gear set that couples power transfer with the main shaft system. It incorporates oil squeeze film for reduced dynamic amplifications of rigid body modes excited during speed excursions below idle, and provides backup flexibility for effective isolation during transfer of power. Ref. Figure 15

The initial design of the front compressor bearing mount used a squeeze film mass isolator with two rubber O-rings to contain the oil and provide the spring force. Dynamic spring rate testing revealed that the O-rings were sensitive to temperature. For instance, using the 90 durometer O-rings at about 500 Hz frequency, the spring rate drops



ORIGINAL PAGE IS
OF POOR QUALITY

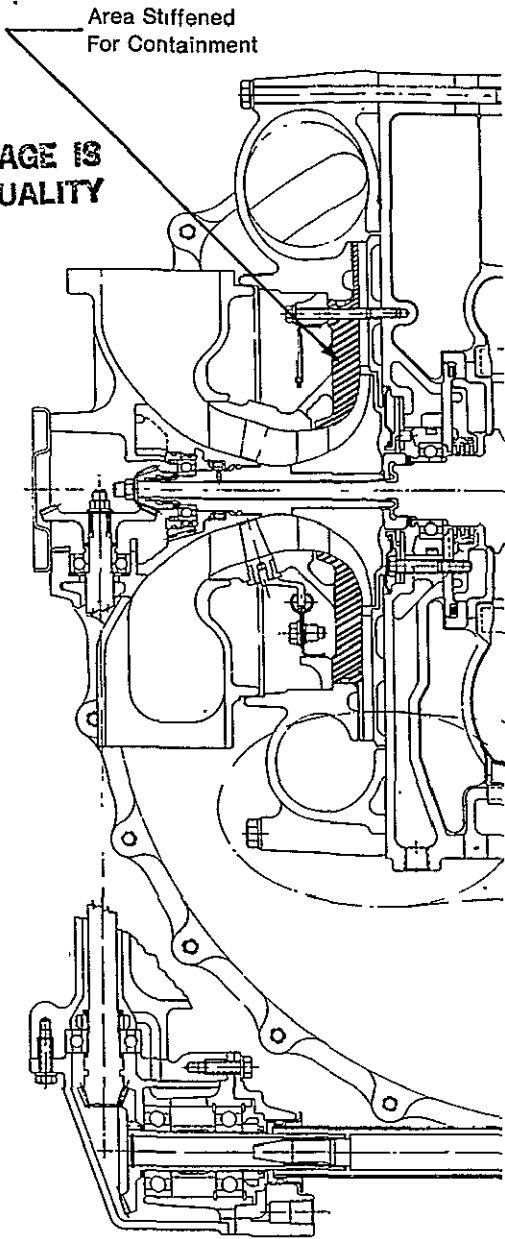


Figure 13 — Model for Gasifier Shroud Deflection

from 9280 kN/m (53,000 lbs/in.) to 2800 kN/m (16,000 lbs/in.) to 1750 kN/m (10,000 lbs/in.) as the temperature increased from room temperature to 66°C (150°F) to 93°C (200°F). At the same time damping also falls off rapidly as temperature is increased.

Although precise temperature control is virtually impossible in an engine, good control can be obtained on the compressor rig. It was decided to use the O-ring mounting system for the compressor rig only and redesign the engine mount.

POWER TRANSFER DRIVE

The power transfer bevel drive configuration (Ref. Figure 16) in conjunction with the mass isolator was completed

Bearings

BEARING SOAK BACK TEMPERATURE

As illustrated in Figure 16, the metal temperature of the gasifier bearing rises from 117°C (350°F) [at steady state maximum power, 52°C (125°F) day] to 257°C (494°F) 240 seconds after a three second deceleration to ambient conditions. At the same steady state conditions, the amount of heat flowing into the coolant oil from the gasifier bearing is 140 W (447 Btu/hr) to maintain the bearing at 177°C (350°F). The bearing receives an excess of heat through the transient deceleration, represented by the curve of net heat flow versus time (NQ) in Figure 16. The first calculated value of heat flow is 90 W (308 Btu/hr) at 20 seconds. A finite element model of the gasifier region used in this analysis is presented in Figure 17. The gasifier bearing is represented by element A-11.

Figure 14 — Compressor Module

BEARING POWER LOSS

Only the high speed bearings were analysed for power loss as the low speed bearing losses were considered to be insignificant. The bearings analysed are shown by number on Figure 18.

To predict bearing power losses the following expression generated by R. J. Trippett, General Motors Research, was used.

$$\text{Power, kW} = (1.29 \cdot 10^{-10})(V^{0.2})(Q^{0.16})(D_m^{2.2})(N^{1.56}) + (4.37 \cdot 10^{-8})(D_m)(W^{0.98})(N^{0.44})$$

where

V = oil viscosity (m^2/s)

Q = oil flow (ml/s)

D_m = mean bearing diameter (mm)

N = speed RPM

W = bearing thrust load (N)

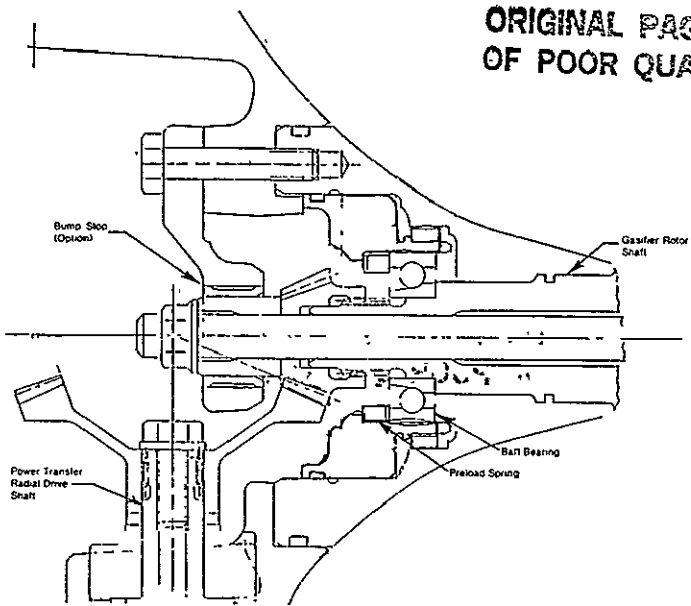


Figure 15 — AGT 100 Gasifier Rotor Damper

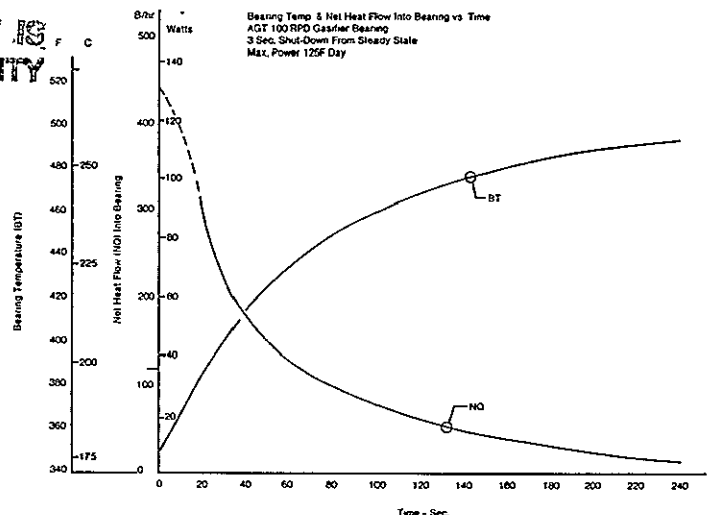


Figure 16-- Gasifier Trust Bearing Temperature and Heat Transfer

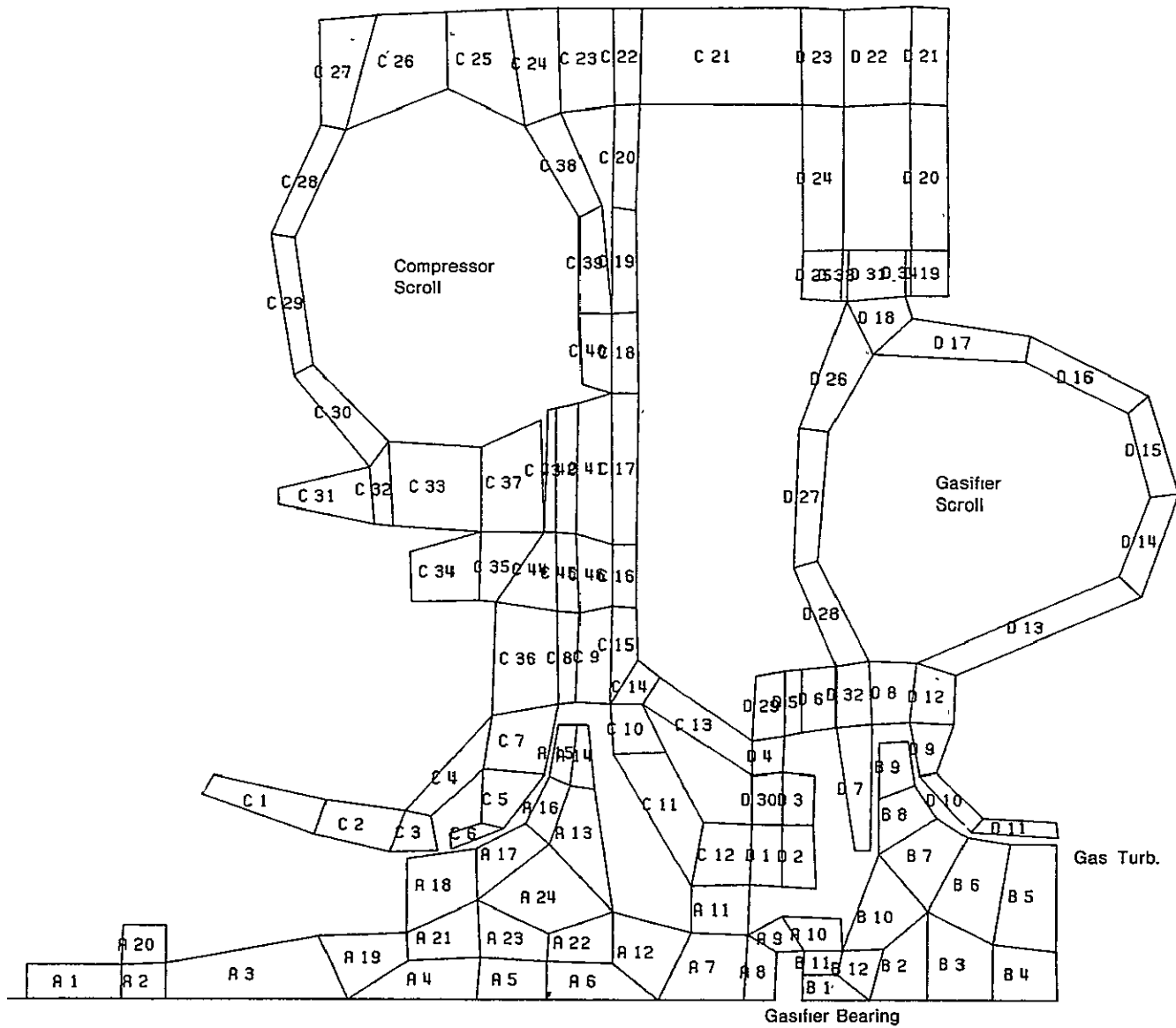


Figure 17 — Finite Element Model of the Area Surrounding the Gasifier Bearing

To prove the acceptability of using the above equation a test was conducted on DDA shaft test rig with a 30 × 55 × 13 mm existing ball bearing. A speed limitation of (55,000 RPM) on the test rig restricted the maximum speed value of 1.65×10^6 DN.

The measured bearing loss was 28% higher than that predicted by the GMR correlation, Figure 19. In view of the very low torque and high speed, as well as the state of the art in loss prediction, this result is considered to be acceptable accuracy.

Calculated bearing loss for the high speed bearings was broken down into two areas the gasifier bearings #1, 2, 32, 33, 34, and 35; and the power turbine bearings #3, 4, 5, and 6 (Ref. Figure 18) The results (Figure 20) show that the maximum bearing loss for all the high speed bearings is 3.8 kW (5.08 HP); of this total 2.17 kW (291 HP) is gasifier and 1.62 kW (2.17 HP) is power turbine bearing loss

ORIGINAL PAGE IS
OF POOR QUALITY

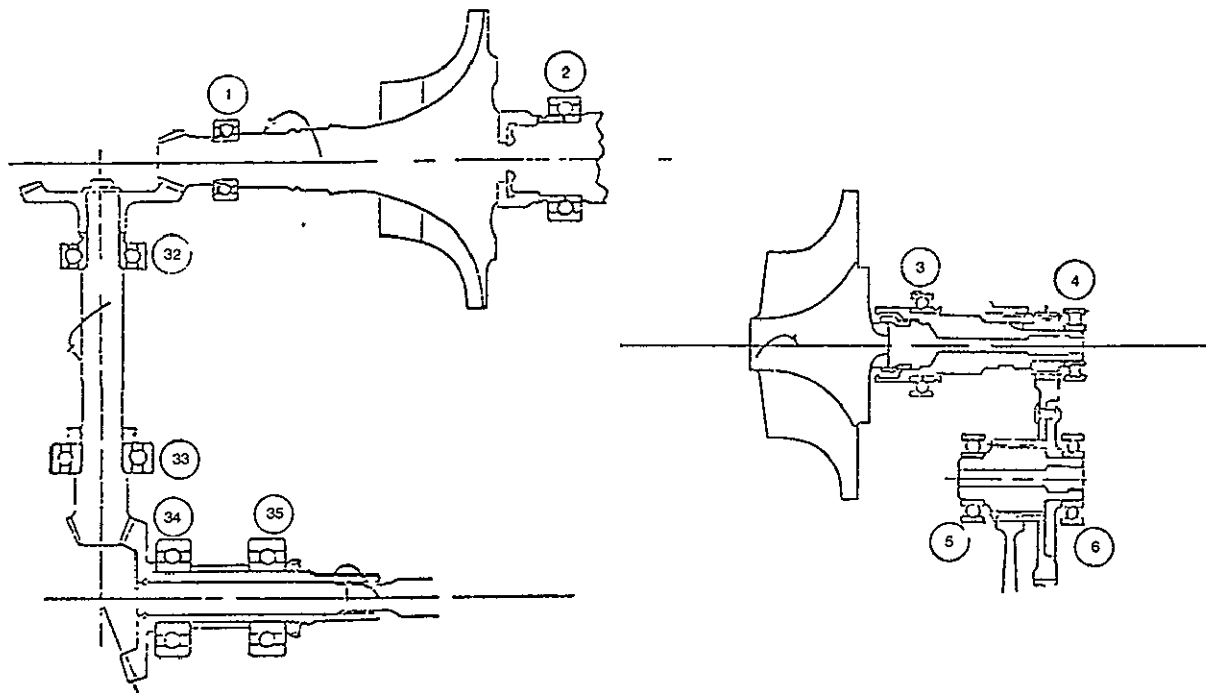


Figure 18 — Power Loss Analysis—Bearing Positions

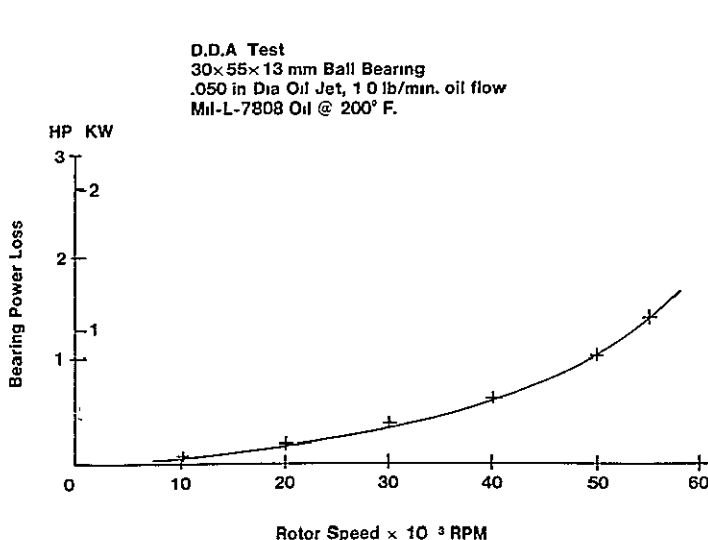


Figure 19 — Measured HP Loss #2 Bearing

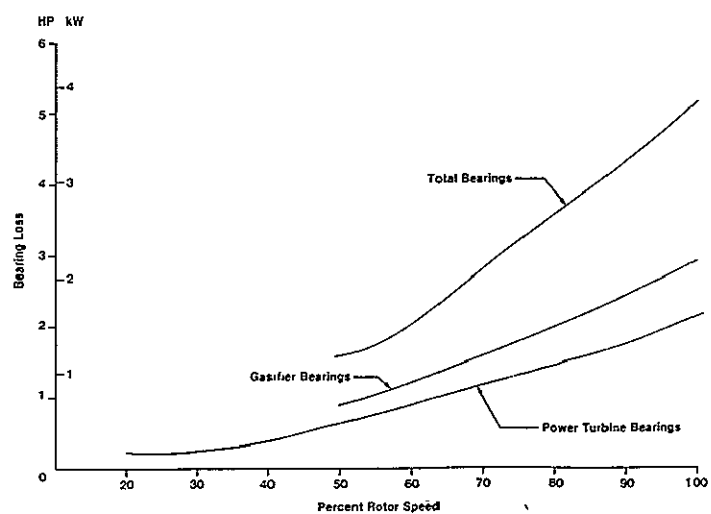


Figure 20 — AGT 100 Bearing Loss (Predicted)

IV. Gasifier Turbine Development

4.1 Gasifier Turbine Aerodynamic Development

High efficiency over a broad operating range is the primary goal for the gasifier turbine. The aerodynamic design to achieve this goal must be consistent with stress, heat transfer, vibration, and mechanical design requirements. To be competitive in the automotive market, this goal must be achieved with recognition of the requirement for low cost and low inertia.

Development activity has focused on design of the Mod I turbine, fabrication of the gasifier turbine rig hardware, torquemeter calibration, test rig installation, and facility checkout.

Mod I Gasifier Turbine Design

The Mod I engine cycle requirements for the gasifier turbine at the maximum power, sea level static condition are:

Inlet temperature, °C (°F)	1080 (1976)
Inlet pressure, kPa (psia)	438.6 (63.62)
Fuel/air ratio	0.0110
Equivalent flow, kg/s (lb_m/s)	0.163 (0.360)
Equivalent work, kJ/kg (Btu/ lb_m)	51.66 (22.21)
Equivalent speed, rpm	40348
Mechanical speed, rpm	86240
Expansion ratio (total-total)	2.24
Efficiency with inlet scroll (total-total)	82.6

The Mod I gasifier turbine flow path is patterned from the RPD flow path described in the First Semi-Annual Technical Report. Because of packaging constraints and similarity with the RPD work requirements, the Mod I nozzle and rotor diameters (hot) have been selected to be identical to the RPD gasifier turbine design.

Commonality of flow path diameters, although not an aero design pre-requisite, eases mechanical design alterations between the Mod I and Mod II engines. Cycle temperature, turbine work, and flow differences between the Mod I and RPD do dictate a change in nozzle width (from the RPD design) to achieve the desired Mod I flow.

The Mod I gasifier turbine hot flow path is illustrated in Figure 21. This turbine features a symmetrical vane and endwall contouring and a metallic rotor. Salient features of the turbine design are:

Vane inlet diameter, mm (in.)	147.36 (5.802)
Rotor tip diameter, mm (in.)	112.52 (4.43)
Vaneless space diameter ratio	1.078
Rotor tip width, mm (in.)	7.176 (0.2825)
Exducer hub/tip radius ratio	0.300
Rotor tip diameter/exducer tip diameter ratio	1.600
Rotor tip width/rotor tip diameter ratio	0.064

Operating at the sea level static (SLS) maximum power condition, the turbine exhibits a tip speed of 508 m/sec (1667 ft/sec), an aerodynamic loading parameter (U/C-Tip Speed/Isentropic Spouting Velocity) of 0.67 and a specific speed of 70.

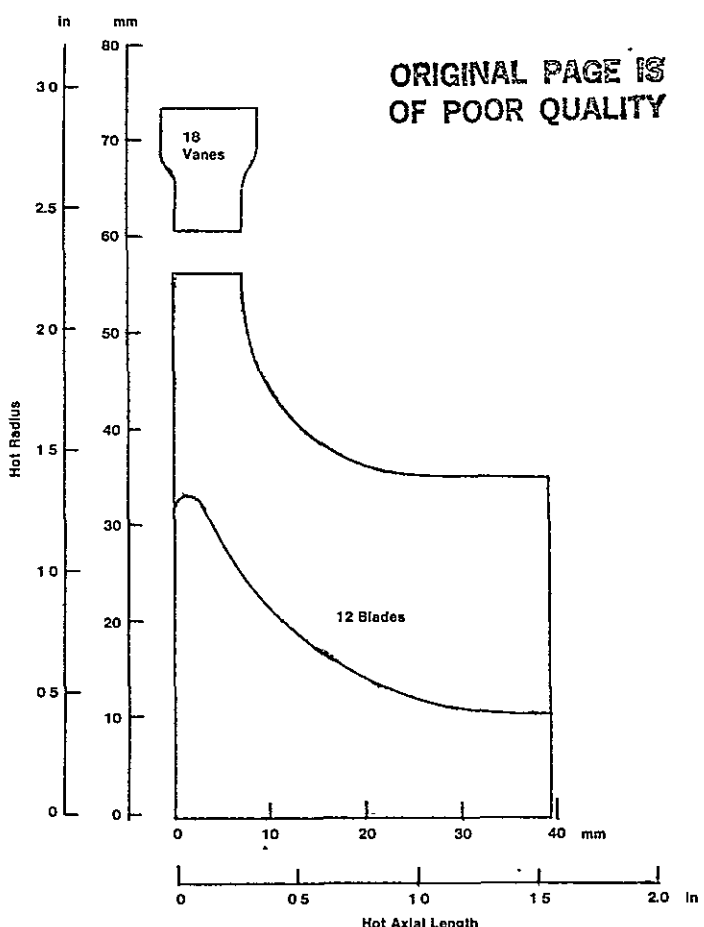


Figure 21 — Mod I Gasifier Turbine Flow Path

Turbine parameters for four operating points under engine road-load conditions are presented in Table V. The RPD characteristic parameters are presented for comparative reference. The Mod I turbine work levels are higher than the RPD turbine. This gives rise to reduced U/C values for the Mod I gasifier. An increase in tip diameter of the Mod I turbine to achieve higher values of U/C, and hence efficiency, is prohibited by stress rupture constraints. Reaction levels are, in general, slightly lower than the RPD design. Exit swirl and Mach number values are comparable to the RPD design. Exit conditions, of course, are important in minimizing the interturbine duct and power turbine losses.

A comparison of efficiency levels for the Mod I and RPD gasifier turbines over the engine road load operating line is illustrated in Figure 22. A degree of conservatism has been factored into the Mod I turbine performance since the Mod I design will not have the benefit of the RPD aero development time. The Mod I design, however, will be updated as necessary to reflect experimental results of the turbine aero development program.

Table V — MOD I and RPD Gasifier Turbine Parameters for Various Engine Operating Points

	Idle		48 km/h (30 mph)		80 km/h (50 mph)		Max Power (SLS)	
	Mod I	RPD	Mod I	RPD	Mod I	RPD	Mod I	RPD
Turbine Power kW (HP)	12.58 (16.86)	5.03 (6.74)	76.69 (22.37)	6.99 (9.37)	25.79 (34.57)	14.51 (19.45)	75.05 (100.6)	71.38 (95.68)
Equivalent Flow kg/sec (lb/sec)	.139 (.306)	.128 (.282)	.147 (.323)	.140 (.309)	.159 (.350)	.162 (.357)	.163 (.360)	.178 (.391)
Equivalent Work kJ/kg (Btu/lb)	27.24 (11.71)	16.40 (7.05)	31.17 (13.40)	16.00 (6.88)	35.85 (15.41)	23.24 (9.99)	51.66 (22.21)	42.08 (18.09)
Expansion Ratio (T-T)	1.49	1.26	1.59	1.26	1.75	1.41	2.24	1.87
Efficiency (T-T)	84.2	86.6	83.6	84.2	80.7	83.7	82.6	84.7
% Equivalent Speed	70.8	63.5	73.8	51.9	71.8	62.2	100.	100.
U/C	.660	.719	.642	.587	.572	.582	.670	.700
Reaction	.443	.515	.427	.396	.369	.393	.471	.510
Exit Swirl	+11.5	+16.0	+5.9	-7.8	-9.0	-11.6	-2.3	-2.4
Exit Mach Number	.140	.112	.154	.119	.186	.154	.239	.219

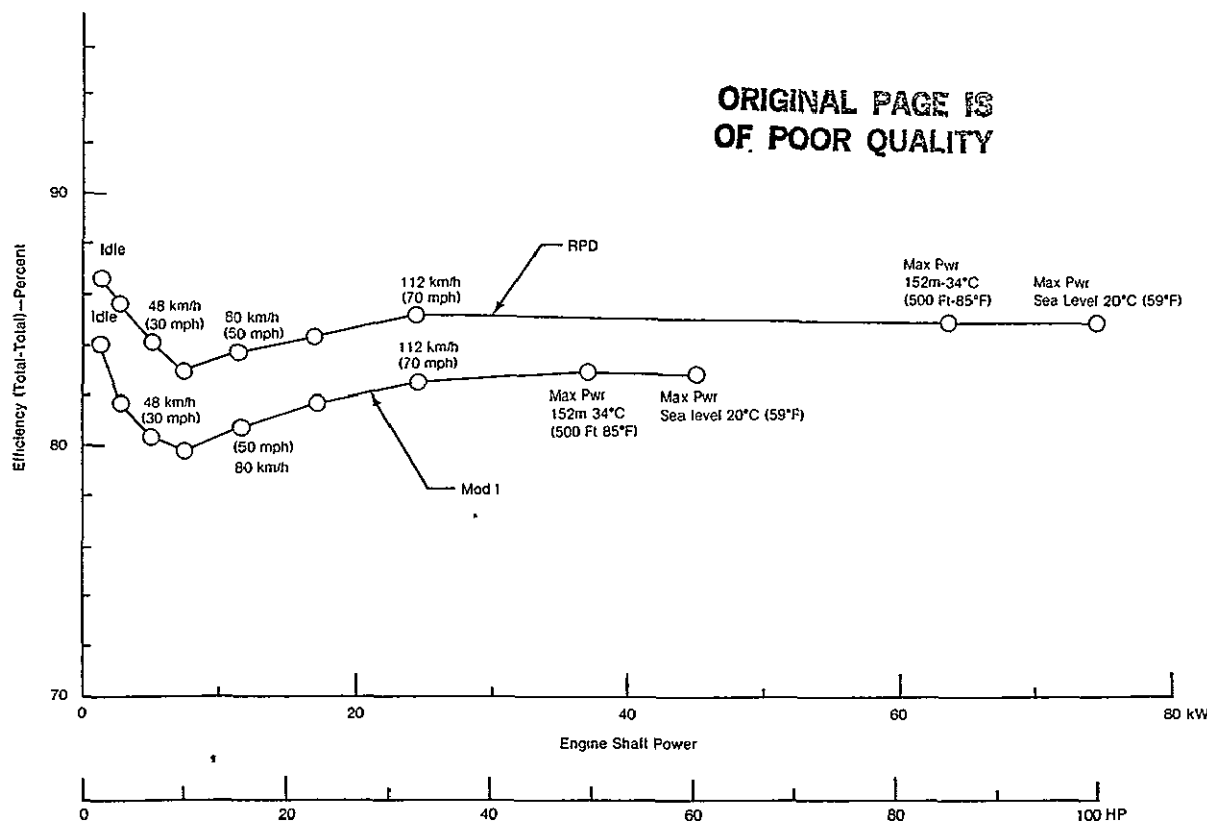


Figure 22 — Efficiency Goal—RPD and Mod I Gasifier Turbine with Inlet Scroll

Turbine Inlet Scroll

Model testing of the interturbine duct and power turbine scroll combination has verified the basic design approach of the gasifier scroll. Those results (discussed under Item 5.1 in this report) indicate a low level of circumferential mass flow distortion ($\pm 3.5\%$) and low loss. Both benefits are a result of low through flow Mach number. Although the geometry of the gasifier scroll has not been independently tested, similarly to the power turbine scroll provides confidence in the projected performance of the scroll as configured.

Mod I Vane Design

The Mod I gasifier turbine vane is illustrated in Figure 23. These vanes feature endwall contouring and ceramic construction. The vanes are symmetrical to reduce production assembly costs. A set of metallic vanes for Mod I will be procured for backup to the ceramic vanes.

The vane exhibits a trailing edge diameter of 0.508 mm (0.020 in.), a leading edge diameter of 5.08 mm (0.20 in.), and a true chord of 27.153 mm (1.069 in.). The vane number of 18 results in a solidity based on true chord of 1.283, a throat width of 6.270 mm (0.2468 in.), and a trailing edge blockage of 7.5%.

Endwall contouring has been incorporated to improve aerodynamic loading of the vane. Suction and pressure surface velocity distributions for the SLS max power design point are illustrated in Fig. 24. Velocity distributions of the Mod I vane are similar to the RPD vane, but display higher velocity levels.

Mod I Rotor Design

The Mod I rotor has been designed with emphasis on low cost through use of radial blading, low inertia through use of fully scalloped backplate and deeply cut hub, low exit Mach number to minimize transition duct loss, and relatively high maximum power reaction to achieve a broad efficiency band.

The mean streamline velocity distributions for idle, 48 km/h (30 mph), 80 km/h (50 mph), and SLS maximum power operating conditions are illustrated in Figures 25 through 28. The higher blade loading levels reflect the increased turbine work requirement of Mod I as compared to the RPD configuration.

Design Features:

- Symmetrical Design
- Endwall Contouring
- Ceramic Construction

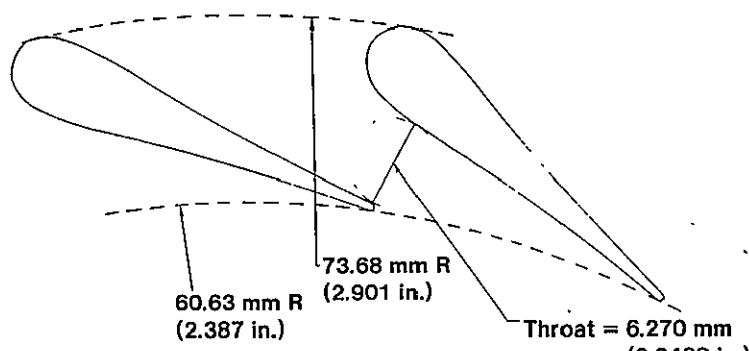


Figure 23 — Mod I Gasifier Vane Design

ORIGINAL PAGE IS
OF POOR QUALITY

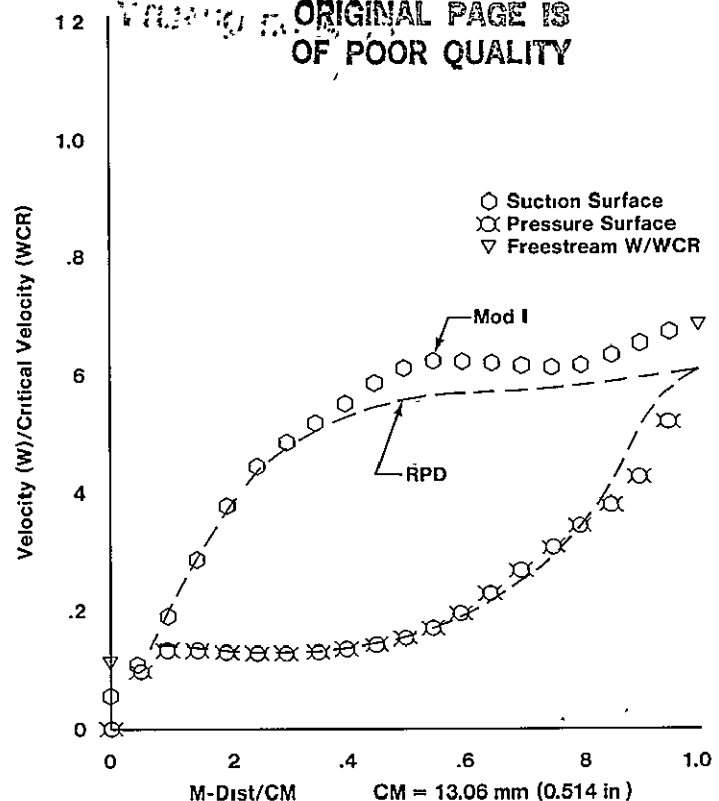


Figure 24 — Mod I Vane Velocity Distribution

Gasifier Turbine Aerodynamic Development Rig

MECHANICAL DESIGN AND FABRICATION

Fabrication has been completed on the basic rig, inlet scroll, and interturbine duct. The basic rig has been assembled and instrumented for initial testing. The existing backplate and shroud hardware will be subsequently re-worked to incorporate vane endwall contouring.

Primary activity for this period has consisted of rebuilding the rig module and water brake dynamometer with new parts after a destructive failure during torquemeter calibration. A bearing failure in the vendor purchased water brake dynamometer was identified as the cause of the failure. The damaged turbine rig module is illustrated Figure 29. The rebuild required replacement of all rotating parts and some static parts of the rig module and water brake dynamometer.

The gasifier turbine test wheel and vanes are shown in Figure 30. The backplate bolts were filled with epoxy during build-up to assure a smooth backplate surface. Assembly of the gasifier turbine in the facility plenum is illustrated in Figure 31.

TEST

The AGT-100 Gasifier Turbine rig test experienced problems in the development of a satisfactory torque measurement system. The gas turbine design torque is about 4 N·m (35 pound-inches) at 45,500 rpm. Data accuracy within 1% requires measurement capabilities of ± 0.04 N·m (± 0.35 pound-inches). A torquemeter with this capability has been designed and fabricated by DDA.

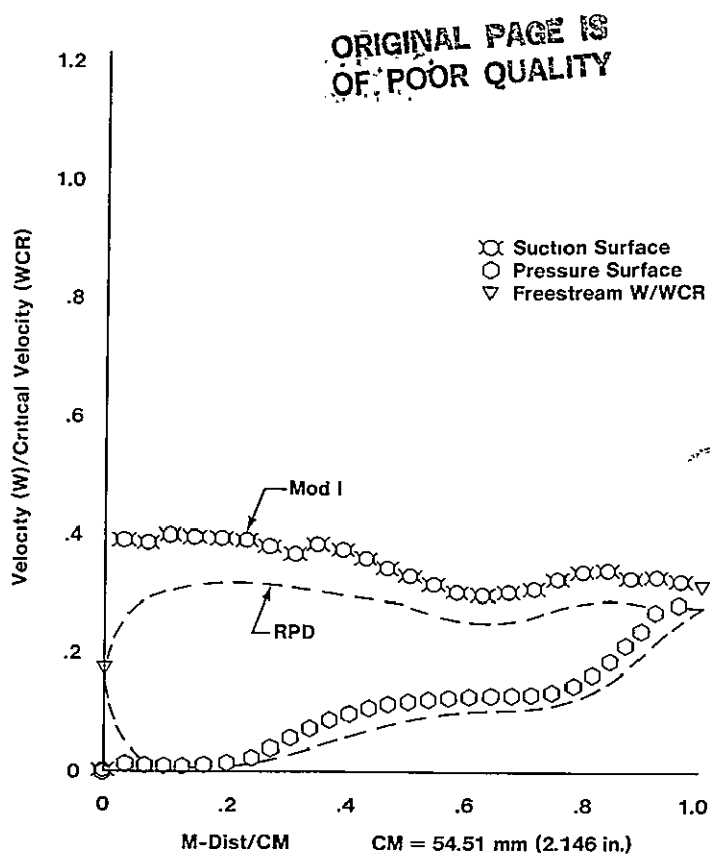


Figure 25 — Mod I Gasifier Rotor Mean Velocity Distribution — Idle

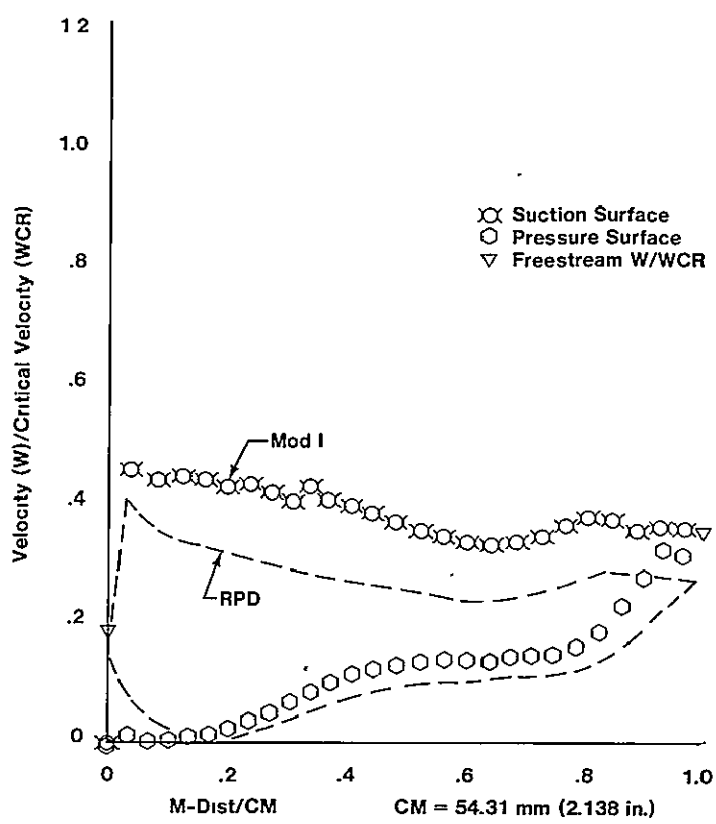


Figure 26 — Mod I Gasifier Rotor Mean Velocity Distribution — 48 km/h (30 mph)

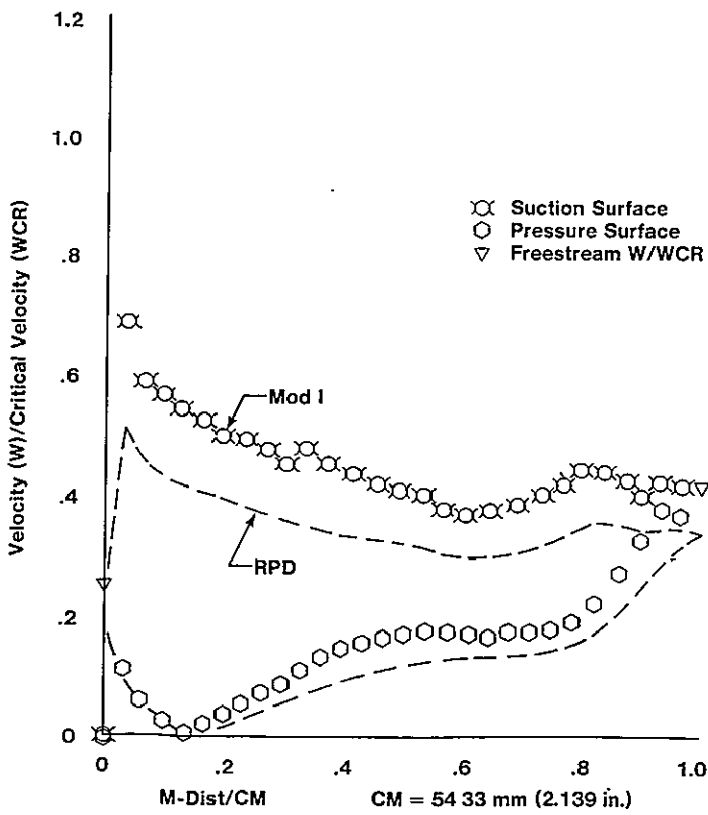


Figure 27 — Mod I Gasifier Rotor Mean Velocity Distribution — 80 km/h (50 mph)

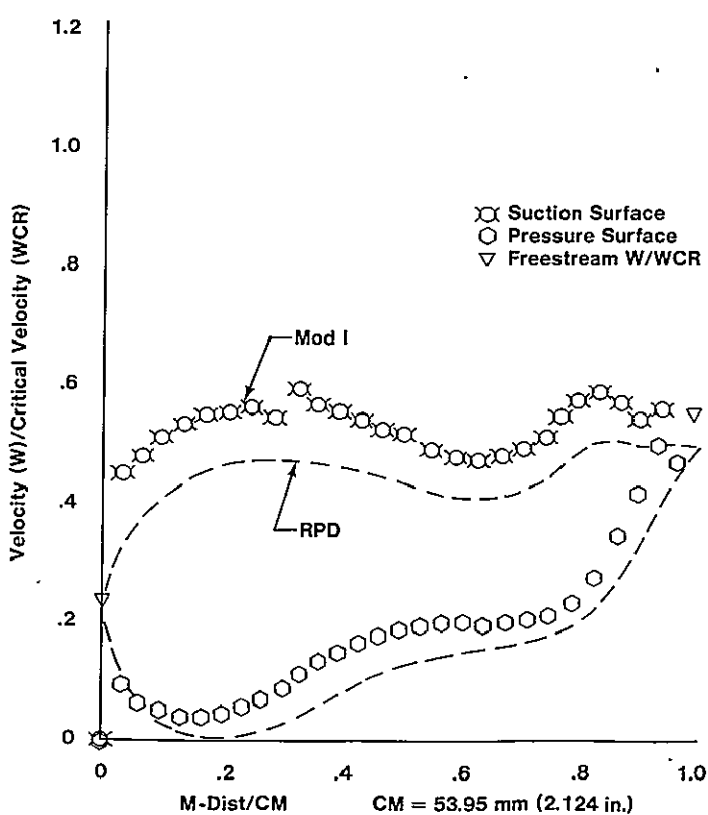


Figure 28 — Mod I Gasifier Rotor Mean Velocity Distribution — Maximum Power

The problem is associated with developing a means for conducting an accurate dynamic calibration of the torquemeter. The approach has been to use a high speed water brake dynamometer to load the torquemeter to a known value and record the torquemeter voltage signal vs. water brake torque. Installation of the water brake is illustrated in Figure 32.

The first problem encountered in this calibration process was the failure of the water brake. Subsequent problems have been centered around a hysteresis loop in the calibration procedure; i.e. the torquemeter vs. water brake data indicates higher values of torque with a decreasing load as compared to an increasing load. The difference is on the order of 0.7 N·m (6 pounds-inches). The problem

has been traced to a residual torque in the water brake and appears to be associated with the journal bearings. Currently a study is being made to replace the two journal ball bearings with hydrostatic air bearings.

A calibration of the torquemeter, based on acquired data, has been accomplished so that turbine testing may proceed. During test the voltage signal from the torquemeter will be recorded together with the calibrated torque value used for turbine efficiency calculation. A subsequent calibration of the torquemeter will be accomplished and data corrections may be made if the need is indicated. Testing of the basic (initial) turbine configuration will begin early in the next reporting period.

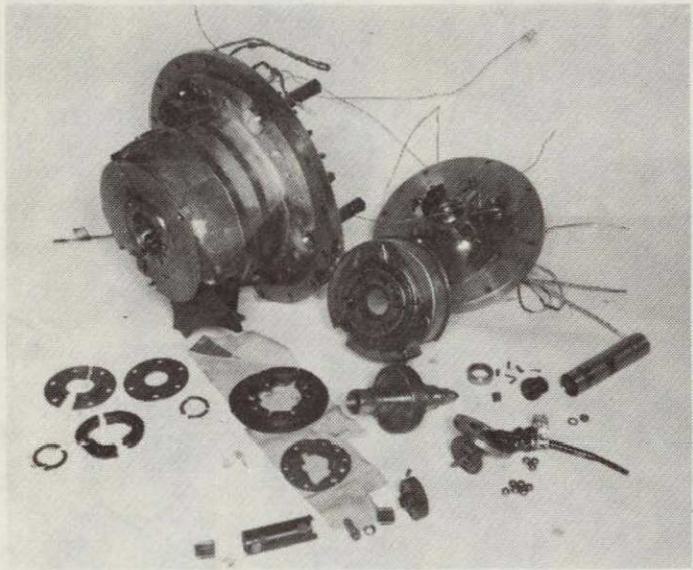


Figure 29 — Damaged Turbine Rig Module Hardware

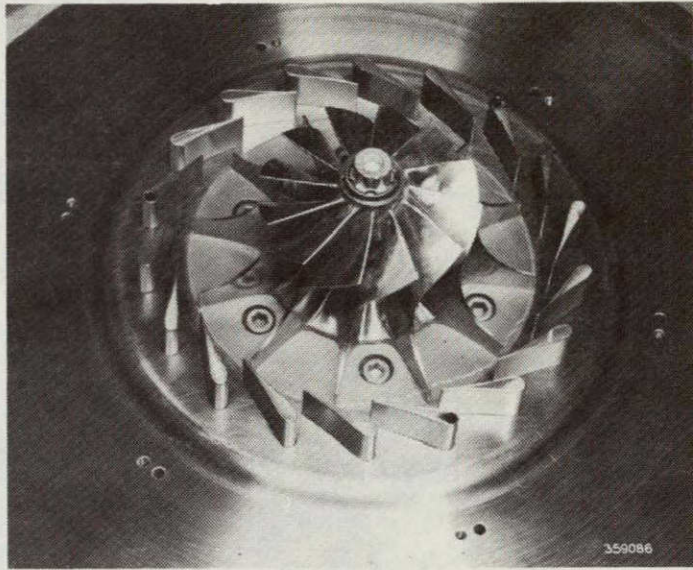


Figure 30 — Test Rig Vane and Rotor Assembly

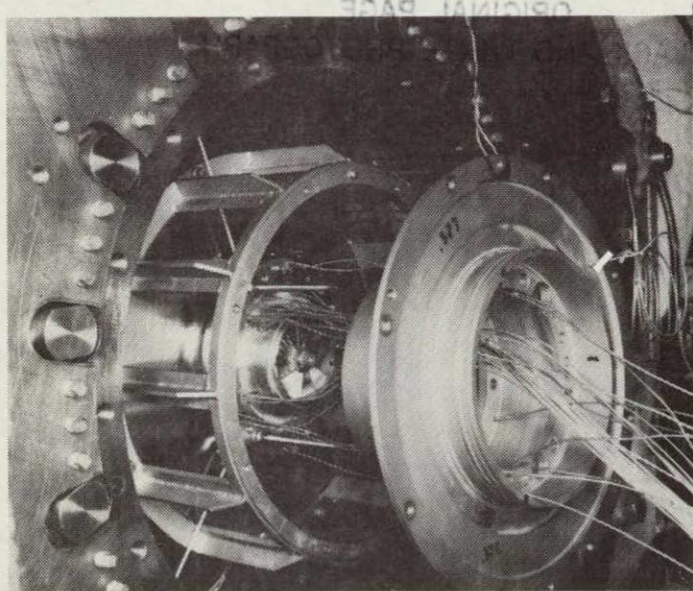


Figure 31 — Assembly of Gasifier Turbine Rig

**ORIGINAL PAGE
BLACK AND WHITE PHOTOGRAPH**

4.2 Gasifier Turbine Mechanical Development

RPD

SCROLL DESIGN

The scroll assembly was one of the parts involved in the design iteration and only the work accomplished prior to the new design will be discussed in this section.

Temperature distributions were run for the inner backplate, outer backplate, scroll, and vanes.

Figure 33 shows the inner backplate viewed from the flowpath side. Figures 34 and 35 present temperature distributions in the outer backplate for the flowpath and outside surfaces respectively. Similarly Figures 36 and 37 present the same data for the scroll. Vane temperatures are presented in Figure 38. These analyses were run at standard day maximum power conditions for the Mod I engine.

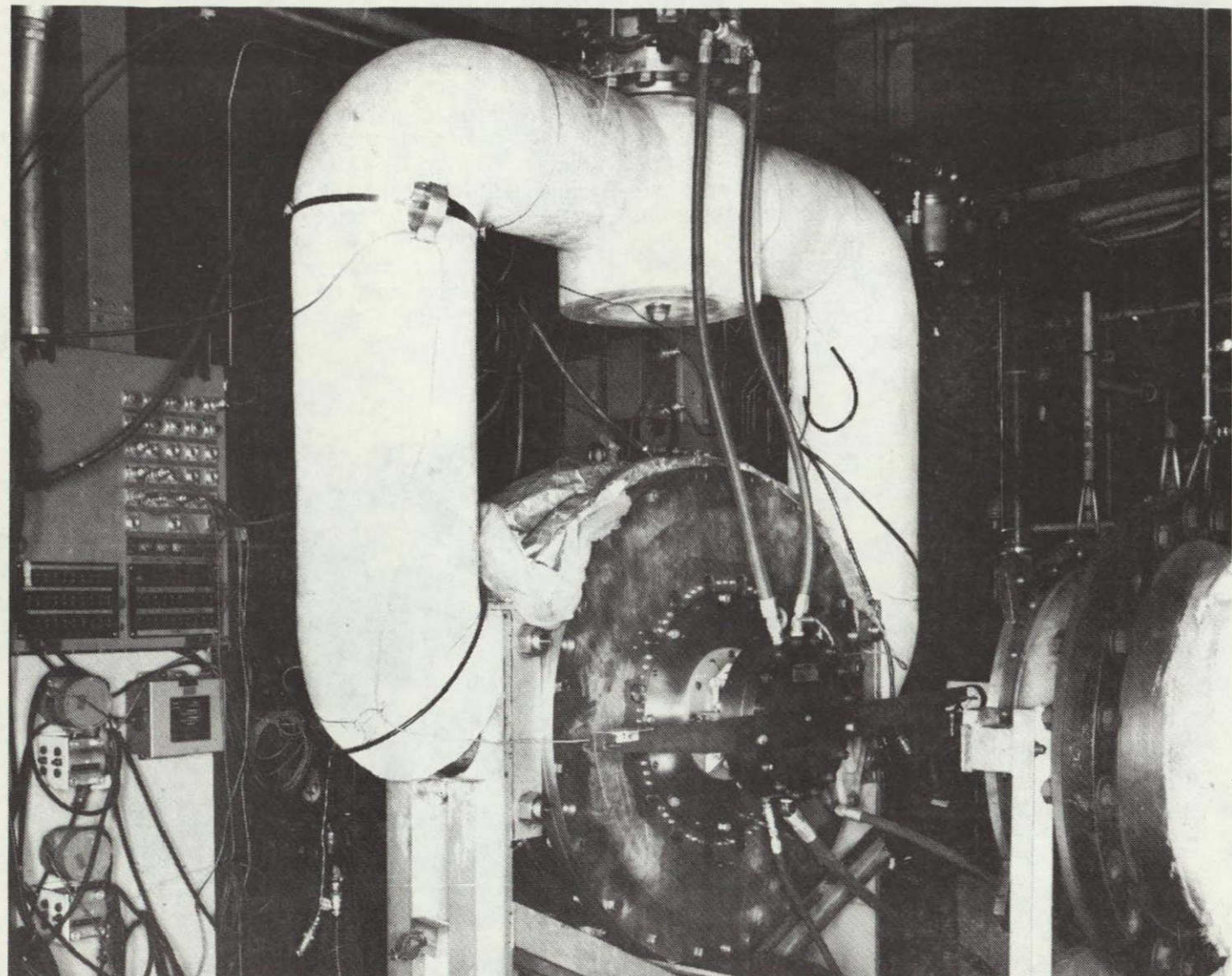


Figure 32 — Water Brake Installation

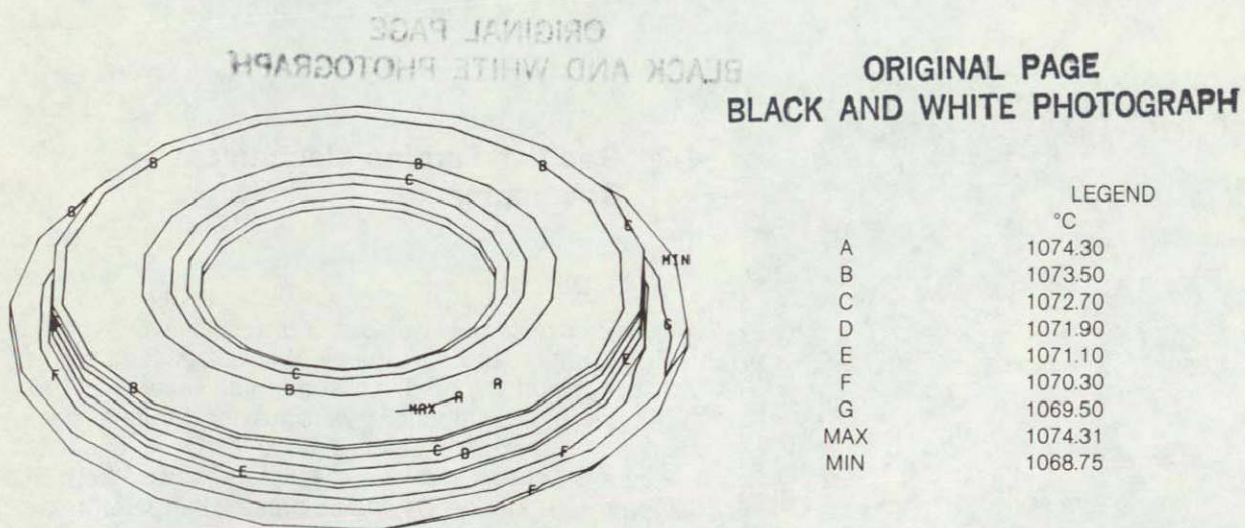


Figure 33
AGT 100 Ceramic Gasifier Turbine Inner Backplate
Contour Plot of Temperature—Maximum Power

ORIGINAL PAGE IS
OF POOR QUALITY.
ROUTE 40

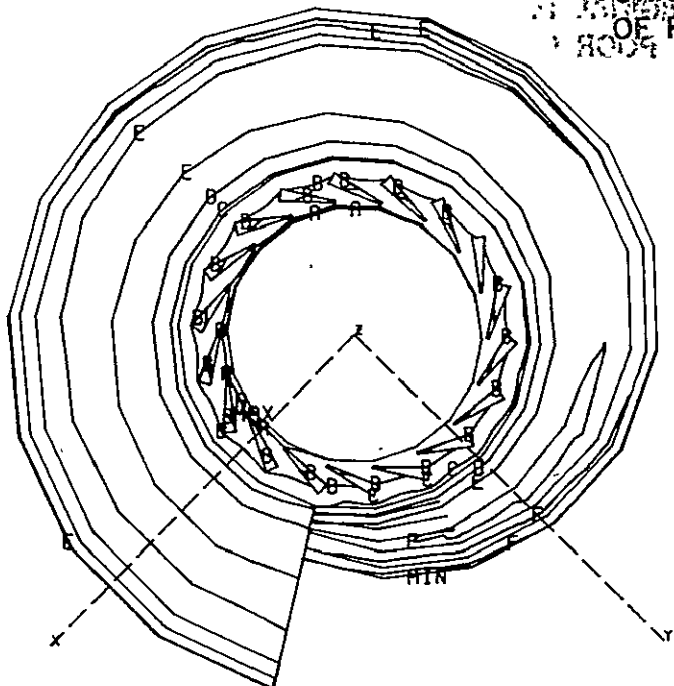


Figure 34
AGT 100 Ceramic-Gasifier Turbine Outer Backplate
Contour Plot of Temperature—Maximum Power

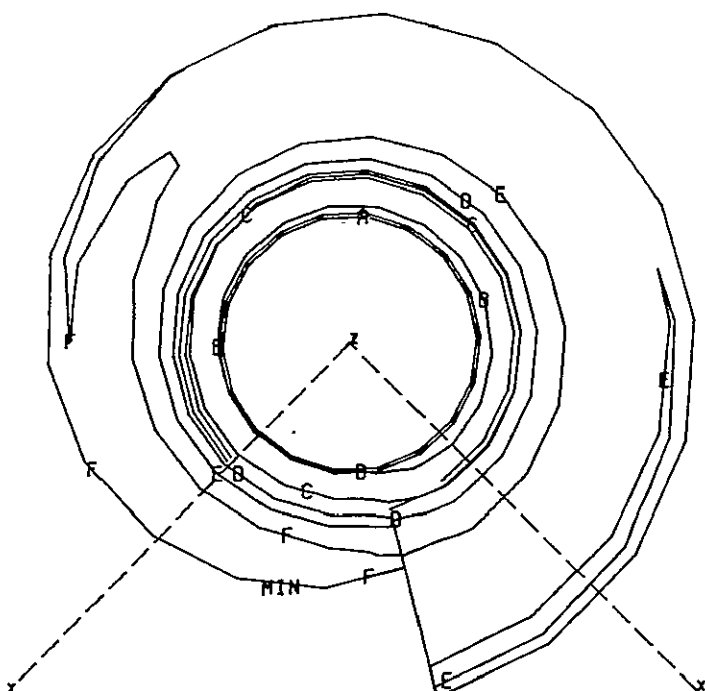


Figure 35
AGT 100 Ceramic Gasifier Turbine Outer Backplate
Contour Plot of Temperature—Maximum Power

ORIGINAL PAGE IS
OF POOR QUALITY

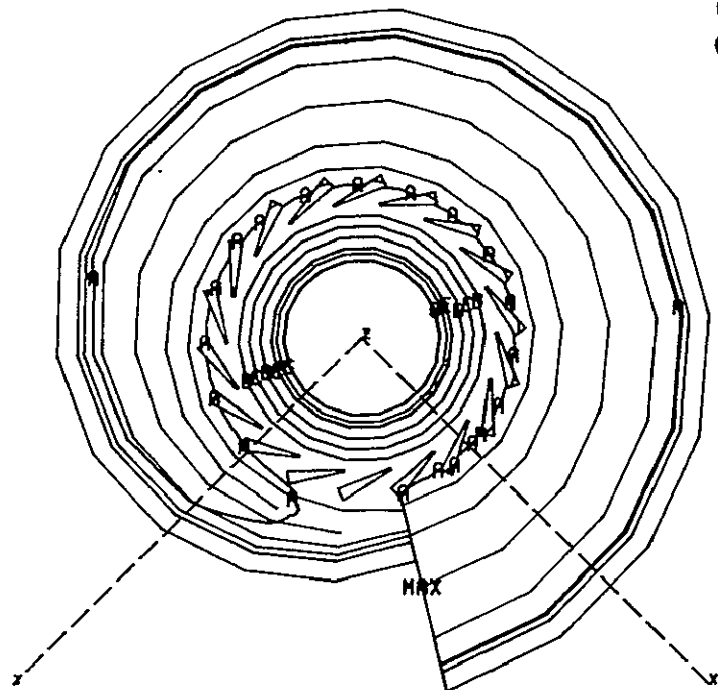


Figure 36
AGT 100 Ceramic Gasifier Turbine Scroll
Contour Plot of Temperature—Maximum Power

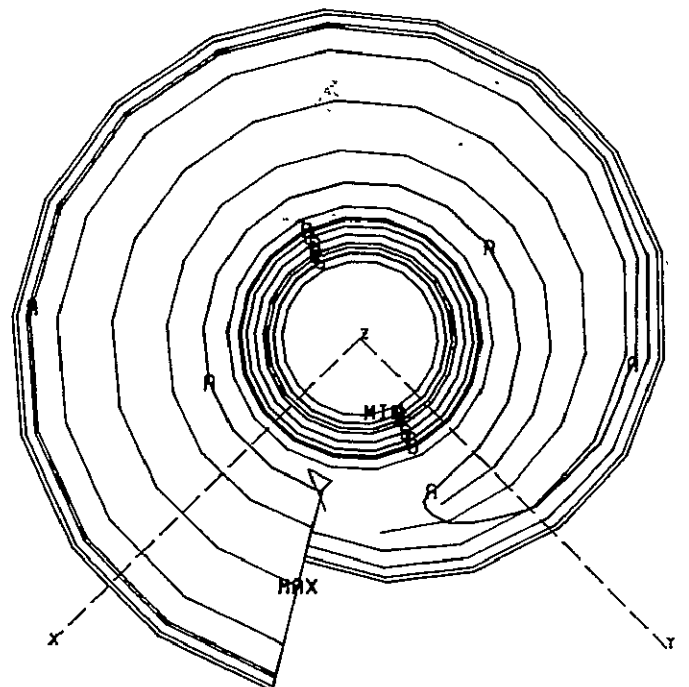


Figure 37
AGT 100 Ceramic Gasifier Turbine Scroll
Contour Plot of Temperature—Maximum Power

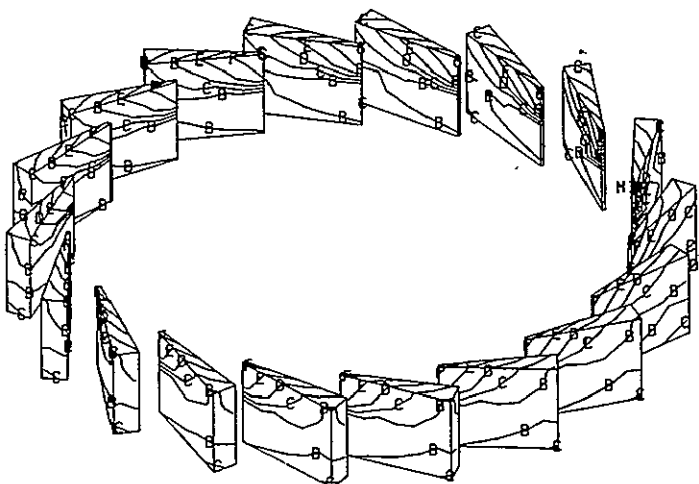


Figure 38
AGT 100 Ceramic Gasifier Turbine Guide Vanes
Contour Plot of Temperature—Maximum Power

ORIGINAL PAGE IS
OF POOR QUALITY

Mod I

SCROLL DESIGN

Layouts were essentially completed for the original Mod I metal configuration and the Mod I ceramic configuration.

4.3 Ceramic Gasifier Turbine Rotor

A three-dimensional (3-D) finite element model of the ceramic gasifier turbine rotor has been constructed to evaluate the effects of blade camber (circumferential twist) and fillets at the blade root. Previous analyses utilized an axisymmetric (2-D) model which cannot evaluate these effects. The 3-D model is shown in Figure 39 and consists of a one-blade (30°) sector of the wheel. Balance stock and a small stub shaft for attachment were added to the basic model that is generated by an automated modeling routine. The final model contains 459 20-node solid elements. Solution time on the computer is long; therefore this model is being used only for final design verification. Most of the preliminary design iterations were evaluated using the much less costly 2-D model.

Steady state and transient heat transfer and stress analyses have been performed using the properties of sintered alpha silicon carbide material. The results indicate the most critical operating condition occurs approximately 30 seconds after the initiation of cold start transient shown in Figure 40. The probability of survival computed using Weibull material parameters was used to establish the "worst-case" condition. The stress distribution at this condition is shown in Figure 41.

The minimum survival probability point occurs at an elapsed time that is in close agreement with 2-D analysis results reported previously. However, the peak stress and location differ markedly. Transient stresses at the blade root are much less in the 3-D model, probably because of

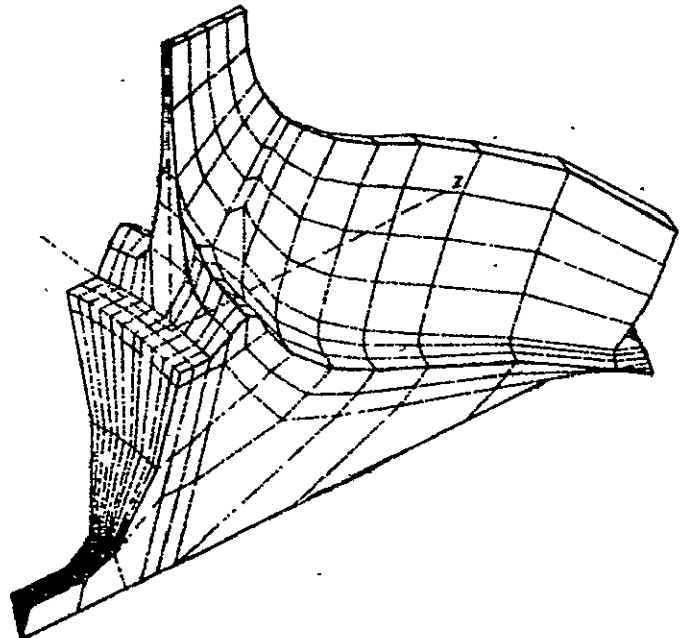


Figure 39 — 3-D Finite Element Model of Gasifier Turbine

the presence of the fillet. The peak stress at the mid-span location on the blade trailing edge is a result of airfoil twist caused by the local thermal profile. Differences in the pressure and suction side thermal boundary conditions help to cause the discrepancy between 2-D and 3-D results.

The effect of the worst-case transient stress state on required material strength is presented in Figure 42. The 3-D results indicate a higher strength requirement than previous 2-D analyses. The strength level shown is the median value from 4 point MOR (flexural) strength tests using 3.18 x 6.35 x 50.8 mm (.12 x .25 x 2 in.) specimens with a load span of 19.05 mm (75 in.) and a support span of 38.10 mm (1.5 in.).

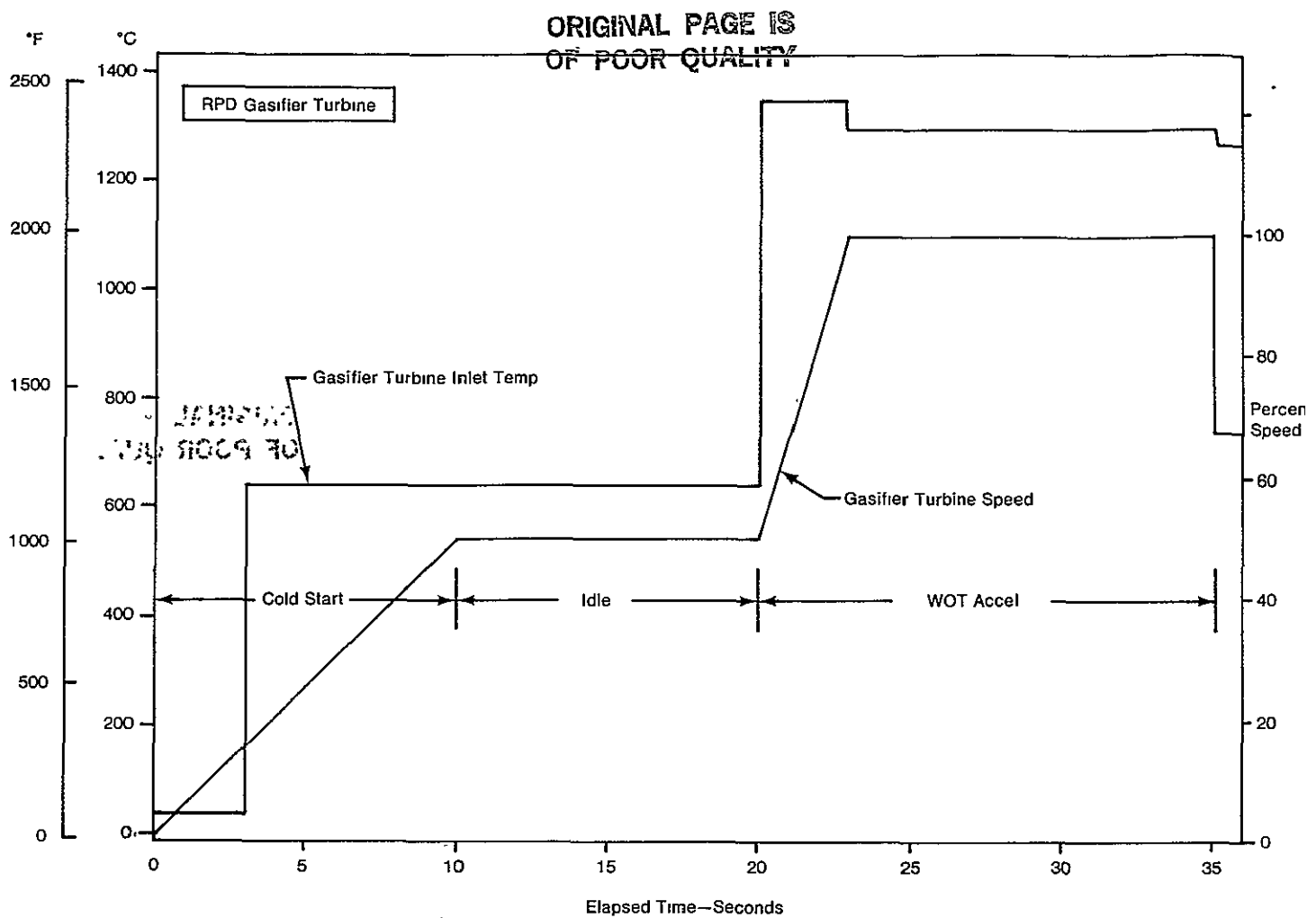


Figure 40 — AGT-100 Cold Start to Max Transient

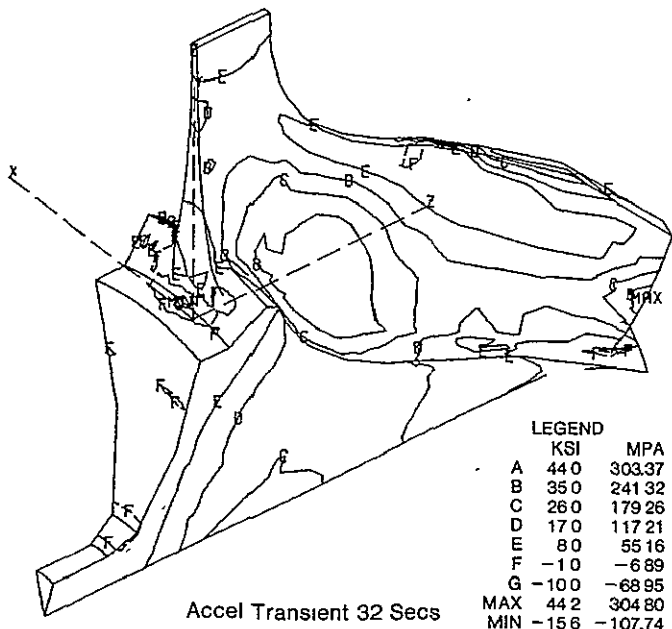


Figure 41 — Ceramic Gasifier Turbine Max Principal Stress Distribution

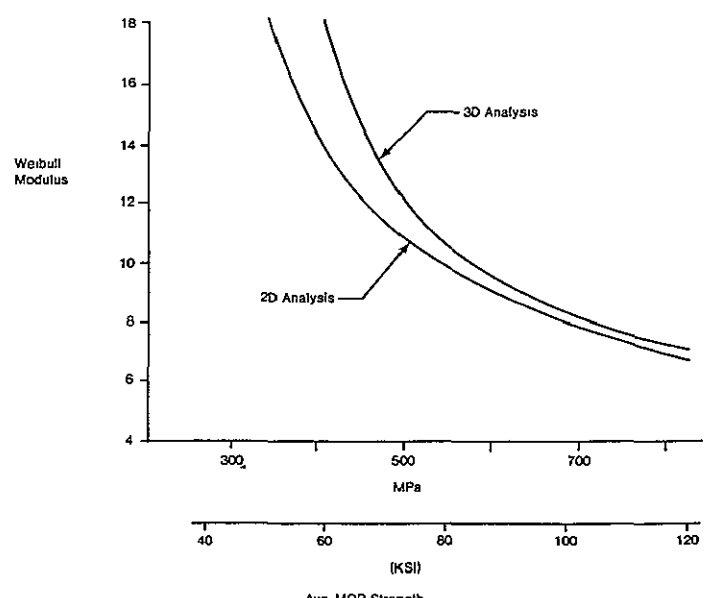


Figure 42 — Required Material Strength for Sintered Silicon Carbide Gasifier Turbine at Maximum Transient Operating Condition

5.1 Power Turbine Aerodynamic Development

Similar to other AGT 100 components, the power turbine is required to operate over a wide range with high efficiency. Aerodynamic design to achieve this goal must be consistent with stress, heat transfer, vibration, and mechanical design requirements. To be competitive in the automotive market, the high efficiency must be achieved with recognition of the requirement for low cost and low inertia. Although larger than the AGT 100 gasifier, the design of the power turbine is challenging because of the small size, ceramic construction, and relatively low Reynolds number.

Development has focused on aero-design of the Mod I power turbine, design and fabrication of the power turbine test rig, and experimental evaluation of the interturbine duct/power turbine scroll assembly.

Mod I Power Turbine Design

The Mod I engine cycle requirements for the power turbine at the maximum power, sea level static condition are

Inlet temperature, °C(°F)	881.0 (1618.)
Inlet pressure, kPa (psia)	195.8 (28.39)
Fuel/air ratio	0.0111
Equivalent flow, kg/sec(lb _m /s)	0.348 (0.767)
Equivalent work, kJ/kg (btu/lb _m)	36.52 (15.70)
Equivalent Speed, rpm.	27511.
Mechanical Speed, rpm	54290.
Expansion ratio, (total-total)	1.720
Efficiency w/o inlet scroll (total-total)	84.7

The Mod I power turbine flow path is patterned from the RPD flow path described in the First Semi-Annual Technical Report. In order to provide an optimum aero design and maintain commonality of dimensions (at operating temperatures) between the Mod I and RPD engines, the max power mechanical speed of the Mod I turbine has been reduced to 54390 rpm compared to 68000 rpm for the RPD engine. This speed reduction was accommodated by a relatively minor gear box change. Cycle temperature, turbine work and flow differences between the Mod I and RPD engines give rise to an increased nozzle width for the Mod I power turbine.

The Mod I power turbine hot flow path is illustrated in Figure 43. This turbine features a symmetrical vane with endwall contouring and a metallic rotor. Salient features of the turbine design are:

Vane inlet diameter, mm (in.)	186.0	(7.323)
Rotor tip diameter, mm (in.)	148.1	(5.830)
Vaneless space diameter ratio		1.06
Rotor tip width, mm (in.)	13.13	(0.5168)
Exducer hub/tip radius ratio		0.30

Rotor tip diameter/exducer tip diameter ratio	1.65
Rotor tip width/rotor tip diameter ratio	0.0886

Operating at the sea level static (SLS) maximum power condition, the turbine exhibits a tip speed of 422m/s (1384 ft/s), an aerodynamic loading parameter (U/C—tip speed/isentropic spouting velocity) of 0.724 and specific speed of 82.7.

Turbine parameters for four operating points under engine road-load conditions are presented in Table VI. The RPD characteristic parameters are presented for comparative reference. The Mod I work level at maximum power is substantially less than the RPD turbine. The speed change between Mod I and RPD effectively compensates the change of work and provides a good match of U/C. Work levels under part power operating conditions are comparable between the two turbines:

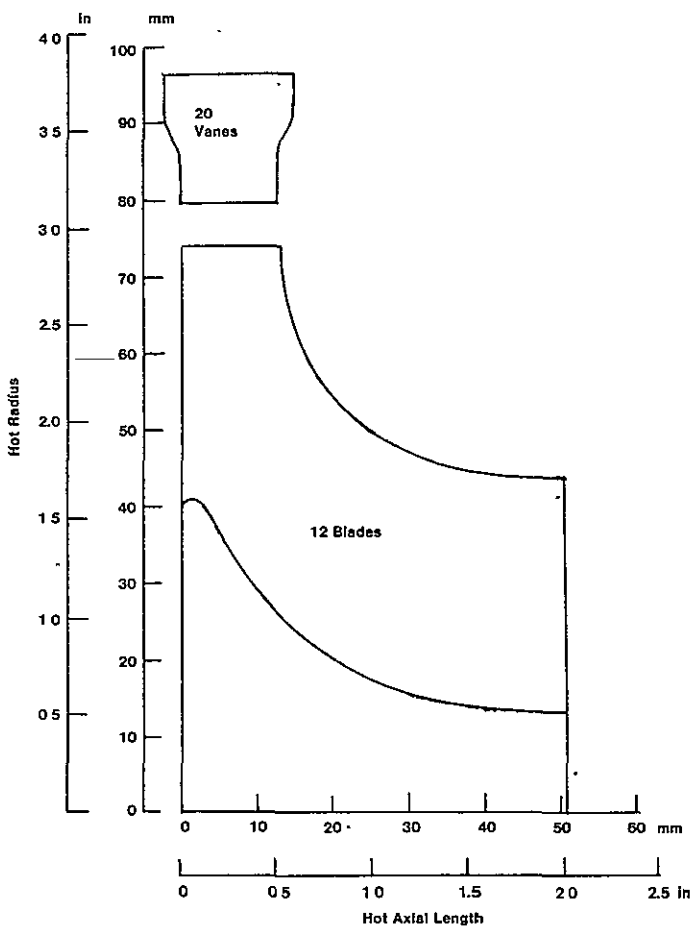


Figure 43 — Mod I Power Turbine Flow Path

In order to provide an acceptable swirl range for the Mod I turbine, the rotor exit blade angle was reduced by approximately 1.7 degrees from the RPD design. A com-

Table VI — Mod I and RPD Power Turbine Parameters for Various Engine Operating Points

	Idle		48 km/h (30 mph)		80 km/h (50 mph)		Max Pwr (SLS)	
	Mod I	RPD	Mod I	RPD	Mod I	RPD	Mod I	RPD
Turbine Power kw (HP)	1.86 (2.49)	1.48 (1.98)	4.92 (6.59)	4.30 (5.76)	8.91 (11.94)	9.32 (12.49)	45.47 (60.94)	74.14 (99.36)
Equivalent Flow kg/sec (lb/sec)	.201 (.442)	.159 (.350)	.225 (.496)	.175 (.385)	.268 (.590)	.224 (.493)	.348 (.767)	.321 (.707)
Equivalent Work kJ/kg (Btu/lb)	4.37 (1.88)	5.07 (2.18)	10.10 (4.34)	10.30 (4.43)	13.77 (5.92)	15.96 (6.86)	36.52 (15.70)	49.25 (21.17)
Expansion Ratio (T-T)	1.08	1.08	1.15	1.15	1.21	1.24	1.72	2.06
Efficiency (T-T)	68.8	84.0	86.8	88.6	85.6	89.0	84.7	86.7
% Equivalent Speed	22.5	24.5	48.1	47.0	52.1	53.0	100.	100.
U/C	.421	.545	.672	.751	.619	.688	.724	.724
Reaction	.325	.356	.490	.543	.445	.479	.555	.533
Exit Swirl	-21.8	-9.9	+6.4	+23.0	-2.5	+9.2	+2.5	-2.0
Exit Mach Number	.096	0.71	.107	.092	.135	.117	.247	.269

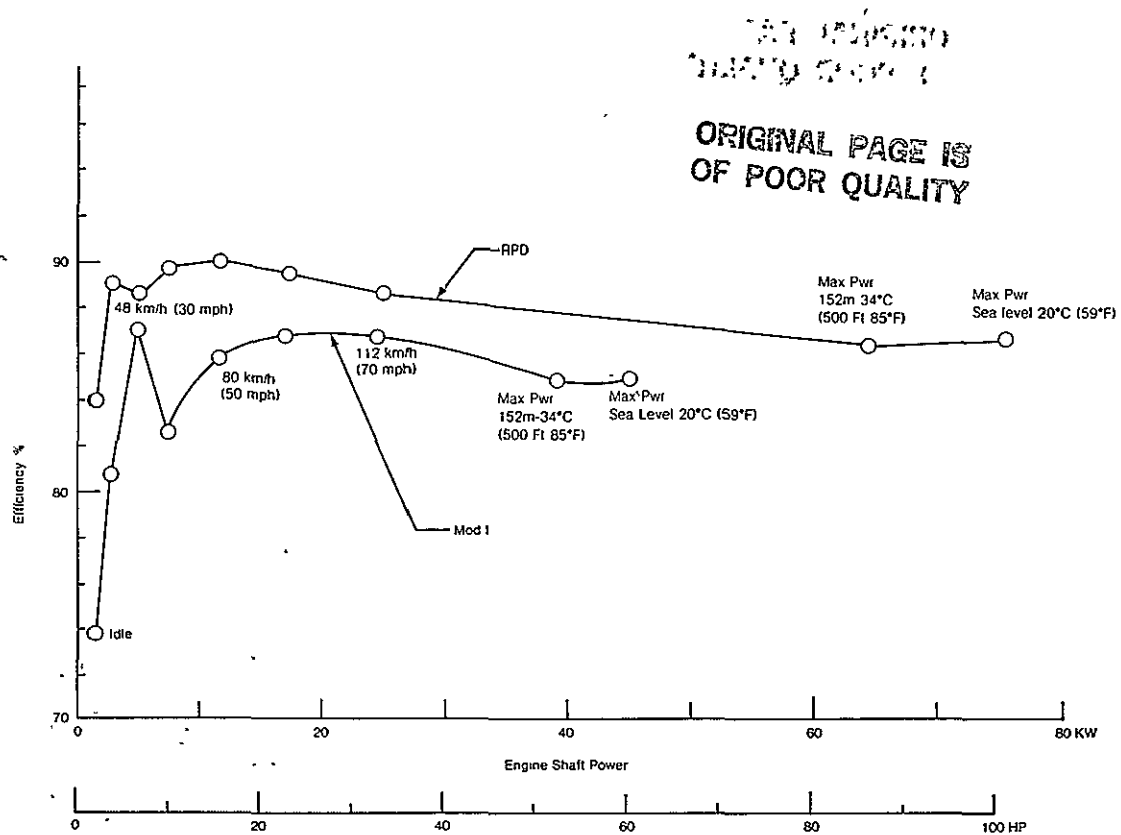


Figure 44 — Efficiency Goal—RPD and Mod I Power Turbine
Without Inlet Scroll

parison of the Mod I and RPD power turbines over the engine road-load operating line is illustrated in Figure 44. Similar to the Mod I gasifier, a degree of conservatism has been factored into the Mod I turbine since the Mod I design will not have the benefit of the RPD aero development time. The most conservatism has been applied to the idle condition wherein the highest risk of attaining RPD design goals exist. The sharp drop in efficiency at the lowest power points is a result of estimated cycle component matching. The Mod I design and performance estimates will be updated as necessary to reflect experimental results of the turbine aero development program.

Turbine Inlet Scroll

Model testing of the inter turbine duct and power turbine scroll has verified the basic design approach of the power turbine scroll. The scroll design was presented in the First Semi-Annual Technical Summary Report.

Mod I Vane Design

The Mod I power turbine vane is illustrated in Figure 45. These vanes feature endwall contouring and ceramic construction. The vanes are symmetrical to reduce production assembly costs. A set of metallic vanes for Mod I will be procured as backup to the ceramic vanes. The vane exhibits a trailing edge diameter of 0.508 mm (0.020 in.), a leading edge diameter of 5.08 mm (0.20 in.), a true chord of 31.27 mm (1.231 in.) and a trailing edge blockage of 6.4%.

Vane suction and pressure surface velocity distributions for the SLS maximum power design point are illustrated in Figure 46. Velocity distributions of the Mod I vane are similar to the RPD vane, but display lower velocity levels due to the reduced work requirement.

Mod I Rotor Design

The Mod I rotor has been designed with emphasis on low cost through use of radial blading, low inertia through use of fully scalloped backplate and deeply cut hub, low exit machine number to minimize exhaust duct loss, and relatively high maximum power reaction to achieve a broad efficiency band.

Mean streamline velocity distributions for Mod I rotor under idle, 48 km/h (30 mph), 80 km/h (50 mph) and maximum power are presented in Figure 47 through 50. The velocity distributions are similar to the RPD design particularly at part power.

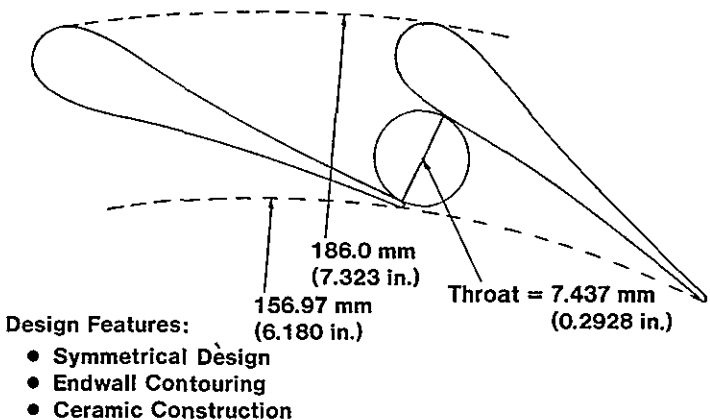


Figure 45 — Mod I Power Turbine Vane Design

ORIGINAL PAGE IS
OF POOR QUALITY

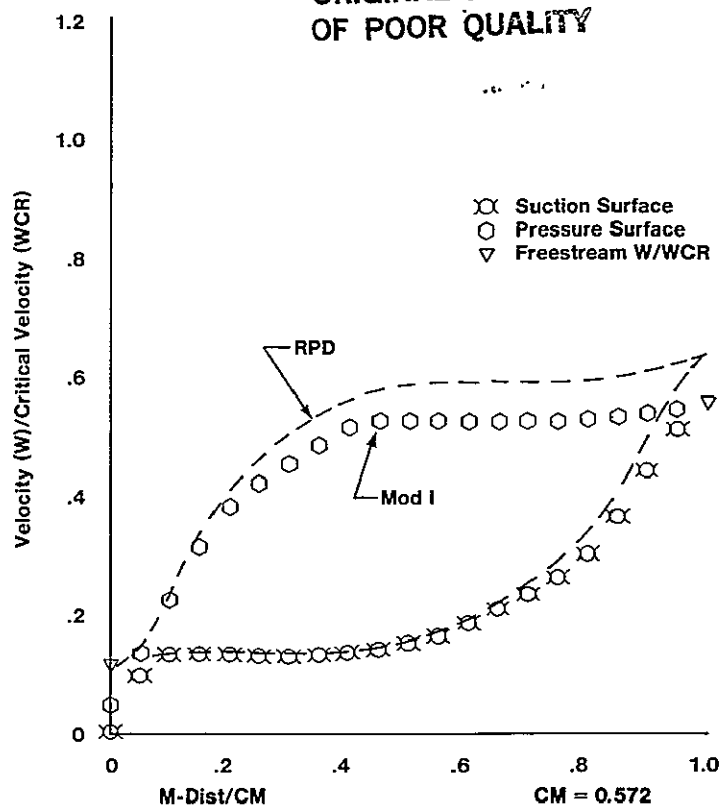


Figure 46 — Mod I Power Turbine Vane Velocity Distribution

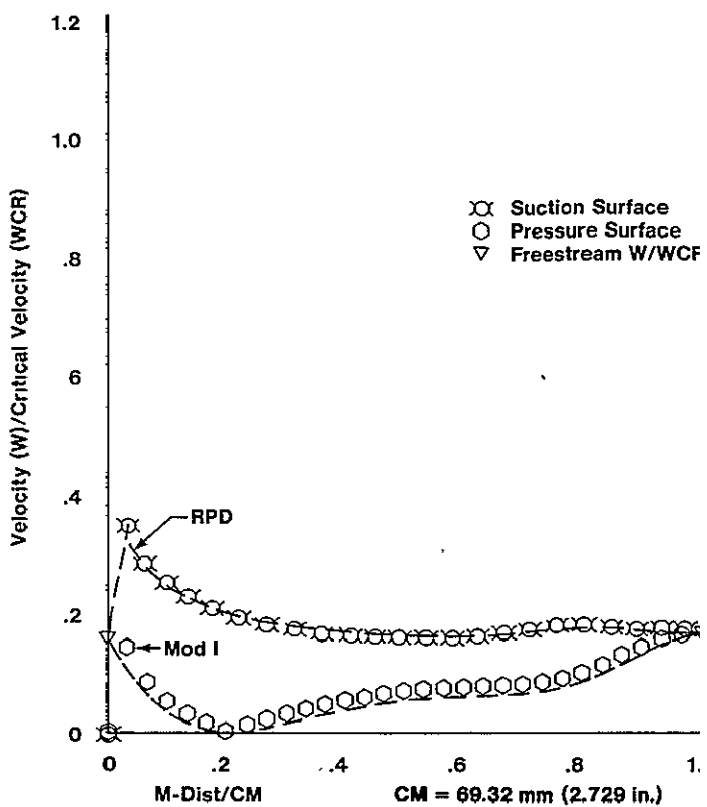


Figure 47 — Mod I Power Turbine Rotor Mean Velocity Distribution — Idle

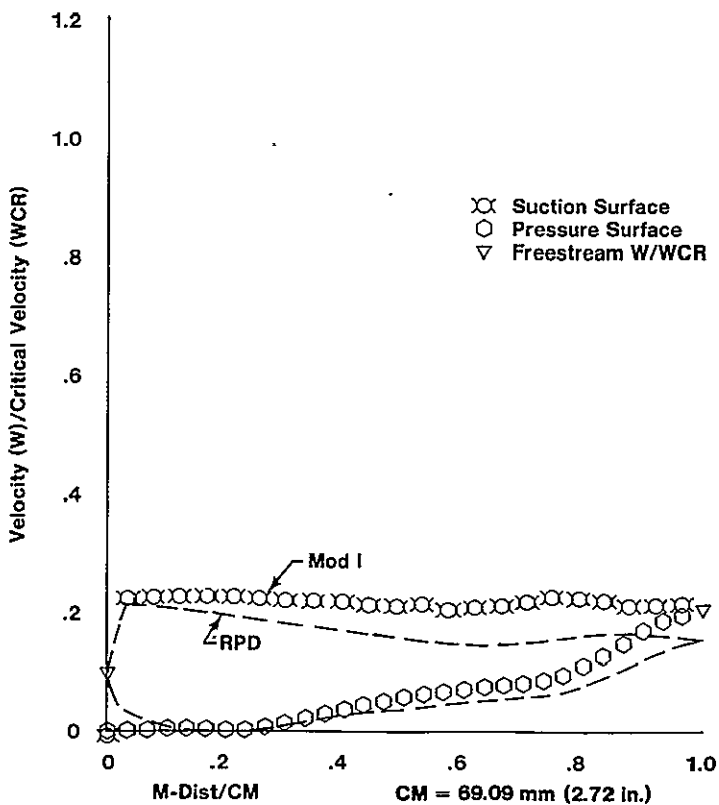


Figure 48 — Mod I Power Turbine Rotor Mean Velocity Distribution — 48 km/h (30 mph)

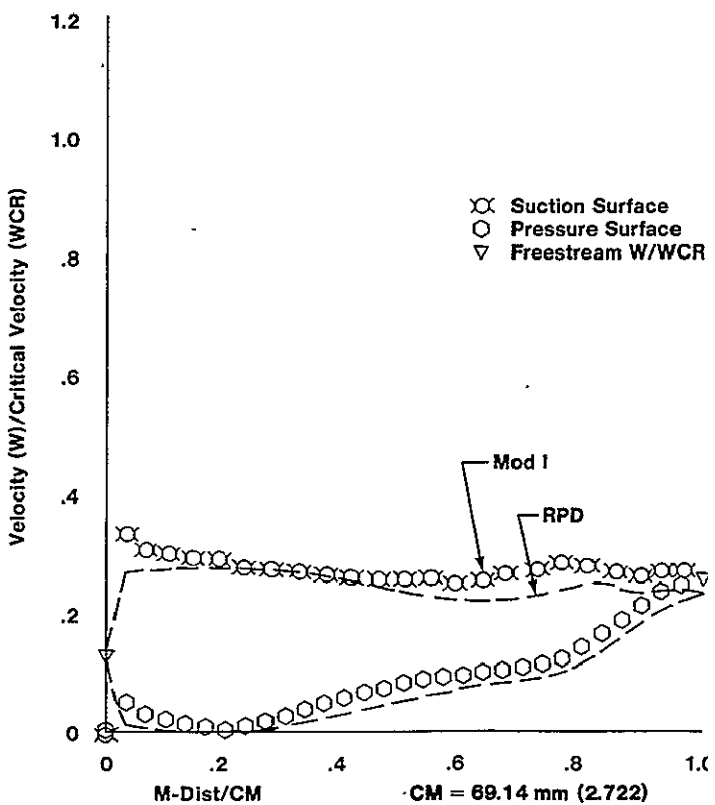


Figure 49 — Mod I Power Turbine Rotor Mean Velocity Distribution — 80 km/h (50 mph)

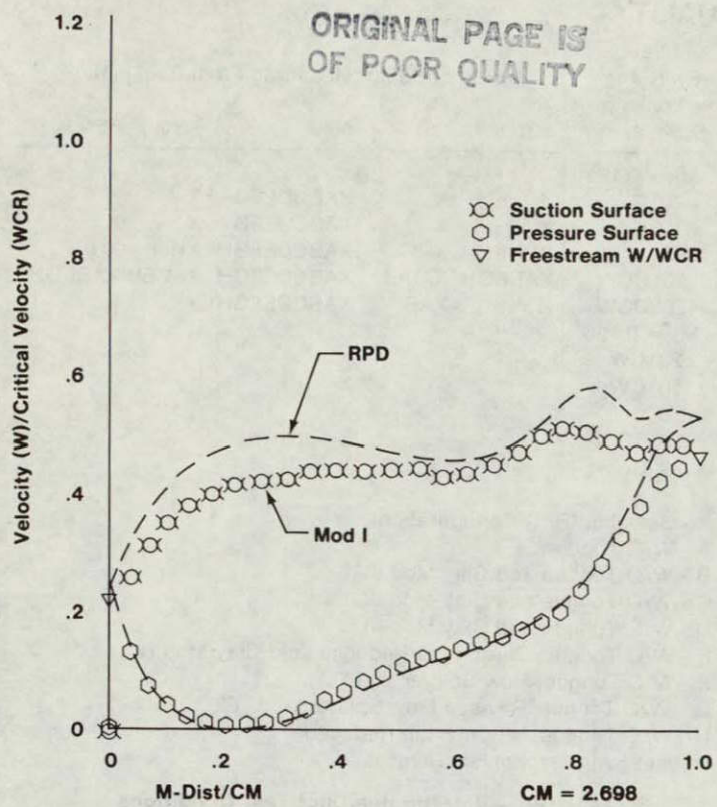


Figure 50 — Mod I Power Turbine Rotor Mean Velocity Distribution — Max Power (SLS)

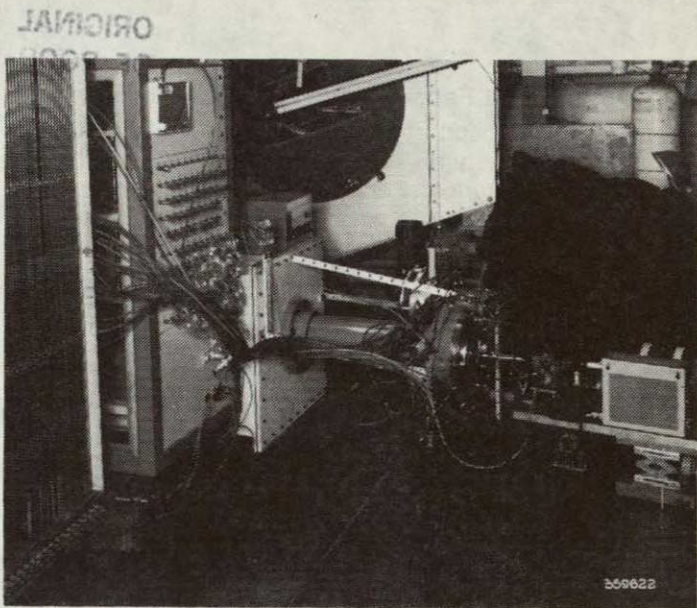


Figure 51 — Interturbine Duct and Scroll Test Rig Setup

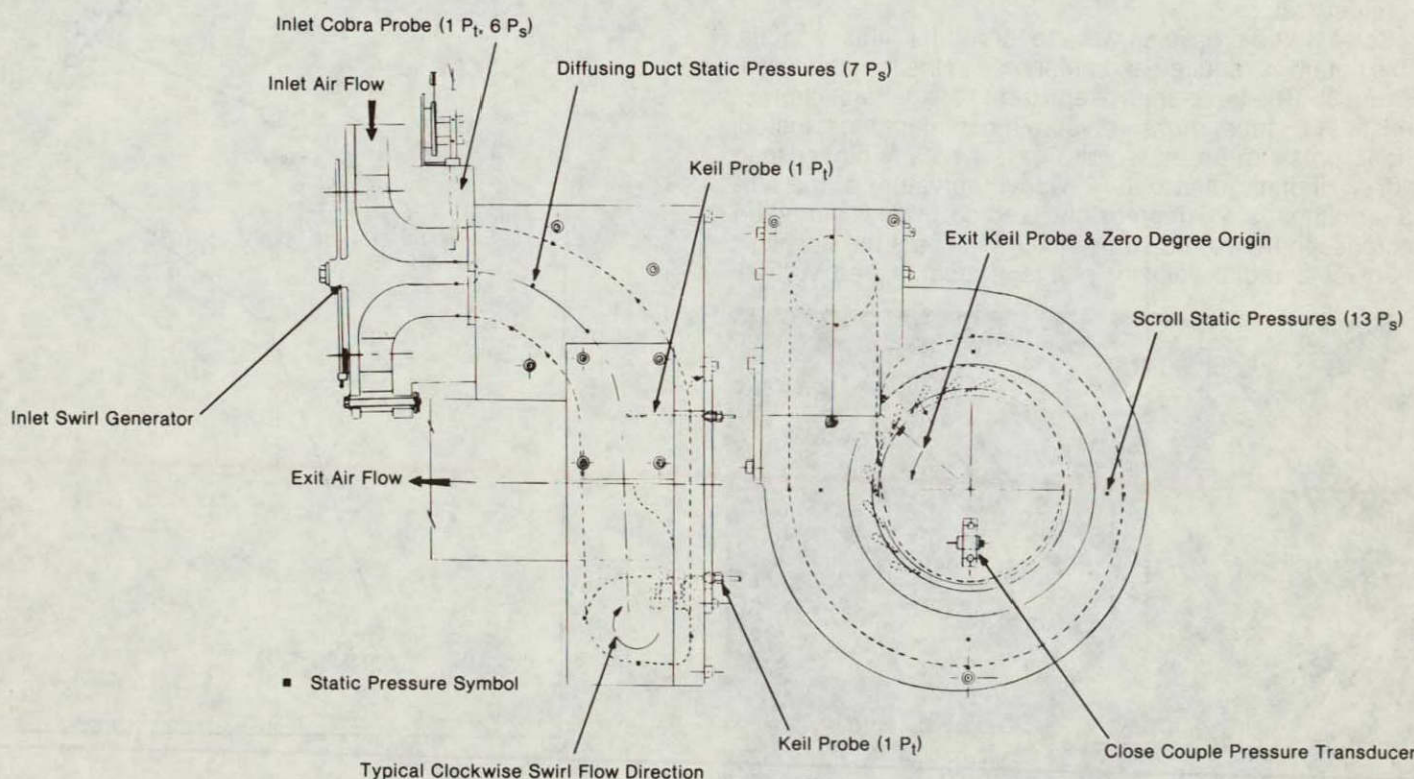


Figure 52 — Test Rig Instrumentation

Rig Design and Fabrication

Design, layout, and detailing were completed for the basic rig, inlet scroll and exhaust duct. Fabrication of the basic rig is 1/3 completed. Hardware is scheduled for completion in March 1981. The vanes and rotor are machined of 410 stainless steel.

Interturbine Duct and Scroll Cold Flow Testing

The interturbine duct and power turbine scroll configuration has undergone extensive cold flow testing. Testing was accomplished using ejector test rig set-up shown in Figure 51. This test rig modeled the duct scroll flowpath from GT exit to PT vane exit. A radial inflow swirl generator was utilized at duct inlet to provide inlet swirl conditions covering the range expected in engine operation. Flow was measured using an orifice downstream of the rig.

The test rig with instrumentation is shown schematically in Figure 52. The back face of the test rig was purposely made from clear plexiglass to permit the use of flow visualization. Rotating total and static pressure instrumentation was provided to measure vane exit circumferential pressures. Figure 53 shows the transversing mechanism and clear scale face.

Approximately 150 hours of testing have been accomplished. Table VII summarizes the configurations tested. A baseline configuration and seven modifications were tested.

Interturbine duct static pressures were reduced and presented in the form shown in Figure 54. Only small variations in the illustrated trends were observed as a function of inlet swirl or scroll geometric modifications. Circumferential variation in static pressure at duct exit is believed to be the result of secondary flows induced by scroll curvature.

Scroll static pressures were recorded for all test points. This data was reduced and presented in the form shown in Figure 55. The trend shown represents the general characteristic of static pressure for all configurations tested. Static pressure on the scroll OD is typically higher than side wall static due to the concave curvature of the surface. In the first 90 degrees of the scroll, there is a marked increase in measured static which indicates the development of a radial velocity profile (probably free vortex).

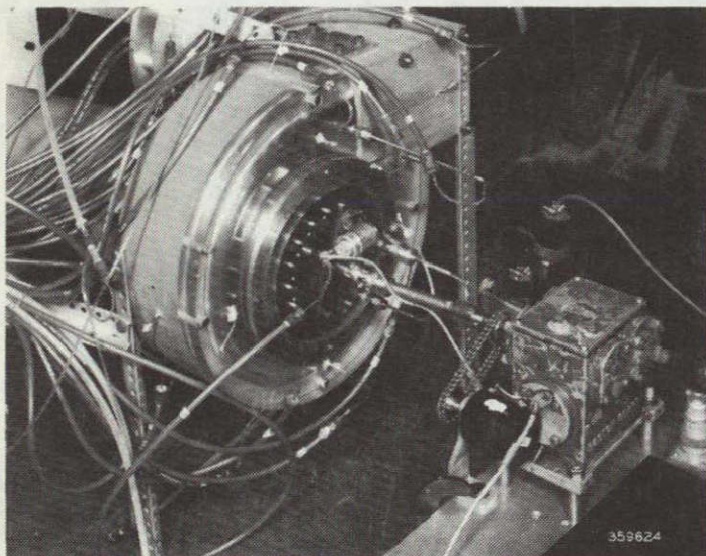


Figure 53 — Traverse Mechanism and Plexiglass Backplate

Inlet Swirl Angle Looking Downstream	Percent Span Measured From Backplate				
	10%	25%	50%	75%	86%
$M_N = 0.194$					
20° CW	X	X	XABCDEFG	X	X
10° CW	X	X	XABCDEFG	X	X
0°	XBI	XHI	XABCDEFGHI	XHI	XHI
10° CCW	XABEGH	XABEH	XABCDEFGH	XABEH	XABEGH
20° CCW	X	XAB	XABCDEFGH	X	X
$M_N = 0.125$					
20° CW				X	
10° CW				X	
0°				X	
10° CCW				X	
20° CCW				X	

X - Baseline (RPD Configuration)

A - W/O Tongue

B - W/O Tongue and Clay Mod I

C - W/O Tongue and Clay Mod II

D - W/O Tongue and Clay Mod III

E - W/O Tongue, Shroud Lip Reduced, and Clay Mod IV

F - W/O Tongue, Flow Splitter and "E"

G - W/O Tongue, Revised Flow Splitter, and "E"

H - W/O Tongue, No Clay, Lip Reduced

I - Inlet Swirl Mechanism Removal

Table VII — Interturbine Duct Test Conditions

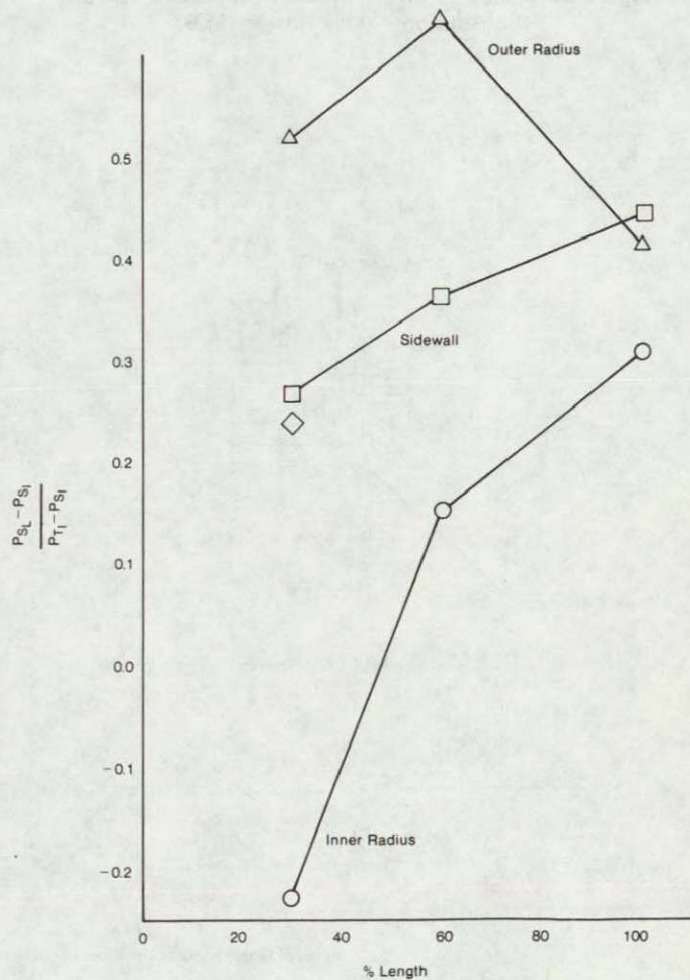


Figure 54 — Interturbine Duct Wall Static Pressures

ORIGINAL PAGE IS
OF POOR QUALITY

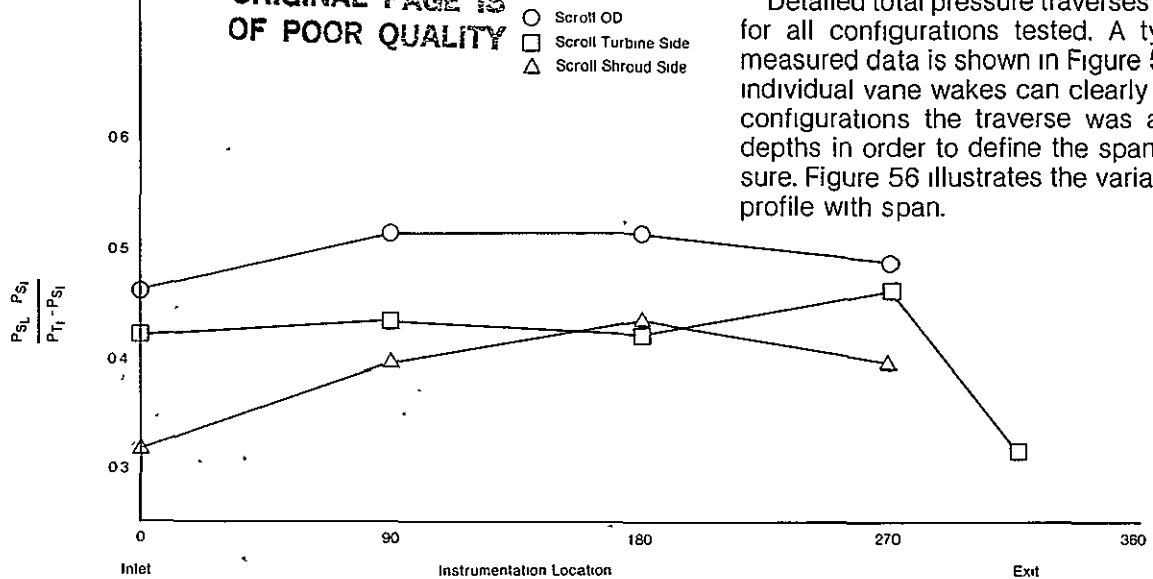


Figure 55 — Scroll Wall Pressure Coefficient

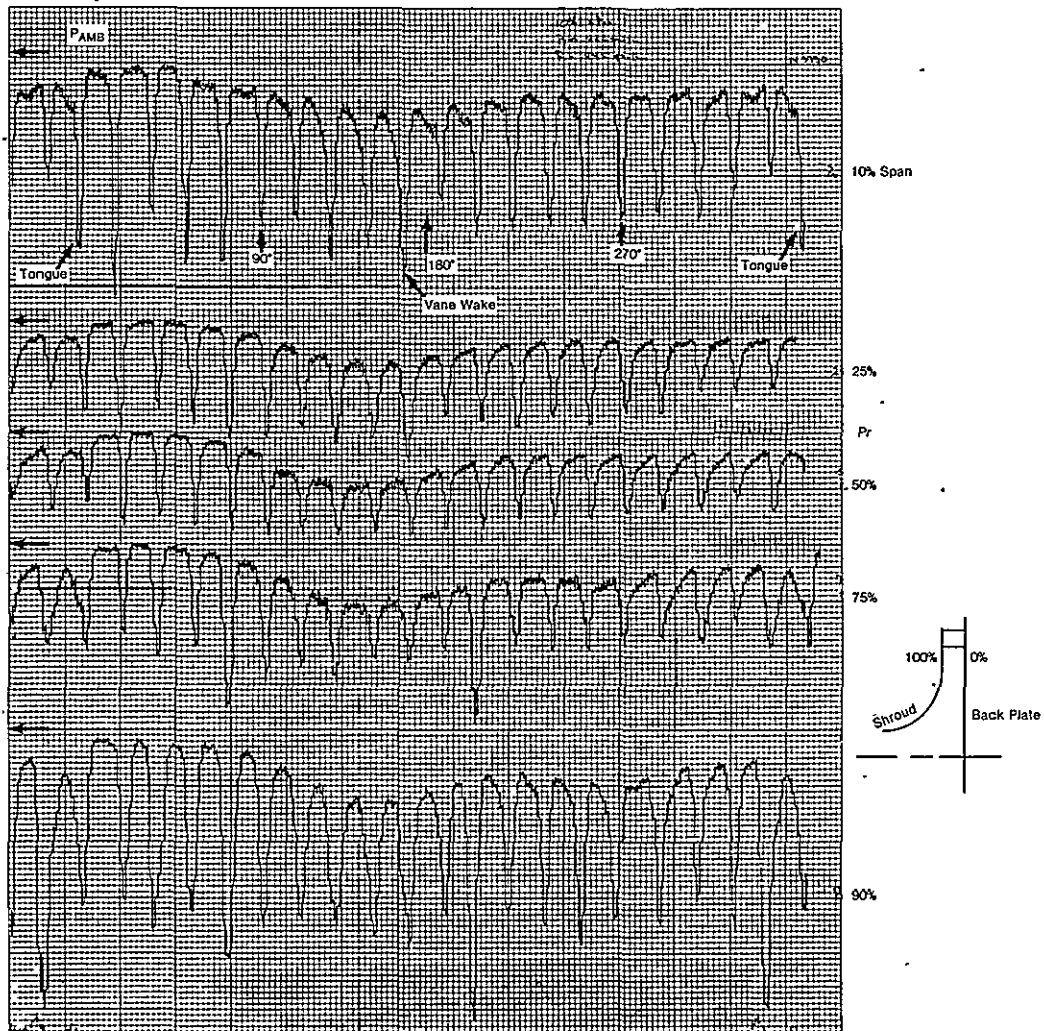


Figure 56 — Circumferential Total Pressure Traverses

Beyond 270 degrees, the scroll cross sectional area begins to close. The sidewall static decreases as the flow approaches the tongue, probably due to the turning and accelerating flow into the last vanes.

Detailed total pressure traverses were made at vane exit for all configurations tested. A typical example of the measured data is shown in Figure 56. In each traverse the individual vane wakes can clearly be identified. For most configurations the traverse was acquired at five probe depths in order to define the spanwise variation of pressure. Figure 56 illustrates the variability of circumferential profile with span.

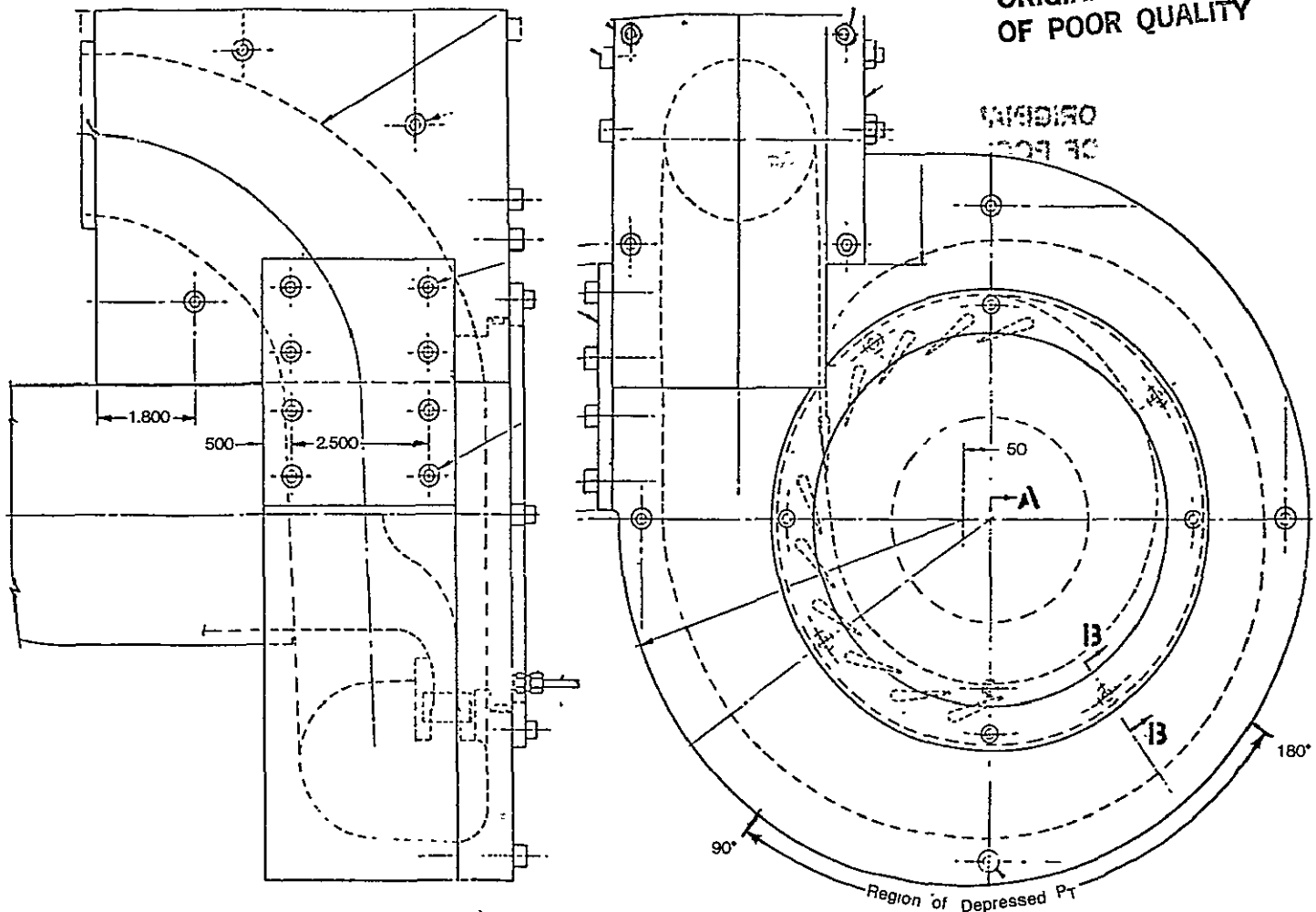


Figure 57 — Region of Depressed Total Pressure

A particularly important trend noted in the measured total pressure transverse is that the circumferential traverse indicates a high total pressure near the tongue, a "low" total pressure between 90 and 180 degrees, followed by an increase in total pressure to a plateau magnitude approximately mid way between and near tongue maximum and the depression minimum. The region of depression is located as shown in Figure 57. Based on data analysis, it was concluded that this depression in vane exit total pressure is due to increased incidence on the power turbine vanes. Apparently the scroll requires approximately 180 degrees of circumference to achieve a stable, uniform radial flow condition. For the first 90° of circumference, the vanes "scoop" the flow resulting in high total pressure. Between 90° and 180°, a developed radial flow has not yet been accomplished so the vanes must achieve greater turning inducing higher loss. After 180° the radial flow profile is established and vane turning is more consistent with design requirements.

Modifications were made to the scroll configuration to reduce the magnitude of depression in total pressure. The most successful Mod is illustrated in Figure 58. A flow splitter was installed in the scroll which captured the flow near 90 degrees and directed the flow toward the 180 degree vane. This modification did increase substantially the total pressure in the depression. However, a significant splitter wake was measured in the vane passage just downstream of the splitter.

The circumferential variation in unit mass flow at the vane exit plane was calculated from measured total pressure and static pressure traverses. The maximum variations, corresponding to the maximum and minimum total pressure points, were $\pm 3.5\%$ from the unit mass flow calculated from the average total and static pressures. This magnitude of variation is not expected to significantly affect turbine performance.

Spanwise variations in the total pressure traverse revealed a greater endwall effect on the turbine shroud side than on the turbine backface side. Modifications to the scroll using clay were made to improve this condition. Only small improvement in spanwise variation was achieved.

Testing with varying amounts of interturbine duct inlet swirl was accomplished and typical results in mid channel traverse data are shown in Figure 59. Some variation in circumferential traverse was observed due to direction of swirl. As shown in Figure 59, clockwise swirl produced more of a notable depression in total pressure at 90 to 180 degrees than counter clockwise swirl. The explanation for this is that CW swirl produces a natural "peeling" of the flow into the vanes where CCW swirl requires a backflow to feed the vanes (See Figure 60). Although circumferential variation with swirl is noted, average total pressure loss variation was only slight for the range of swirl expected in the engine, (10 degrees CW to 20 degrees CCW). Average total pressure was calculated for each tra-

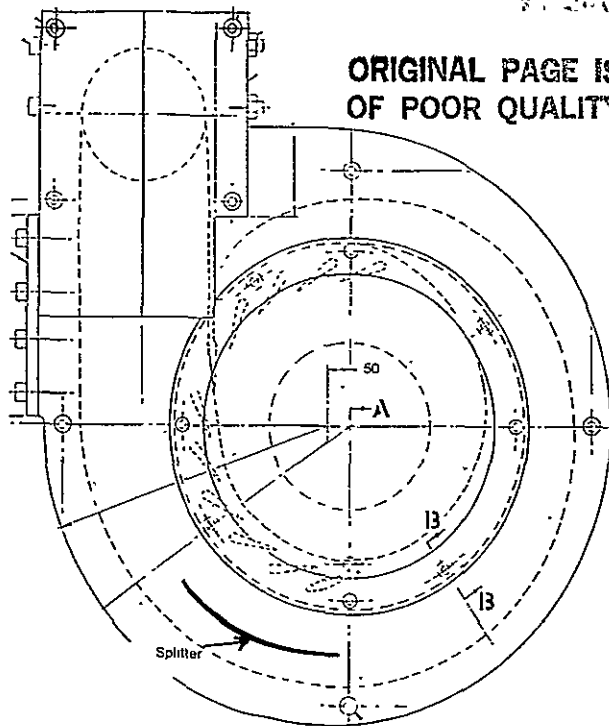


Figure 58 — Scroll Flow Splitter

pected in the engine, (10 degrees CW to 20 degrees CCW). Average total pressure was calculated for each traverse using two approaches: a) the entire traverse including vane wakes was averaged, and b) averaging was accomplished using just the peaks between vanes of the measured traverse. Peaks-only data represents the delivered pressure by the scroll to the vanes.

The complete traverse data represents the total loss of the system

In summary, the following conclusions are based on the overall experimental program:

- Measured interturbine duct loss is 0.65% less than the RPD design goal (1.15% vs 1.8%) at maximum power conditions.
- Measured power turbine vane loss agrees closely with the RPD design goal.
- Measured duct total pressure loss is insensitive to simulated gasifier exit swirl.
- The vane exit plane circumferential unit flow variation, defined by the maximum and minimum total pressure points, was $\pm 3.5\%$ compared to the unit flow calculated from the circumferential average pressures.
- Using a splitter in the scroll can reduce total pressure circumferential variation at the expense of a localized splitter wake

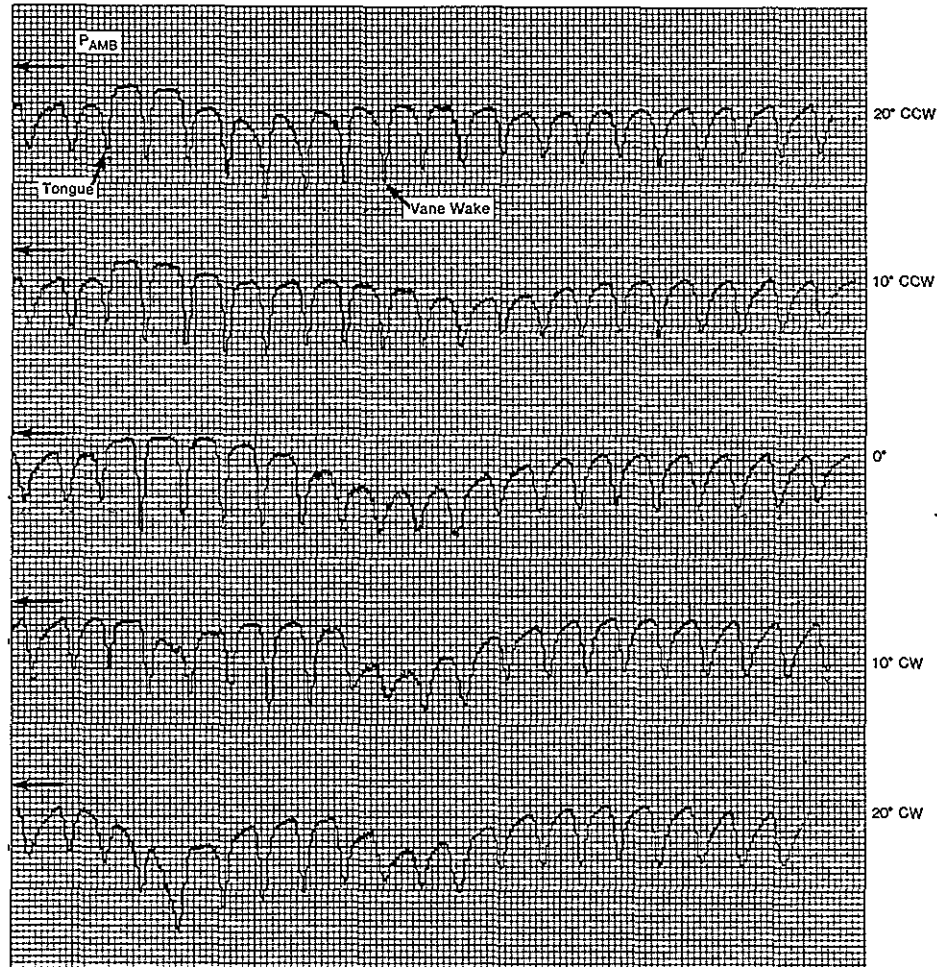


Figure 59 — Variation in Circumferential Traverse with Swirl at Vane Mid Span

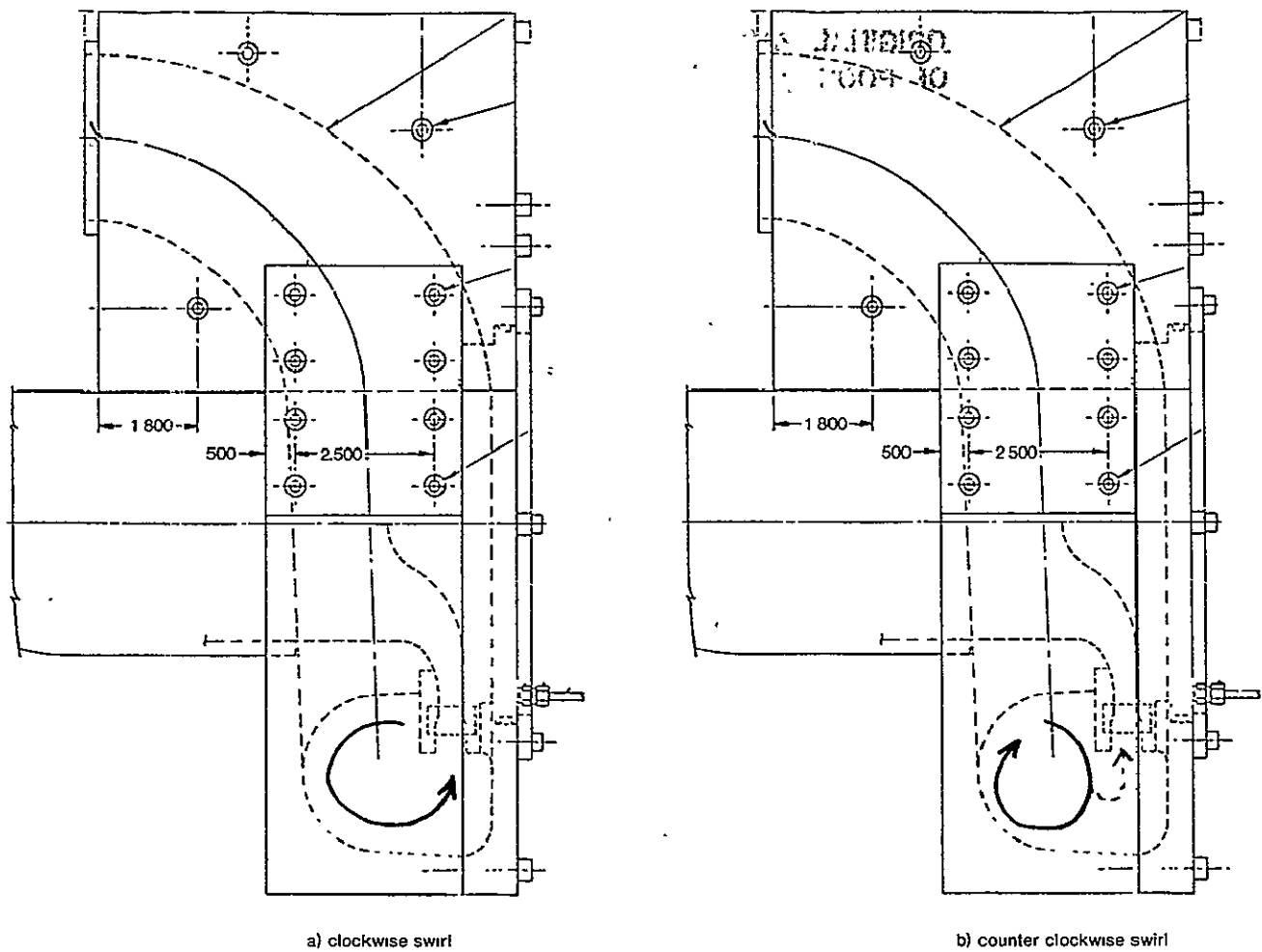


Figure 60 – Swirl Effect of Vane Feed

- Removal of the scroll tongue did not produce a significant deleterious effect upon circumferential distortion
- Modification of the scroll cross sectional shape did not significantly alter spanwise total pressure variations.

5.2 Power Turbine Mechanical Development

RPD—Static Parts

The RPD original power turbine scroll design was described in the first semi-annual report CR-165178. The scroll analytical analysis effort was continued and the three-dimensional finite element geometric model is near completion.

Mod I—Static Parts

Two Mod I design layouts of the power turbine were completed. One was an all metal configuration and the second was a metal-ceramic configuration in which the rotor was metal and the static flow path components were ceramic. This analysis would allow ceramic parts to be incorporated into the engine test program at the earliest possible opportunity.

A three-dimensional finite element geometric model of the metal scroll was completed. A computer simulation model is shown in Figure 61

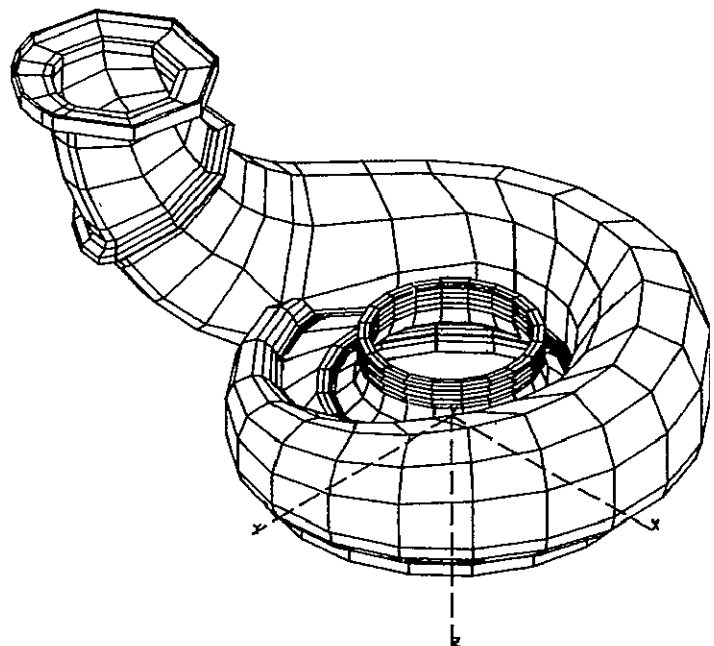


Figure 61
AGT 100 MOD 1 Metal Power Turbine Scroll Computer Model
Simulation

VI. Combustor Development

6.1 RPD

Heat Transfer and Stress Analysis

A finite element model, which has been used to analyze the heat transfer rates and the resulting thermal gradients of the RPD combustor was described in the first semi-annual report. Temperature profiles were generated for the conditions corresponding to a vehicle speed of 96 km/h (60 mph), and also for a nine step transient acceleration cycle which began with a start up from ambient temperature and finished at maximum power. The temperature profile at the 96 km/hr (60 mph) condition is shown in Figure 62. The stresses which result from the calculated thermal gradients have been analyzed. The maximum thermal gradients occur eight seconds after the start of the transient cycle and therefore this condition was chosen for analysis. The second largest thermal gradient occurs six seconds after the start and the resulting stresses were determined for this condition as well.

A summary of the thermally induced stresses is given in Figure 63. It can be observed that the maximum stress during the transient cycle is more than four times the stress at steady state. However, the stress is still very low and leads to a probability of failure of 1.7×10^{-8} (1 failure in 59 million). The stress at the six second condition was considerably less than that at eight seconds.

Variable Geometry Sensitivity

The RPD combustor for the AGT 100 engine uses variable geometry to maintain control over the primary zone flame temperature. The variable geometry must be positioned accurately because a relatively small change in flame temperature may cause a considerable change in exhaust emissions.

The RPD combustor was designed to operate at a specific variable geometry position to maintain a desired flame temperature for each operating point. A calculation was made to determine the effect of small changes in the variable geometry position on flame temperature and hence exhaust emissions.

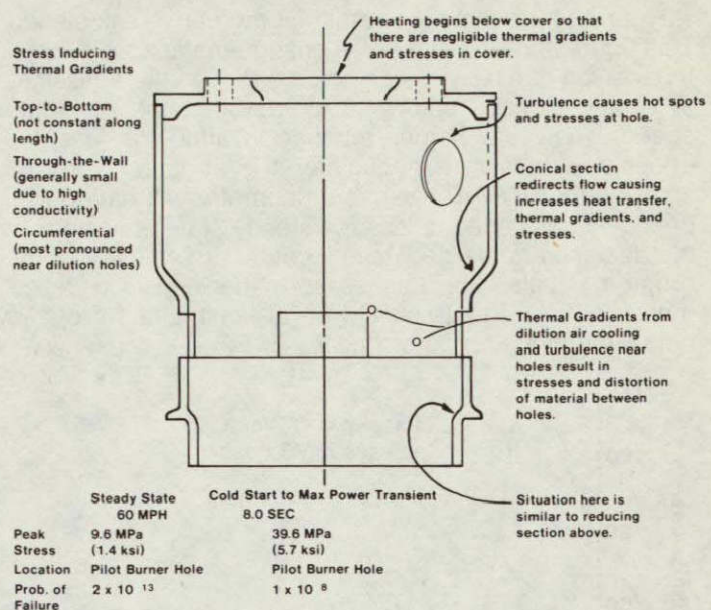


Figure 63—AGT 100 Combustor Thermal Gradient and Stress Overview

Using the data for % primary flow which were presented in the first semi-annual report, new flame temperatures were calculated for variable geometry positions ± 1.27 mm (± 0.050 in.) away from the design value.

The exhaust emissions were assumed to change with flame temperature according to equations which had been used to correlate early GT-225 experimental data. These relations were:

$$CO \propto T(e^{-0.0055T})$$

and

$$NO_x \propto e^{0.005T/T}$$

where

T is in $^{\circ}R$

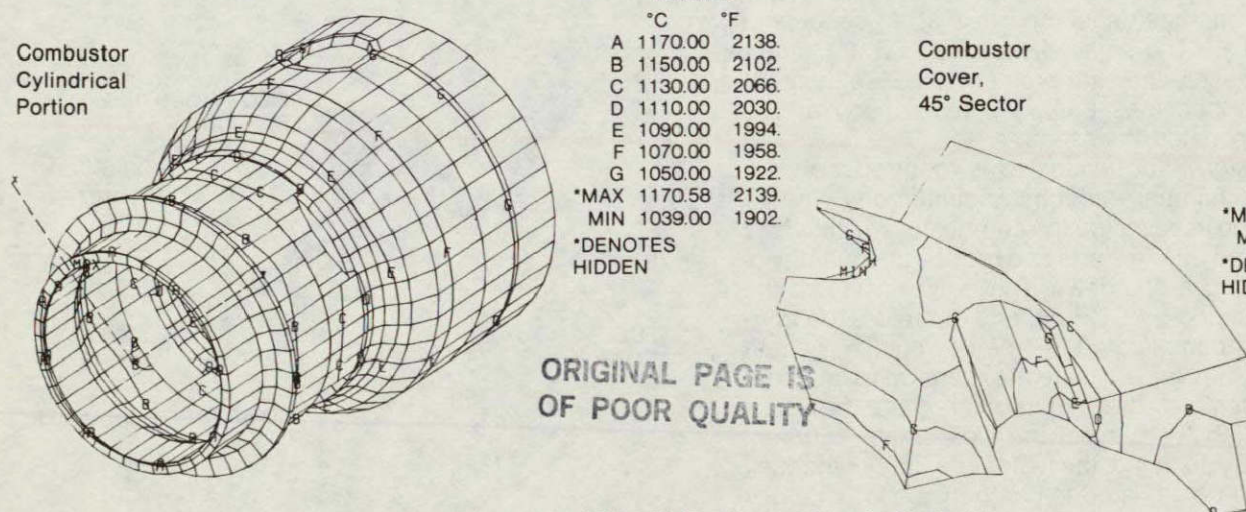


Figure 62—AGT 100 Combustor Steady-State 96 km/h (60 mph) Temperature Profiles

The change in exhaust emissions which resulted from the small change in variable geometry position was calculated as a percent change from the emissions that would have been produced at the design variable geometry position.

Figure 64 presents the results of the above calculation. This figure shows that a small change in variable geometry position can have a significant effect on the emissions at vehicle speeds below 48 km/h (30 mph). At higher speed, where the percent change in airflow is less, the effect on emission is negligible. It is apparent from the analysis that the RPD variable geometry will have to be precisely positioned unless the steady state emissions at the design variable geometry location are well below the program goals. For this reason, the emission levels measured in rig tests should be at least a factor of two below the overall program goals.

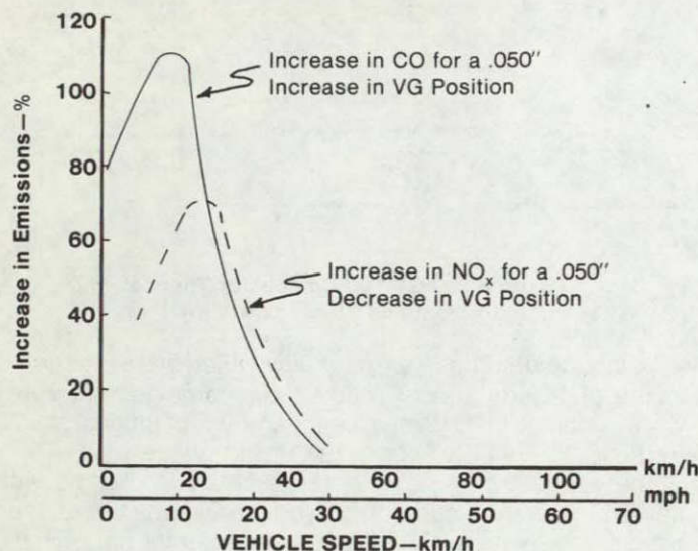


Figure 64—Effect of Variable Geometry Position Accuracy on Emissions

Alternate Fuel System

The RPD combustor design follows closely the design of previous DDA low-emission combustors. In these designs, the main fuel is introduced through the outer wall of the prechamber. Because of the high RPD operating temperature, it is necessary to cool the fuel supply tubes and manifolds. This has been accomplished using concentric tubes and CDP air. The small size of the AGT 100 combustor, however, increases the problem because the concentric fuel line becomes bulky by comparison and is somewhat complicated to assemble.

A simpler design to be evaluated is to introduce main fuel into the prechamber through the centerbody. Shorter fuel lines could be used inside the combustor which would reduce the fill time during starts and reduce the quantity of fuel purged during a shutdown. The entire inside of the centerbody is cooled by CDP air, and, therefore, no concentric tubing or complicated geometry would be necessary. This fuel system would be less expensive to fabricate and also to assemble. The biggest advantage, however, might be in the ability to inject the fuel through different axial positions. By so doing, the residence time of the fuel/air mixture could be adjusted to compensate for changes in auto ignition time brought about by changes in burner inlet temperature.

All of the previous DDA low-emission experiments investigated fuel injection only through the outer wall, and, therefore, no data exists to evaluate the premix/pre-vaporization quality of centerbody injection. It would appear, however, that there are enough potential advantages with this system to consider it as an alternate for the RPD design. Considerable experimental effort would be required, either with the Mod I combustor or with the bench test prechamber model, to determine the most attractive method of fuel injection.

6.2 Mod I

Combustor

The Mod I combustor is shown in Figure 65 and the pilot assembly for this combustor is shown in Figure 66. In Figure 65, the variable geometry bands are positioned such that the primary zone is closed and the dilution zone is opened. The two straps connecting these bands were welded together after the photograph was taken.

The initial combustor build revealed several inter-

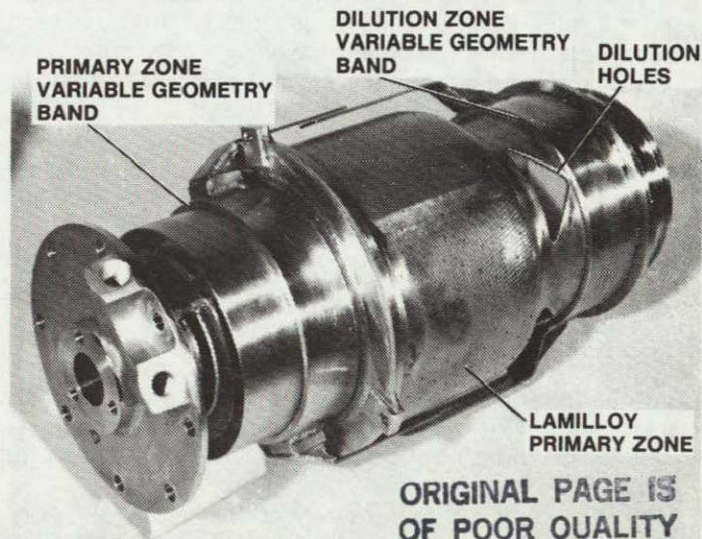


Figure 65—AGT 100 Mod I Combustor

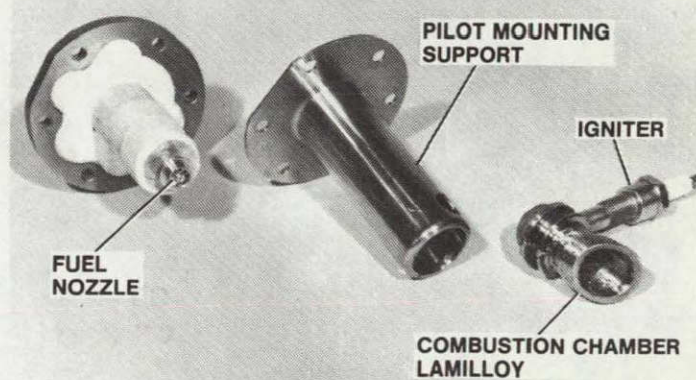


Figure 66—AGT 100 Mod I Pilot Assembly

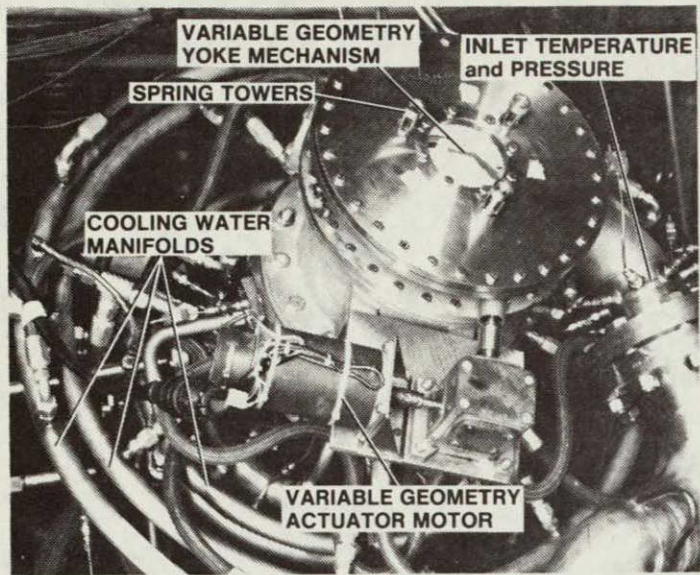


Figure 67 — AGT 100 Combustor Rig - Top View

ference and alignment problems. These difficulties were corrected by reworking the combustor. The major items corrected by this rework were:

- shorten the combustor overall length by 2.03 mm (0.080 in.)
- increase the gap between the variable geometry bands and the body
- repair a leak in the main fuel manifold
- improve the fit between the variable geometry bands and the actuating yoke.

In addition, several instrumentation holes were added to facilitate installing eleven thermocouples. Two thermocouples were installed in instrumentation holes at different radial locations within the dome. One thermocouple was attached inside the end of the centerbody, and five thermocouples were welded to the outer skin of the Lamilloy. Two thermocouples were attached to the uncooled metal wall downstream of the dilution variable geometry band, and one thermocouple was positioned to measure the fuel cooling air temperature.

The burner was installed in the combustion rig and a calibration was made of variable geometry position. The hysteresis of the mechanism was found to be 1.9 mm (0.075 in.). The initial test was conducted at inlet conditions corresponding to a steady vehicle speed of 32 km/h (20 mph). At a burner inlet temperature of 593°C (1100°F), ignition was accomplished without difficulty and the pilot operated stably at less than 0.22 kg/h (0.5 lb/hr) fuel flow.

When fuel was introduced through the main nozzle, a

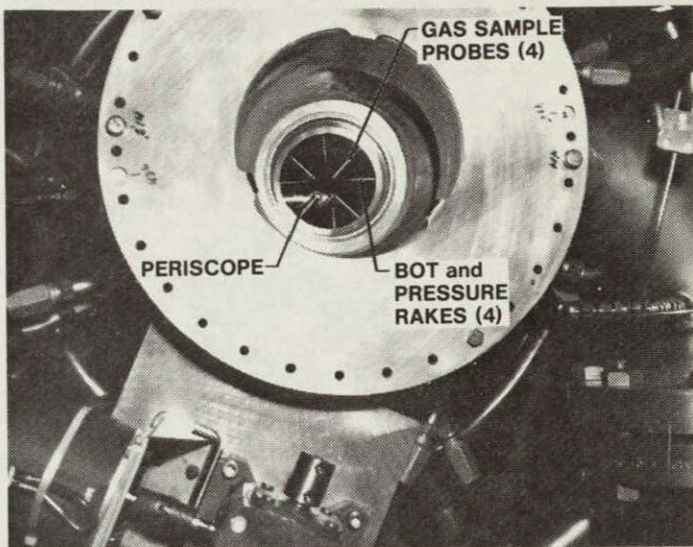


Figure 68 — AGT 100 Combustor Rig - Exhaust Instrumentation

fire stabilized in the prechamber annulus, and the flow had to be shut off to prevent damage to the uncooled metal parts. During this operation, it was discovered that the alignment between the variable geometry band and the yoke actuator was quite critical. As a result of slight movement caused by thermal expansion of the parts during the initial test, the variable geometry mechanism became very difficult to move. The initial test was terminated in order to better align the combustor with the actuator yoke.

Test Rig

The combustor rig was described in the previous semi-annual report. The rig was assembled in the Research Combustion Laboratory and is shown in Figure 67. Figure 68 is a view from a similar location except that the upper portion of the rig has been removed to expose the exhaust instrumentation. The BOT rakes, sample probes, and periscope are each located at increasing axial depths. In this photograph and for the initial testing, the BOT rakes have been replaced by four single, chromel-alumel thermocouples. Except for the variable geometry alignment problem and some minor water leaks, the rig has performed satisfactorily.

A purchase order was placed for a non-vitiated, gas fired preheater. This heater will be capable of increasing the temperature of the combustor inlet air from 538°C (1000°F) to a maximum of 1081°C (1978°F). To minimize heat loss, the heater will be installed as close as possible to the combustor test rig.

ORIGINAL PAGE
BLACK AND WHITE PHOTOGRAPH

BLACK AND WHITE PHOTOGRAPH
ORIGINAL PAGE

VII. Regenerator Development

ORIGINAL PAGE IS
OF POOR QUALITY

7.1 RPD

Design analysis of the original RPD regenerator system, concentrated on the disk/ring gear assembly, inboard (hot) seal assembly and the outboard (cold) seal assembly (Figure 69).

Late in the reporting period work was initiated on the revised regenerator for the AGT 100, the general arrangement of which is shown in Figure 70. The objective in the revised regenerator design was to retain parts commonality with the original design wherever possible while incorporating changes for reduced weight and cost.

Regenerator Disk and Ring Gear Assembly

The disk and ring gear design described in the first semi-annual report was not changed and the design analysis of the disk and ring gear assembly was continued during this period and included the following:

- Thermal analysis of the disk matrix to define disk temperature gradients at four steady state conditions and during a simulated full throttle acceleration.
- Effects of gas side flow distortions on disk thermal gradients and the resulting regenerator performance

- Correlation of predicted performance from the heat transfer model with known IGT 404 performance.
- Evaluation of temperatures in the elastomer joint between the ring gear and disk.
- Ring gear deflection and weld joint fatigue.
- Completion of a 3D stress model of the disk

The disk thermal analysis was completed at the four steady-state conditions detailed in Table VIII and at the transient parameters shown in Figure 71. Combining these conditions with sample flow distributions resulted in data such as shown in Figure 72 (regenerator disk axial isotherms for both a uniform flow distribution and a severely distorted flow distribution).

At steady state conditions, it was found that regenerator effectiveness and thermal gradients were nearly insensitive to engine power level; however, pressure drop across the disk was strongly dependent on engine operating conditions. The critical parameter was the gas flow distribution into the regenerator, a severely distorted flow (compared to uniform flow) lowers effectiveness from 0.95 to 0.89 while increasing pressure drop threefold with significant increases in the local disk temperature gradients.

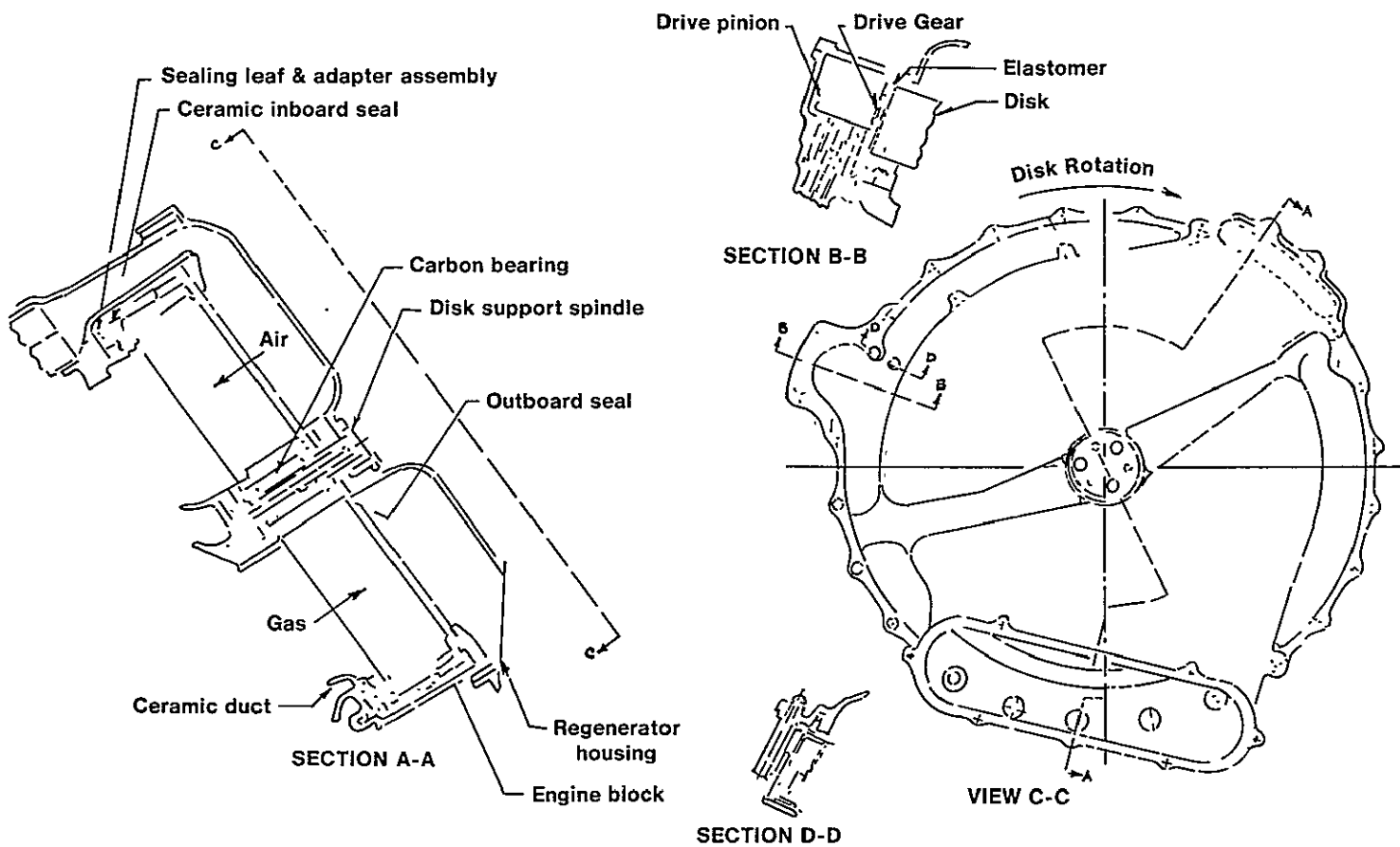


Figure 69 — AGT-100 RPD Initial Regenerator General Arrangement

It was also determined that flow distortion in the radial directions significantly reduced regenerator effectiveness while circumferential maldistribution had little effect on performance. Additionally, the correlation of the model predictions of performance with known IGT 404 and 505 regenerator characteristics verified the need for good flow distribution into the regenerator disk. These results emphasize the importance of the cold flow rig testing early in the AGT 100 program to define the optimum flow fields for the AGT 100 regenerator.

The disk ring gear drive is attached to the disk with an elastomer joint. Using the disk temperature distributions, an estimate of elastomer temperatures was calculated to

ensure the temperature limits of the RTV 106 was not exceeded. The finite element model of the rim configuration and the resulting temperature profiles are shown in Figure 73.

The maximum temperature of 244°C (472°F) occurred when the engine is operating at maximum power on a hot day and is within the material limits established by the elastomer manufacturer.

Stress analysis studies of the disk/ring gear were conducted in two areas, ring gear deflection/stress and disc matrix stress. The ring gear was analyzed to determine the deflected shape and stresses resulting from the drive loads 290N (65lb.) radial, 1114N (250lb.) tangential re-

ORIGINAL PAGE IS
OF POOR QUALITY.

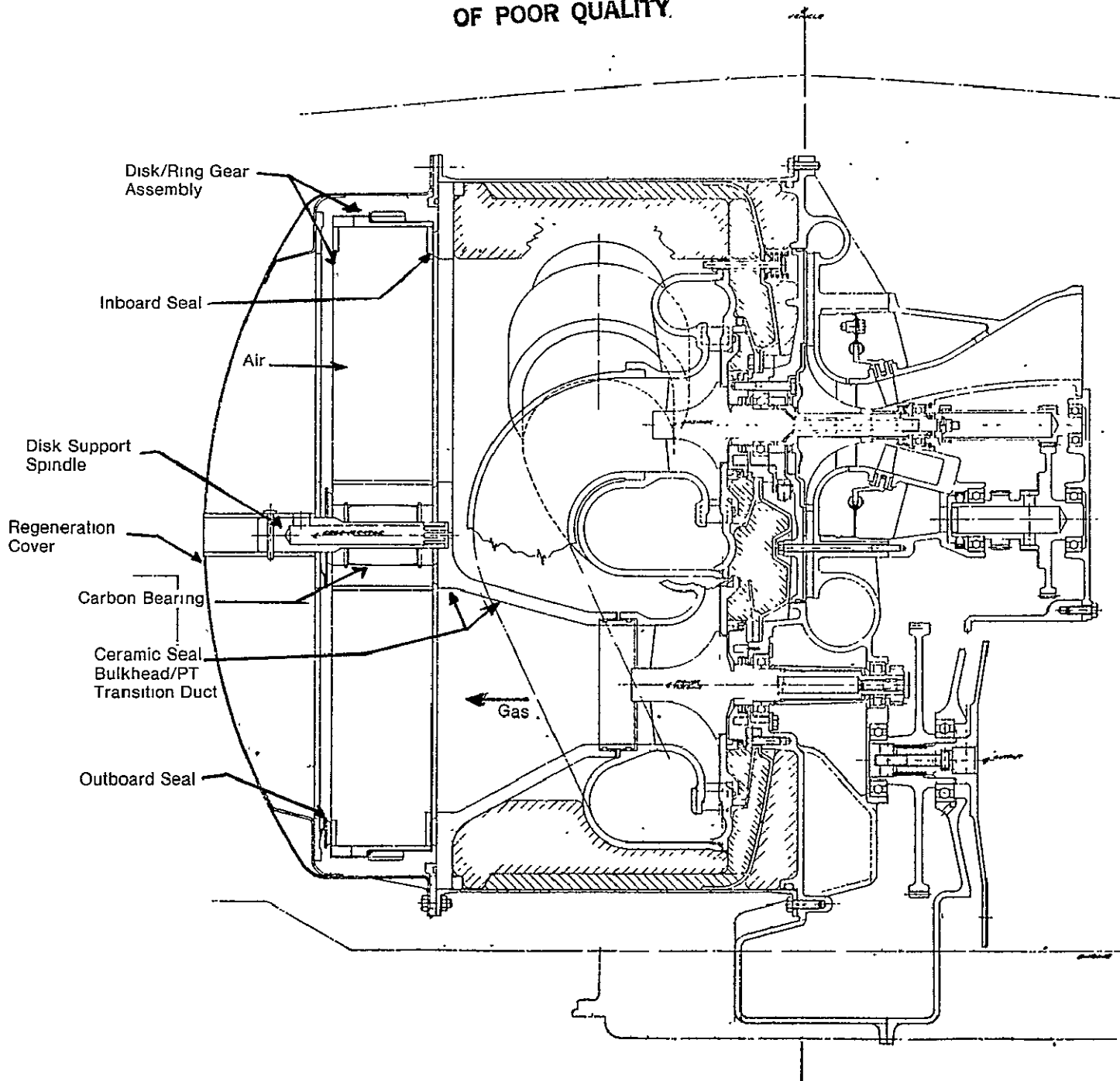


Figure 70 — Revised RPD Regenerator Preliminary Design

Table VIII—Steady State Regenerator Operating Conditions

Cold Side	Full Power	96 km/h (60 mph)	48 km/h (30 mph)	Idle
		Part Power	Part Power	
Inlet Air Flow kg/sec (lb/sec)	298 (657)	.143 (315)	.091 (200)	.096 (211)
Inlet Air Pressure MPa (PSIA)	420 (60.89)	.209 (30.37)	.152 (22.08)	.140 (20.35)
Inlet Air Temperature °C (°F)	214 (417)	117 (242)	78 (172)	73 (163)
Exit Air Pressure MPa (PSIA)	417 (60.41)	207 (30.06)	151 (21.88)	139 (20.18)
Exit Air Temperature °C (°F)	889 (1633)	1026 (1878)	1025 (1877)	593 (1100)
Hot Side				
Inlet Gas Flow kg/sec (lb/sec)	305 (672)	146 (321)	092 (203)	097 (214)
Inlet Gas Pressure MPa (PSIA)	105 (15.24)	102 (14.26)	101 (14.62)	.100 (14.57)
Inlet Gas Temperature °C (°F)	932 (1710)	1066 (1950)	1066 (1950)	621 (1149)
Exit Gas Pressure MPa (PSIA)	.100 (14.52)	.100 (14.45)	.100 (14.44)	.100 (14.44)
Exit Temperature °C (°F)	282 (539)	178 (353)	134 (273)	104 (219)
Regenerator RPM	24	16.1	12	12

quired to overcome the estimated 272N·m (200 lb·ft.) face seal torque. The ring gear and associated parts were assumed to be at 242°C (467°F) while the engine was operating at maximum power on a hot day. The results included:

- Maximum deflections of 1.1 mm (.044 in.) of the ring gear will result in the ring gear staying satisfactorily in mesh with the pinion gear.
- Stress values in the gear/adapter/elastomer all within allowable levels (see Table IX).

Table IX—Stress/Strength Comparisons

	Max. MPa	Equiv. kSI	Equiv. Range MPa	Range kSI	$F_{ly}(-3\delta)$ MPa	$F_{ly}(-3\delta)$ kSI
Ring Gear						
Loc A	49.13	7.13	-84.6	-12.27	421.3	61.1
Adapter	66.6	9.7	66.1	9.59	246.2	35.7
Loc B						
Elastomer						
Loc B	-.16	-.023			2241	315
Loc C	-.14	.020			2241	325

- Compressive stresses at the elastomer/ceramic disk interface of 0.92 MPa (135 psi) maximum.
- High shear stresses in the ring gear/adapter weld dictated a design change to increase the weld joint length from 3 mm (0.12 in.) to 25.4 mm (1.00 in.).

A finite element model of the regenerator disk and ring gear assembly, shown in Figure 74, has been prepared for the stress studies of the disk which will be completed for six conditions (maximum power, 96 km/h (60 mph), 48 km/h (30 mph), transient 0-96 km/h (0-60 mph) at 100% power, temperature only and pressure only). Because of change in gas path flow distributions with the revised en-

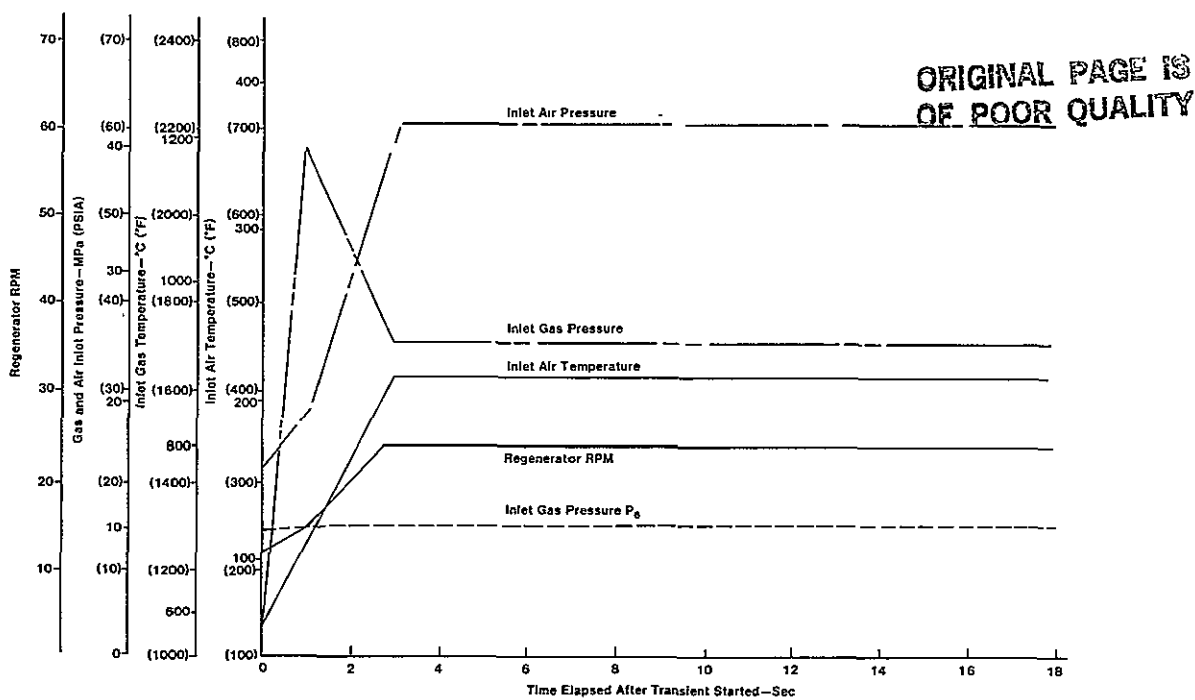


Figure 71 — Transient Cycle Parameters for Idle to Full Power

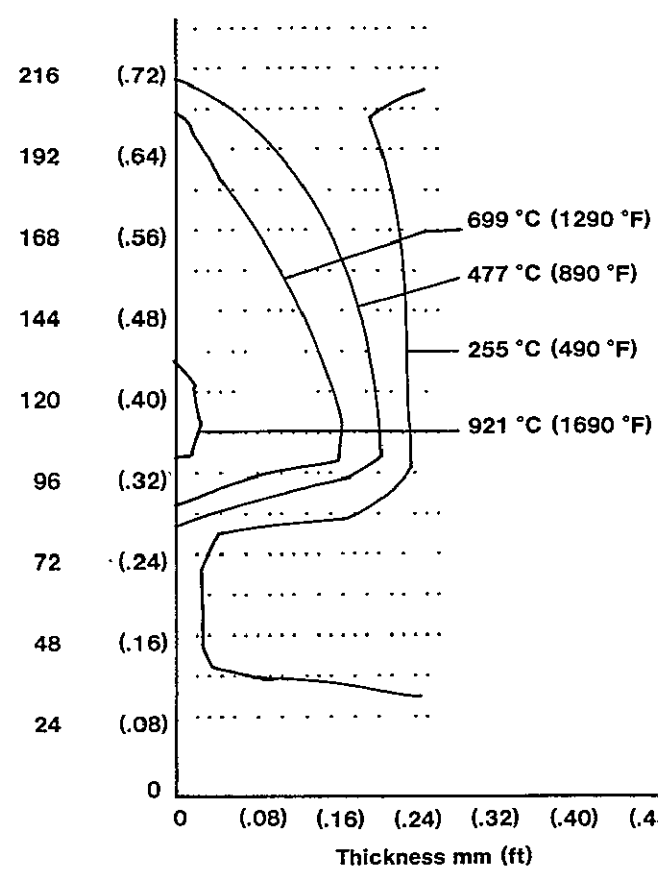
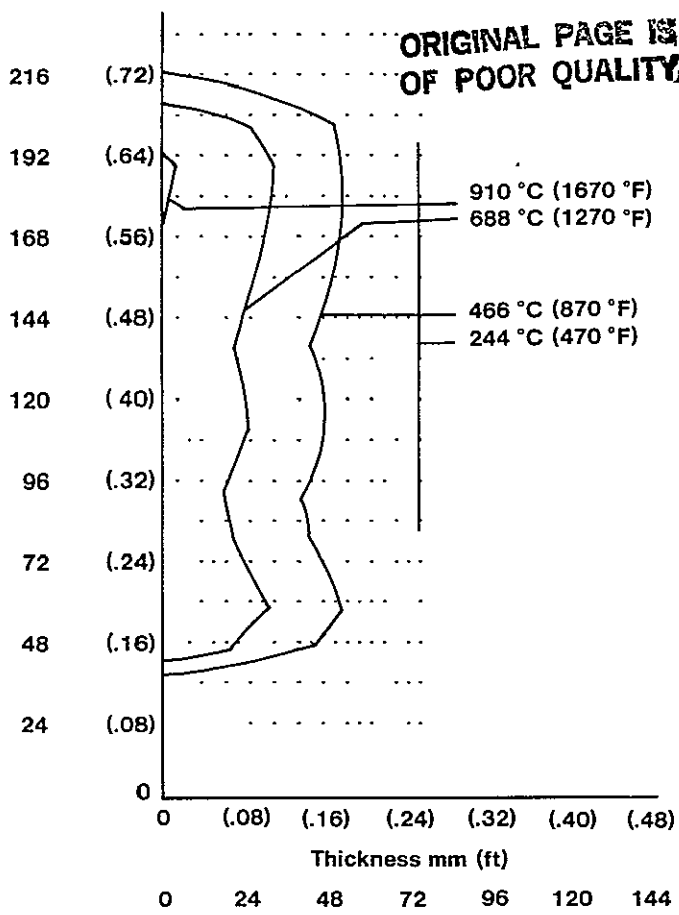
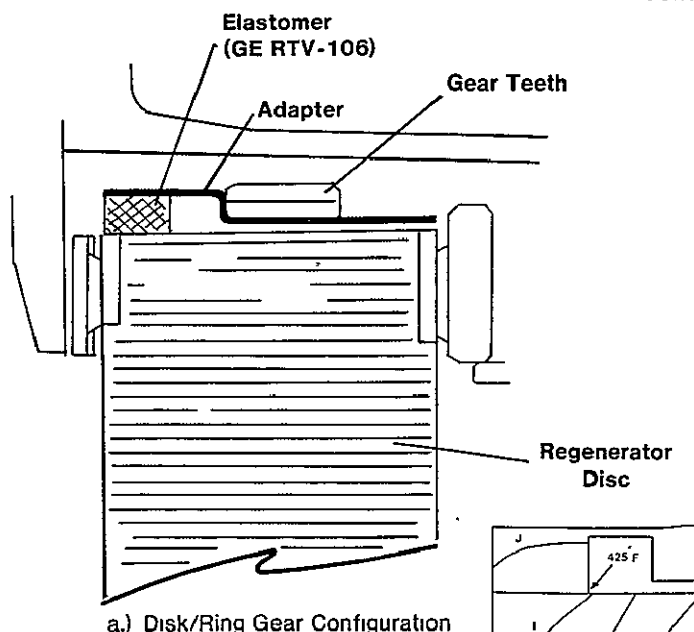
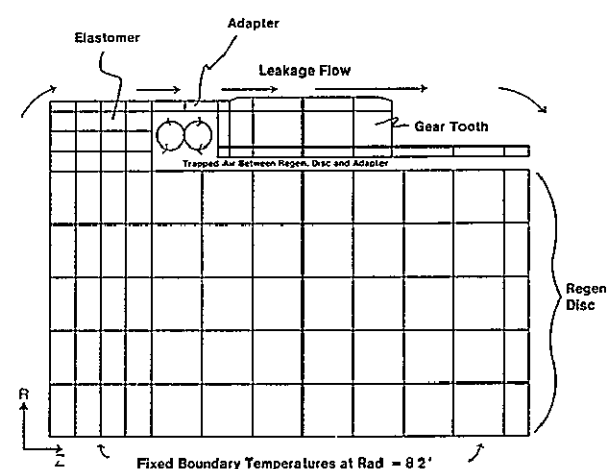


Figure 72 — Comparison of Disk Temperature Distribution for Uniform and Severely Distorted Flow Conditions



a.) Disk/Ring Gear Configuration



b.) Thermal Finite Element Model

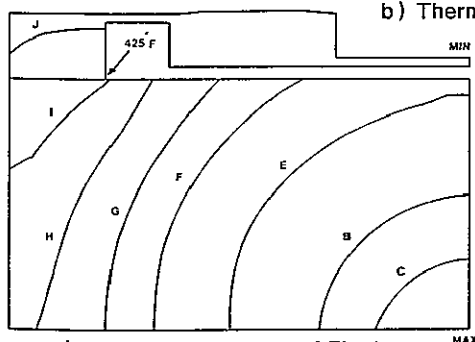


Figure 73 — Estimated Temperatures of Disk/Ring Gear Elastomer Joint

XXX	LEGEND	XXX
A	1200.0	848.89
B	1000.0	537.78
C	800.0	426.67
D	700.0	371.11
E	600.0	315.56
F	550.0	287.78
G	525.0	273.89
H	500.0	260.00
I	475.0	246.11
J	450.0	232.22
K	425.0	218.33
L	400.0	204.44
MAX	1034.0	556.67
MIN	447.0	230.58

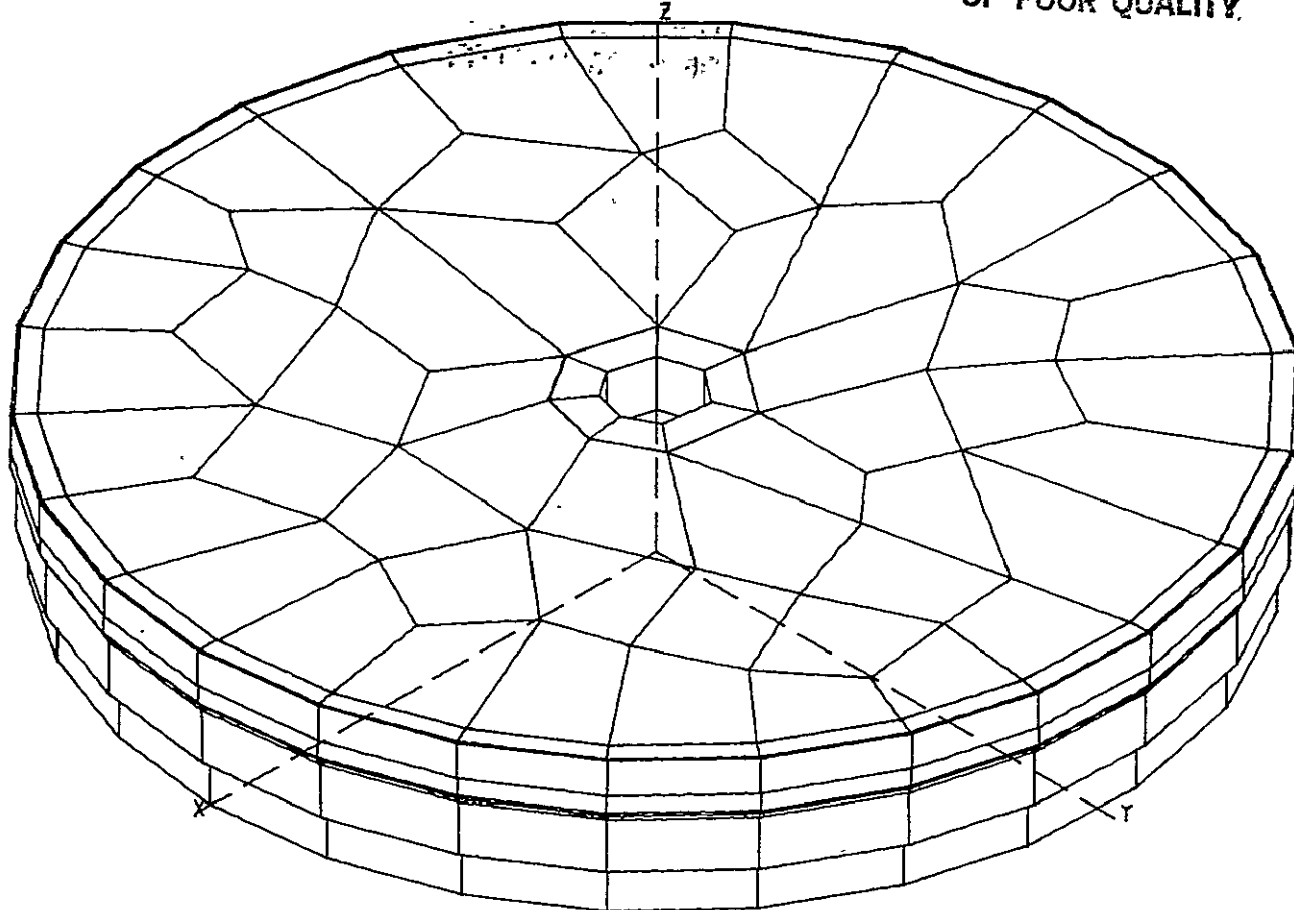


Figure 74 — Regenerator Disk Finite Element Stress Model

gine design, no stress calculations were completed for the original engine design. Flow distribution and the resulting temperature profiles are currently being prepared for the disk stress analysis.

The regenerator disk will utilize Corning Glass Works' (CGW) aluminum silicate (AS) T14-20 matrix with a sinusoidal triangle flow passage. Current CGW disk material is limited to 1100°C (2012°F) maximum operating temperatures; however, work is progressing on a 1200°C (2192°F) matrix which is deemed essential for the AGT 100 operation to provide a margin for local temperature peaks during transients.

In support of the disk stress analysis, work was completed to determine the "as received" strength levels and the intra disk variability in strength of the 1100°C (2012°F) disks. The general approach used is based on multi-sample determinations of the radial and axial strength distributions where the strength value is the tangential modulus of rupture (MOR) in four point bending. The MOR is determined at five radial locations and the axial distribution is defined by six even axial slices from the hot face to the cold face. The as-received strength for the 1100°C (2012°F) AS disk was comparable to the previously reported data from the CATE program. The interdisk variability in strength is noticeably smaller than that of the 1000°C (1832°F) disks and the "as received" strength is approximately 1/3 greater than 1000°C (1832°F) disks with the same separator (flow channel wall) thickness. Separator thickness was determined to have a direct correlation with tangential MOR strength properties.

CGW has developed a satisfactory firing schedule in the laboratory for the 1200°C (2192°F) matrix material. This technique must now be translated to production type furnaces. This work is continuing.

Inboard (Hot Side) Seal Assembly

The inboard seal assembly configuration from the original AGT 100 design (shown in Figure 75) will be changed in the revised engine arrangement now being formulated. The major differences will be the elimination of the metal seal leaf adapter platform and changing the engine block interface from cast iron to a ceramic (LAS) bulkhead. However, the thermal analysis of the wearface environment (rim and crossarm) will be directly applicable in the revised design to define the limiting conditions when severely distorted gas flow conditions are present. These calculated wearface/seal platform temperatures are summarized in Figures 76 and 77 (points A, B, and C on Figures) and illustrate that the 48 km/h (30 mph) operating condition is more severe than maximum power.

Additionally the calculations show the feasibility of using graphite for the wearface material in the rim sections and the need for 1038°C (1900°F) seal face material for the crossarm. The metal leaf seal temperatures in the crossarm region are shown in Figure 78 indicating operational temperatures near 871°C (1600°F) at the critical 48 km/h (30 mph) operating condition.

A finite element model (Figure 79) of the ceramic inboard seal platform was completed for the thermal stress analysis of this part. The similarity of the ceramic

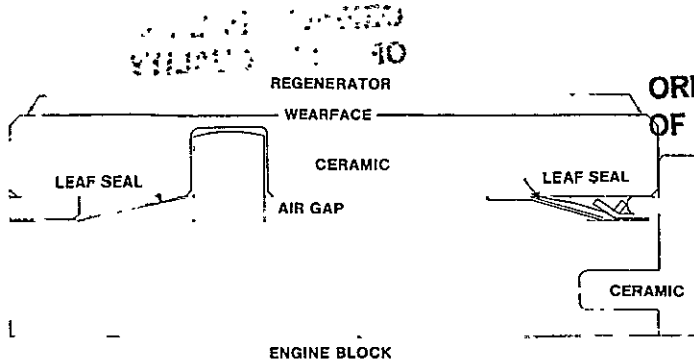
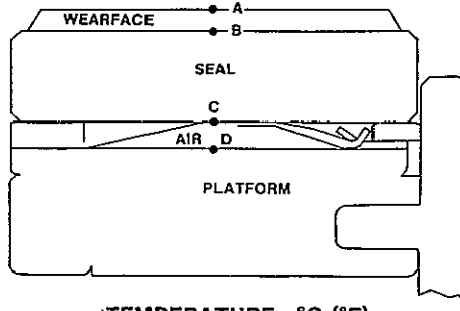
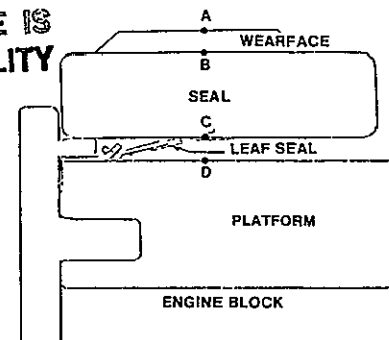


Figure 75 — Cross Section of Regenerator Seal Cross-Arm at Hub (Initial AGT100 Configuration)

ORIGINAL PAGE IS
OF POOR QUALITY



TEMPERATURE—°C (°F)

LOCATION	CONDITION				
	1	2	3	4	5
A Wearface Surface	1039 (1902)	1038 (1900)	1039 (1902)	1039 (1902)	907 (1664)
B Wearface/ Seal Interface	1017 (1862)	1013 (1855)	1026 (1878)	1018 (1865)	893 (1639)
C Coolant Side of Seal	877 (1610)	854 (1570)	882 (1619)	879 (1615)	800 (1472)
D Coolant Side of Platform	712 (1313)	699 (1290)	712 (1314)	753 (1387)	636 (1177)

CONDITION	DESCRIPTION
1 48km/h	(30 MPH), $W_c = 0.5\%$, Wearface Thickness = 100%, Block Temp = 427 °C
2 48km/h	(30 MPH), $W_c = 1.0\%$, Wearface Thickness = 100%, Block Temp = 427 °C
3 48km/h	(30 MPH), $W_c = 0.5\%$, Wearface Thickness = 50%, Block Temp = 427 °C
4 48km/h	(30 MPH), $W_c = 0.5\%$, Wearface Thickness = 100%, Block Temp = 538 °C
5	Max Power Hot Day, $W_c = 0.5\%$, Wearface Thickness = 100%, Block Temp = 427 °C

Figure 76 — Summary of Temperatures Calculated for the Regenerator Cross-Arm (Negative Side) Mid-Span

platform to the ceramic bulkhead in the revised configuration has permitted use of this model in preliminary design studies of the stress/deflection characteristics of the new configuration.

A major development item in the use of a ceramic wearface platform is the need to perfect wearface attachment techniques which are applicable to either the original or revised RPD engine arrangements. Graphite is currently the planned material for the inboard seal rim wearface which will require an attachment design that will accommodate the differences in expansion characteristics of the graphite and LAS. For the seal crossarm wearface, an extension of the nickel oxide/calcium fluoride seal technology currently being developed in the CATE program, is planned. This plasma sprayed wearface also has thermal expansion coefficient significantly different than LAS. Experimental development of these wearface attachments is underway.

LOCATION	TEMPERATURE—°C (°F) CONDITION				
	1	2	3	4	5
A Wearface Surface	388 (731)	386 (726)	384 (724)	310 (590)	309 (589)
B Wearface/ Seal Interface	406 (763)	387 (729)	381 (718)	331 (627)	328 (622)
C Coolant Side of Seal	429 (804)	384 (723)	369 (696)	334 (633)	326 (618)
D Coolant Side of Platform	598 (1109)	608 (1127)	599 (1110)	558 (1036)	549 (1020)

CONDITION	DESCRIPTION				
	1	2	3	4	5
1 48km/h	(30 MPH), No Leakage Air, Radiation Effects Accounted For				
2 48km/h	(30 MPH), 2% Leakage Flow, No Radiation				
3 48km/h	(30 MPH), 4% Leakage Flow, No Radiation				
4	Max Power Hot Day, 2% Leakage Flow, No Radiation				
5	Max Power Hot Day, 4% Leakage Flow, No Radiation				

Figure 77 — Summary of Temperatures for the Regenerator Rim Seal—Hot Side

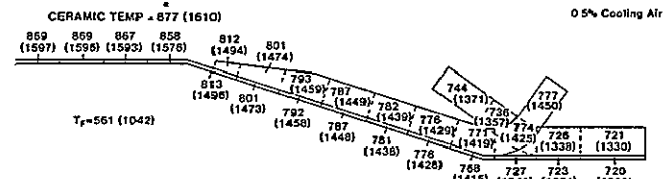
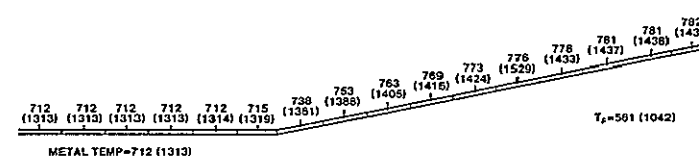
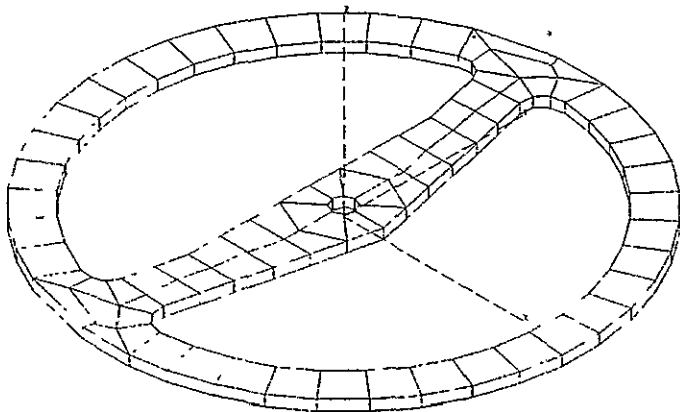


Figure 78 — Regenerator Cross-Arm Metal Leaf Seal Temperatures at 48 km/h (30 mph)

Outboard (Cold Side) Seal Assembly

The AGT 100 outboard seal assembly will experience an operating environment very similar to those of the DDA IGT and CATE regenerator systems. Thus the seal technology being developed in these programs is being utilized in the AGT 100 design. The revised engine arrangement will not alter these requirements and the new RPD outboard seal will be little changed from the original design with the regenerator disk pressure loaded toward the outboard seals thus minimizing seal leaf compliancy



HIDDEN LINES DELETED GEOMETRY PLOT

Figure 79 — Inboard Regenerator Seal Finite Element Model

Regenerator Cover

The regenerator cover in the revised engine will still include the requirements of a 90° turn from the compressor discharge delivery tube into the regenerator cover. Several techniques are being investigated to incorporate the baffling/ducting necessary for flow distribution with structural members within the stamped cover. The final configuration requirements will be based on cold flow rig tests and regenerator hot rig developmental testing.

7.2 Mod I

Engine Parts Design and Fabrication

The original RPD and Mod I regenerator systems differed only in the inboard seal components. This commonality of parts will also be present in the revised engine arrangement.

The design of the Mod I engine hardware was completed and initial hardware orders placed in the fall of 1980. Delivery of parts had started by the end of the reporting period. Long lead items such as castings and the ceramic regenerator disk are on schedule and will be ready by late January, and a complete set of hardware should be ready for test in February 1981.

Rig Design, Fabrication and Test

Supportive rig testing for the development of the AGT 100 regenerator will utilize four rigs: regenerator hot test rig, cold flow distribution rig, seal leaf leakage, and a regenerator core low cycle fatigue (LCF) engine simulation.

Regenerator Hot Test Rig

The regenerator hot test rig, described in the first semi-annual report, is a key element in the developmental testing of the AGT 100 regenerator design and consists of two major subassemblies (hot loop and working section).

The hot loop, designed to simulate power turbine discharge conditions, has been completed and is installed in the test cell. A modification since the last report has been the replacing of the metal flow-measuring orifices with thermally stable ceramic (LAS) orifices for improved flow measurements. The working section shown in Figure 80 simulates the engine/regenerator interface for the installation of engine hardware for engineering tests. Components

for the working section are complete except for the "V" interconnecting ducts which will be finished by the end of January 1981. The working section will be installed in the test cell early in February. Data acquisition and data processing programs are being prepared to match the test cell outputs to the automated DDA data processing network.

Initial developmental testing of regenerator effectiveness and seal performance will be accomplished with the original design Mod I engine components. The hot rig working section will be modified to match the new engine configuration.

Cold Flow Distribution Rig

The cold flow distribution rig will provide the necessary information to allow optimization of the regenerator radial flow distribution. Two separate rigs are being built, one to simulate the regenerator air side conditions and the second to model the regenerator gas side. The rigs use ambient temperature air and simulate Reynolds and Mach numbers by pressurizing the air side with shop air and operating the gas side at subambient pressures by using a steam ejector.

The cold-flow rig designs were completed during the period and released for fabrication. The flow path hardware was completed and ready for shipment to DDA and work is ready to start on the computer interface requirements of data acquisition and reduction. This hardware models the original engine arrangement. A review of the revised engine design indicates that the air side model can be reworked to simulate the new design arrangement but the gas side inlet will require new hardware due to the marked change in flow path.

Seal Leaf Leakage Rig

The seal leaf leakage rig provides the means to measure the leakage levels of a seal design and to observe the mechanism in operation. Using shop air, leakage flow rates can be determined as a function of pressure drop for both the outboard and inboard seals. The ability to observe seal operation is useful as a guide in making design changes.

The seal leaf leakage rig, shown in Figure 81, has been completed. The rig, designed for the original Mod I engine hardware, will be utilized to evaluate the initial regenerator hot rig test hardware and subsequently will be modified to accept seals designed for the revised regenerator.

Regenerator Core LCF Engine Simulation Rig

This rig, previously described in the first semi-annual report, is used to expose regenerator ceramic disk samples to steady state or transient thermal testing to simulate expected engine operating characteristics. The objective of the testing is to identify the design strength levels of candidate disk materials and correlate the strength to the critical parameters. As noted previously, the design goal is to use a 1200°C (2192°F) matrix material for use in the AGT 100 RPD concept. Limited tests were conducted on the 1000°C (1832°F) material to correlate strength properties for initial disk stress analysis and to identify potentially limiting parameters from expected engine operating conditions. Extended testing of the 1000°C (1832°F) and 1100°C (2012°F) are being conducted in the related CATE program at DDA.

ORIGINAL PAGE IS
OF POOR QUALITY

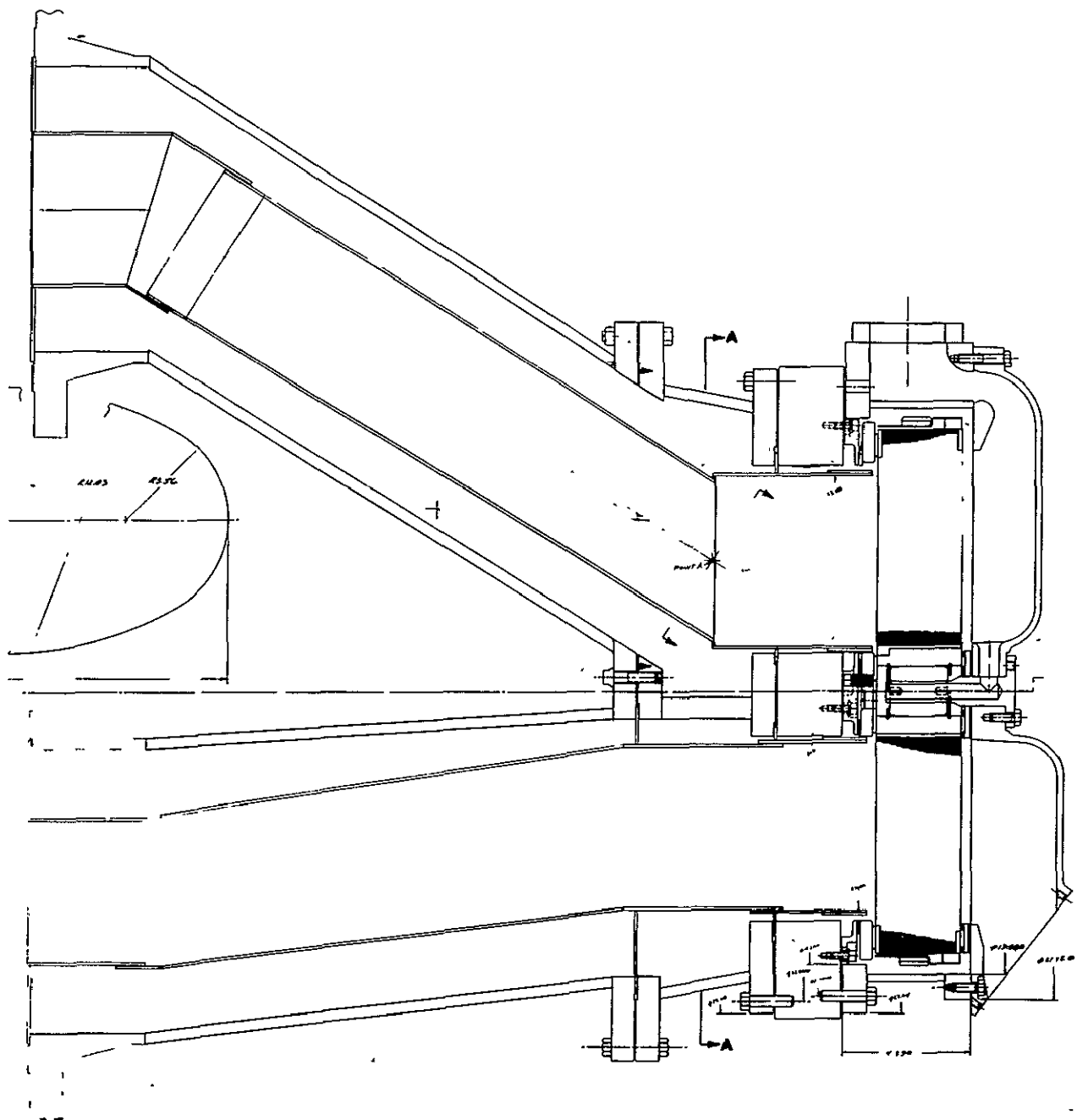


Figure 80 — Regenerator Hot Test Rig—Working Section

Rig samples of 1000°C (1832°F) Aluminum Silicate (AS) matrix were exposed to hot gas acceleration-deceleration thermal transients to 1090°C (2000°F) that were identical to those measured at the engine regenerator disk inlet. The rig samples were then compared to similar matrix samples taken from an engine disk. This disk had not only been thermally cycled but also suffered seal hot-face mass transfer from the seal wear face. The two sets of cyclic test specimens were then compared to similar samples that had been exposed statically to 1093°C (2000°F). These results are summarized in Table X and show the following:

- Static exposure to 1093°C (2000°F) shows little change in strength (mean MOR) from the hot disk face along the disk channel.
- Both cyclic exposures (rig and engine) yielded similar reductions in strength indicating the importance of cyclic thermal fatigue in design life of the matrix.
- Since both cyclic tests yielded the same results the mass transfer of seal surface material to the matrix face does not play an important role in matrix strength properties.

These results will be checked with the 1200°C (2192°F) matrix material as samples become available from CGW.

ORIGINAL PAGE IS
OF POOR QUALITY

Table X

Loss in tangential MOR in 1000°C (1832°F) matrix in static thermal exposure, transient thermal exposure and transient exposure with seal contact mass transfer.

Test	Type	Temp	Time	Cycles	Mean MOR, kPa (psi)		Probability there is a difference between Hot face and Remnant MOR
					°C (°F)	Hours	
Steady State	Rig	1093 (2000)	5	—	2144 (311)	2161 (313)	<<.90
Transient	Rig	1093 (2000)	5	5000	1640 (238)	2138 (310)	.99—.999
Transient w/Seal	Engine	1010 (1850)	3050	35000	1634 (237)	2277 (331)	.90—.95

*Under transient conditions the hot face received high amplitude thermal cycles, the remnant received low amplitude cycles.

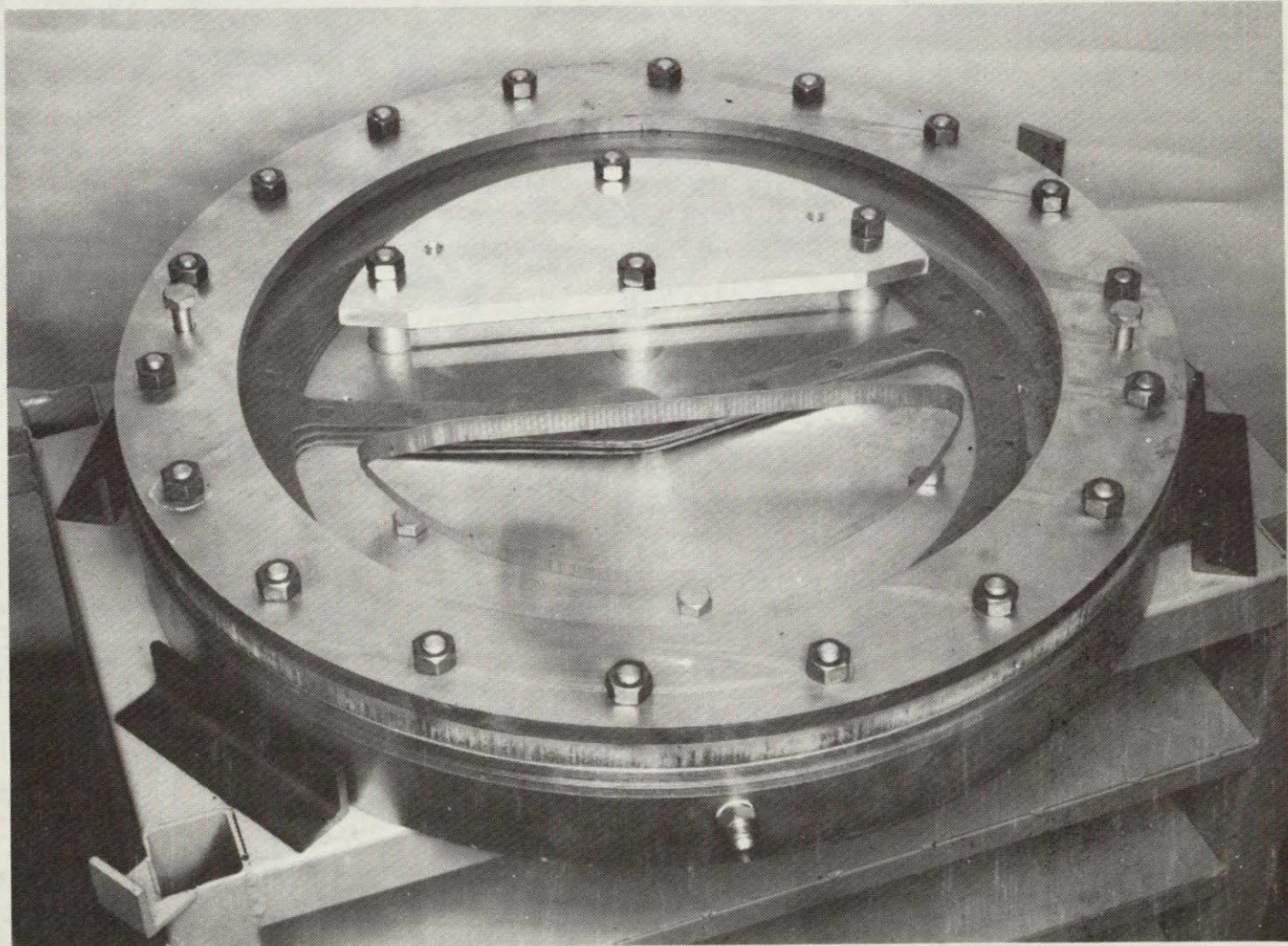


Figure 81 — Seal Leaf Leakage Test Rig

61 2049 151050
CONT'D 8007 20

VIII. Engine Subsystems

ORIGINAL PAGE IS
OF POOR QUALITY

8.1 Block/Insulation

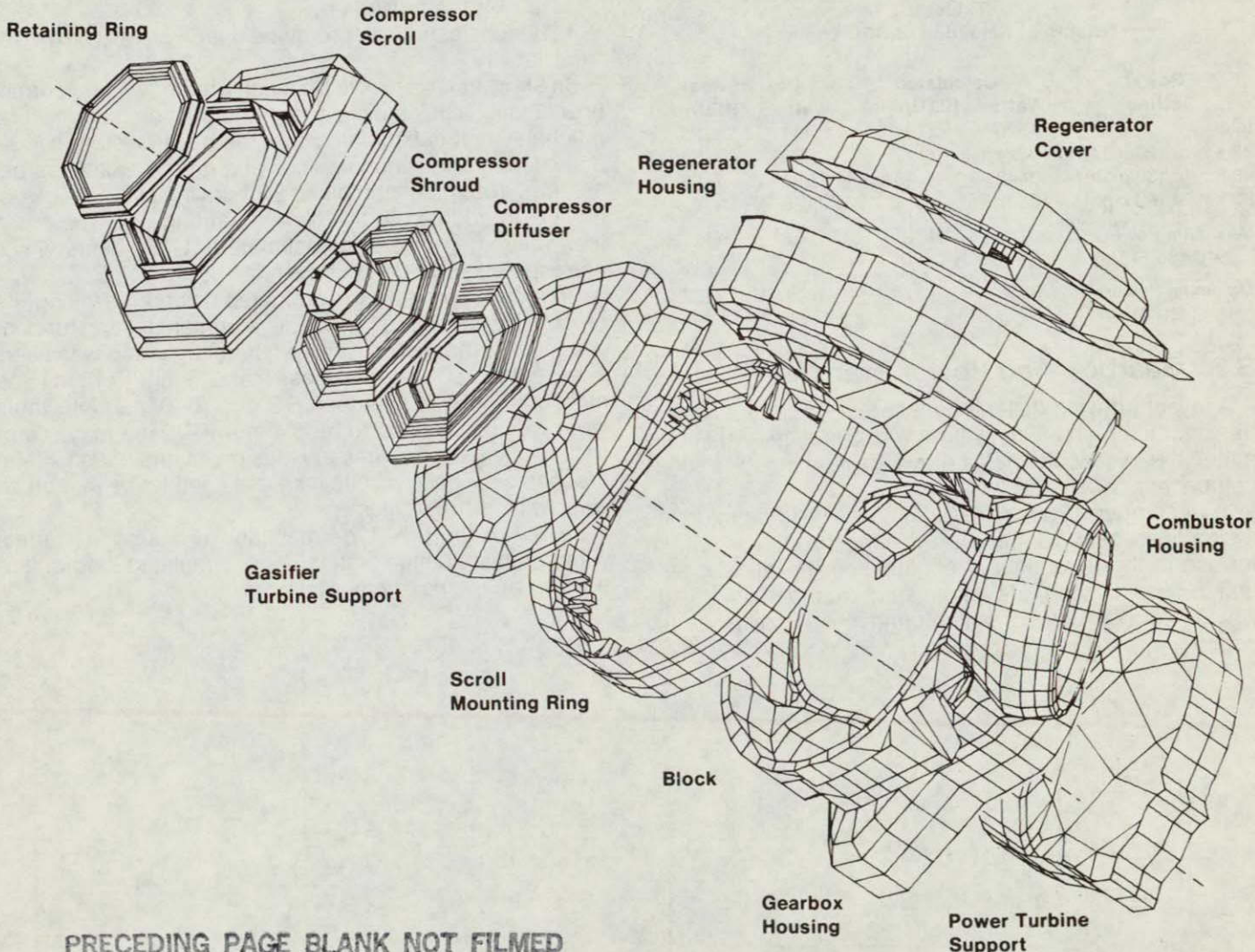
A description of the original block configuration is presented in the first semi-annual report CR 165178 (DDA EDR 10327). Block layout and detail drawings were prepared, pattern equipment was built, and an aluminum pattern check-out casting was poured.

Work on the three-dimensional finite element model of the block and associated submodels continued. While this work is reported as the block model, it is actually a model of all of the engine structural elements. These elements include:

- Compressor Retaining Ring
- Compressor Scroll

- Compressor Shroud
- Compressor Diffuser
- Gasifier Turbine Support
- Scroll Mounting Ring
- Block
- Gearbox Housing
- Power Turbine Support
- Combustor Housing
- Regenerator Housing
- Regenerator Cover

All geometric modeling with submodel node-to-node matching relationships was completed. Figure 82 shows the computer model simulation of these structural elements.



PRECEDING PAGE BLANK NOT FILMED

Figure 82 — Model of Block and Associated Components

The heat rejection calculated for the engine is a summation of 45 discrete heat losses between the hot gas path and the three heat sinks: the ambient air surrounding the block, the oil mist of the gearbox, and the compressor discharge air opposite the back plate of the gasifier turbine scroll. Each of these discrete heat losses was calculated with a one-dimensional composite wall model. Where the heat flows are high and geometry was complex, two and three-dimensional heat conduction models were used. These areas include:

- The cross-key attachments between the gasifier and power turbine scrolls and the engine block
- The attachment area of the power turbine exhaust duct and regenerator housing
- The regenerator cross arm

The calculated heat rejection at RPD engine operating conditions for the original engine design is presented in Table XI. The results show that the heat loss is essentially constant over the vehicle operating range and while the calculated heat rejection absolute values are relatively low they exceed the initial design goal. The design iteration addresses this problem.

Table XI
Total Heat Rejection of RPD Engine

Power Setting	Calculated Watts (BTU/min)	Design Goal Watts (BTU/min)
Idle	1829 (104)	434 (25)
32 km/hr (20 mph)	3024 (172)	967 (55)
48 km/hr (30 mph)	3446 (196)	984 (56)
80 km/hr (50 mph)	3587 (204)	1178 (67)
Maximum Power 29°C (85°F) Day	3728 (212)	1952 (111)
Maximum Power 15°C (59°F) Day	3556 (202)	1841 (105)

8.2 Gearbox And Power Transfer

A layout drawing describing the gears, bearings, power transfer clutch and lube system was completed. This permitted the initiation of detail drawings defining the various component parts.

In December, 1980, a new layout was initiated to define a simplified gear train and power transfer clutch system for use in the reconfigured engine. Four bevel gear sets and a worm mesh are eliminated in the new design which reduces both manufacturing cost and assembly complexity.

8.3 Starter/Boost System

A combination starter-booster motor will be produced by Delco-Remy. The purpose of the booster is to provide extra vehicle acceleration during high demand. This is accomplished through application of booster motor shaft power directly to the engine gasifier which decreases the inherent time lag in achieving full engine power after demand.

To eliminate time lag in application of booster motor shaft power, the motor armature is geared to the gasifier shaft, thus it turns continuously with the gasifier. The motor is controlled by lowering and raising the brushes on the commutator. This provides the high current switch and minimizes the brush wear. Both boost and starting are controlled in this manner.

The effort at Delco Remy is directed toward:

1. Determining the forces and motion distances required in the brush lifting mechanism.
2. Establishing the brush wear rate to determine the required brush length to operate 100,000 miles.
3. Determining what problems exist in making and breaking the high motor currents by lowering and raising the brushes.
4. Bench testing of prototype hardware to prove reliability.

Brush wear is known to be much greater with no current flow than with, thus necessitating the brush lifting mechanism. It is estimated that the boost system will be activated in one-second pulses at a rate of 152 times per 161 km (100 mi) of combined EPA driving cycle. This is, of course, in addition to the normal starting use. The brush life requirement has been estimated at 150 hours which corresponds to 3500 hours vehicle use.

Brush wear tests were conducted using a new long-life brush material already under development testing for conventional starter use. A simple non-lifting setup was used. The wear in 150 hours was less than 2.5 mm (0.10 in.) and at 400 hours was less than 5.3 mm (0.21 in.). Allowable wear was determined to be 6.4 mm (0.25 in.) to be compatible with the preliminary design of the brush lifting mechanism. These results increase confidence that brush wear will be no problem.

Layout of the prototype mechanism has been started, with durability bench testing under simulated load conditions to be the next major task.

IX. Materials Development

9.1 Materials Development—DDA Design Support

The special investigation of LCF improvement of aluminum impellers by peening was continued. An aluminum compressor impeller blank casting (A206.0-77, silverless K01) was sectioned for machining into test specimens for evaluation of potential LCF improvement by pre-stressing by peening. The initial tensile test specimens failed at low values because of oxide inclusions.

New castings have been received and a sample casting is being sectioned for soundness and tensile tests. If these tests are acceptable, machining of specimens for LCF testing will resume.

Mullite Development

The primary structural refractory ceramic under consideration for use in the engine is silicon carbide in either the sintered alpha or reaction bonded form. While silicon carbide exhibits good high-temperature strength and

chemical stability, its high thermal conductivity can pose a problem relative to heat conduction to surrounding structures. Therefore, a material of low thermal conductivity with thermal expansion characteristics similar to those of SiC is needed for transition structures to minimize heat loss.

The transition structures under development include sealing rings, spacers and discrete components possibly bonded to the SiC and or other materials. As such, the components may be removable to facilitate repair or will become permanently incorporated into a composite structure. An acceptable candidate transition material must also exhibit chemical stability and chemical compatibility with SiC at the design temperatures found in various locations in the engine.

Of the various high strength ceramic materials known, only a few exhibit the desired expansion and conduction properties. Most notably, mullite ($3\text{Al}_2\text{O}_3 \bullet 2\text{SiO}_2$) and zircon ($\text{ZrO}_2 \bullet \text{SiO}_2$) or other zirconia based materials can be fabricated using common procedures into appropriately shaped components.

Initial efforts have focused on the use of pressure induced sintering to develop a high strength mullite material. Mullite was chosen primarily because of its availability. To date, commercial grade kyanite has been used as a raw material source with hot pressing performed by Ceradyne, Inc. Kyanite decomposes when heated to form mullite and silica. The silica can be present in crystalline or amorphous form as a function of heat treatment and impurities present.

A representative microstructure of the initial material produced by Ceradyne is shown in Figure 83. Inclusions of zirconia milling media are distributed throughout the

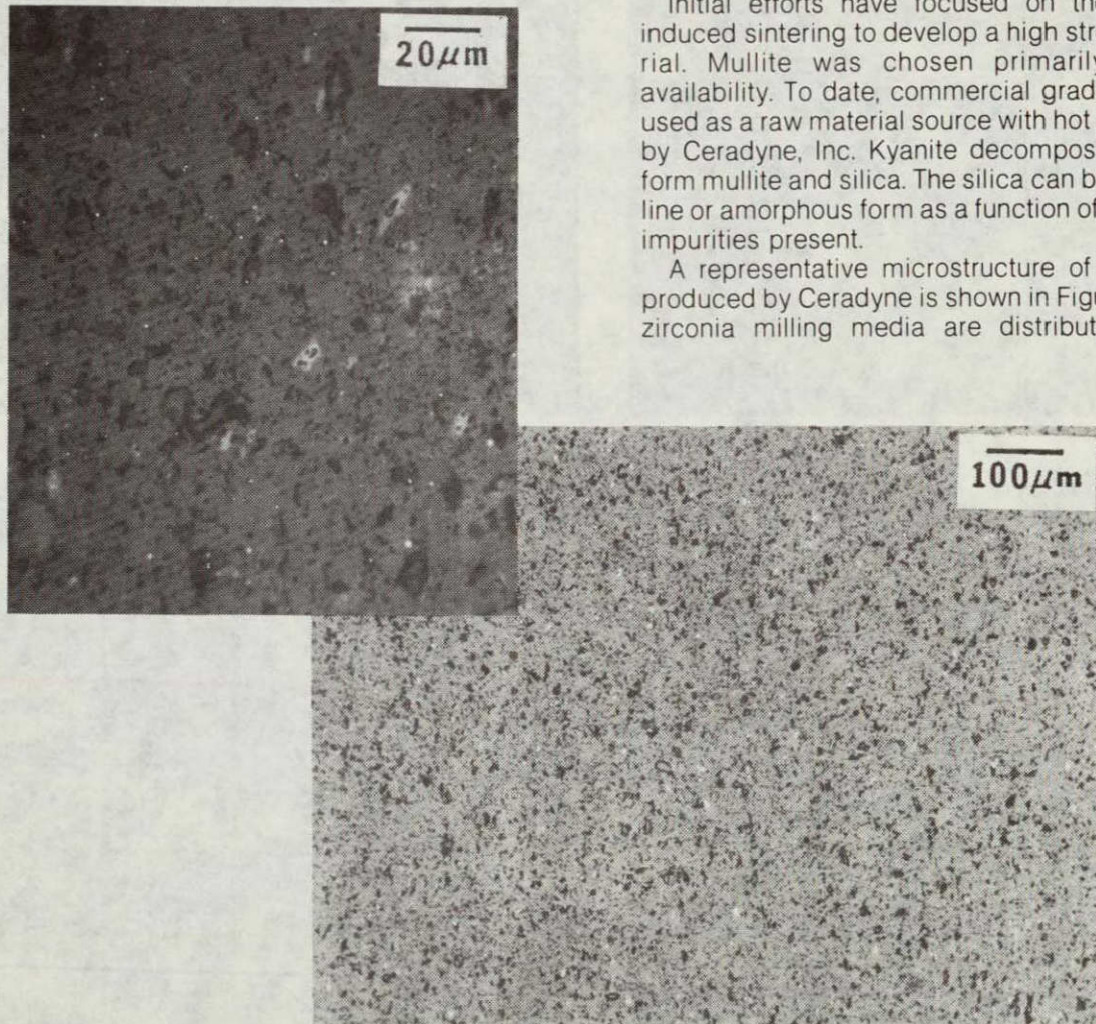


Figure 83 — Etched Polished Surface of Hot Pressed Mullite

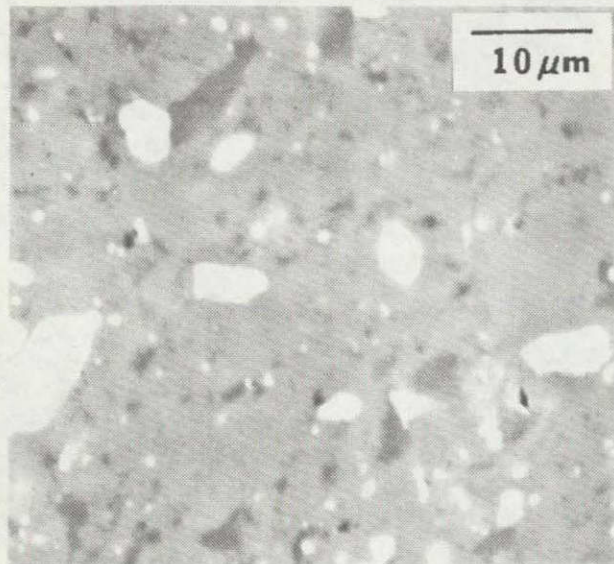


Figure 84 — Elemental Analysis of Impurities in Hot Pressed
Mullite

microstructure. The general level of porosity is quite high. Bulk density has been measured at 2.97 gm/cc. This compares with a theoretical density of 3.16 gm/cc. The porosity observed is thought to be due, at least in part, to the broad particle size distribution in the starting material.

Figure 84 shows the distribution through the microstructure of the major elements within the present material. In addition to the zirconia, a silica phase is also present. X-ray diffraction studies identify this phase to be cristobalite. Further, as shown in Figure 85, small amounts of kyanite are also present.

The flexural strength of the present mullite material measured in four point bending was found to be 277.8 MPa (40.3ksi) at room temperature and 206.8 MPa (30.2ksi) at 1000°C (1832°F).

Heat treatment at 1000°C (1832°F) for 24 hr. prior to testing at 1000°C (1832°F) increased measured strengths slightly. A summary of the strength data is shown in Table XII.

Ambient Test Temp °C (°F)	Heat Treatment	Ave. Flexural Strength MPa (ksi)
RT	none	277.8 (40.3)
1000 (1832)	none	206.8 (30.2)
1000 (1832)	1000 (1832) 24 h	235.8 (34.2)

Table XII — Mullite Strength Summary

An evaluation of specimen fracture surfaces revealed that in most cases the strength controlling defects were either large silica particles, Figure IX-26, or titania particles, Figure IX-27. The latter presumably results from the high level of titanium present in the starting kyanite.

The thermal expansion of the hot passed mullite was measured at 5.49×10^{-6} mm/mm °C (3.05×10^{-6} in/in °F) and as such is comparable to alpha-SiC 4.66×10^{-6} mm/mm °C (2.59×10^{-6} in/in °F).

Present and future work is aimed at realizing a more uniform, dense microstructure free of silica and zirconia/titanium inclusions.

Improvements in particle size distribution, processing parameters and hot pressing techniques have shown improvement in the quality and strength of more recent mullite materials.

9.2 Suppliers Effort—Unique Work

The Alpha Silicon Carbide Division of the Carborundum Company is the primary source of AGT structural ceramic components. Its role is to both supply initial silicon carbide prototype components needed to support the test/development activity and to develop ceramic forming methods and associated techniques for ultimate production use.

The following subsections summarize the progress made to date toward establishing fabrication procedures for producing the major hot section ceramic components.

Gasifier Rotor—Summary

Both reaction bonded and single phase sintered silicon carbide materials are viable candidates for the rotor application. Initially several fabrication techniques were examined for each material type. Thixotropic casting, ultrasonic green machining, and transfer molding were considered for reaction bonded material, while both slip casting and injection molding were evaluated for producing a sintered silicon carbide rotor. Results to date show

transfer molding and injection molding to be the most appropriate techniques for reaction bonded and sintered silicon carbide, respectively. Relatively defect-free rotors have been made from both materials. Further work will concentrate on refining these two material/fabricating systems.

ULTRASONIC GREEN MACHINING—RB SiC

Feasibility studies on green machining isopressed RB SiC were completed. Cast solid tools made from a turbocharger rotor pattern similar in size to the AGT 100 gasifier rotor were used for all tests. While the blade-space contour is tapered such that hollow tools were not suitable, the green material is sufficiently soft compared to the fired material that solid tooling can sink a blade cavity in a reasonable time.

In the initial trial a lathe-turned green isopressed reaction bonded SiC billet had six blade-space cavities sunk by ultrasonic machining with various machine settings and tool configurations. The cutting time per cavity was about 20 minutes and it is expected that this can be reduced to about 10 minutes with optimized conditions.

One intent of these initial cutting attempts was to demonstrate that the blade can be formed with the required thickness. Unfortunately, the cast tools were not accurately brazed to the tool holders and it was impossible to cut a blade without having a knife edge on one end and an overly thick (1/8 inch) dimension on the other end. The curved complex geometry of the space between the blades (the tool shape) makes alignment of the tool for brazing difficult. An ultrasonic machined RB SiC rotor was successfully siliconized, see Figure 88.

This work demonstrates that the ultrasonic fabrication method has potential. At this time, however, the plastic molding processes are even more promising. Therefore, no further work will be done with this rotor fabrication method.

THIXOTROPIC CASTING—RB SiC

Additional plastic patterns of the AGT 100 gasifier were supplied to CBO. One of these patterns was modified by adding additional thickness to both sides of each blade.

Also, the front nose of the rotor has been extended so that the rotor can be securely chucked in a lathe for the machining of the back surface.

Two rotors were successfully cast from the new mold. The back surfaces were machined to remove the resin-rich layer and to obtain a flat surface suitable for joining with the shaft extension. Two shaft extensions were thixotropic cast and green machined. One rotor and one shaft extension were joined in their green state with the same thixotropic casting mix. This rotor was hand altered in the green state such that the trailing edges of the blades form a straight line through the center of the hub-nose. This blade trimming approximates the modifications made to the injection molded rotor. This rotor was successfully siliconized and is shown in Figure 89. However, the joint between the shaft extension and rotor showed cracks in both visual and Zyglo inspection. The X-ray inspection showed that the part was completely siliconized with no indication of interior cracks. Zyglo inspection failed to indicate any problems other than the joint cracks.

Because of the joint difficulty experienced with the first rotor, it was decided to pursue a straight silicon joint ap-

XRD CHARACTERIZATION

- PRIMARY PHASE—MULLITE ($3\text{Al}_2\text{O}_3\text{-}2\text{SiO}_2$)
- SECONDARY PHASE— α CRYSTOBALITE (SiO_2)
- SECONDARY PHASE—KYANITE ($\text{Al}_2\text{O}_3\text{-SiO}_2$)

ORIGINAL PAGE IS
OF POOR QUALITY

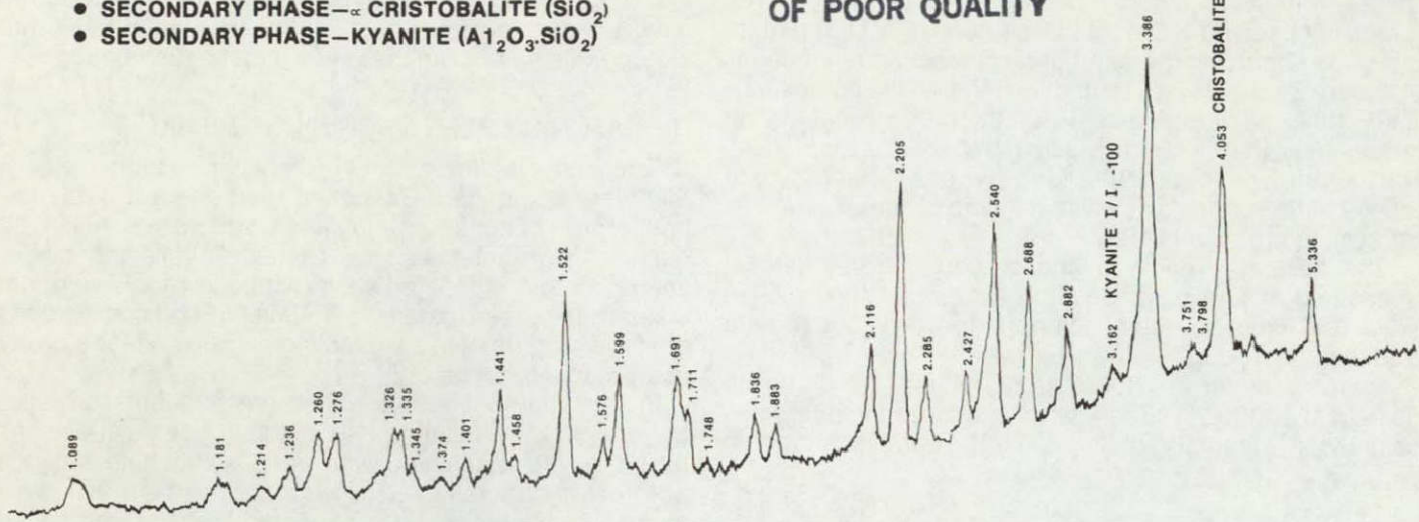


Figure 85 — X-ray Diffraction Pattern of Mullite With Secondary Phases Present

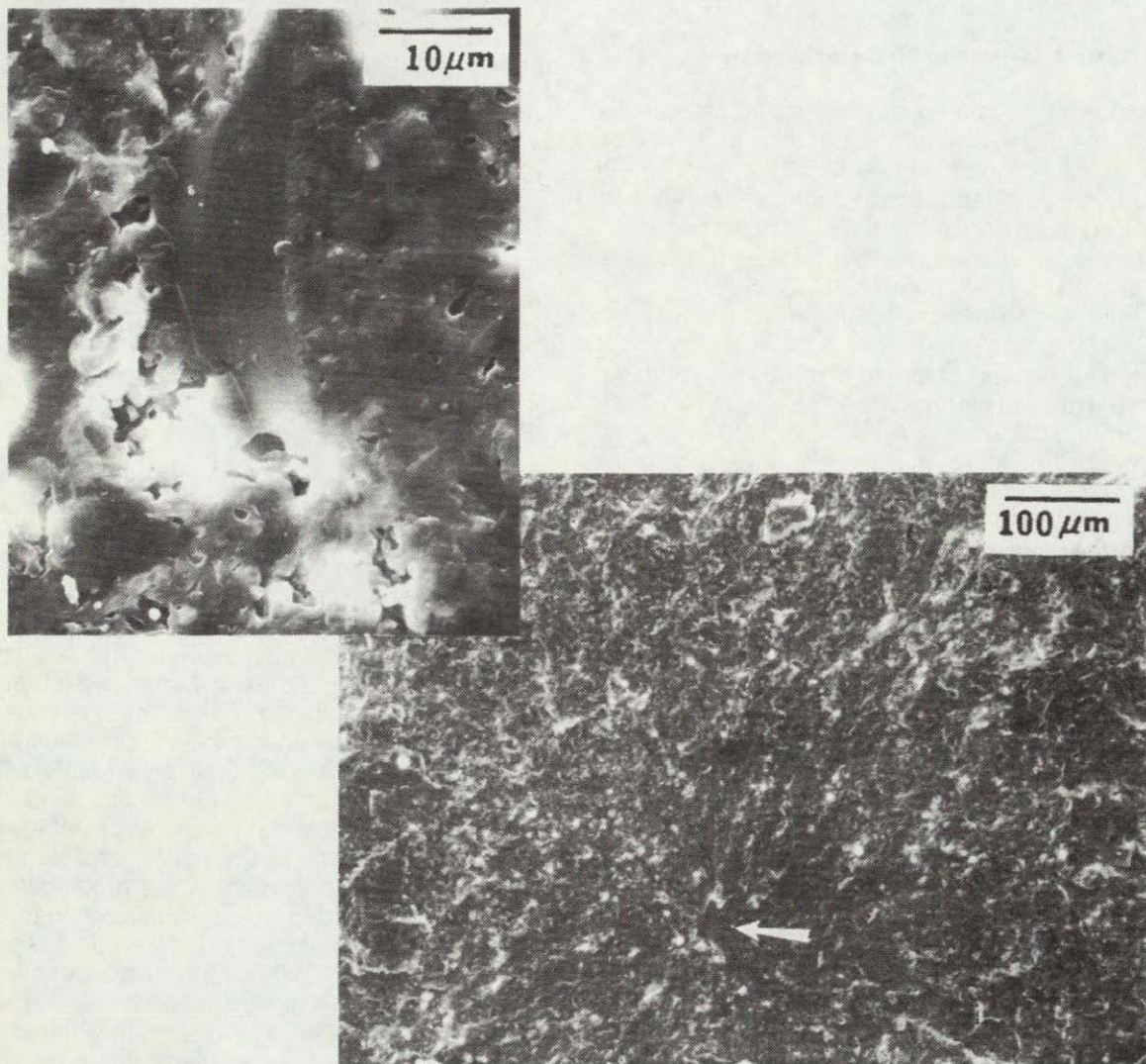


Figure 86 — Fracture Surface Showing SiO_2 Inclusion Failure
Source

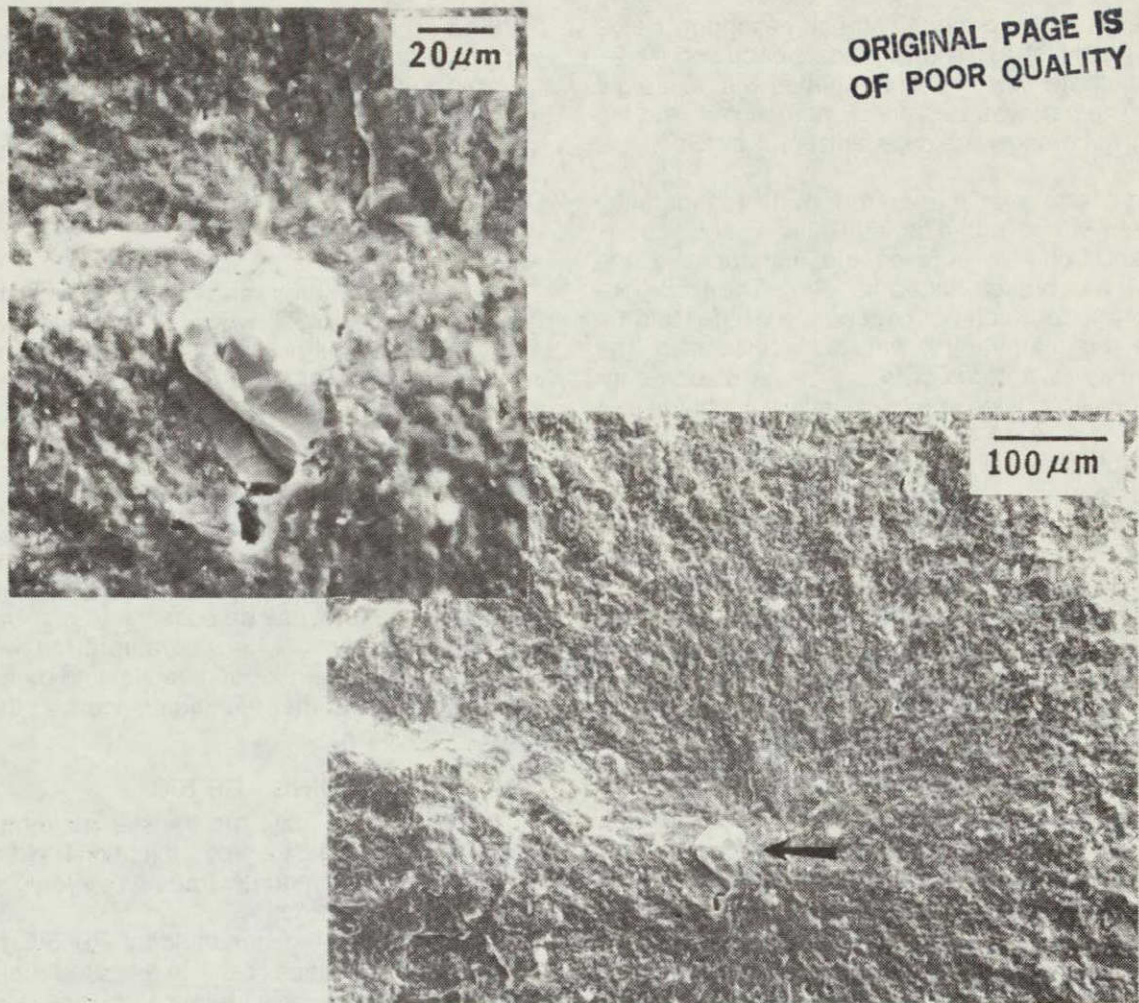


Figure 87 – Fracture Surface Showing TiO_2 Inclusion Failure
Source

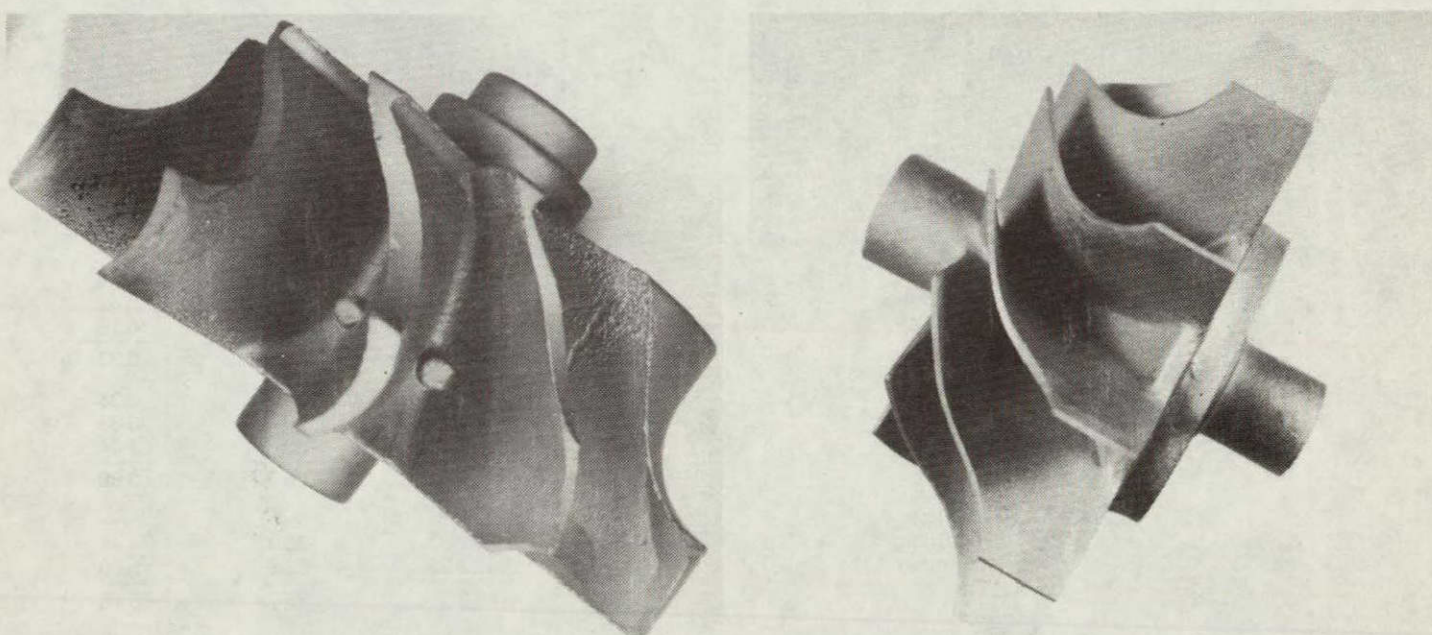


Figure 88 – Green Machined Isopressed RBSiC Gasifier Rotor
After Siliconization

Figure 89 – Thixotropically Cast RBSiC Rotor With Shaft
Extension Attached and Siliconized

proach rather than using the thixotropic casting mix as a glue. For an initial test, two short cylinders each about one-half inch in diameter were bonded together with a straight silicon joint. The part was sectioned and polished and the photomicrographs show an excellent bond between the two pieces.

The second rotor with the altered shaft configuration was successfully fired with a straight silicon joint. The excess surface silicon was removed and, unfortunately, one of the blades was broken during handling. The final density was 2.974 g/cc which corresponds to what would be expected for this material if it were fully siliconized. The rotor, however, was not defect-free. Several blades contained open or silicon filled cracks, mostly in the blade root areas.

The mechanical properties of three thixotropic casting mix compositions were evaluated during this reporting period. Initially, two compositions of differing grain size, including that used to produce the rotors described above, were examined. Each composition was evaluated for two firing conditions. Each of these combinations was made as a large block from which bars were cut from the top, middle, and bottom portions to determine if the material strength was a function of position within a casting. The four-point bend test bars were NDE, Zyglo and X-ray inspected but no attempt was made to test only flaw-free bars. All bars were tested because each represents regions within a casting. Table XIII summarizes the results.

The position within the casting does not appear to affect the average strength. However, the standard deviation seems to increase consistently and significantly going from top to bottom.

From the combined results it appears that the firing temperature difference tried had no appreciable effect upon strength, whereas the mix grain size did—Mix A was finer than Mix B.

The two rotors described earlier were made of the B/T₂ variation which had a strength of 43.5 ksi and a Weibull modulus of 8.3.

A third experimental composition of very fine grain size was also processed and evaluated. Material was only produced for a T₁ firing condition. The results are summarized below along with previously tested materials.

Mix/Firing Temperature	Mean Strength		Std. Dev.	
	MPa	ksi	MPa	ksi
A/T ₁	337.9	49.05	45.9	6.47
B/T ₁	289.2	41.98	26.2	3.80
C/T ₁	224.5	32.59	67.9	9.86

Photomicrostructures and SEM failure analysis are being done to determine why the C mix had low strengths.

The first rotor shipped to DDA (D602-87) and the second one shipped (D602-96) described above were both made from composition C/T₁.

While it appears that defect free rotors can be produced and siliconizing of thick sections has been demonstrated, it is not clear that sufficient strength can be developed to make the material compatible with rotor requirements. Improvements in strength through reductions in grain size seem to be offset by increased difficulty in casting bubble free components. It may be possible to resolve this problem, but it is clear that considerable effort would be required. In view of the greater potential and more promising results offered by other techniques work in this area will be de-emphasized.

TRANSFER MOLDING—RB SiC

In order to investigate the transfer molding procedure the sintered alpha gasifier rotor injection molding tool was modified to accommodate transfer molding of reaction bonded silicon carbide.

The established transfer molding RB SiC mix uses a thermoset binder which "sets" in a heated mold. Because the binder goes through a chemical change, it takes a considerably longer mold time to accomplish a solidification than the simple cooling of the injected molded material. While this increase in molding solidification time is somewhat disadvantageous economically, it creates another problem which is much more severe: the transfer molding

Composition	Firing Temperature	Position	No. of Bars	Mean Strength		Std. Dev.	
				MPa	ksi	MPa	ksi
A	T ₁	Top	—	—	—	—	—
		Middle	8	339.1	49.22	40.0	5.81
		Bottom	10	347.4	50.53	45.4	6.59
A	T ₂	Top	4	387.0	56.17	32.6	4.73
		Middle	22	326.3	47.36	40.6	5.89
		Bottom	30	323.2	46.91	42.6	6.19
				330.0	47.9	42.9	6.23
B	T ₁	Top	8	284.9	41.36	16.2	2.35
		Middle	17	287.9	41.79	26.4	3.83
		Bottom	16	292.8	42.50	30.6	4.44
				289.3	42.0	26.2	3.80
B	T ₂	Top	—	—	—	—	—
		Middle	18	293.6	42.62	30.4	4.41
		Bottom	30	302.8	43.95	38.6	5.60
				299.7	43.5	35.7	5.18

Table XIII — 4-Point Bend Test Results of Thixotropically Cast RBSiC

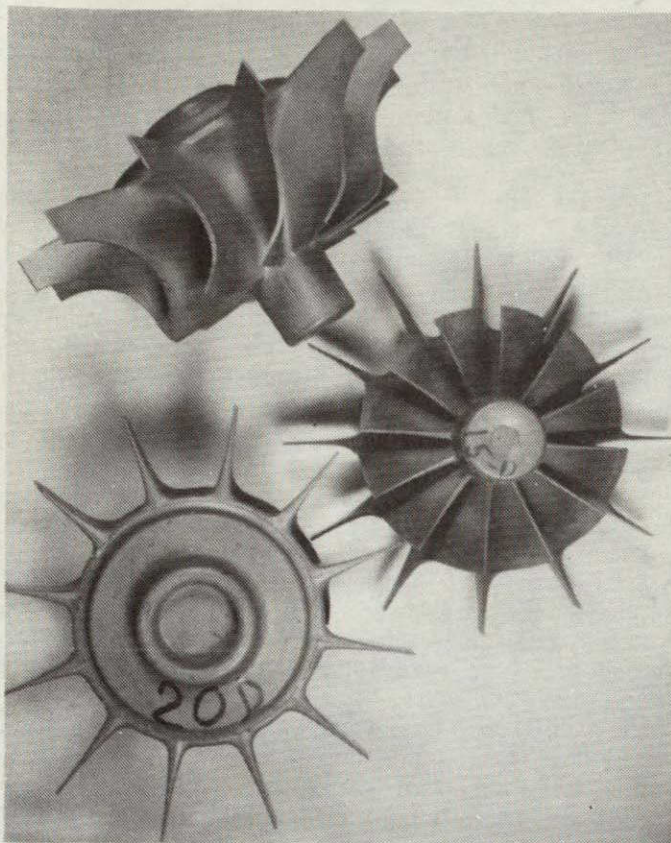


Figure 90 — Green Transfer Molded RBSiC Gasifier Rotors, New Mix Composition

mix has a tendency to extrude through all of the mold joints to form a considerable amount of flash. For a complex mold such as the rotor tool it is anticipated that mold clean-up between moldings might be as much as an hour or two, thus the cycle time is many times longer than injection molding.

To avoid the problems associated with the existing transfer molding mix, an injection molding RB SiC composition was evaluated. Several new mix binders were tried each with several different binder levels. Various mixes were evaluated in the Brabender Rheology testing machine to determine suitability for injection molding. One composition was found to be promising and several small sample pucks were warm-compression molded, baked to remove the temporary binder, and siliconized. The pucks were cut in half and revealed no internal defects.

While this molding mix was successful for small parts it did not have sufficient green strength for removal from the

rotor molding tool. Also numerous knit lines and the overall grainy surface finish which is a result of inadequate flow characteristics of this mix composition were apparent.

This mix composition was eventually abandoned after variations in molding conditions failed to significantly improve the quality. Another mix was evaluated and several good quality rotors were molded after the proper machine settings were found. Thirteen additional rotors were produced. Three of these rotors were given a gradual bake out in an inert atmosphere and the rotors displayed good dimensional integrity with an absence of cracks, but molding knit lines on the bottom became very evident after baking. One of these rotors siliconized well although NDE inspection has not yet been completed. The knit lines on the rotor bottom previously noted were also apparent after siliconizing.

It is anticipated that the knit line problem is inherent with this mix composition and alternate mixes are presently being made for further molding trials.

About two dozen rotors of an alternate mix were molded with various molding conditions to establish the optimum conditions. Notice in Figure 90 the greatly diminished knit lines which were so prevalent in the previously molded rotors. These rotors were in a baking step and some will be siliconized in the next reporting period.

INJECTION MOLDING—ALPHA SiC

The AGT 100 gasifier rotor injection molding tool was received early in this reporting period. The tool was installed in a screw-type molding machine. After initial debugging, a matrix of various molding conditions and mix types was completed. A total of 76 rotors was molded in this matrix. Two of the initial molded rotors were given a standard bake. Both showed very fine cracks at the fillet radius of the attachment hub. Both rotors were sintered and the cracks opened up considerably due to a density gradient that developed, i.e., the center of the rotor was low density while the outer surface was high density.

Two other rotors from the initial matrix were given an extended bake. However, fine cracks were still present after baking.

While the above parts were being baked, an additional total of 85 rotors were molded from three different matrix compositions.

At the same time, development work continued on new mix compositions which have greater thickness capabilities.

To date, 19 alpha SiC rotors have been sintered and seven rotors have been shipped to DDA. These rotors have

Table XIV — Rotor Mix Identities

Rotor Numbers 1 to 64	Rotor Numbers 65 to 76	Rotor Numbers 77 to 110	Rotor Numbers 111 to 140	Rotor Numbers N1 to N13
Experimental Molding Matrix For High Polymer Mix.	Experimental Molding Matrix For Low Polymer Mix.	Production Run With Best Condition Of Experimental Matrix for High Polymer Mix.	Production Run With Best Condition Of Experimental Matrix for Low Polymer Mix.	Development Mix Composition
Rotors Supplied to DDA: No. 7-3.08 g/cc (High Polymer Mix)	Rotors Supplied to DDA: None	Rotors Supplied to DDA: No. 83-3.13 g/cc (High Polymer Mix) No. 103-3.07 g/cc (High Polymer Mix)	Rotors Supplied to DDA: No. 111-3.10 g/cc (Low Polymer Mix) Mp/112-3/00 g/cc (Low Polymer Mix) No. 115-3/15 g/cc (Low Polymer Mix)	Rotors Supplied to DDA: No. N12-2.96 g/cc.

been made from three different mix compositions and Table XIV summarizes the mix identities of the rotors molded, and those supplied to DDA:

Progress has been made in reducing molding, baking, and sintering defects. The alternate mix composition bakes out more readily and two out of the three rotors fully processed were crack free (No. N4, and No. M11) and passed dye penetrant testing. Their densities were 3.10 g/cc and 3.09 g/cc respectively but both showed porosity in X-ray examination which indicates a need for optimizing the molding conditions for this mix. These preliminary results with the new composition are very encouraging for making solid one-piece rotors and additional rotors will be molded with this new mix. Figure 91 shows a typical rotor.

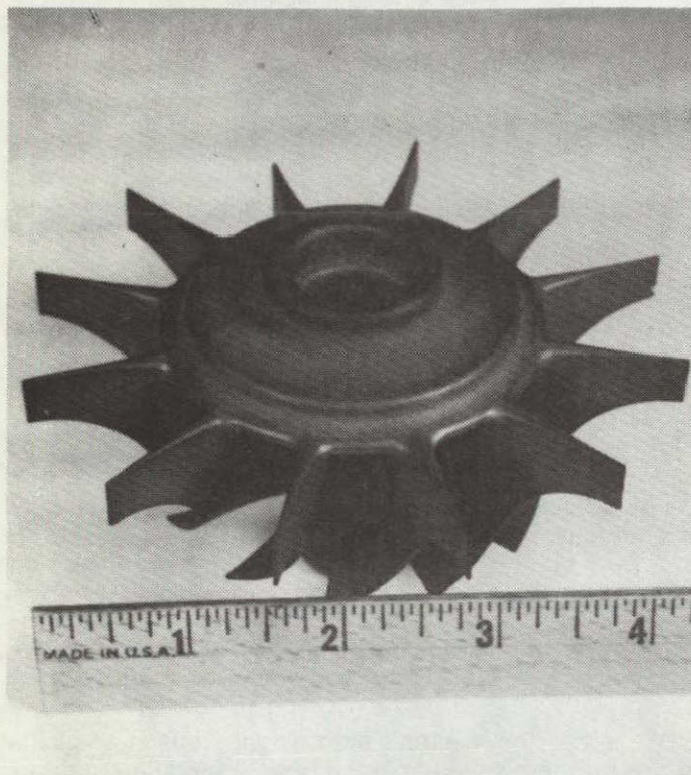


Figure 91 — Solid One-Piece Injection Molded Sintered Alpha-SiC Gasifier Rotor

SLIP CASTING—ALPHA SiC

The slip casting process has significant potential for producing rotors of thick hub section where removal of large amounts of temporary plastic binders pose problems for molding techniques. The process considered for fabrication of AGT 100 rotors consists of the following steps:

1. Injection molding or casting of wax rotor patterns.
2. Coating of the patterns with a ceramic slurry to build up a shell similar to that used by the investment casting industry.
3. Removal of the wax from the shells by baking or solvent leaching.
4. Centrifugal casting of alpha SiC water slip into a spinning mold.
5. Sintering of the whole mold and casting such that mold degrades and falls away and the free-standing casting sinters.

The difficult part of this forming method approach lies in the development of the shell mold material. It must be porous for the dewatering of the slip. It must also be compatible with the slip and strong enough to survive spinning. Further, it must disintegrate prior to the sintering of the SiC to accommodate the SiC's shrinkage. Finally, the disintegration products must be chemically compatible with SiC at the sintering temperature.

A dozen wax patterns for the truck turbocharger rotor were supplied. Three shell binders have been evaluated to date: the first was a water soluble binder which was claimed to be rendered water insoluble after curing. Shells made with this binder could not have the wax pattern removed by heating; the shells would slump and distort because the wax patterns had a melting point too close to the softening point of the binder.

Attempts at removing by wax solvent extraction were unsuccessful because the various wax solvents tried would also dissolve the resin binder. Although this binder might be suitable if a lower melting point were used for the patterns, it was also found that the shell could be softened in water despite claims by the resin manufacturer's literature.

The second resin tried was a thermoset type. The use of a standard investment casting technique, flash heating, to remove the wax pattern, was unsuccessful. Several of the shell blade tips were burnt off in the heating. Solvent extraction was also unsuccessful again because the solvents would dissolve the resin binder.

The third resin enabled the wax pattern to be removed by solvent leaching; however, the shell was softened by the aqueous SiC slip during casting.

The slip casting process, while attractive, requires the solution of several formidable problems. In view of the less-than-encouraging results to date and the positive progress achieved with injection molding, no additional work on slip casting is planned.

Combustor Body

The combustor body for the AGT 100 is being produced from slip cast Alpha-SiC.

An aluminum pattern was delivered and three different molds have been made. The differences involve whether or not the air intake slots are cast-in, cut-in in the green state, or cut-in in the fired condition.

The first mold had a one-piece barrel with cross bars bolted to the bottom, Figure 92, and a resultant casting is shown in Figure 93. Three of the four castings made had small cracks in the corner areas from shrinkage.

The mold design was changed to have a removable bottom, so the cross bars could be removed while the casting was still in the mold before it had a chance to shrink. Although this solved the cracking problem, there was a considerable amount of green machining necessary. Also the four projections might be susceptible to warpage during sintering.

The aluminum pattern was filled with wax in the cross bar grooves and another mold was made, Figure 94, and the resultant casting, Figure 95, will have the slots cut in after sintering. The bottom can be cut out in the green state to reduce the amount of final grinding.

To date 74 combustors have been cast, 55 have been dried, and 30 have been fired. Of the 30 fired, only a few were sintered with the new fixtures and three combustors

ORIGINAL PAGE
BLACK AND WHITE PHOTOGRAPH

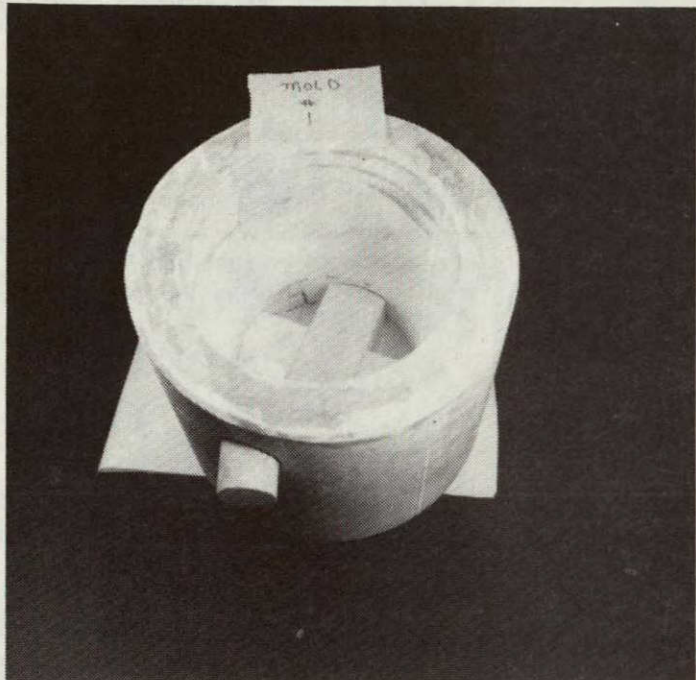


Figure 92 — One-Piece Barrel Plaster Mold for Combustor Body

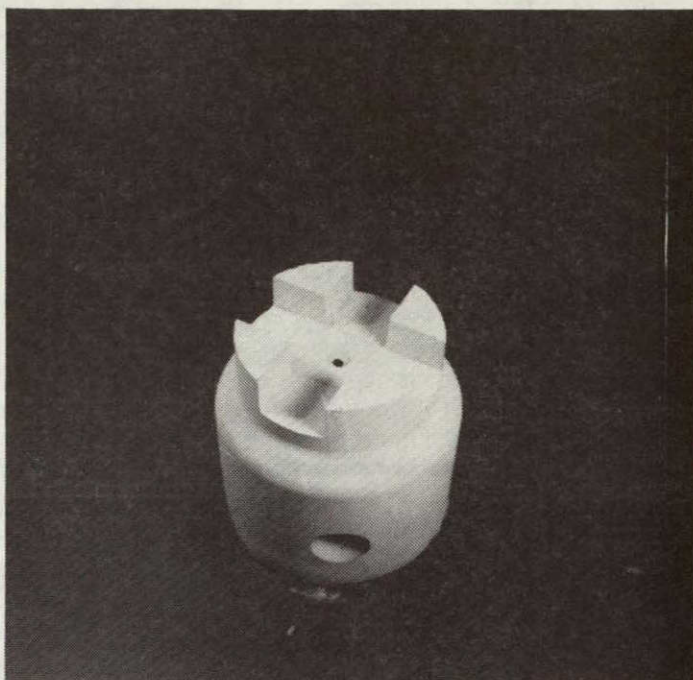


Figure 93 — Green Slip-Cast Alpha SiC Combustor Made from One-Piece Mold

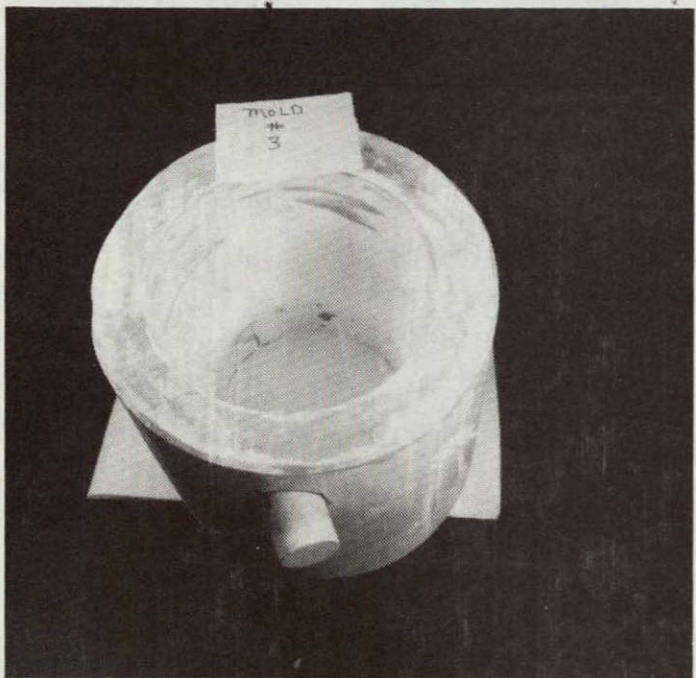


Figure 94 — One-Piece Barrel Plaster Mold for Combustor Body Without Cross Bars

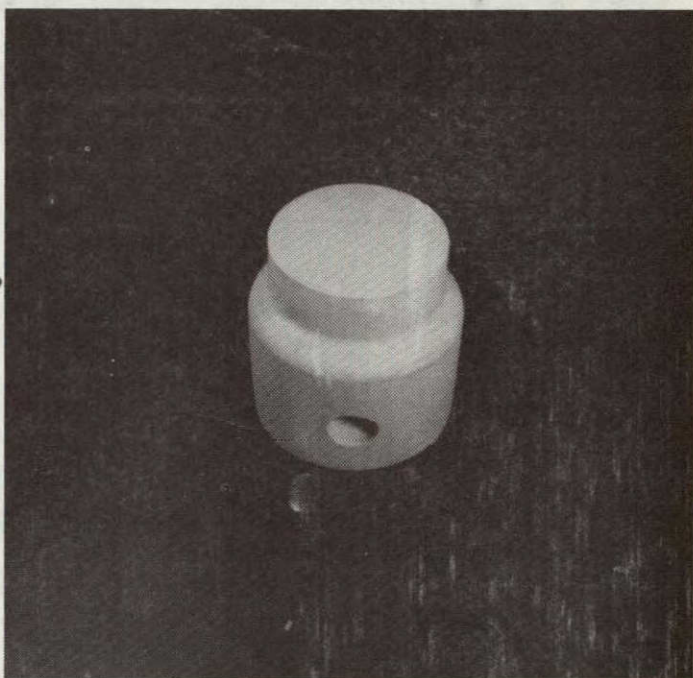


Figure 95 — Green Slip-Cast Alpha SiC Combustor Without Air Intake Slots

have the correct dimensions.

One of these, number 41, is shown in Figure 96.

The two dimensionally correct combustors have been NDE inspected. One was rejected due to an excessive amount of internal air bubbles and a Zyglo indication of a crack in the pilot flame holder hole. The other combustor has a green machining defect in the pilot flame holder hole which will probably not be removed in final final grinding. A third combustor has been found to be X-ray and Zyglo defect-free and is now being dimensionally inspected. Seven more combustors have been submitted for NDE inspection.

Outer Backplate

The primary fabrication technique for the outer backplate is injection molding. The tool has been designed, built and delivered. Molding trials will be initiated early in the next reporting period.

As a back-up process, the outer back plate will also be made by slip casting. A wood pattern and an epoxy pattern have been delivered, Figure 97 and 98. The epoxy pattern was made from a mold which was made from the original wood pattern. The epoxy pattern is used to cast the plaster molds used for slip casting. This avoids having to cast plaster molds off of the wood pattern which is susceptible to warpage due to the wet plaster.

The slip casting plaster mold for the outer back plate was made, Figure 99, and six castings were made. The first three were not successful due to core and lug shrink

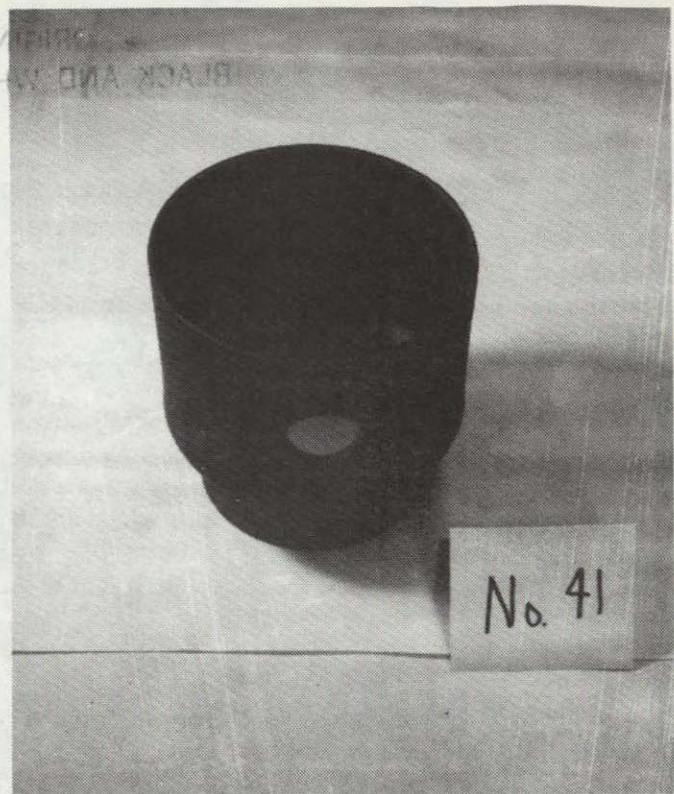


Figure 96 — Sintered Alpha SiC Slip-Cast Combustor

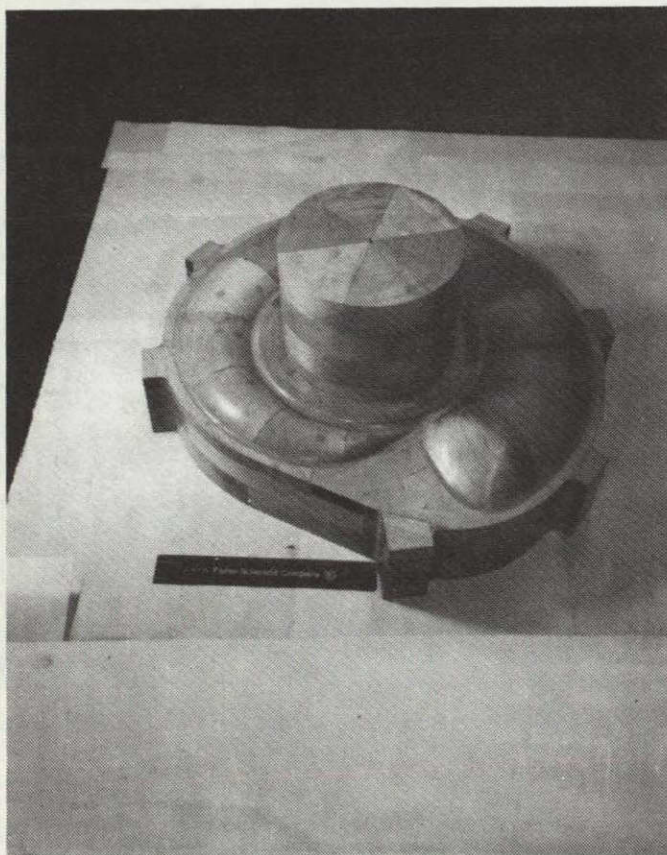


Figure 97 — Wood Gasifier Turbine Outer Backplate Model



Figure 98 — Epoxy Gasifier Turbine Outer Backplate Pattern for Making Slip-Cast Molds

ORIGINAL PAGE
BLACK AND WHITE PHOTOGRAPH

crack problems which were subsequently corrected.

The gasifier scroll back plate mold had to be modified for better part release in the flange area. Eight more parts were cast. One of the original six was successfully sintered and was supplied to DDA, Figure 100.

Scroll

The gasifier scroll is being produced from slip cast alpha silicon carbide.

The slip casting pattern for the gasifier scroll has been delivered, Figure 101, and an epoxy and silicone rubber mold, Figure 102, has been made to make a new plastic

pattern. This will allow plaster molds to be made without using the original warpage-prone wood pattern.

A plaster mold has been made, Figure 103, which consists of seven separate segments, some of which require careful disassembly while the part is in the mold. This part is very difficult to remove from the mold or perhaps more accurately, the mold is very difficult to remove from the casting.

A total of 13 gasifier scrolls have been cast, Figure 104; 6 have been dried, and one has been sintered, Figure 105. Visual inspection of the sintered scroll shows one crack in

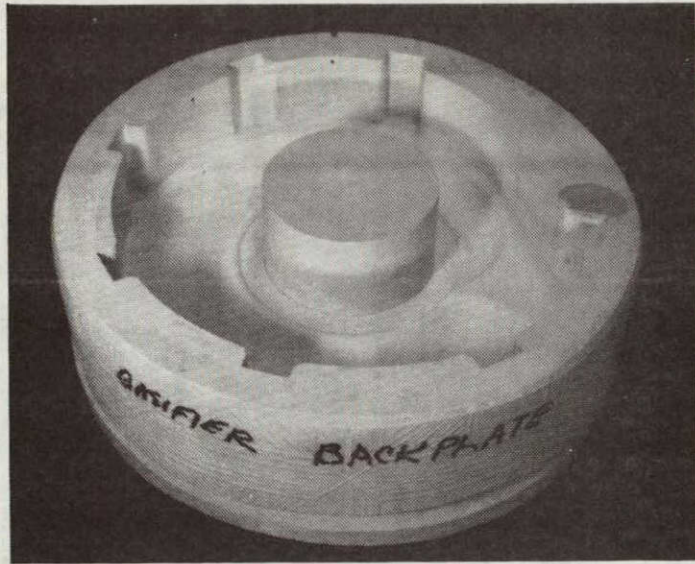


Figure 99 — Plaster Slip-Casting Mold for the Outer Gasifier Backplate

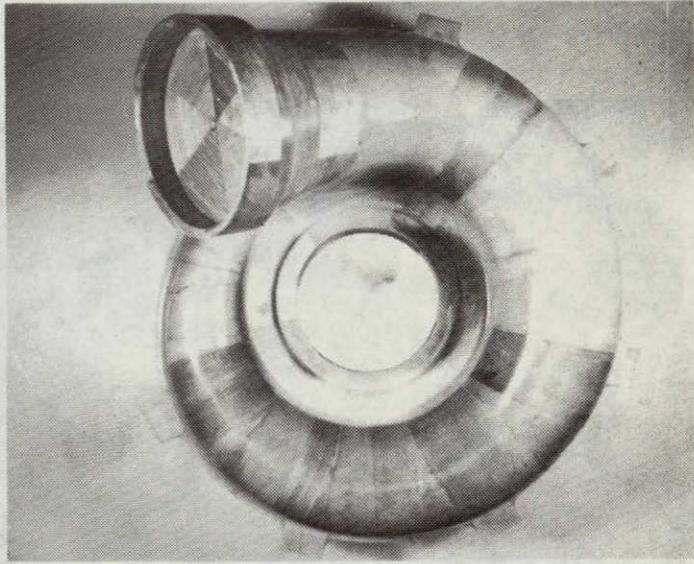


Figure 101 — Gasifier Scroll Slip-Casting Pattern



Figure 100 — Sintered Alpha Slip-Cast Gasifier Rotor Scroll Black Plate With Thick Tab and Vane Pocket Regions



Figure 102 — Epoxy Mold Castings Made from the Original Wood Gasifier Scroll Slip-Casting Pattern

crack in the inlet neck area but the part appears virtually undistorted in the tab and snail regions. The neck sagged somewhat during sintering and this points out a need for sintering fixtures.

Gasifier Turbine Vanes

Gasifier turbine vanes will be produced from injection molded alpha silicon carbide. The injection molding tool has been designed, built and delivered to CBO. Preliminary molding trials will be initiated early in the next reporting period.

Combustor Parts

The AGT-100 combustor assembly consists of five separate ceramic parts, all to be made from alpha silicon carbide. The combustor body as described above is to be slip

cast. The remaining four parts (dilution ring, swirl plate, flange and flame tube) are to be fabricated from green machined, isopressed and sintered alpha silicon carbide. Final dimensions will be achieved by dimensional grinding. Two sets of these parts have been fabricated to date without difficulty. Examples of each part are shown in Figures 106 through 109.

Strength of SiC Components

The most recent strength data obtained for sintered alpha SiC and reaction bonded SiC is shown in Table XV. The method of fabrication is also included. The slip cast bars were cut from cast crucibles, and should be equal to the strength obtained in components. In the case of injection molding, strength can be very dependent on part de-



Figure 103 — Plaster Mold for Slip-Casting Gasifier Scroll

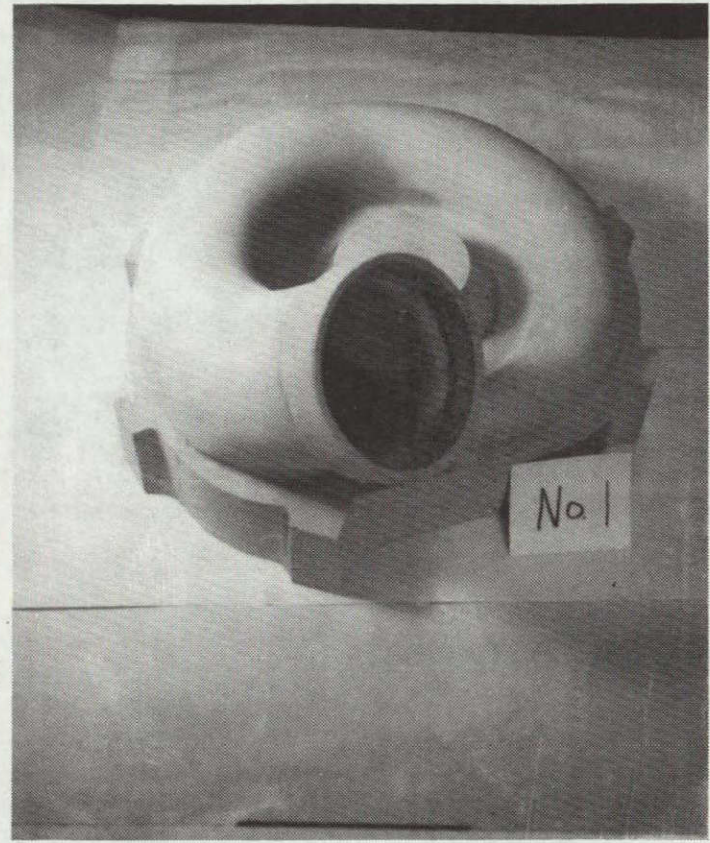


Figure 104 — Green Slip-Cast Alpha SiC Gasifier Scroll

		Slip Cast Bimodal Sintered Alpha SiC	Slip Cast Sintered Submicron Alpha SiC	Injection Molded Sintered Alpha SiC	Isopressed Sintered Alpha SiC	Cold Pressed Sintered Alpha SiC	Warm Compressed Molded Reaction Sintered SiC
Mean Strength	MPa (ksi)	310.9 (45.13)	375.2 (54.46)	455.8 (66.16)	427.4 (62.03)	423.7 (61.50)	434.1 (63)
Standard Deviation	MPa (ksi)	41.34 (6.00)	78.5 (11.39)	81.4 (11.82)	41.4 (6.01)	27.8 (4.04)	80.5 (11.68)
Weibull M.		7.86	4.84	—	11.4	—	5.13
No. of bars		20	30	10	21	16	18
Size (in.)	mm (.in.)	3.1 x 6.2 x 50.4 (.125 x .250 x 2)	3.1 x 6.2 x 50.4 (.125 x .250 x 2)	2.5 x 5 x 50.4 (.1 x 0.2 x 2)	2.5 x 5 x 50.4 (.1 x .2 x 2)	3.1 x 6.2 x 50.4 (.125 x .250 x 2)	3.1 x 6.2 x 50.4 (.125 x .250 x 2)
Condition		Ground	Ground	As fired	As fired	Ground	Ground
Test Date		2/17/81	7/24/80	10/16/80	4/14/80	1/5/81	1/23/81
Comments		Cut from Crucibles	Cut from Crucibles	Old Compounder New Mix	New Compounder Old Mix	—	—
							AGT Common Study

ORIGINAL PAGE
BLACK AND WHITE PHOTOGRAPH

Table XV—Strength of SiC Components

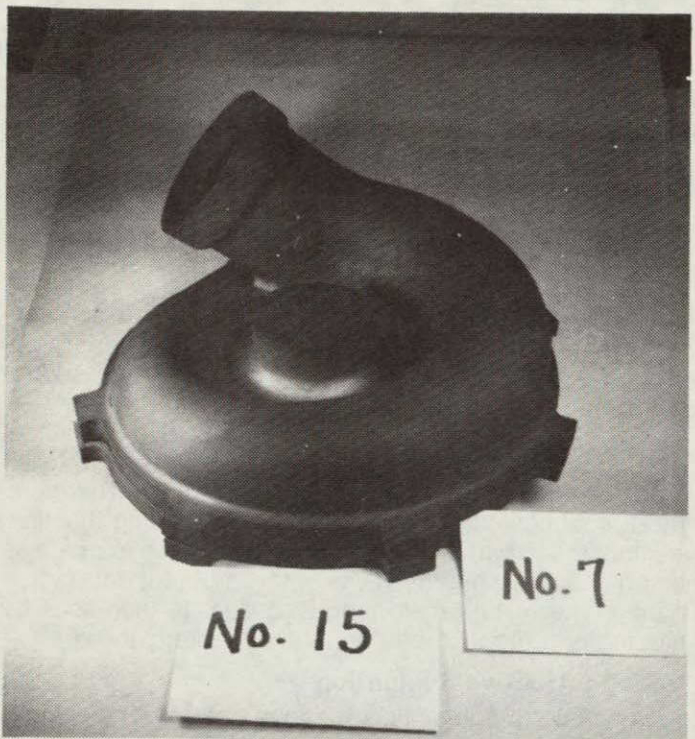


Figure 105 — Sintered Alpha SiC Slip-Cast Gasifier Rotor
Scroll and Backplate

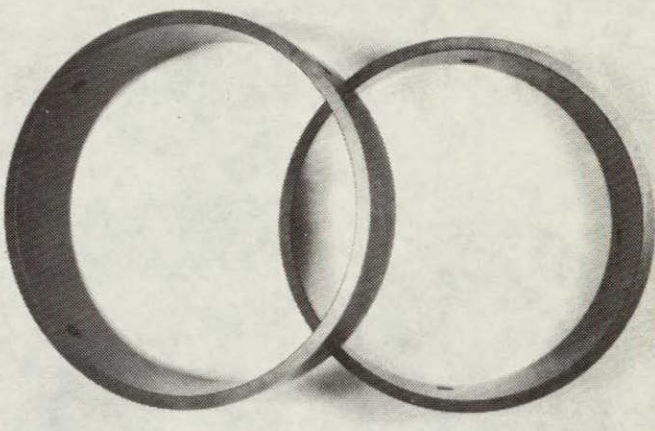


Figure 106 — Isopressed Sintered Alpha SiC Combustor
Dilution Ring, Finish Ground

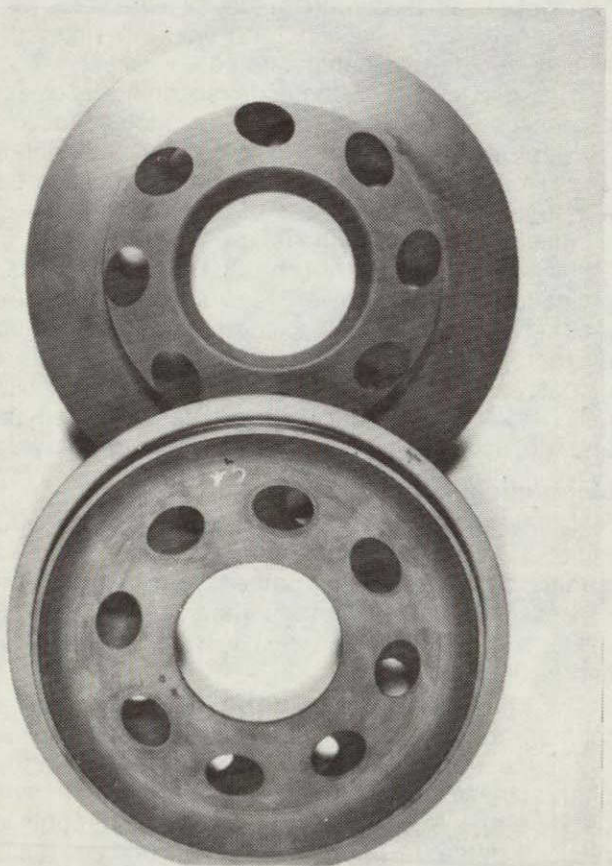


Figure 107 — Isopressed Sintered Alpha SiC Combustor Swirl
Plate, Finish Ground



Figure 108 — Isopressed Sintered Alpha SiC Combustor
Flange, Finish Ground

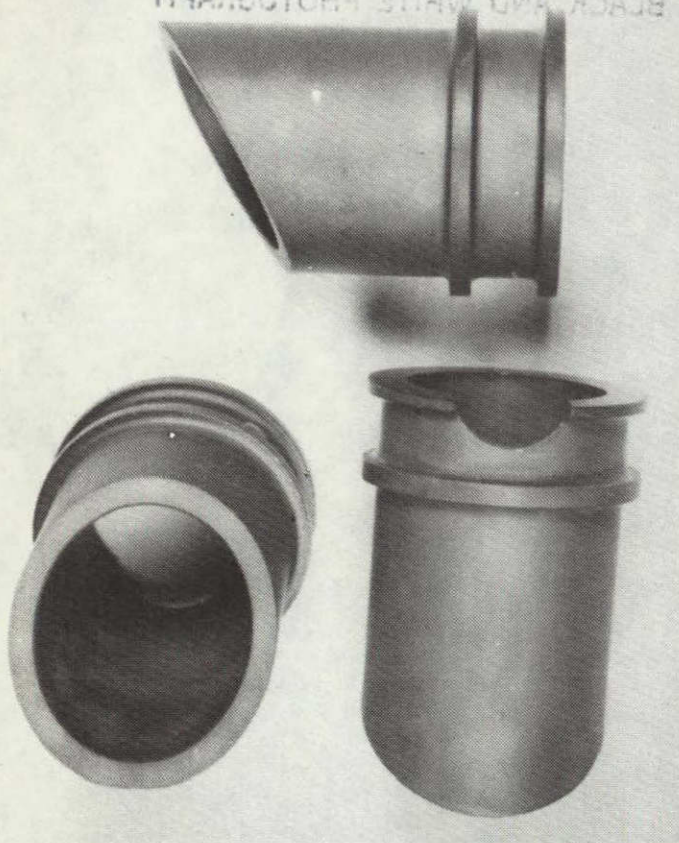


Figure 109 – Isopressed Sintered Alpha SiC Pilot Flame Tube, Finish Ground

sign and molding parameters such as gating. However molding conditions are always optimized until microstructure, density, etc. of the components are equal to that observed in test bars. Also, data from other programs has produced strength in components (e.g. rotors) equivalent to that indicated for test bars. An internal program at Carborundum has produced injection molded test bars with a strength of 65 ksi and a Weibull modulus of 12. Procedures are underway to incorporate these improvements in the AGT components.

9.3 Suppliers Effort—Common Work⁷ Summary

This report is classified into four broad areas of activity, which include developmental efforts in rotor fabrication, non-destructive evaluation, mechanical properties, and physical properties. Appendix A presents the details of these studies as reported by Carborundum.

This report details rotor fabrication activities including hot pressing of a core, evaluation of chemical vapor deposition (CVD) coatings, and hot isostatic pressing (hipping).

Baseline fractography data on alpha silicon carbide manufactured by injection molding are also reported. The non-destructive evaluation efforts which include micro-focus X-ray, high frequency ultrasonics, scanning laser acoustic microscopy, and scanning photoacoustic microscopy are reviewed. Thermal diffusivity versus temperature for both sintered alpha silicon carbide and fine grain reaction bonded silicon carbide are reported.

Rotor Fabrication

Hot pressed silicon carbide was investigated as a hub material for the AGT rotor program. Room temperature MOR (modulus of rupture) results indicated that very high strengths are possible for certain compositions. These high strengths were obtained on small hot-pressed disks. However, translating these strengths to large, thick sections needs further development. The results have indicated the potential usefulness of hot pressed SiC as a core material for the AGT rotor.

The coating of SiC by CVD processes onto alpha SiC substrates was evaluated by room temperature strength determinations, microstructure, and failure analyses. There was no significant strength enhancement or reduction in the variability of the original strength distribution. Microstructural examination revealed that, in general, coatings are well bonded to the substrate and with an absence of microporosity in the CVD coatings. Therefore, these coatings can accomplish a useful sealing function.

Hipping of partially sintered alpha silicon carbide is being accomplished by NASA with Carborundum participating. The results have indicated density increases by hipping of up to 98.5 percent of the theoretical value.

Non-Destructive Evaluation

Significant progress was made in detection of approximately 0.1 to 0.12 mm (0.004- to 0.005-in.) voids in 2.5 mm (0.1-in.) thick disks. The defect detection capability level was increased from 4.3 to 3.5 percent of section thickness by using microfocus X-ray radiography.

The applicability of high frequency ultrasonics (35 MHz) to examine B₄C inclusions and voids in sintered alpha silicon carbide was demonstrated.

The advanced NDE methods, scanning laser acoustic microscopy (SLAM) and scanning photoacoustic spectroscopy (SPAM), were investigated for both sintered alpha silicon carbide and reaction bonded silicon carbide. Although surface roughness of as-fired surfaces causes difficulties for both methods, useful NDE signals can be obtained from both SPAM and SLAM. Complex shape examination seems to be very feasible by SLAM. The SPAM method is also applicable to complex shaped components by appropriate cell design. However, both methods require extensive experience for correct interpretation of NDE signal. In addition, it is not possible to describe the type, size, and location of defects directly from the primary data.

Mechanical Properties

Failure analysis of baseline strength bars produced by injection molding sintered alpha SiC has indicated that in a majority of cases (>60 percent), failure occurred from processing-related volumetric flaws located at or close to the tensile surface. Similar results were observed also with slip cast silicon carbide.

The characteristic strength of 445.7 MPa (64 ksi) at room temperature of injection molded test bars is among the highest observed in our laboratories, as well as the characteristic strength of 409.2 MPa (59 ksi) at room temperature for slip cast silicon carbide. The strengths of dry pressed sintered alpha silicon carbide and fine grain reaction bonded silicon carbide are approximately 20-25 percent lower than that reported earlier and have been traced back to processing anomalies. Corrective measures have been implemented. The excellent retention of room temperature strength at 1200°C (2192°F) for all silicon car-

bide materials investigated in this program is significant. The time-dependent mechanical properties investigations such as creep and stress rupture were also begun during this reporting period. Compression molded reaction sintered silicon carbide exhibited no time-dependent failure in 100 hours at applied stress levels of 275.6 to 385.8 MPa (40 to 56 ksi) in 4-point bend at 1000°C (1832°F). Creep deflections ranging from 3500 to 8000 micro inches were also observed. Time-dependent failure in stress rupture occurred in 1200°C (2192°F) for applied stresses less than 372.0 MPa (54 ksi). Creep deflections range from 5,900 to 25,900 micro inches were also observed

Four-point bend creep experiments at 1200°C (2191°F) were completed for this material for three applied stress levels. Minimum creep rates ranged from $2.03 \times 10^{-7}/\text{h}$ to $9.06 \times 10^{-7}/\text{h}$, with an experimental value for stress exponent, n , of approximately 3

Physical Properties

Thermal diffusivity measurements were made as a function of temperature by using the laser flash method for both sintered alpha silicon carbide and fine grain reaction bonded silicon carbide. The range of all values was between $0.10-0.17 \text{ cm}^2/\text{sec}$ at 600°C to 0.03-0.07 at 1600°C.

X. Controls PRECEDING PAGE BLANK NOT FILMED

10.1 Delco Electronics

Delco Electronics has provided DDA with environmental and operating electrical characteristics of automotive electronic controls and has generated estimates of control size, weight, and physical characteristics. This has allowed a DDA control specification to be drafted and approved.

Based on this specification, design has started on the DC-coupled, isolated thermocouple amplifiers required for the Turbine Outlet (TOT) and Burner Inlet (BIT) Temperature thermocouples.

Software studies are underway to adapt existing speed calculation algorithms to serve with the frequencies available from the AGT-100 magnetic speed pickups. Power supply design is underway based on electrical load information supplied by DDA.

Many 12VDC components will not operate below approximately 7VDC, even though the electronic control can operate down to 4.5 VDC. Therefore either a bootstrap control power supply must be designed or a separate battery employed to avoid low voltages which would occur during starter operation. A trade-off study of bootstrap power supply versus separate battery is underway.

10.2 Detroit Diesel Allison

Hardware Definition

Electronic Control: Physical constraints and electrical requirements for the Electronic Control Unit (ECU) were defined by a specification. The specification reflected several changes in control operating interface (from those reported in the last semi-annual report) as listed below:

1) drive circuits were incorporated for electrohydraulic servo valves used to control Burner Variable Geometry (BVG) and Inlet Guide Vane (IGV) positions—an electrical motor drive was initially proposed

2) adjustment potentiometers were added for trimming engine variations in such parameters as power transfer clutch current threshold and engine idle speed (output shaft)

3) spare channels were added for solenoids and relays (outputs) and for signal conditioning of additional discrete inputs

4) the test connector of the ECU was defined to enable direct access to the microprocessor data and address buses

5) provisions were added to drive a convertor lock-up inhibit solenoid in the transmission and to use a pressure switch signal from the transmission to limit engine output torque.

Sensors:

Functional requirements have been defined for all sensors and detailed design has started on all items. The ultraviolet pilot flame sensor has been eliminated because of high cost and complexity. The control logic was revised to allow flame-out detection using the TOT thermocouple signal. The TOT and BIT thermocouple designs have been completed, but they will require modification to fit the new engine configuration. Magnetic pickups for gasifier and

power turbine speeds will also require tailoring for the new engine configuration because of the selection of new pickup gears and mounting locations.

Fuel System:

No functional alterations have been made to the fuel system concept, however, the following improvements were made:

1) the electrical fuel throttling valve, minimum flow valve, and pilot orifice have been integrated into a single assembly to be procured from Rochester Products Division of GM.

2) a low pressure fuel transfer pump has been added to supply fuel to the main pump.

3) the low pressure fuel filter has been modified to incorporate a water separator and dewaxing heater.

The air pump to supply pilot nozzle atomization air has been selected after evaluation testing of three candidate types of air pumps. The pump selected is a diaphragm type with modified eccentric drive by Gast Manufacturing Co. Testing confirmed adequate flow and pressure capabilities of this pump and data were obtained for operation at reduced power levels.

Actuators:

An electro-hydraulic control system has been selected for the BVG and IGV actuator systems. This selection followed testing on electro-mechanical actuator systems which required very high drive currents. Two-stage electro-hydraulic servo valves will be used with hydraulic actuators coupled with Linear Variable Differential Transformers (LVDT's) or linear potentiometers to provide closed loop position control. Control logic has been revised to allow positioning of the actuators as soon as engine oil pressure is available.

Power Transfer Clutch Control:

No changes in the basic operation of the power transfer clutch electro-hydraulic control system have been made; however, the pressure control valve has been changed to a single flapper-single nozzle pilot stage followed by a three-way second stage spool valve.

Control Mode Definition:

General. A complete set of control mode diagrams, including constants and schedules, was defined for the Electronic Control Specification. Also included was all logic required for start, shut-down, diagnostics, limp home and other operating modes or conditions. The specification was written for the RPD engine. Control constants and schedules have also been developed for the Mod I engine design using the same basic logic and control modes.

The basic operation of the control remains as defined and several additional control modes have been added as described below.

Underspeed Governor:

The basic control modes provide for governing of the gas generator (N1) speed with the power transfer clutch.

This provides governing only if N1 attempts to run faster than the reference signal obtained from throttle position. When engine power is reduced to idle, both the gas generator and power turbines may tend to run underspeed. The power turbine speed (N2) is also influenced by the accessory load horsepower. Therefore, underspeed governors were considered necessary for both N1 and N2 control.

The first attempt at underspeed control was to modulate the temperature reference as a function of N1 and N2 underspeeds. This mechanization was evaluated on the digital simulation and proved to be unworkable for two reasons: a) at the normal N1 idle speed of 50%, the TOT required to achieve the necessary output horsepower to support the maximum accessory load is greater than the maximum allowable temperature [TOT = 1066°C (1950°F) for RPD]. b) response lags in the TOT control loop and in the engine cause multiple overshoots and undershoots in the power turbine speed. The engine temperature responds rapidly to increases in fuel flow but slowly to decreases in fuel flow because of the stored heat in the regenerator. A different idle underspeed control mode (than temperature) is required, one using the Inlet Guide Vanes (IGV's).

Inlet guide vane authority was increased to reduce the engine idle horsepower below that required for idle. An N1 underspeed governor is provided to decrease the IGV angle if the gas generator is underspeed. If the power turbine is underspeed, the N1 reference signal is proportionally increased to obtain the output horsepower required to keep N2 near a reference N2 idle speed. A block diagram of the underspeed control modes is shown in Figure 110. The feasibility of this approach has been verified on the digital transient simulation.

Start Control:

A control scheme for starting the engine has been developed. A light-off fuel flow is calculated as a function of BIT. When light-off is detected from a rapid rise in the TOT signal, the fuel flow is calculated from a start fuel schedule as a function of BIT and N1. A start temperature control loop reduces the fuel flow to gradually bring TOT from its initial value up to a limit calculated as a function of N1 speed.

A block diagram of the start control is presented in Figure 111. A special purpose, simplified start simulation was written to validate this approach. Initial results indi-

ORIGINAL PAGE IS
OF POOR QUALITY

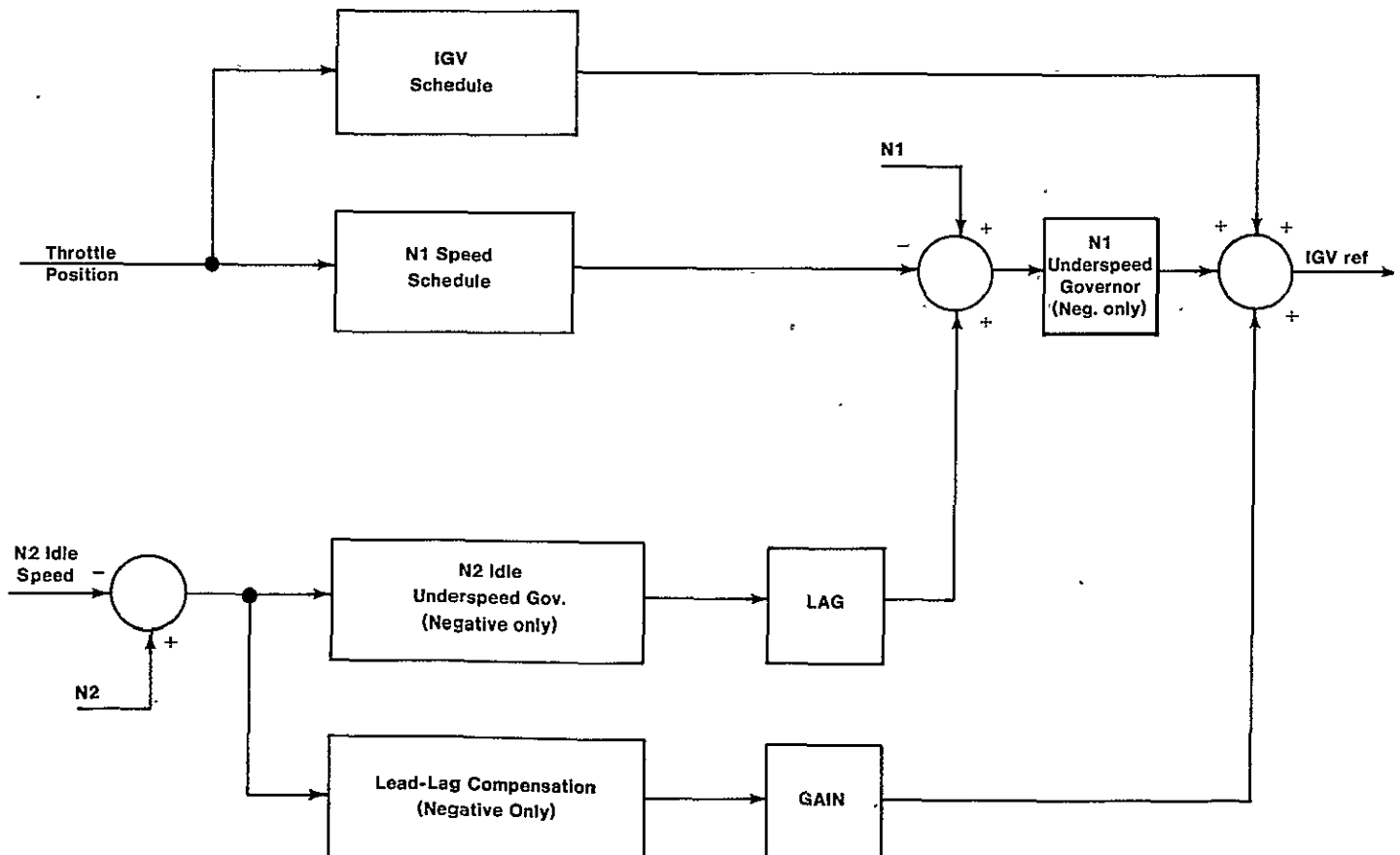


Figure 110 — Underspeed Control Modes

cate that temperature overshoots are minimized if light-off is delayed until N1 reaches 20%.

Overspeed Protection:

Overspeed protection in addition to the overspeed shutdown logic is desired. Present plans are to lockup the power transfer clutch if N2 tries to go overspeed and to reduce fuel flow if N1 goes overspeed. Operation of overspeed protection loops has not yet been validated on the digital simulation.

Burner Variable Geometry:

A BVG transient simulation was developed and exercised to determine baseline performance. This simulation used a second order underdamped actuator model, synthesized flame temperatures, and predicted emission levels of NO_x and CO. Preliminary constants and schedules for the BVG control were assigned based on simulation results. However, additional BVG work will not be accomplished until actual burner test results are available for correlation.

ORIGINAL PAGE IS
OF POOR QUALITY

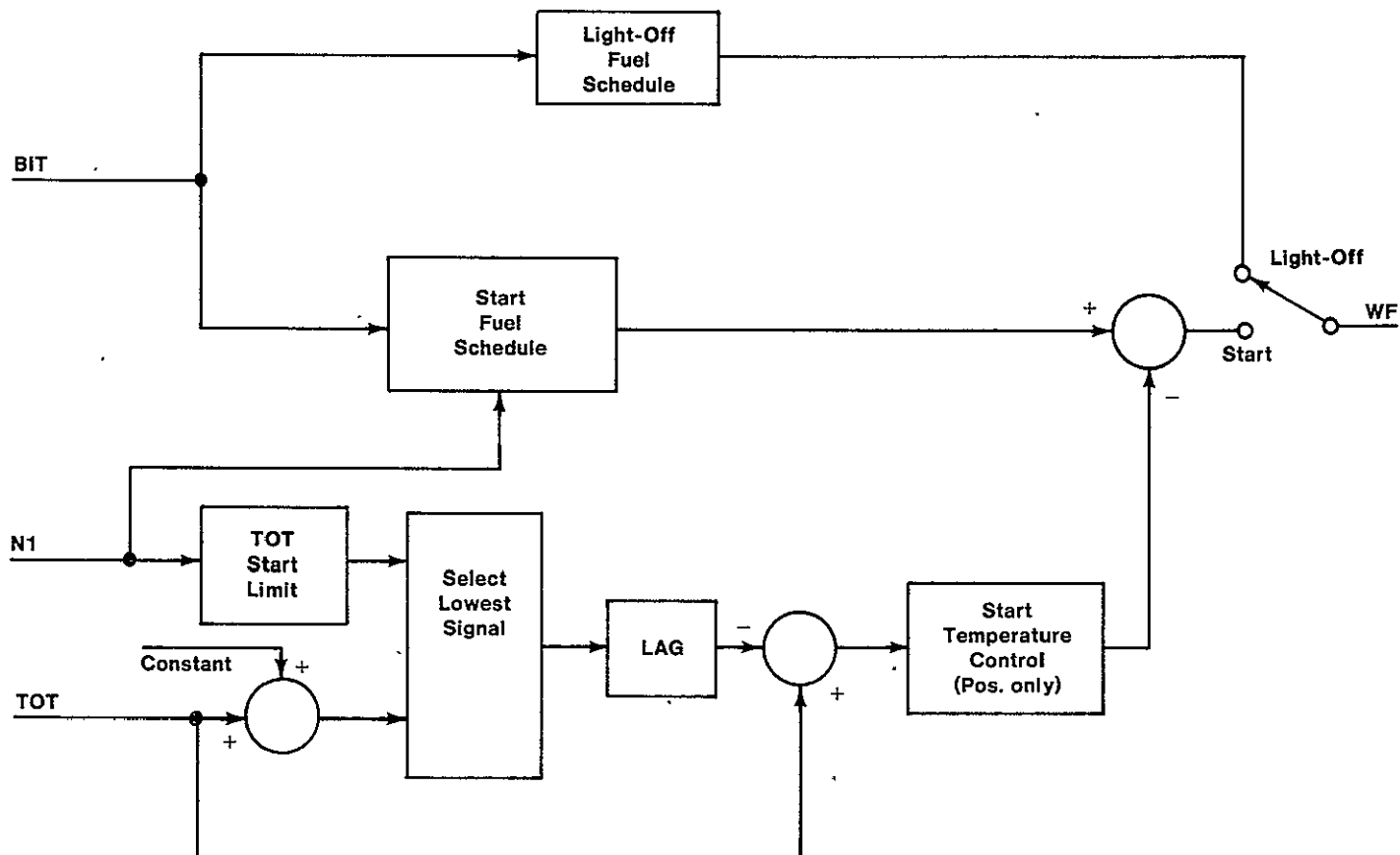


Figure 111 – Start Control Modes

XI. Transmission Development

ORIGINAL PAGE IS
OF POOR QUALITY

11.1 DDA Transmission Activity

The first semi-annual technical report discussed powertrain optimization using the production GM four-speed transmission with overdrive (THM-125). The analysis showed that the best steady state road load fuel economy is obtained by selecting second gear operation in the 16 to 32 km/h (10 to 20 mph) range; third gear operation in the 32-54.4 km/h (20-34 mph) range; and fourth gear above 54.4 km/h (34 mph).

Shift schedules have now been developed for gasoline and diesel automotive applications using the newer THM 440-T4 transmission. These schedules are shown in Figure 112. The current automobile is geared for relatively high vehicle speeds in third gear (1.00:1) and fourth gear overdrive is used only at part throttle operation to reduce engine speed requirements at road load cruising.

To maximize vehicle acceleration characteristics with the gas turbine engine, full ratio coverage of the four speed transmission is utilized to obtain desired maximum vehicle speed. For the AGT 100/THM 440-T4 powertrain, maximum geared vehicle speed in third gear (1.00:1) converter operation is 94.8 km/h (59.3 mph) (.91 speed ratio) and with the converter clutch applied is 104 km/h (65 mph), in fourth gear (7.04:1) with converter clutch applied, max vehicle speed is 147.7 km/h (92.3 mph).

To obtain these vehicle speeds and performance characteristics, changes are required in the THM 440-T4 shift controls to allow an automatic shift into fourth gear above 94.4 km/h (59 mph) at full throttle. A proposed modified 3-4 and 4-3 modulated shift pattern is superimposed on Figure 112.

Fixed shift points (1-2; 2-3; 3-4) can be obtained in a gasifier speed range (50%-65% speed) at power required to meet steady state road load conditions from 0 to 96 km/h (60 mph). Above 65% gasifier speed (approximately 25% throttle setting), a modulated shift schedule is obtained.

The fixed shift schedule described in the first semi-annual report was established as follows from zero to 100% throttle:

- 1-2 — Shift made at 16 km/h (10 mph)
- 2-3 — Shift made at 32 km/h (20 mph)
- 3-4 — Shift made at 54.4 km/h (34 mph)

Computer simulation of the AGT/THM 440-T4 powertrain over the Federal Driving Cycle using this fixed shift pattern resulted in the following fuel economy projections:

29°C (85°F) Day Urban Cycle—14.3 km/L (33.8 mpg)
HiWay Cycle—22.6 km/L (53.6 mpg)
Combined Cycle—17.1 km/L (40.5 mpg)

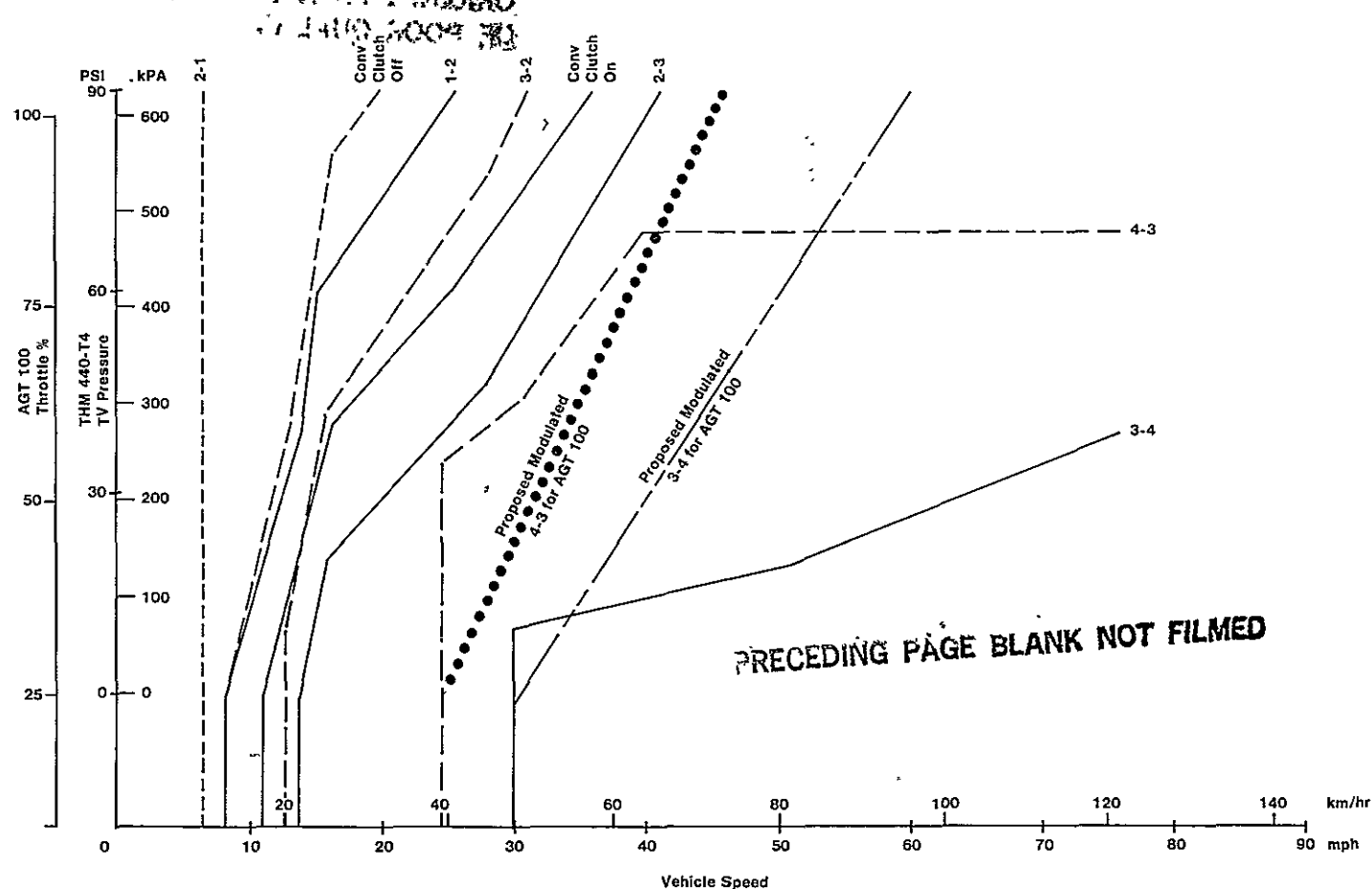


Figure 112 — Typical THM 440-T4 Shift Pattern

Adapting the typical THM 440-T4 production prototype shift schedule as indicated in Figure 112 for the 1-2 and 2-3 shift, and the proposed modified 3-4 and 4-3 shift schedules to the AGT powertrain resulted in the following fuel economies over the simulated Federal Driving Cycle:

29°C (85°F) Day Urban Cycle—14.5 km/L (34.4 mpg)
HiWay Cycle—22.8 km/L (54.0 mpg)
Combined Cycle—17.3 km/L
(41.1 mpg)

An option in the General Motors GPSIM vehicle simulation program is to "always" select the optimum gear range for obtaining maximum fuel economy of a given powertrain. Exercising this option for the AGT 100 powertrain resulted in a combined cycle fuel economy of 17.3 km/L (41.2 mpg).

The results show that maximum fuel economy can be obtained with the current production prototype shift scheduling with only modifications to the 3-4 shift valve. Preliminary studies indicate that allowing TV pressure (throttle modulated pressure signals) to act directly on a modified pressure sensing valve and sleeve in the current 3-4 shift valve assembly will produce the desired shift patterns.

Torque ratings for the THM 440-T4 transmission have been established as follows when specifying the 1.1212 underdrive chain ratio and 3.33:1 final drive:

Max. input torque to range gear set—336 N·m (248 lb-ft)

Max. output torque (input to F.D. gearing)—1100 N·m (812 lb-ft)

Output governor pressure switches within the transmission will be used as an input signal to the engine control system to limit the gasifier speed to approximately 90% speed at zero to low vehicle output speeds at steady state full power in low gear operation from vehicle stall. Maximum output torque developed at this power setting is 1032 n·m (762 lb-ft) which is within the transmission maximum rating as indicated in Figure 113.

Dynamic full power acceleration torques from vehicle at rest developed on a -40°C (-40°F) and +29°C (85°F) day are superimposed on the steady state full power performance curve indicating that maximum output torques attained are within the transmission maximum ratings.

During CY 1981, the control modifications required to obtain optimum gear range selection will be completed. Dynamic studies of clutch line pressure versus torque to provide optimum vehicle feel during range shifting will be evaluated. This work is targeted to be completed in the third quarter of CY 1981. The first THM 440-T4 four speed overdrive transmission for the AGT 100 program is scheduled to be purchased during the last quarter of 1981.

ORIGINAL PAGE IS
OF POOR QUALITY

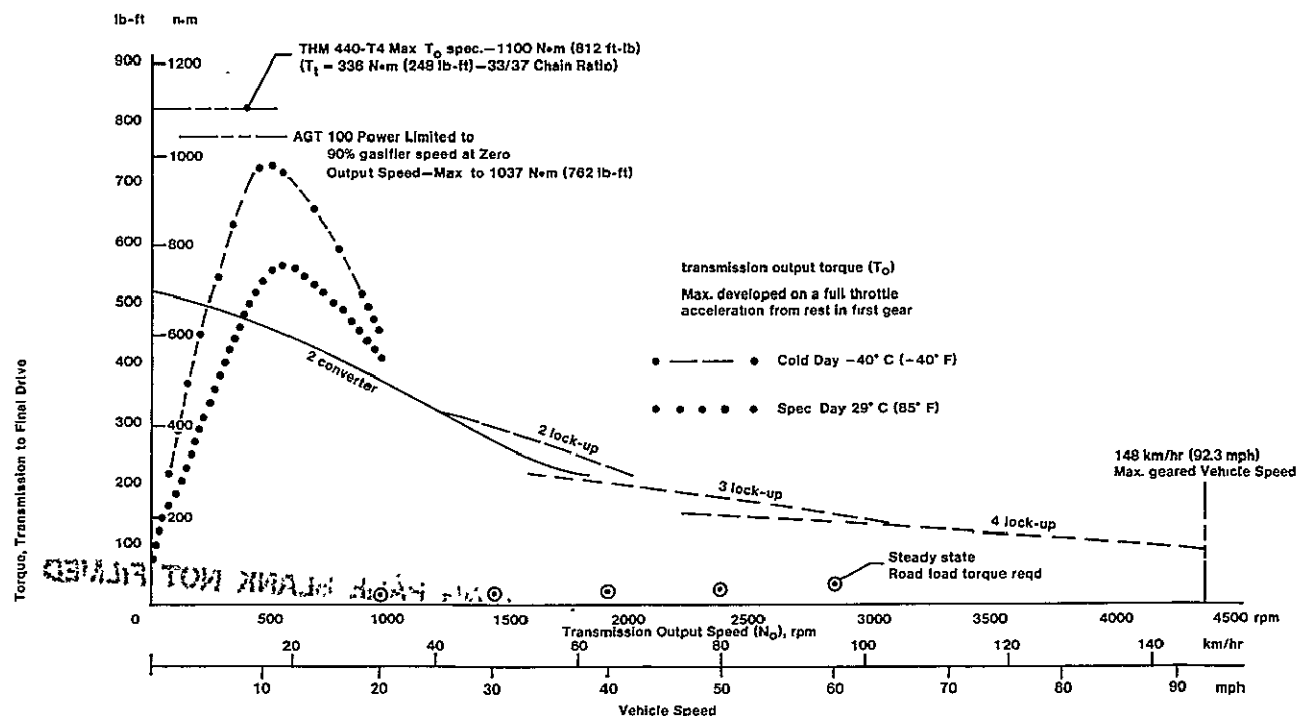


Figure 113 — AGT 100 with THM 440-T4. Powertrain Performance at steady state

XII. Supportive Manufacturing, Cost and Marketability

12.1 Manufacturing Feasibility—Pontiac Motor Division

Cost estimating and feasibility analysis continued on the original RPD engine design as detail drawings were received during the second half of 1980.

Engine Block

Final estimates await the completion of the prototype casting and preliminary estimate from Ingersoll Milling Machine Company. In the meantime, updated drawings of the block continue to become increasingly complex with the addition of numerous mounting pads, oil holes, air passages and other miscellaneous machining operations. Without Ingersoll's input the estimate for the block machining is \$25,000,000 to \$30,000,000 per line. This part is replaced with a sheet metal unit in the engine redesign.

Investment Cast Parts

Several quotations for parts have been received during this period. The results were disappointing in that prices were high and no one vendor was willing to quote the part volumes that would be required. Also several features of the parts, that we had expected to be cast in, were omitted from the quotes. Additional vendors must be contacted before final processes can be selected for these parts.

Inlet Guide Vane

This part is under continuing study as it is the highest volume part to be machined (1095/h at 400,000 volume—2175/h at 800,000 volume). Therefore, to do the minimum amount of metal cutting possible, machining the airfoil should be avoided. So far, die casting has been investigated, but this process appears to be unsatisfactory because of tolerances required. As alternate methods, both forging and powdered metal processing offer promise of producing parts with minimal finish machining.

Compressor Shroud

Pontiac had expressed concern about possible movement of the throat section when the boundary layer air groove is machined. DDA has altered the supporting ribs for the throat section along lines suggested by Pontiac to overcome this problem. In addition, Pontiac is concerned with the thin outer flange of this part being highly susceptible to breakage caused by handling. Pontiac has suggested that the flange could possibly be a separate steel piece.

Combustor Assembly

Many of the changes Pontiac has suggested to reduce the complexity of this assembly have been approved by DDA for the RPD. More work could be done in examining still less complex designs of this assembly to reduce production costs still further.

Power Transfer and Starter Bevel Gears

This engine uses three sets of bevel gears which are expensive to machine and assemble. This entire gear arrangement was reviewed by DDA with an eye toward re-

ducing these costs, and the new design eliminates these gear sets.

Regenerator Drive Bevel and Worm Gear Sets

This drive uses a worm gear set and a bevel gear set to achieve the necessary low speed and reach the location of the regenerator drive pinion. In addition to requiring expensive gaging and shimming operations, this arrangement requires on-line drilling, reaming and pinning of the worm gear during assembly. This is not a good high production operation in that it creates chips that can easily get into the engine. (This drive system was replaced with a harmonic drive in the engine redesign.)

Compressor Impeller Assembly (AA-100056)

This design requires a complex process of machining and assembly performing the following steps:

1. Machine the impeller and shaft as separate parts
2. Draw the shaft into the impeller with an extreme interference fit 0.08 mm to 0.11 mm (0.0033 in. to 0.0043 in.) without heating the impeller
3. Remachine the draw bar end of the shaft
4. Finish machine the impeller blade tip profile.
5. Balance the assembly

Steps 1, 4 and 5 are unquestionably required. However, step 2 could become a simple matter of slipping two parts together and step 3 could be eliminated if the impeller could be heated and the parts shrunk together. This simpler process is much better for a high production process in that it eliminates a number of machining operations, the entire press operation, the extra equipment and operators.

If satisfactory from an engineering standpoint the shrink fit process would result in a substantial savings in machining time, equipment and labor costs.

12.2 Cost Analysis—Pontiac Motors Division

The objective of the manufacturing cost studies is to achieve a developed vehicle cost (sticker price) of the AGT 100 powered Phoenix comparable to the V6-powered baseline Phoenix. The studies to date have been directed toward incorporating high volume machining and processing philosophies into the RPD design. Where practical, these philosophies have also been applied to the Mod I design. This approach has been very effective in making design changes for manufacturability reasons.

A cost analysis summary was developed for the RPD review meeting in September 1980. The summary was necessarily incomplete but did serve to update the original analysis completed for the Conceptual Design Study.

The significant changes are:

1. New parts added to the original design, such as the power transfer system, were added to the analysis.
2. Parts eliminated from the original design, such as turbine variable geometry, were deleted from the cost analysis.
3. The 4-speed automatic transmission was substituted for the 3-speed automatic.

4. Costs of specific components were updated to reflect the most recent design changes, e.g. ceramic parts, hot section bearings, electronic controls
5. Adjustment was made for the 1981 vs 1977 economic differential.

Preliminary studies indicate the cost concerns are being greatly reduced by the new design

References

1. Johnson, R. A Conceptual Design Study of an Improved Gas Turbine (IGT) Powertrain, July 1979 Detroit Diesel Allison EDR 9719 NASA/DOE CR-150604.
- 2 Advanced Gas Turbine (AGT) Powertrain System Initial Development Progress Report. March 1980, Detroit Diesel Allison EDR 10086. NASA CR-159804.
3. Ceramic Applications in Turbine Engines (CATE), DOE/NASA Program Contract No. DEN3-17
4. M Srinivasan and R H Smoak, "Elevated Temperature Fracture Toughness Determinations of Sintered Alpha SiC," Proc of Intl Conf. of Fracture Mechanics in Engineering Applications, Bangalore, India, March 26-30 (1979)
5. Data Sheet, Carborundum Co. (1978).
6. S. M Hudson, M. A. Janovicz, and F. A. Rockwood, "Ceramic Applications in Turbine Engines," NASA Report CR-159865, May (1980).
7. Work "common" to both the AG-100 and AGT-101 engines, and jointly funded by DDA and the Garrett Corp.—See Appendix.

Terms & Definitions

Symbol/Term	Definition	
A	Ampere	m
AGT 100	The AGT Model being developed by DDA	M-dist
AS	Aluminum Silicate	mm
BIP	Burner inlet pressure	mpg
BIT	Burner inlet temperature	mph
BOT	Burner outlet temperature	Mod I
.Btu	British thermal unit	Mod II
B/U or BU	Build up	MOR
BVG	Burner variable geometry	N
C; C_T	ISENTROPIC sputting velocity — $2gJ \Delta h_{is}$	NASA
°C	Degrees Celsius	NDE
CATE	A NASA/DOE development program "Ceramic Applications for Turbine Engines"	N_G
CBO	Carborundum Corporation	N·m
cc	Cubic centimeter	NO_x
CCW	Counter clockwise (rotation)	N₁
CDP	Compressor discharge pressure	N₂
CGW	Corning Glass Works	P
CIT	Compressor inlet temperature	Pa
CO	Carbon monoxide	PAS
CVD	Chemical vapor deposition	PMD
CW	Clockwise (rotation)	psi
CY	Calendar year	psia
D_m	Bearing speed parameter	P_T
DDA	Detroit Diesel Allison Division of General Motors	Q
DOE	US Department of Energy	°R
ECU	Electronic control unit	rad/s
EDR	Engineering Development Report (of DDA)	R_c
°F	Degrees Fahrenheit	RBSiC
ft	Foot	REGEN
g	Gravitational constant, gram	RPD
gm	Gram	rpm
GM	General Motors Corporation	RTV
GMR	General Motors Research	Sec or s
GT	Gas turbine	SiC
GTE	General Telephone and Electronics Corp	SLAM
GPSIM	General purpose simulation	SLS
h or hr	Hour; enthalpy	SPAM
HP or hp	Horsepower	T
HRD	Harrison Radiator Division of General Motors	T.E. or t.e.
Hz	Hertz (frequency)	THM 440-T4
in	Inch	T/L
IGV	Inlet guide vane	TOT
J	Conversion factor, Btu to ft-lb, Joule	T-S
k	Kilo- (thousand)	T-T
°K	Degrees Kelvin	U
kg	Kilogram	U/C_T
km	Kilometer	U_T
ksi	Thousand pounds per square inch	V
L or l	Liter	VG
LAS	Lithium aluminum silicate ceramic	W
Ibm	Pound mass	W_A
LCF	Low cycle fatigue	W_c
L.E. or l.e.	Leading edge	WCR
LVDT	Linear variable differential transducer	W_f
M	Mega- (one million)	WOT

2-D	Two-dimensional (analysis)	μ	Micro- (one million)
3-D	Three-dimensional (analysis)	Θ	Temp/temp std
IGT 404	An industrial gas turbine engine by DDA	Θ_{cr}	$(V_{cr}/V_{cr, std})^2$
IGT 505	An industrial gas turbine engine by DDA	Equivalent flow	flow $\Theta_{cr} E/8$
γ	Ratio of specific heats	Equivalent speed	speed/ Θ_{cr}
Δh	Specific work	Equivalent work	$\Delta h_T/\Theta_{cr}$
Δh_{is}	Ideal specific work (total-static)	Green matching	Machining a ceramic before it is fired
ϵ	$(0.740/\gamma) (\gamma + 1/2)\gamma/(\gamma - 1)$	Thixotropic casting	Casting enhanced by vibration to reduce viscosity of the cast fluid
η	Efficiency		

Appendix—Carborundum Common Work

Rotor Fabrication

Hot Pressed Silicon Carbide

Hot pressed alpha silicon carbide was investigated because of its potential higher strengths than sintered alpha silicon carbide.

Submicron alpha silicon carbide powder was hot

pressed at 1700°C (3092°F) to 2000°C (3632°F) temperature range into approximately 31.8 mm (1.25 in.) diameter disks using four different additives as hot pressing aids. MOR bars were sliced out of these disks to 2.5 × 1.3 mm (0.1 × 0.05 in.) cross section with edges chamfered. Room temperature flexural strength was measured in 3-point bend by using a span of 19 mm (0.75 in.). The effect of compositional variation is summarized in Table XVI.

Table XVI — Effect of Chemistry on Strength of Hot Pressed Alpha Silicon Carbide

Additive	Hot Pressing Temperature °C (°F)	Bulk Density		Strength —	
		g/cc	(lb/in. ³)	MPa	(ksi)
1% A	1800 (3270)	3.10 — 3.15	(1120 — 1138)	439.06 ± 35.03	63.68 ± 5.08
1% A	2000 (3630)	3.18 — 3.19	(1149 — .1152)	557.44 ± 37.78	80.85 ± 5.48
1% B	1800 (3270)	3.14 — 3.17	(1134 — .1145)	584.54 ± 127.42	84.78 ± 18.48
1% B	2000 (3630)	3.18 — 3.19	(1149 — .1152)	827.10 ± 95.84	119.96 ± 13.90
1% C	1800 (3270)	2.90 — 2.94	(1048 — 1062)	586.13 ± 32.75	85.01 ± 4.75
1% C	2000 (3630)	3.10 — 3.15	(1120 — .1138)	758.84 ± 97.42	110.06 ± 14.13
2% C	1800 (3270)	3.05 — 3.10	(1102 — .1120)	774.97 ± 54.26	112.40 ± 7.87
2% C	2000 (3630)	3.17 — 3.18	(1145 — .1149)	661.21 ± 19.86	95.90 ± 2.88
2% D	1700 (3090)	3.16	(1142)	465.47 ± 46.20	67.51 ± 6.70
2% D	1800 (3270)	3.20 — 3.24	(1156 — 1171)	712.85 ± 93.63	103.39 ± 13.58
2% D	1900 (3450)	3.20	(1156)	702.24 ± 91.29	101.85 ± 13.24
2% D	2000 (3630)	3.20	(1156)	738.50 ± 60.81	107.11 ± 8.82

Flexural strengths of over 690 MPa (100 ksi) indicate the potential of this approach. The hot pressing efforts were halted after these efforts under the common work and were transferred to an appropriate unique program. The challenge there will be to hot press thicker and larger bodies with homogeneous microstructure and to translate the high strengths obtained on specimens machined from hot pressed large bodies.

Evaluation of CVD Coatings

Earlier Carborundum work, which has been confirmed by work done under this contract has demonstrated that a majority of failure-causing flaws are processing-related, void-like defects lying at or close to the tensile surface of a flexural bend bar. Therefore, it was hypothesized that chemical vapor deposition (CVD) of silicon carbide could offer an attractive technique for potential strength enhancement.

In this study, 125 injection-molded test bars were fabricated and inspected, and were divided into 5 groups of 25 bars. Twenty-five (25) bars were retained as a control to evaluate strength. Thirty (30) bars each (which included 5 each for establishing coating conditions) were shipped to:

- San Fernando Laboratories
- Materials Technology Corporation

- Deposits and Composites, Inc.
- Refractory Composites, Inc

The bars were tested at room temperature in 4-point bend with a 19 mm (0.75 in.) inner span and a 38.1 mm (1.50 in.) outer span. The complete strength results of CVD coatings on injection molded and sintered alpha SiC in the as-fired condition are as shown in Table XVII. The strength of the control is lower than the 424 MPa (61.5 ksi) for injection molded bars reported elsewhere in this report. The bars for the CVD study were fabricated at an earlier date when 345 MPa (50 ksi) was the strength obtained by injection molding.

It can be seen that the changes in both room temperature strength and Weibull modulus are mixed on CVD and CNTD coated alpha SiC bars. It should be noted that coating thickness varied significantly for specimens from the same vendor precluding meaningful comparisons. In the case of CNTD bars, two bars gave unusually low strengths of 124 MPa (18 ksi). Elimination of these two specimens from the group increases the Weibull modulus to 4.9. Figure 114 shows the strength levels achieved in various density ranges for CVD coated bars. For the RCI-coated bars, strength enhancement is observed for low density specimens. In the case of the San Fernando Lab CNTD-coated bars, strength enhancement is seen for all density ranges except for the 3.12—3.129 g/cc (1127—1130 lb/in.³) density range.

Table XVII — Strength Evaluation of CVD-Coated Alpha SiC Bars

Vendor	Average Coating Thickness (in)	Number of Specimens	$\sigma_f \pm S.D.$		Weibull (m)	σ_e MPa (ksi)	Low σ_f MPa (ksi)	High σ_f MPa (ksi)
			MPa	(ksi)				
Control	—	25	336.88 ± 39.65	(48.86 ± 5.75)	8.9	355.01 51.49	237.66 (34.47)	419.00 (60.77)
DCI-Coated	0.004	24	302.61 ± 60.67	(43.89 ± 8.80)	4.8	330.33 47.91	157.20 (22.80)	407.83 (59.15)
MTC-Coated	0.012	25	327.30 ± 37.99	(47.47 ± 5.51)	9.0	342.67 49.70	247.32 (35.87)	385.97 (55.98)
RCI-Coated	0.003	20	362.11 ± 53.64	(52.52 ± 7.78)	6.9	386.38 56.04	256.28 (37.17)	439.68 (63.77)
San Fernando Labs (CNTD)	0.004	23	342.53 ± 96.53	(49.68 ± 14.00)	3.0	388.32 56.32	127.00 (18.42)	452.23 (65.59)
San Fernando Labs (CNTD)	0.004	21	362.53 ± 73.43	(52.58 ± 10.65)	4.9	395.14 57.31	220.77 (32.02)	452.23 (65.59)

In Figure 115, the microstructure and failure origin for injection molded and sintered alpha silicon carbide are shown for a control specimen. The unetched microstructure shows micropores which are located primarily at grain boundary triple points as revealed in the etched microstructure. The failure origin for this specimen which failed at 418.5 MPa (60.7 ksi) is a processing-related unbonded SiC inclusion. In addition to this flaw type, voids in the range of 70 to 200 μm (.003 to .008 in.) were also seen to be failure causing in many other specimens. No machining was performed for these control specimens and also all CVD coatings were deposited on the as-fired surfaces of injection molded and sintered alpha silicon carbide. In Figure 116, the nature of the coatings is examined via optical and scanning electron microscopy for MTC-coated specimens. The cauliflower-like appearance of the deposit indicates the size of individual grains. Good adhesion is evident with the absence of micropores in CVD SiC compared to sintered silicon carbide. The columnar growth of B-SiC grains during the CVD process can also be seen in one of the figures. MTC samples appeared to have the CVD coating applied three times. On the fracture shown, no obvious processing defect can be identified despite the low strength of 24.0 MPa (35.82 ksi).

In Figure 117, the coatings established by DCI are examined. Good CVD adhesion is evident. Some isolated micropores can be seen in the CVD SiC layer. The as-deposited CVD B-SiC surface shows that there exists a range of distribution of size of the CVD-SiC spheres deposited. The columnar growth of these spheres can also be seen in one of the figures. The failure origin for a specimen with a strength of 379.2 MPa (55.0 ksi) is shown as an internal processing-related 3-dimensional void.

The coating established by Refractory Composites, Inc. is shown in Figure 118. The as-deposited surface shows the spheres smaller than the earlier cases reported. The etched microstructure confirms this hypothesis. The deposit seems to be broken at several places. The grain size and distribution of CVD B-SiC is very similar to that of -SiC so that it is very difficult to visualize the boundary or the interface. The failure origin for a specimen shown in the figure is a processing-related internal void [$(\sigma_1 = 439.7 \text{ MPa (63.77 ksi)}$].

The CNTD coating produced by San Fernando Laboratories is examined in Figure 119. The surface appearance of the coating indicates that the CNTD coating process deposits a smoother layer of B-SiC on -SiC substrates than other CVD processes examined. Examination of the microstructure in the unetched condition indicates good adhesion of the CNTD coating to the -SiC substrate. The absence of micropores in the CNTD coating is noticeable. The etched view indicates that the etching conditions are not optimum for the CNTD B-SiC. The fracture origin for a specimen [$(\sigma_1 = 452.2 \text{ MPa (65.59 ksi)}$] is shown in one of the figures to be a small void [approximately 50 μm (.002 in.)] lying in the interior.

In summary, microscopy investigations on several selected CVD-coated specimens from different vendors have shown that:

- Coating thicknesses vary vastly from specimen to specimen (even among the same vendor).
- Coating adherence, in general, is very good.
- No advantage in strength enhancement is seen even in cases where fracture origin seems to be in the CVD SiC region.

Possible residual stresses introduced during the coating process can influence the fracture strengths significantly. Because no annealing was performed prior to strength test in order possibly to remove or minimize residual stresses, the absence of strength enhancement by CVD coating can be expected. In addition, in many cases processing-related voids control fracture of CVD coated bars. However, the completely dense microstructure of the coatings indicates they can perform useful sealing functions.

Hot Isostatic Pressing: "Hipping"

During this reporting period, several plates of sintered alpha silicon carbide supplied by Carborundum were returned by NASA after hot isostatic pressing at Lewis Research Center. The details of hipping are given in Table 3. Hipping did not improve the bulk density of initially 88-92 percent dense sintered alpha SiC. For plates which were initially 98 percent dense, hipping further increased the density by approximately 1 percent. The water accessible surface-connected porosity decreases significantly by

Table XVIII — Results of "Hipping" Plates of Pre-Sintered Alpha Silicon Carbide

Plate No.	HIP Conditions 2h @ 137.9 MPa (20.0 ksi) and Temperature	Initial Density g/cc (lb/in ³)		Apparent Porosity (%)	Hipped Density g/cc (lb/in ³)		Apparent Porosity (%)
		Carbo	NASA		Carbo	NASA	
D646-14-2	2050°C (3720°F)	2.836 (.1025)	2.820 (.1019)	10.27	2.842 (.1027)	2.821 (.1019)	3.24
D646-33-2	2050°C (3720°F)	2.927 (.1057)	2.950 (.1066)	4.62	3.012 (.1088)	2.991 (.1081)	0.36
D646-18-1	2050°C (3720°F)	3.084 (.1114)	3.063 (.1107)	0.27	3.172 (.1146)	3.161 (.1142)	0.00
D646-11-4	1950°C (3540°F)	3.162 (.1142)	3.134 (.1132)	0.04	3.180 (.1149)	3.164 (.1143)	0.01
D646-12-7	1950°C (3540°F)	3.153 (.1139)	3.131 (.1131)	0.00	3.179 (.1148)	3.162 (.1142)	0.01
D646-13-8	1950°C (3540°F)	3.160 (.1142)	3.142 (.1135)	0.00	3.177 (.1148)	3.167 (.1144)	0.01
D646-13-9	2050°C (3720°F)	3.155 (.1140)	3.136 (.1133)	0.00	3.187 (.1151)	3.173 (.1146)	0.00
D646-13-10	2050°C (3720°F)	3.152 (.1139)	3.126 (.1129)	0.00	3.187 (.1151)	3.168 (.1145)	0.00
D646-13-11	2050°C (3720°F)	3.154 (.1139)	3.132 (.1132)	0.00	3.188 (.1152)	3.172 (.1146)	0.00

Note: Carborundum densities measured by water immersion method. NASA used dimensional method.

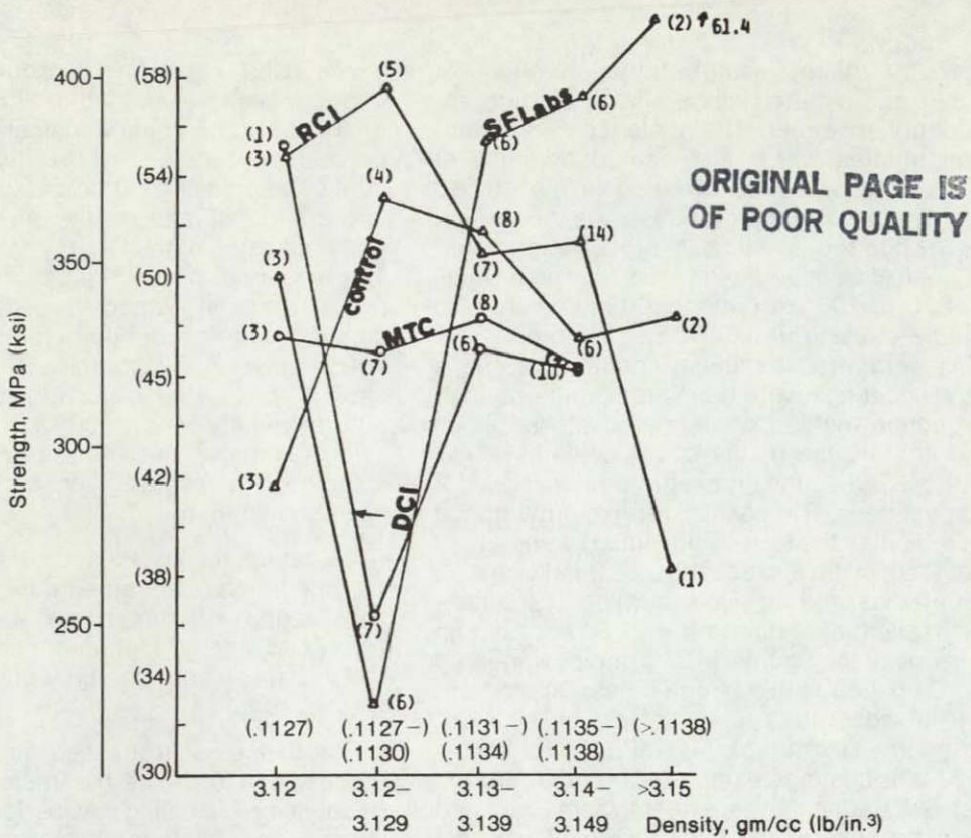


Figure 114 — Strength Levels Achieved in Various Density Ranges for CVD Coated Bars

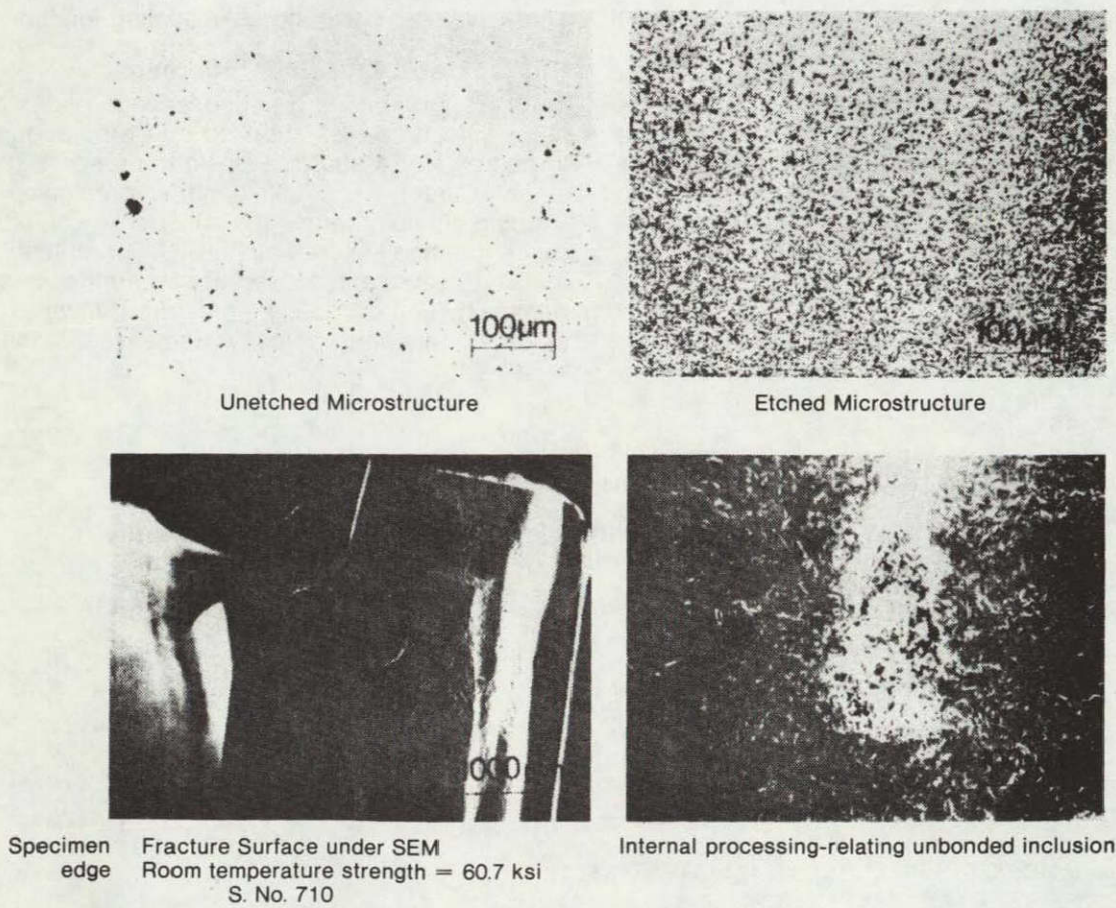


Figure 115 — Microstructures and Failure Origins for Injection Molded SiC Specimen Used as Control in CVD Evaluation Studies

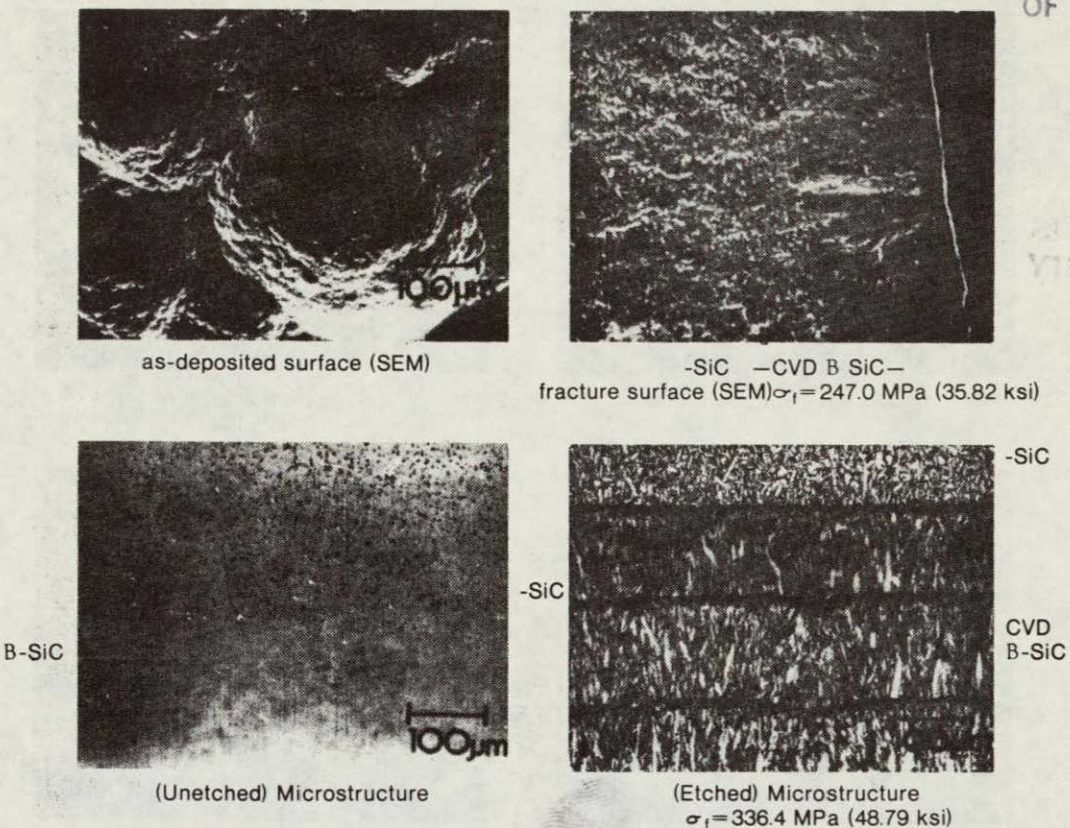


Figure 116 — Coating Evaluation for MTC-Coated Specimens

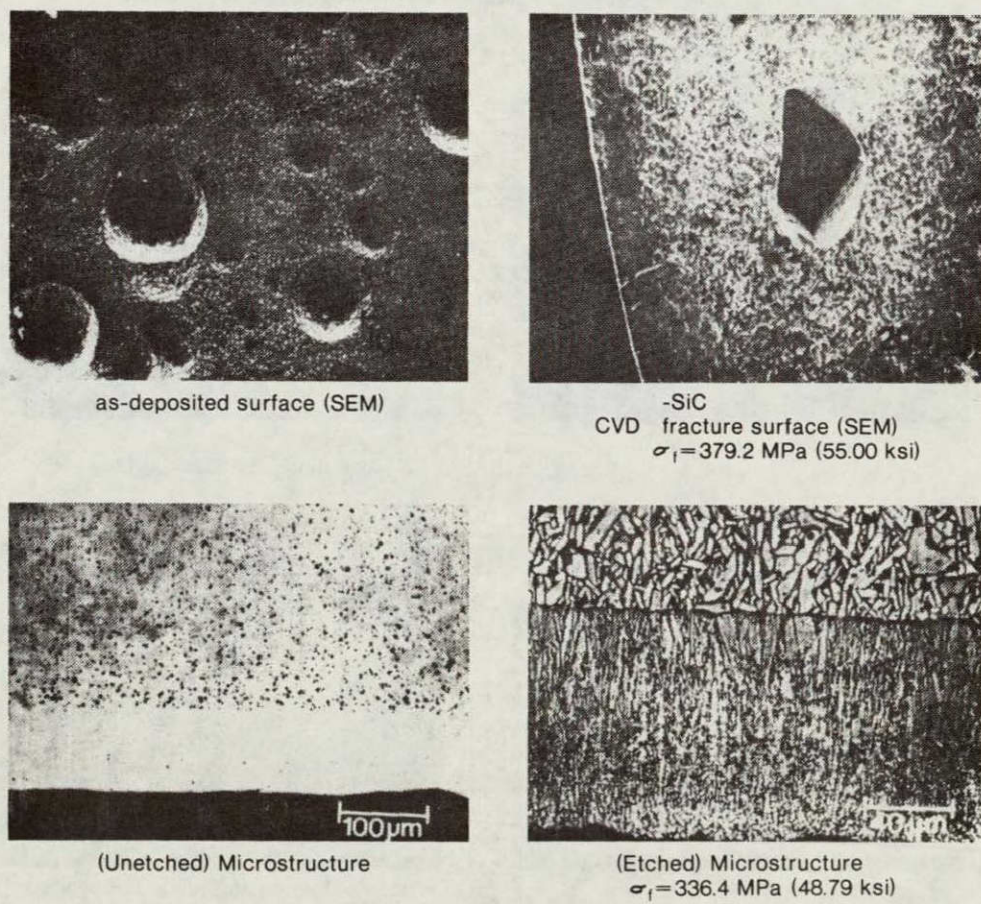


Figure 117 — Coating Evaluation for DCI-Coated Specimens

ORIGINAL PAGE IS
OF POOR QUALITY

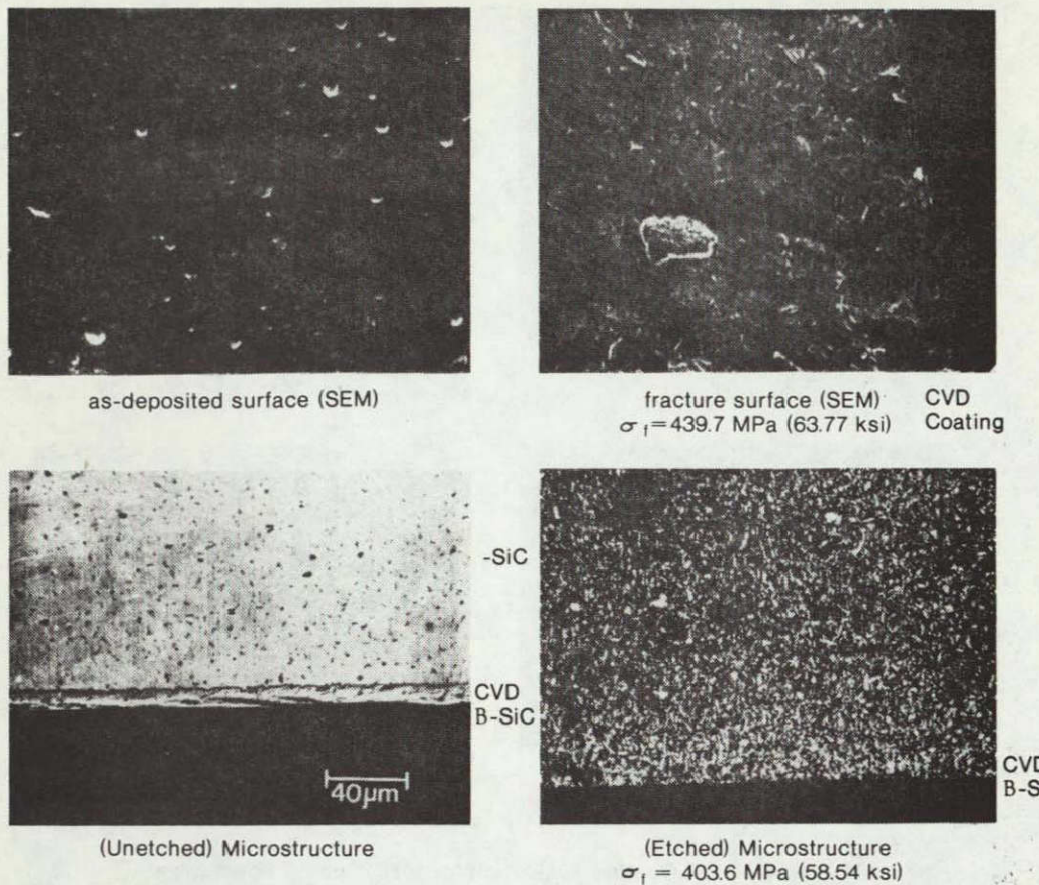


Figure 118 — Coating Evaluation for RCI-Coated Specimens

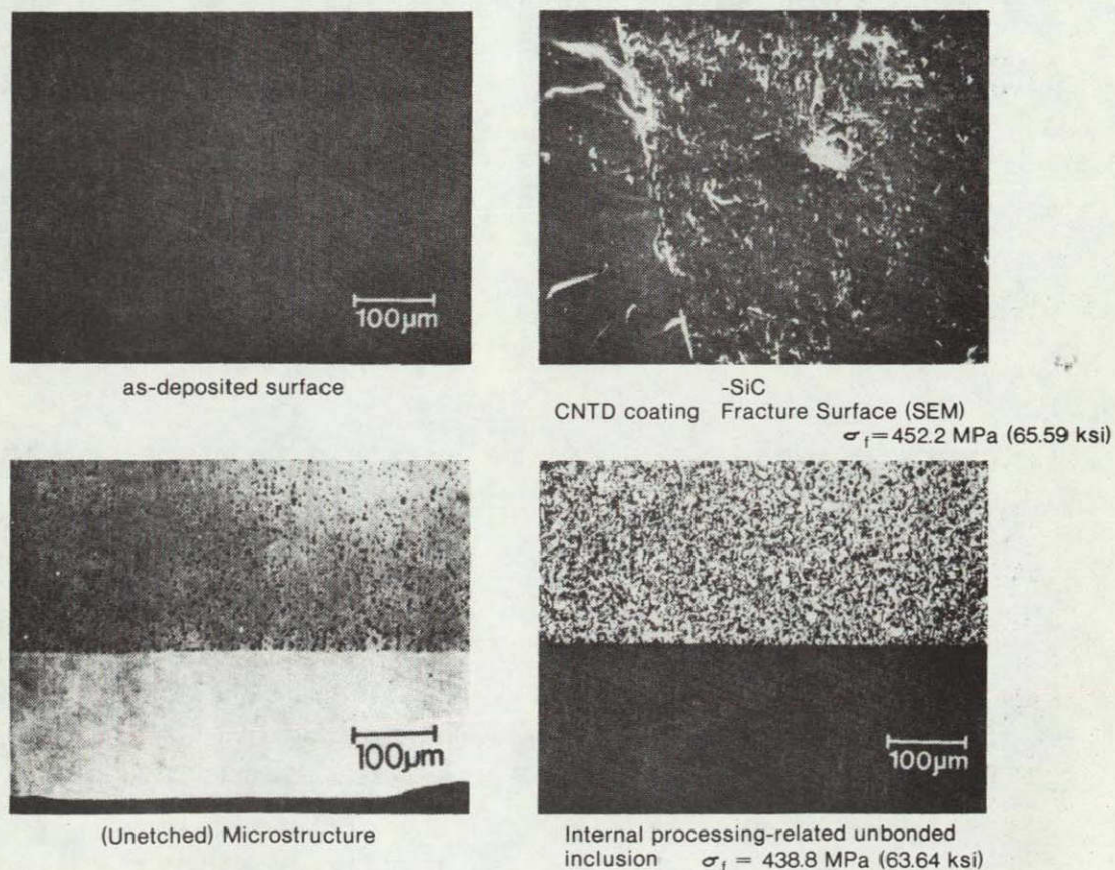


Figure 119 — San Fernando Laboratories CNTD-Coating Evaluations

hipping even on low density (88-92% theoretical) plates—indicating potential for surface flaw healing by hipping. Densities of plates hipped at 2050°C (3720°F) are very impressive.

Test bars have been cut from hipped plates. Careful bar location identifications in the plate have been kept and the bars have been returned to NASA for SLAM NDE and correlation with NDE of plates. Carborundum will test the bars for strength when these are returned from NASA.

Non-Destructive Evaluation

Microfocus X-Ray

Disks with intentionally fabricated voids, B₄C and carbon inclusions were examined with microfocus x-ray. The results are given in Table XIX.

Table XIX — Detection of Defects in Seeded Disks of Sintered Alpha SIC By Microfocus X-ray

Disk Thickness	Void Size		Carbon Inclusion Size		B ₄ C Inclusion Size	
mm (inch)	A	B	A	B	A	B
2.54 (0.1)	D	D	D	D	PI	D
3.18 (0.125)	D	D	D	D	ND	D
6.35 (0.25)	ND	D	—	D	—	D
12.70 (0.50)	—	D	—	D	—	D

D = Detected

ND = Not Detected

PI = Possible Indication

A = 50-125 μ m (.002-.005 in.)

B = 125-250 μ m (.005-.010 in.)

The results are very encouraging, especially in the 50-125 μ m (.002-.005 in.) size defects. Destructive sectioning of a 0.1-inch thick seeded defect (void) disk was continued in order to correlate with the microfocus x-ray indications. This disk was seeded with voids in the range of 50 to 125 μ m (.002-.005 in.). The maximum defect lengths (in the x-ray direction) have been 110, 130, 160, and 190 μ m (.004, .005, .006 and .007 in.) for a series of five (5) defects (Figure 120). In addition, two voids of 90

Non-Destructive Evaluation

X-ray Direction

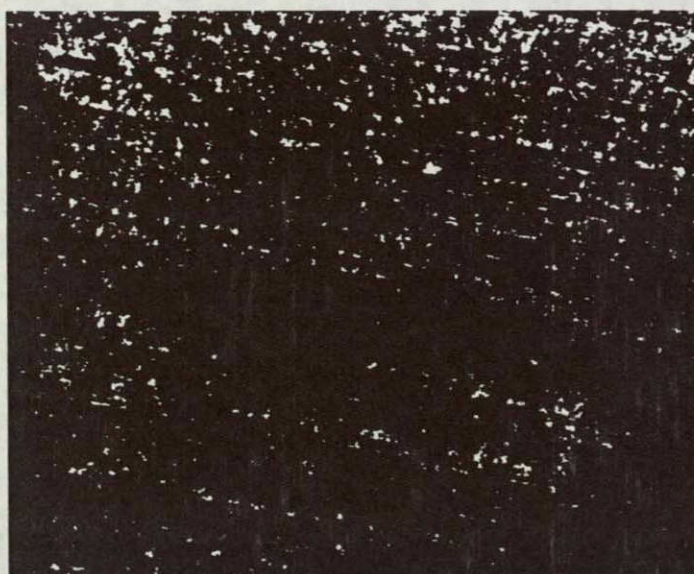


Figure 120 — Appearance of a 110 μ m (.004) Void Detected by Microfocus X-ray

μ m (.0035 in.) maximum diameter were also seen on sectioning which were not detected by microfocus x-ray. These observations have confirmed our detection sensitivity to be 4.3-3.5 percent of section thickness examined. However, this detection capability is at the cost of time. At 30 kV, the shots take about 22.5 minutes at a 381 mm (15.0 in.) focal spot to film distance. At 45 kV, the time drops to 4 minutes at a 508 mm (20 in.) focal spot to film distance. The 50-125 μ m (.002-.005 in.) voids are clearly seen at 30 kV source voltage and the indications are only vague at 45 kV.

Ultrasonics

Two seeded disks were examined by an ultrasonics technique using a 50 MHz beam. The results of a C-scan and some selected areas of an A-scan are shown (Figures 121 and 122). The disks were examined two times each and excellent reproducibility in defect imaging was seen. Many more defects were detected in addition to the seeded defects. The defect location of the seeded defects was the same as the expected location in some cases, and in some cases it was not.

A 50.8 × 50.8 × 9.4 mm (2 × 2 × .37 in.) plate of sintered alpha silicon carbide which was fabricated with large voids [approximately 250 μ m (.010 in.)] was examined both by microfocus x-ray and high frequency pulse-echo ultrasonics. At 55 kV and 0.5 ma, with a focal spot to film distance of 711 mm (28 inches) and a 15-minute exposure, no x-ray defect indications could be identified. However, when this plate was examined with 36 MHz ultrasonics, several defect indications were observed as seen in Figures 123 and 124.

The plate was scanned from both sides and for each side, two successive scans were made to ascertain reproducibility. Therefore, in the copy reproduction, two indications may actually correspond to one single defect due to slight differences in recorder pen repositioning. The two scans often overlapped. Very good correspondence was thus observed. In order to document the consistency in the defect locations, some defects were marked with edges marked with numbers for proper superimposition.

All the indications in the C-scans may not always be due to the existence of defects. In fact, because of the non-parallel specimen surfaces of the as-fired sample, the gate location was affected with respect to the front and back surface. The non-equal distances at different points (ultrasound travel length) of the front and back reflections causes the echo to move back and forth in the time domain of the gate (A-scan) and can trigger the pen (exceeding the peak threshold detection) on the X-Y plotter (C-scan). This can be observed as long lines in Figures 123 and 124. It should be noted that the C-scan is larger than the plate cross section by virtue of the magnification obtained by using the plotter range calibration. Because the beam width was 2 mm (.008 in.) and the pen in the plotter dictates the size of dots in the C-scan, the general size of the flaw indication should not be construed as being representative of the actual flaw size.

The streaks observed in the C-scan depend very much on the attenuation characteristics. For example, in one test bar which was examined (Figure 125), a one-digit change in attenuation dramatically changed the number and the length of the indications in the C-scan. Until plates are cut through indicated defects and inter-correlated, these defect indications should be interpreted with caution.

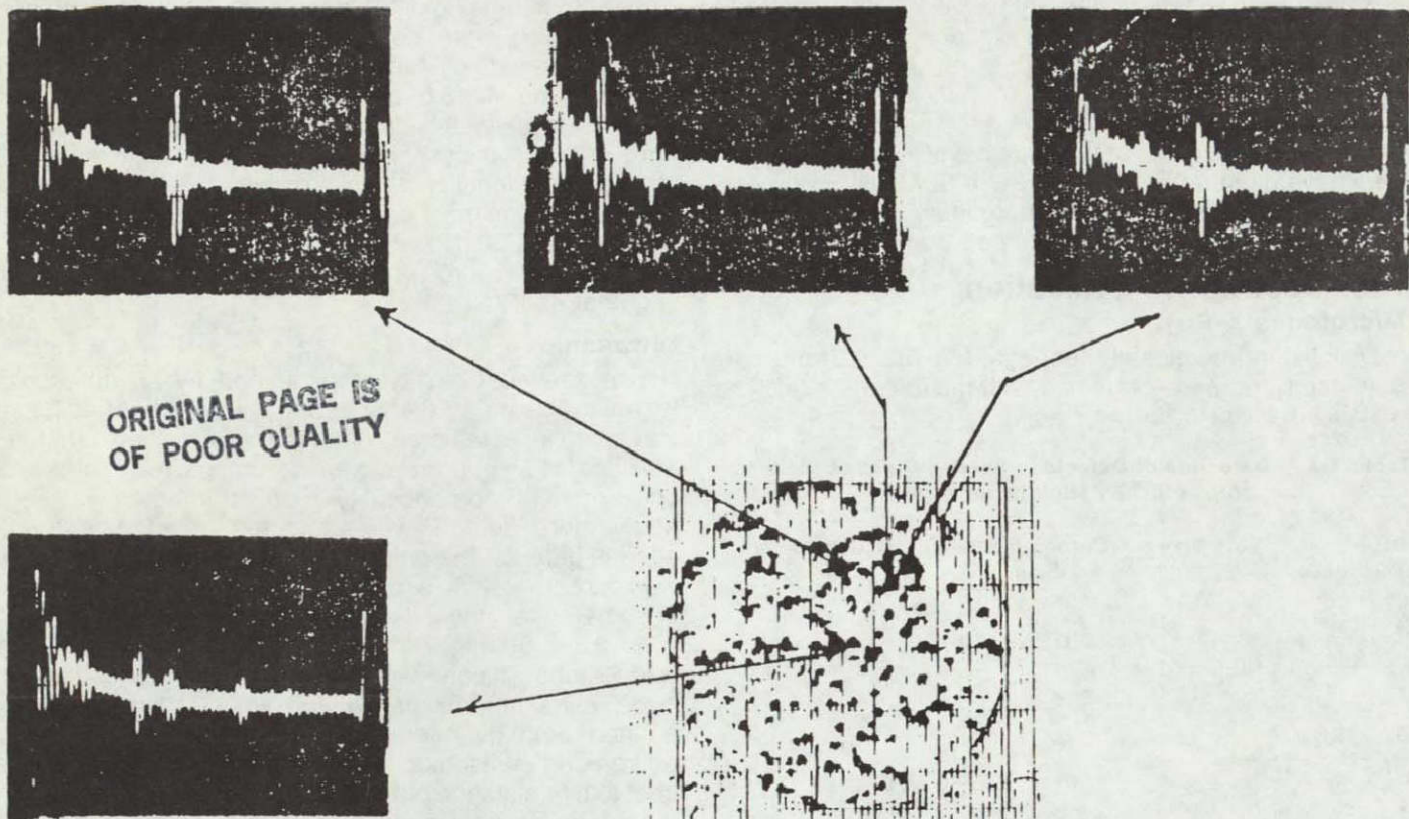


Figure 121 – Ultrasonic A- and C-Scans for 12.7mm (0.50 in.) Thick Disk of Alpha SiC Containing Seeded 125-250 μm Voids. Longitudinal Wave Velocity, $v_e = 11.80 \times 10^3 \text{ m/s}$.

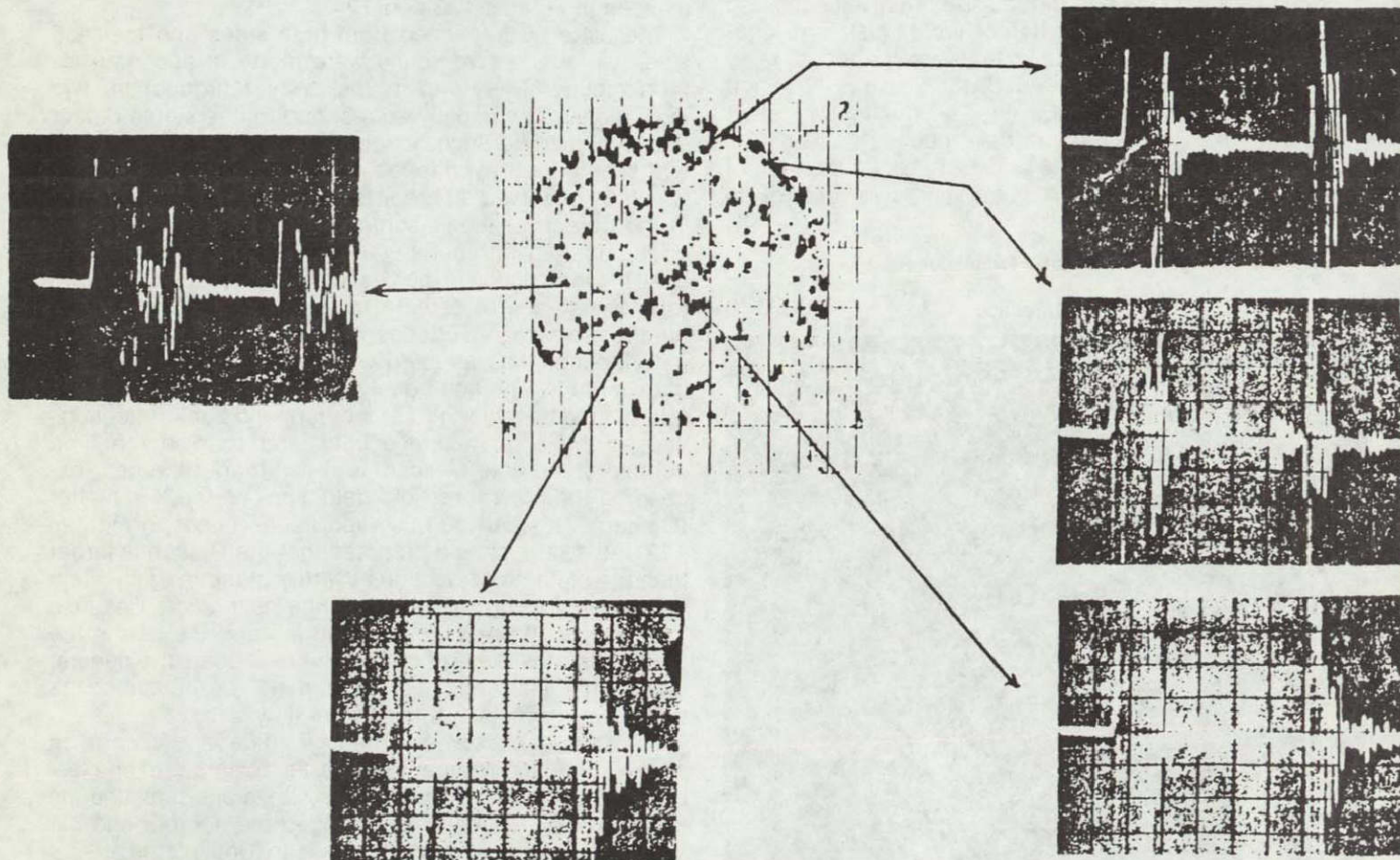


Figure 122 – Ultrasonic A- and C-Scans for 6.3mm (0.25 in.) Thick Disk of Alpha SiC Containing Seeded 125-250 μm B_4C Inclusions. $v_e = 11.9 \times 10^3 \text{ m/s}$.

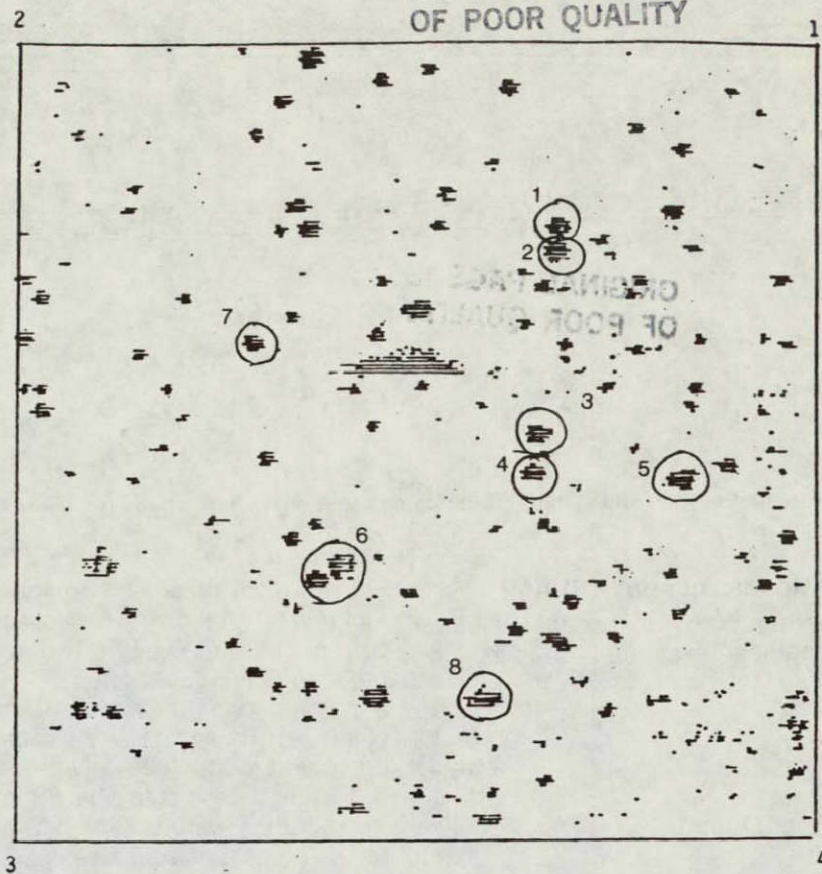


Figure 123 — Ultrasonic C-Scan of Seeded Void Plate at 36 MHz. The Scan Was Performed Twice and Good Consistency in Defect Detection Was Seen.

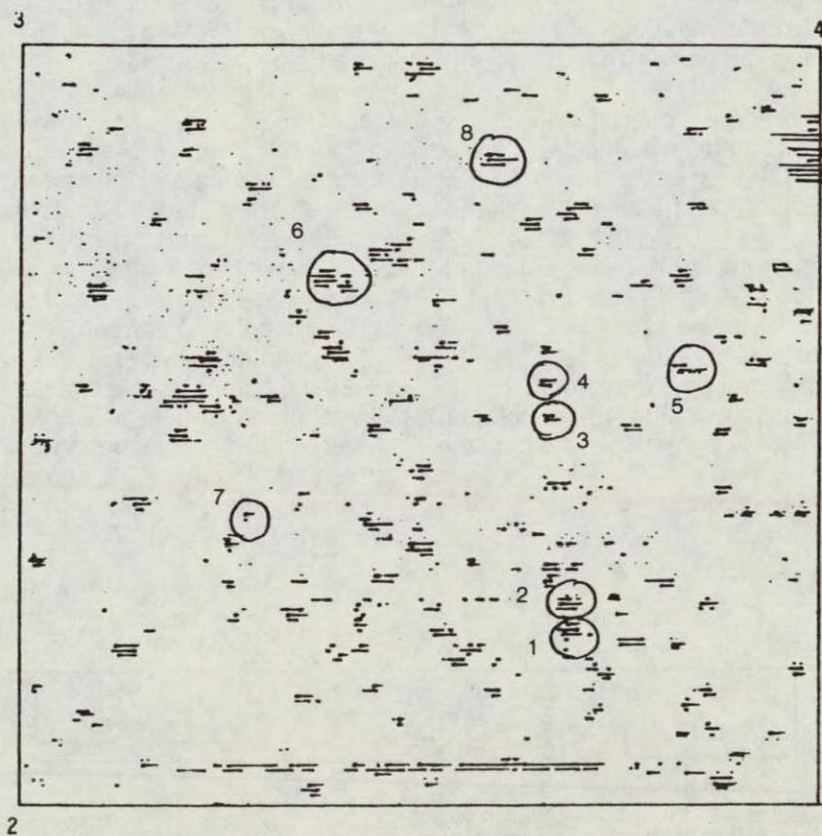


Figure 124 — Ultrasonic C-Scan of Seeded Void Plate at 36 MHz Corresponding to Figure 10 With Transducer on The Opposite Face of The Plate.

ORIGINAL PAGE IS
OF POOR QUALITY

Figure 125 — Effect of Attenuation Selection Characteristics on the C-Scan Indications for Alpha Silicon Carbide Test Bar

Scanning Laser Acoustic Microscopy (SLAM)

The SLAM work was performed by Sonoscan, Inc. on a separate subcontract. Sono-scan examined the following silicon carbide articles:

- I. Flexural Bars
 - (a) Reaction sintered
 - (b) Sintered
- II. Seeded Disks (Sintered Alpha)
- III. Turbine Components
 - (a) Reaction bonded vanes
 - (b) Injection molded alpha SiC vanes
 - (c) Injection molded alpha SiC blades

Reaction Bonded Flexural Bars

All samples were found to be compatible with the SLAM operating at 100 MHz and high resolution images were obtained.

All samples contained a large linear flaw which is typically one millimeter wide and several times that in length, oriented parallel to the bar's long axis. This flaw was peculiar in that its visibility was sensitive to the insoufication direction.

Acoustic background structure in the bars is substantially "cleaner" than that found in the seeded disks, but similar to that of the RBSiC vanes.

In the ten samples investigated, surface flaws, buried flaws and micro-structural variations were located and photodocumented. Flaw density was 3 to 4 flaws per bar (data on a 25.4 mm (1.0 in.) long segment centered on the bar).

An example of the documentation is shown on the next page.

The sketch presented above gives the location of flaws found in flexural bar 175. Micrographs illustrating the typical structure, as well as two zones containing flaws are presented in Figures 126, 127, and 128. In addition to the documented features, several small surface pits were also observed. Those that were most visible acoustically are presented in the sketch (the dots).

It should be noted that unless otherwise stated, the micrographs were obtained at a sound frequency of 100 MHz. The field of view size is 2.3 by 3.0 mm (.090 by .120 in.).

Sintered Alpha SiC Flexural Bars

All samples were found to be compatible with the SLAM operating at 100 MHz and high resolution images were obtained.

No major microstructural changes or peculiar flaws (like that of RBSiC bars) were found.

Acoustic background structure is substantially "cleaner" than that of the seeded discs, but similar to that of the sintered blades and vanes.

In the ten samples investigated, surface flaws, and buried flaws were located and photodocumented. Average detected flaw density is 2 to 3 per bar [data on a 25.4 mm (1.0 in.) long segment centered on the bar].

All samples were examined at 100 MHz using both shear and compressional waves. Flaw visibility was generally better using shear waves. Micrographs showing a typical structure and illustrating some of the flaw types are presented (Figures 129 and 130). Detailed flaw maps were also documented with an example as shown in Figure 131.

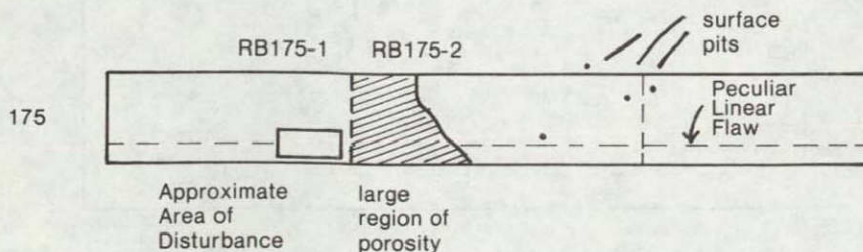


Figure 126 — RBSiC Bar 175

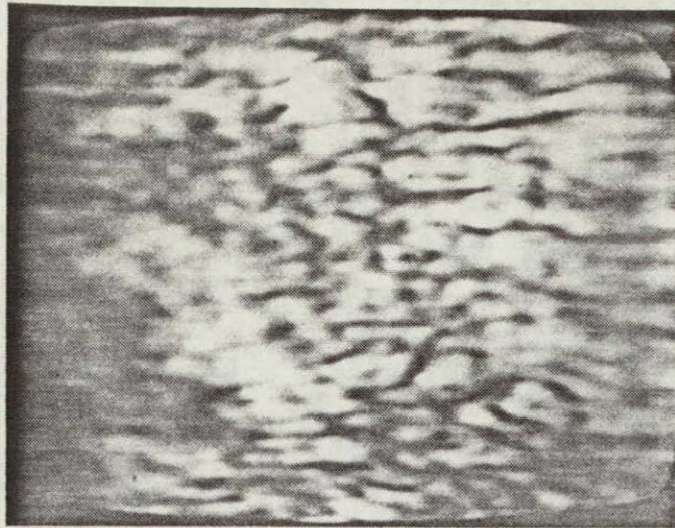


Figure 127

Figure 127 was taken in the region outside of the central area of the bar. This zone contains considerable structure and a scrambling of the interferogram fringes. This may correspond to a region of unreacted material.

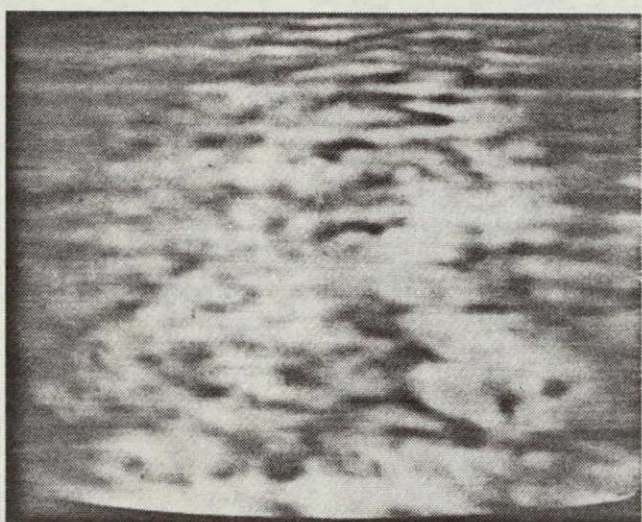
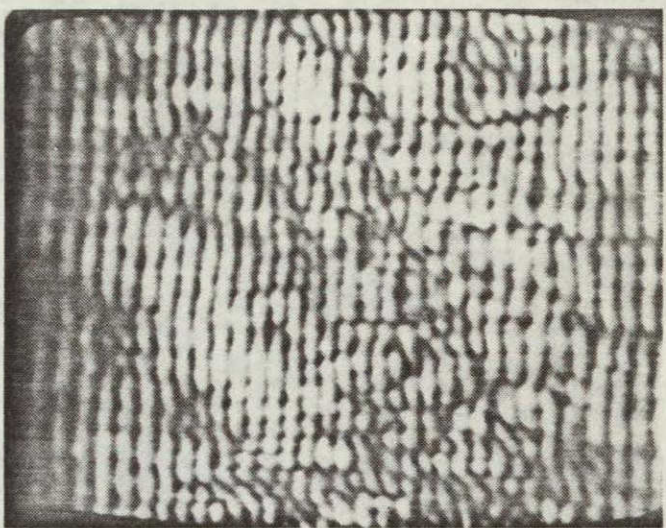


Figure 128

Figure 128 shows a zone of transmission variation found in the central zone of Bar 175. This zone contains little acoustic speckle and is interpreted as a zone of increased porosity.

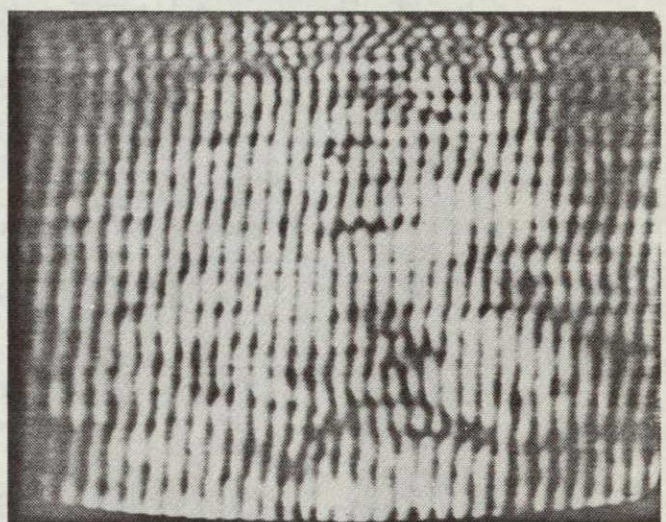


Figure 129

100 MHz micrographs showing two low contrast flaws in Bar 39-1.

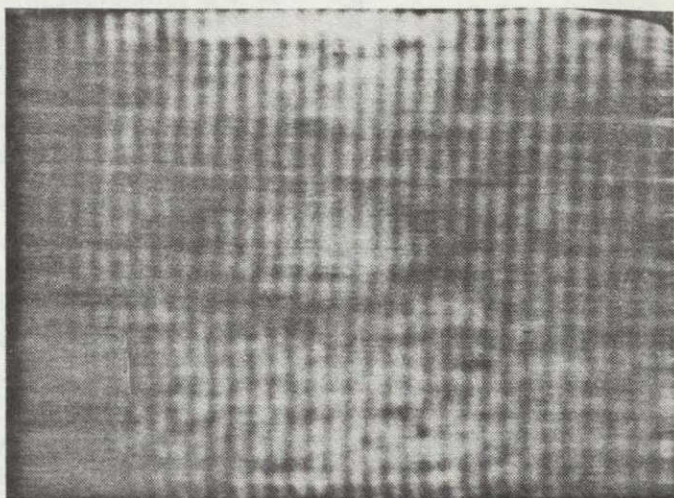
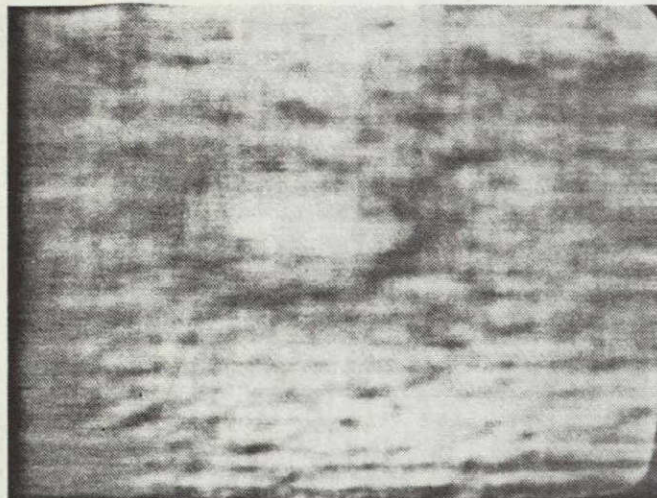
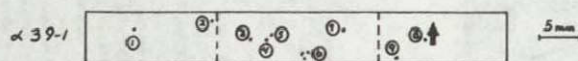


Figure 130

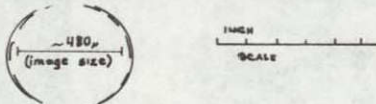
Acoustic micrographs showing large high contrast flaw found in Sample 39-1.

ORIGINAL PAGE IS
OF POOR QUALITY



DESCRIPTIONS

① LOW CONTRAST CIRCULAR = 1200μ below marked surface



INCH SCALE

② VERY LOW CONTRAST, CIRCULAR = 500μ below surface



3.4 ⑤ GROUP OF NON DISTINCT LOW CONTRAST FEATURES



RING PATTERN

⑥ GROUP OF LOW CONTRAST CIRCULAR FEATURES



⑦ LARGE, LOW CONTRAST, DARK EDGES, BRIGHT CENTER
(very deeply embedded)



⑧ EXTREMELY
LOW CONTRAST
LARGE CIRCULAR
LYING DEEP
BELOW THE SURFACE.

⑨ LOW CONTRAST CIRCULAR
= Immdee.



Figure 131

Seeded Defect Disk Examination

Flaws were detected in all four of the 100 MHz compatible seeded disks. In some cases the flaw location correlates with penciled marks on the surface, in other cases they do not.

Acoustic background structure and acoustic attenuation properties of the disks differ substantially from the flexural bar samples. Typically the disks exhibit more background structure and increased attenuation.

A carbon coating on the disc samples was found to increase acoustic attenuation and produce a very "busy" acoustic background which complicates the detection of small flaws. Removal of carbon improves the technique.

Utilization of these samples as calibration sample requires:

- Further documentation and confirmation of type, size, and location of implanted flaws.
- Understanding of the origin of the flaws which are detected but not implanted.
- Delineation of the differences in material properties between the disks and the bars.

The flaw location information was sent to Carborundum in the manner described in Table XX.

Table XX — Flaw Location—Seeded Disks

Figure	Sample	Comments
SD-1	V2-3	See diagram accompanying micrograph (in the original report).
SD-2	V2-3	See diagram accompanying micrograph (in the original report).
SD-3	V2-3	See diagram accompanying micrograph (Figure 20).
SD-5	V5-3	a) Marked on sample in green. b) Marked in orange.
SD-6	V7-2	Circled in green on sample.
SD-7	C3-2	Circled in green on sample.
SD-8	C3-2	Circled in orange on sample.
SD-10	B6-2	2 similar areas marked on sample with green dots.
SD-11	B8-2	Marked on sample with green dot.

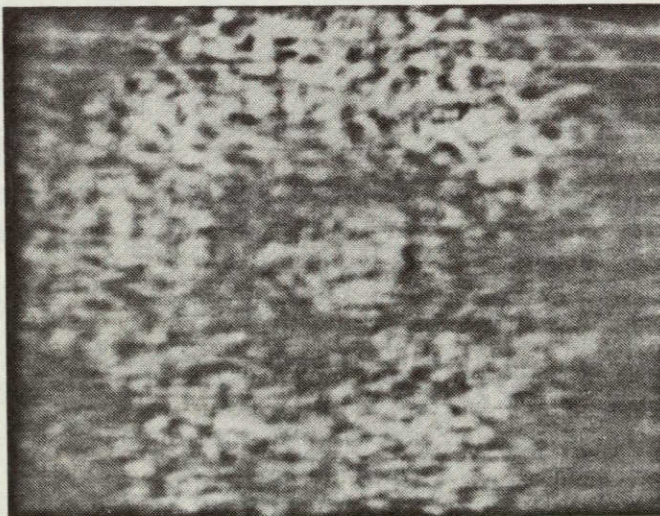


Figure 132 — Vane 184

The above figures are AM and I modes of structures found in another zone in the airfoil of 184. This dark ring pattern is 1.5 mm across (field of view is 3 mm horizontally). Several structures like this one were found and the areas of the vanes were circled in pencil.

Reaction Bonded Silicon Carbide Vanes

Vanес can be imaged and micrographs obtained using standard insonification stages at 100 MHz.

Routine testing of the vanes will require fixturing in order to make the test systematic and improve testing speed.

The quality of SLAM images obtained on the vanes is comparable to that obtained on the flat bars.

Background structure, flaw characteristics, and microstructural variations imaged in the vanes are similar to those found in flat bars. Thus, the results on bars are directly applicable to the vanes.

Vanес are more susceptible to microstructural variations attributed to pockets of unreacted material (relative to the RBSC bars).

An example of a defect appearance for Vane 184 is shown in Figure 132.

Injection Molded Vanes and Blades

Vanес and portions of the blades can be imaged and micrographs obtained using standard insonification stages at 100 MHz.

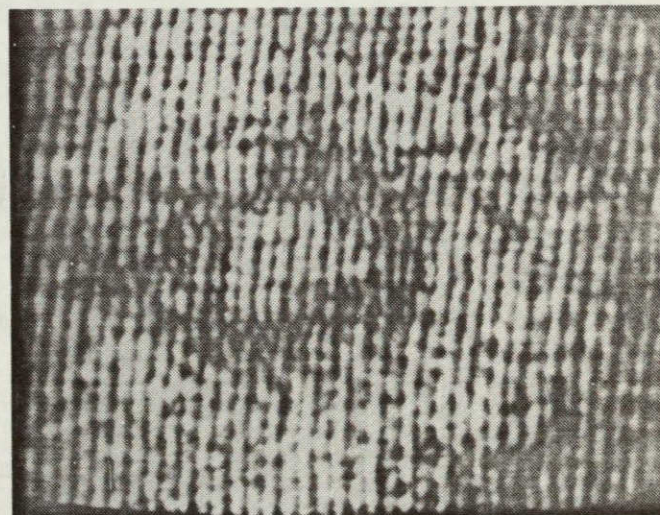
Routine testing of the vanes and blades will require fixturing in order to make the test systematic, improve test speed, and eliminate sound reverberation artifacts.

SLAM images of the vanes and blades are of a quality comparable to those obtained on bars.

Background structure, and flaw characteristics of the vanes and turbines is similar to that of the bars. Thus, results obtained on the bars are directly applicable to components.

Surface flaws, bumps and pits were detected but do not appear to interfere with visibility of buried structures.

Methods—Five injection molded vanes were examined using the standard 100 MHz soundcells and no special fixturing was required. Without fixturing, it was possible to cover 90 percent of the total blade volume. In some cases and in some areas of the vanes, the micrographs show a number of imaging artifacts resulting from sound reverberation. These artifacts which depend on both the vane geometry and insonification angle are easily distinguished from buried flaws because the SLAM has real-time imaging capabilities. However, artifacts may confuse the reading.



ORIGINAL PAGE IS
OF POOR QUALITY

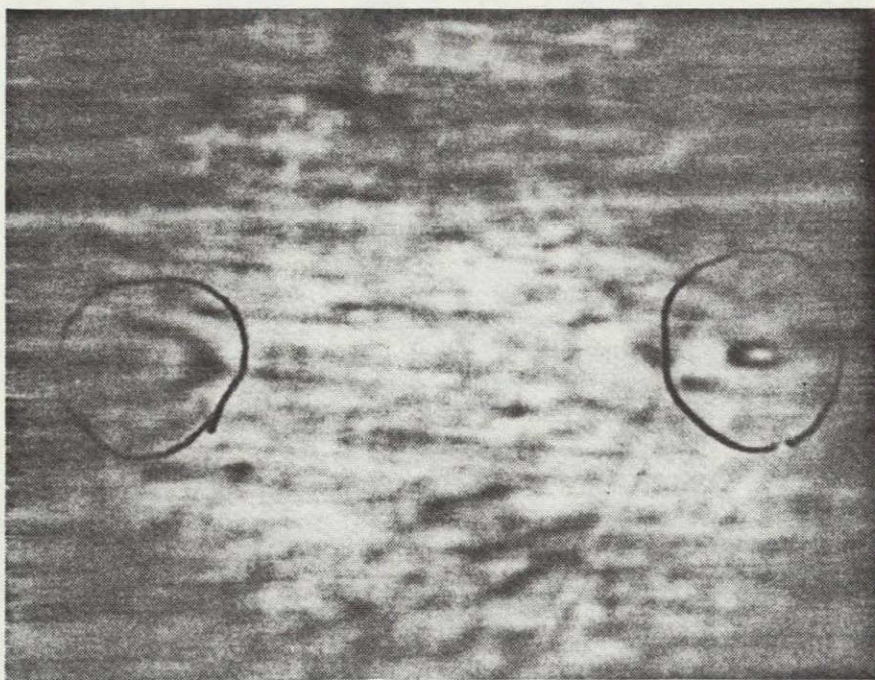


Figure 133

Figure 133 was taken on Sample V2-3. This amplitude micrograph shows two flaws found with the raster over the circled dot mark of the sample (circled).

er on the static micrographs and are noted in the figure captions. With appropriate fixturing and sample insonification, the reverberate artifacts can be eliminated from the images.

The flaw locations were identified on specimens and returned to Carborundum (Table XXI). Some typical defect appearances in SLAM are shown in Figures 21, 22, and 23.

Table XXI — Carborundum Flaw Locations

Figure	Sample	Sample Marked
RBV-1	DDA Vane 186	Circle on airfoil.
RBV-2	DDA Vane 184	Circle.
—	DDA Vane 183	Surface bumps circled.
—	DDA Vane 183	2 circles airfoil.
—	DDA Vane 175	X marked on airfoil.
1MB-5	DDA Blade 24	Large crack in root visible.
1MB-4	DDA Blade 16	Not marked (inclusion in root).
1MB-2	DDA Blade 17	Circled tip of airfoil.
1MB-3	DDA Blade 445	Large Crack in root.
1V-V-1	Vane 142	Square area on airfoil.
1MV-3	Vane 321	Square area on airfoil and leading edge.
RS91-1	Alpha SiC 39-1	Flaw 6 in drawing.
RS91-2	Alpha SiC 39-1	Flaw 7 in drawing.
RS95-9	Alpha SiC RS95-9	In group of surface flaws near upper edge.

Scanning Photoacoustic Microscopy (SPAM)

The scanning photoacoustic microscopy (SPAM) of silicon carbide materials was performed at the Physics

Department of Wayne State University under the direction of Prof. R. L. Thomas.

The alpha silicon carbide specimens were polished and Knoop indentations were made ranging from 1 kg to 3.5 kg loads (90 to 170 μm (.0035 to .0067 in.) flaw radius).

Preparation for SPAM

The SiC ceramic disks (both No. 13 and No. 8) were sectioned into pieces that would be accommodated by the photoacoustic spectroscopy cell (PAS-cell) used in the previous study of the unpolished SiC Knoop indented ceramic disks (see Figure 137). (The same PAS-cell and microphone were used for both the study of the unpolished and the polished SiC surfaces.) Each Knoop flaw was positioned with respect to the edges of its respective sectioned piece and examined optically to determine length, width at mid-point, relative depth at mid-point, and also occurrence of visible surface cracks extending beyond the length of the Knoop flaw (see Table XXII). Optical photographs were made of each Knoop flaw and the surrounding sample surface. The Knoop flaws were easy to locate, and easily distinguished from their surrounding surface structure. There was good correspondence between Knoop load and length, relative depth, and frequency of surface cracking; correspondence between load and width was not good and in several cases difficult to determine due to side chips occurring at or near the indentation mid-point, particularly for Knoop loads exceeding 2.0 kg.

Table XXII

Knoop Flaw Number	Load (kg)	Length μm (in.)	PAS- Length μm (in.)	Width μm (in.)	PAS- Width μm (in.)	Depth	Surface Cracks Number
1	1.0	79 (.0031)	143 (.0056)	9 (.00035)	160 (.0063)	2	0
4	1.5	97 (.0038)	170 (.0067)	9 (.00035)	130 (.0052)	2.7	1
7	2.0	110 (.0043)	160 (.0063)	12 (.00047)	190 (.0075)	3	2
16	3.5	167 (.0066)	310 (.0122)	16 (.00063)	280 (.0110)	5	2
17	3.5	160 (.0063)	260 (.0102)	17 (.00067)	140 (.0055)	6	2
18	3.5	154 (.0061)	270 (.0106)	16 (.00063)	140 (.0055)	4.2	3

ORIGINAL PAGE IS
OF POOR QUALITY

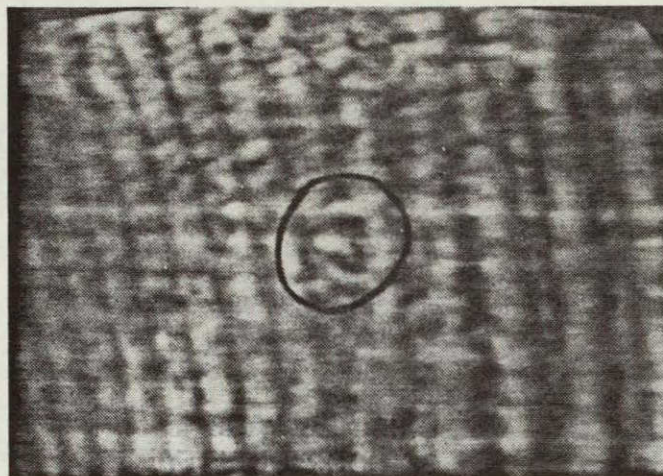


Figure 134

Figure 134 shows an amplitude micrograph from the airfoil region of Vane 142. The micrograph shows an isolated pore (circled) and its location was marked on the sample. Similar features were found throughout the vane. (The vertical lines are sound reverberation artifacts.)

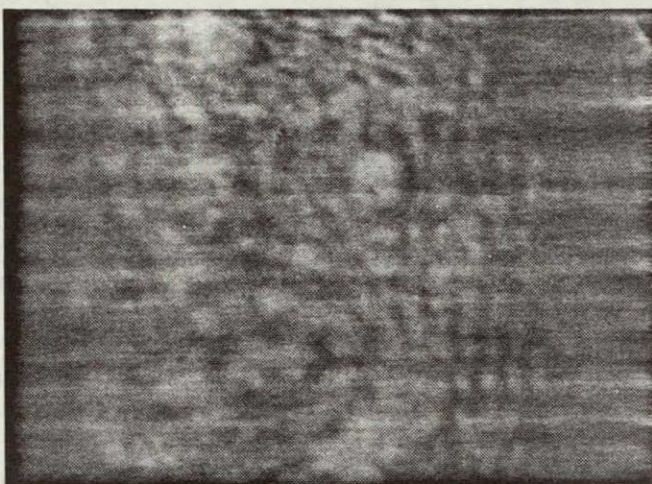


Figure 135

Figure 135 shows two circular structures found near the tip of the airfoil in Blade 17. Similar structures were found in Blade 94.

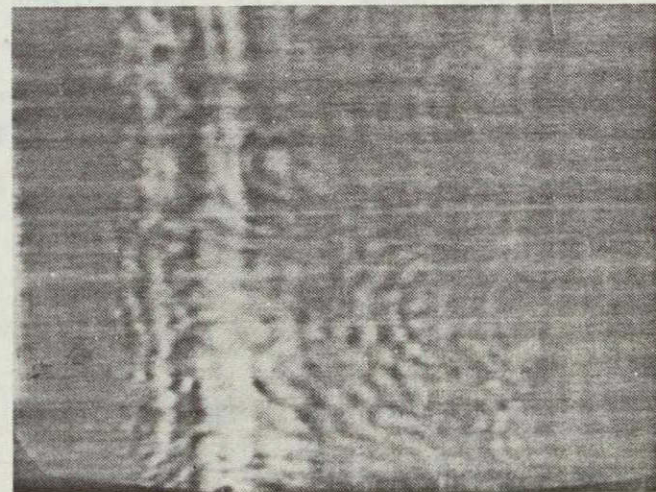
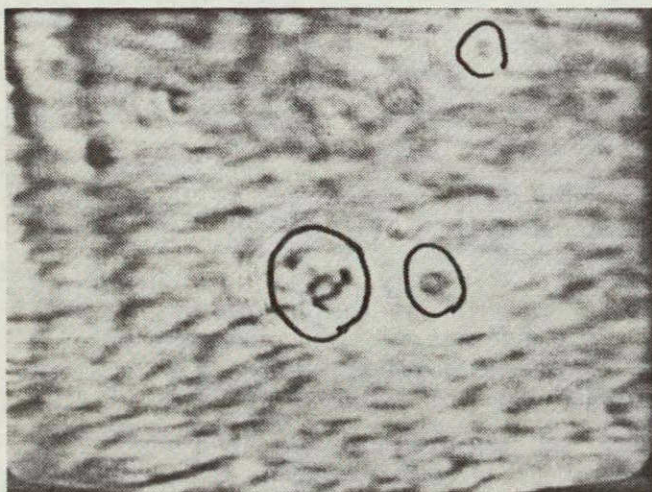


Figure 136

Figure 136(a) was taken in an area of the airfoil of Vane 321 with many surface pits (circled), while (b) was taken near the leading edge. Several large, isolated pores lead to the ring patterns observed in this micrograph.

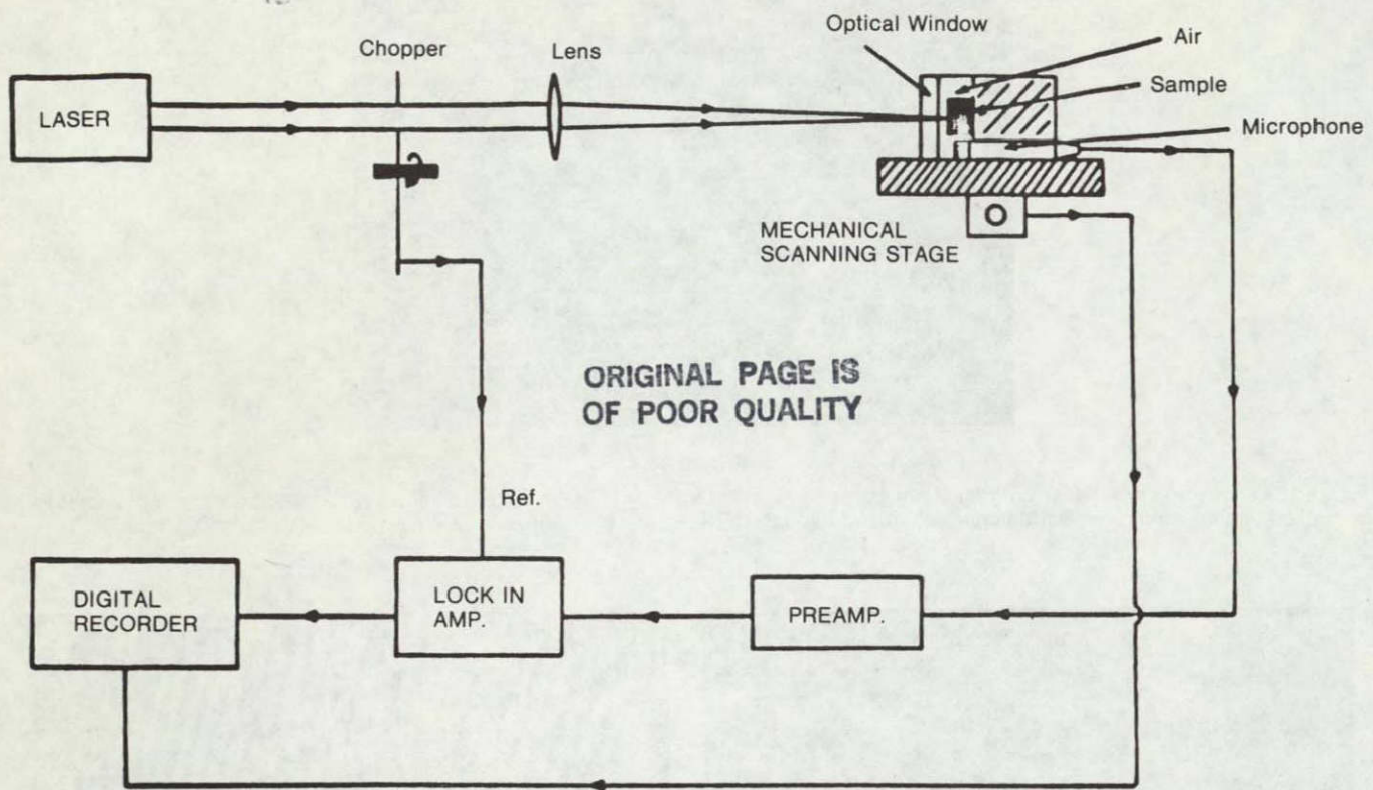


Figure 137 — Block Diagram of the Apparatus

SPAM Processing and Data Analysis

A block diagram of the system and the PAS cell used to study the polished SiC samples is attached (see Figure 137). An Argon beam was chopped at 1 K Hz, then focused onto the sample with a beam spot size of approximately $10 \mu\text{m}$ (.0004 in.). The sample was mounted on a mechanical stage which allowed the beam to scan the sample surface in both the x and y directions to produce area scan traces on an x-y plotter. Traces were made of each sample covering a $2.54 \times 2.54 \text{ mm}$ (.1 x .1 in.) area surrounding the Knoop flaw. The Knoop flaws were located using the sectioned sample edges measured with respect to the mid-point of the Knoop flaw, and also observing the speckle and diffraction patterns produced by the flaws. Repeatability in locating the Knoop flaws in this manner was excellent.

All traces were made on the same scale for comparison. In addition, the same time constant was used (30 ms) for each sample with the exception of No. 7 where a 100 ms time constant was used due to a higher noise level. The Signal-to-Noise was good for all samples, the background signal from the samples being between $150 \mu\text{V} - 170 \mu\text{V}$ for all samples at a laser current of 14.5A. The power incident on the sample was measured to be approximately 45 mW. The noise level for all samples was approximately $\pm 1 \mu\text{V}$. Repeatability of the traces was excellent for all samples with the exception of No. 7 where the noise level was higher.

Figure 138 shows a photo of a 1 kg. load Knoop indentation along with the corresponding PAS signal traces. The

blocked area drawn on the signal traces shows the boundaries of the photograph (marked A, B). The Knoop flaw and its signal are marked K, and a large surface structure below the flaw and its signal are marked S. Note that the signal due to the Knoop flaw is larger than the signal due to the surface structure. This was also the case for flaw No. 18 (see Figure 139). The small inset at the left of the photo is a reduced area scan with less expansion in the y-direction to give a more 3-dimensional view of the flaw. Note: there were no surface cracks for any of the 1.0 kg load Knoop indentations. Knoop flaw No. 18 (Figure 139) had the most extensive amount of surface chipping and the most number of cracks. The large chips extending from the side of the flaw was deeper than the flaw itself. The photo shows the Knoop flaw (k) with a large surface structure (s) below it. Note the corresponding photoacoustic signal for the surface structure is much smaller than the signal for the Knoop flaw.

Figure 140 shows Knoop flaw No. 7 with a 2.0 kg load. The noise level was highest for this sample ($\pm 1 \mu\text{V}$) and the photoacoustic background signal was not as reproducible for this sample as for the others. The signal due to the Knoop flaw was very reproducible, however.

Figure 141 shows traces and a photograph made from the unpolished back surface of one of the SiC sample pieces where there is no Knoop flaw but the surface structure was similar to the previous unpolished Knoop indented surfaces. Note that the surface structure gives rise to a more structured photoacoustic signal.

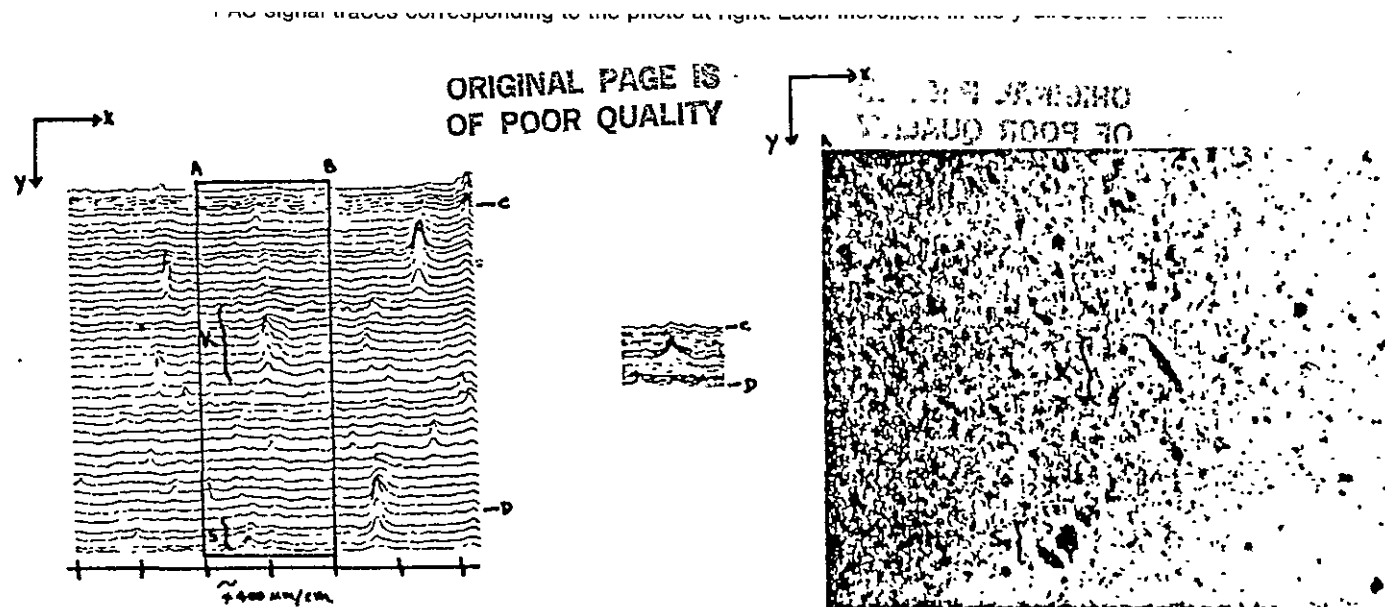


Figure 138 – Polished SiC Knoop Flaw #1

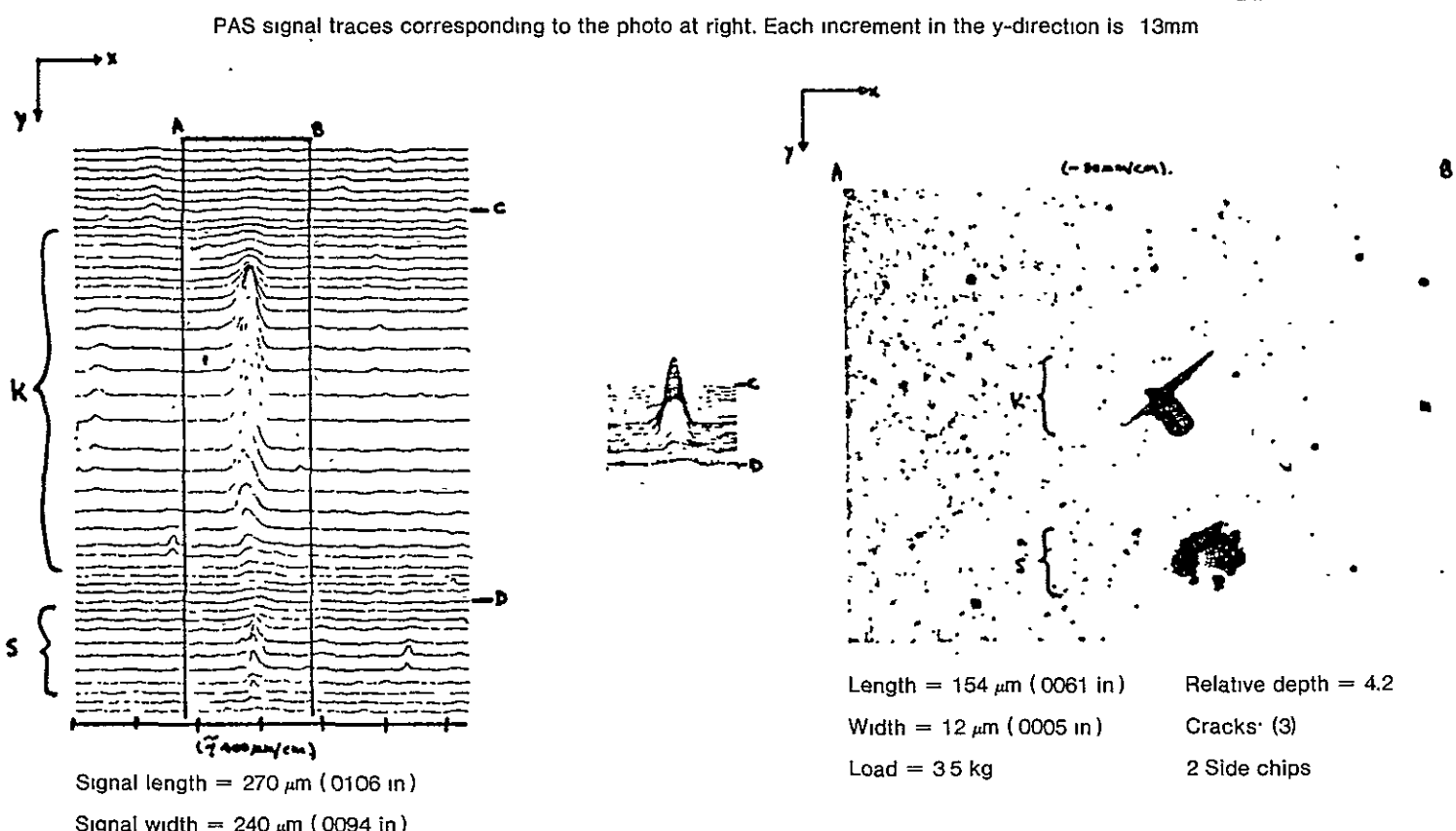
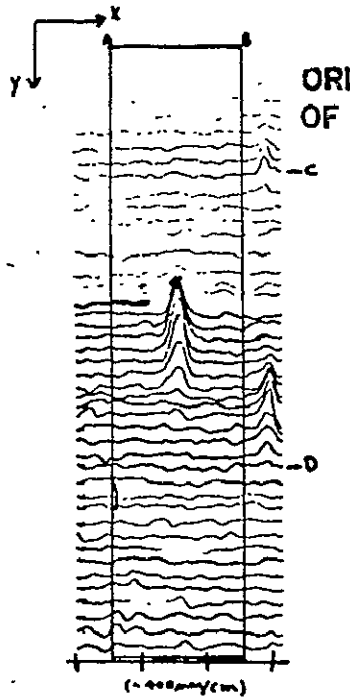
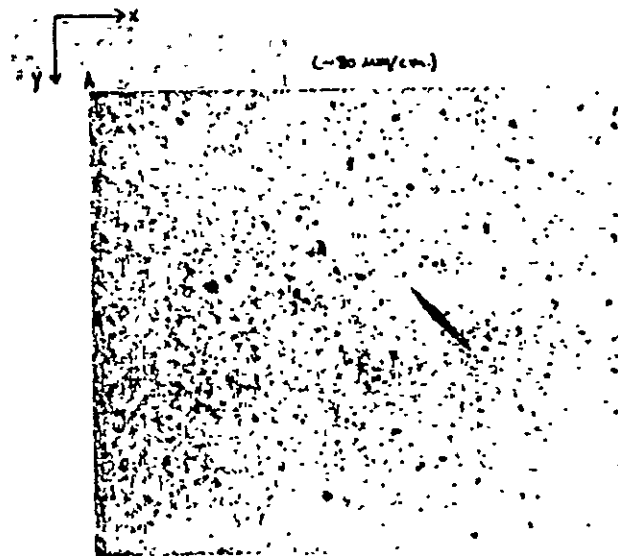


Figure 139 – Polished SiC Knoop Flaw #18



ORIGINAL PAGE IS
OF POOR QUALITY

Signal length = 160 μm (.0063 in)
Signal width = 190 μm (.0075 in)



Length = 110 μm (.0043 in) Relative depth = 3
Width = 12 μm (.0005 in) Cracks: (2)
Load = 20 kg.

Figure 140 — Polished SiC Knoop Flaw #7

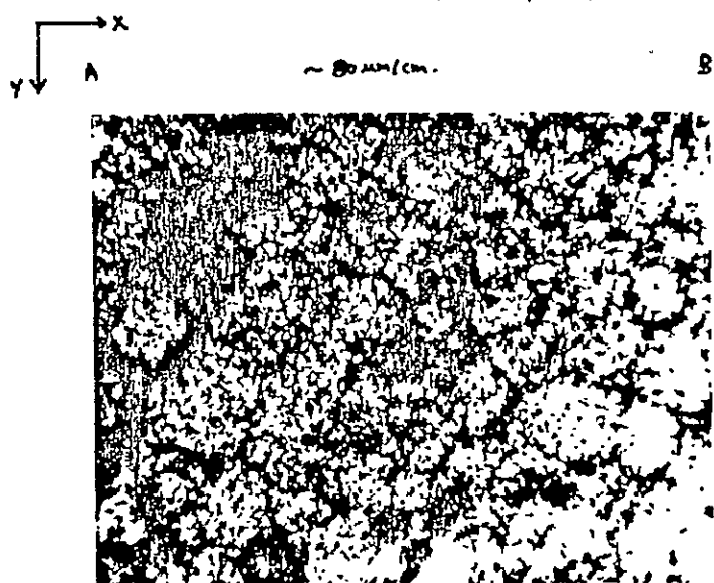
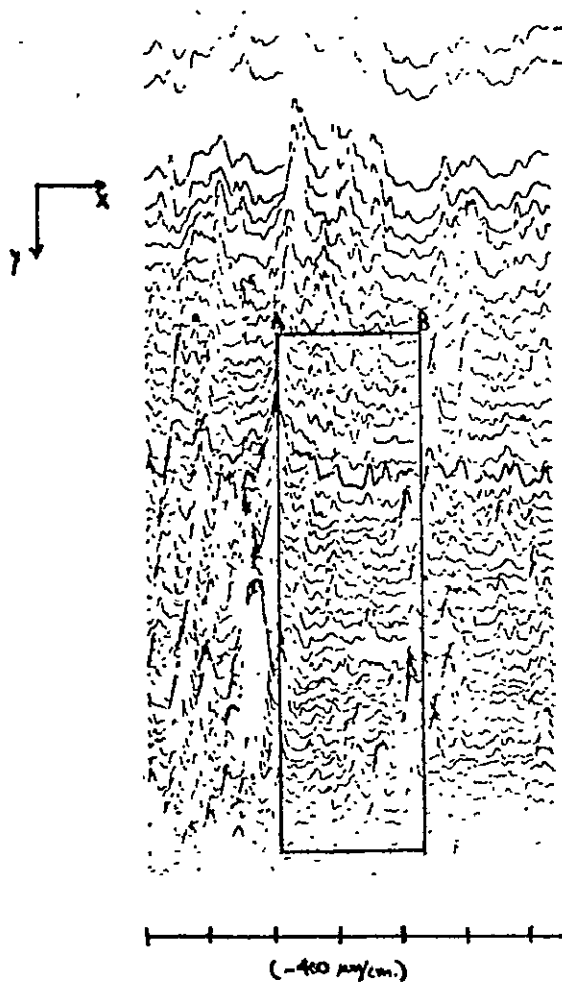


Figure 141 — Unpolished SiC Surface (No Knoop Flaw)

ORIGINAL PAGE IS OF POOR QUALITY

Summary of NDE Task Accomplished

The applicability of microfocus x-ray, high frequency ultrasonics, SLAM, and SPAM technology to detecting defects in silicon carbide materials has been evaluated. Further work is needed in areas of

- (a) Flaw characterization (type, size, shape, and location).
- (b) Destructive evaluation—NDE/signal coupling
- (c) Evaluation of different methods to detect and characterize the same flaw
- (d) Acoustic emission studies.

Mechanical Properties

Baseline Properties Determination

Baseline properties data for alpha silicon carbide manufactured by different processing techniques have been evaluated and the results are shown in Figure 142.

Specimen cross section was 3.18 mm (.125 in.) by 6.35 mm (.25 in.) and a total of 30 specimens were tested per each baseline datum. Tests were done in the 4-point bend mode using a 19 mm (0.75 in.) inner span and a 38.1 mm (1.5 in.) outer span. The 1200°C (2192°F) data for reaction bonded silicon carbide consisted of thirteen specimens, and therefore no Weibull modulus is noted.

Strength data obtained for injection molded specimens were obtained for an as-fired surface. The cold pressed and slip cast samples were machined. Test bars were annealed for 2 hours in an inert atmosphere prior to flexural test.

Strength levels reported here for both cold pressed alpha SiC and fine grain reaction sintered SiC are lower than previously observed. In earlier investigation, strength levels corresponding to the shaded area have been reported for cold pressed sintered alpha SiC^(4,5) and for fine grain reaction sintered SiC⁽⁶⁾. For fine grained reaction sintered SiC, the shaded high temperature area corresponds to test done at 1300°C (2372°F). The Weibull modulus was 10.9 at this temperature and 9.6 at room-temperature. The lower strengths observed in the present investigation have been traced back to improper furnacing during specimen preparation.

Failure Analysis of Test Bars

Failure analysis, via SEM, was conducted on broken test bars of sintered alpha silicon carbide manufactured by both injection molding and slip casting. The majority of failure-causing flaws were processing-related 3-dimensional voids lying at or close to tensile surface. (See Tables XXIII to XXV)

Stress Rupture

Static creep stress rupture tests were conducted with compression molded fine grain reaction sintered silicon carbide in air at 1000°C (1832°F) and 1200°C (2192°F) in 4-point bend. In 100 hours of testing, failure occurred at and above 379.2 MPa (55 ksi) of applied stress at 1200°C (2192°F). No failure occurred for stresses up to 386.1 MPa (56 ksi) at 1000°C (1832°F) (Figure 143). Creep deflections were seen during the stress rupture test, especially at 1200°C (2192°F). Based on the static fatigue data, the slow crack growth deformation aspect for these materials seems to be insignificant at these temperatures at the very high applied stress levels.

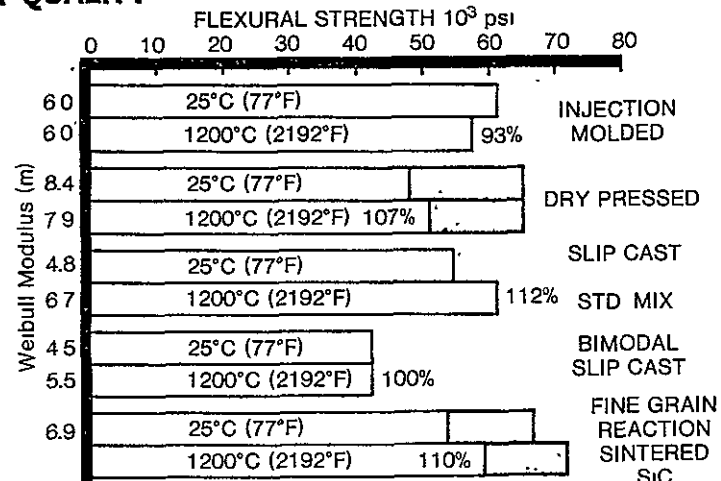


Figure 142 — High Temperature Strength Retention of Silicon Carbide Materials

Table XXIII — Defective Types and Distributions in Flexural Strength Specimens

Injection Molded SASC — Annealed Tested at 25°C (77°F)

Type	Number	Percent
Surface Flaws*	17	57
Internal Flaws	7	23
Corner Flaws**	4	13
Others***		
Total	30	100

* Includes subsurface origins [located within 100 μm (0.04 in) from the tensile surface] and surface originated failure without any specific origin

** Includes chamfer damage

*** No apparent fracture origin found

Table XXIV — Distribution of Failure Origins

Injection Molded SASC—Annealed Tested at 1200°C (2192°F)

Flaw Type	Number	Percent
Surface*	23	77
Internal	4	13
Corner	2	7
Others**	1	3
Total	30	100

* Includes subsurface voids located within 100 μm (0.04 in) from the tensile surface

** No apparent fracture origin noticed

Table XXV — Distribution of Failure Origins

Slip Cast SASC—Annealed Tested at 25°C (77°F)

Flaw Type	Number	Percent
Surface*	21	70
Internal	6	20
Corner**	2	7
Others***	1	3
Total	30	100

* Includes subsurface voids located within 100 μm (0.04 in) from the tensile surface

** Includes chamfer damage

*** No apparent fracture origin noticed

Creep

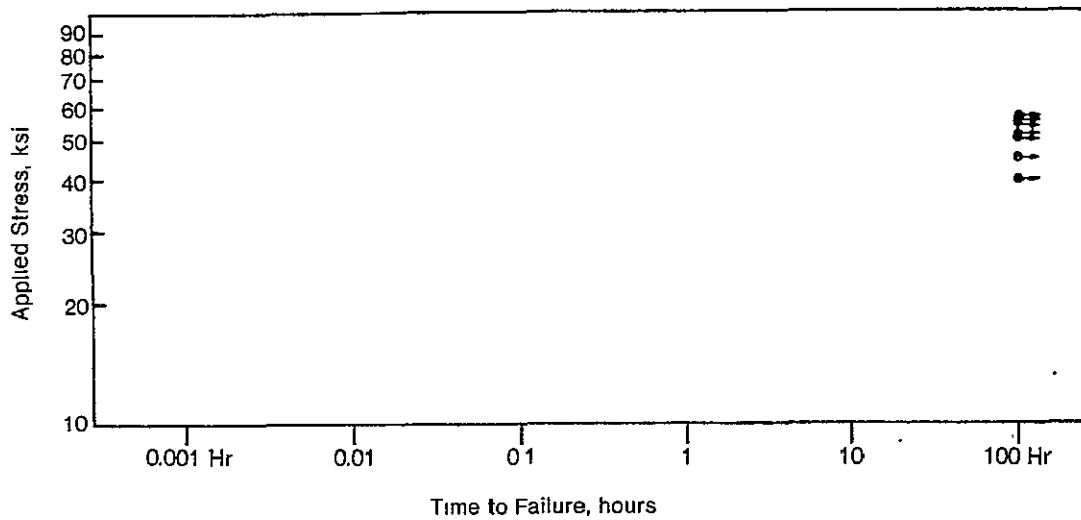
Creep tests were conducted with compression molded fine grain reaction sintered silicon carbide at 1200°C (2192°F). The deflection of beams [3.18 mm (.125 in) × 6.35 mm (.25 in) cross section] in 4-point bend was measured as a function of time by using a 3-point probe and LVDT set-up. The creep curves are shown in Figure 144. The dependence of steady-state creep rate on applied stress is plotted in Figure 145.

Physical Properties

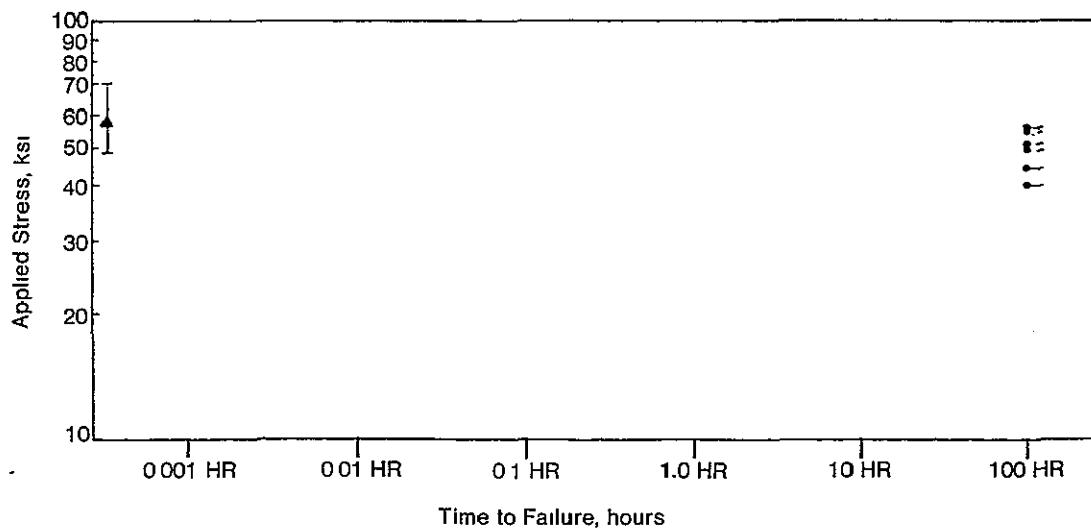
Thermal Diffusivity

Thermal diffusivity measurements were made by using laser the flash method for both sintered alpha SiC (Figure 146[a]) and reaction bonded SiC (Figure 146[b]) at Virginia Polytechnic Institute

ORIGINAL PAGE IS
OF POOR QUALITY



(a)



(b)

Figure 143 — Static Stress Rupture Plots for Compression Molded Reaction Bonded SiC (a) at 1000°C (1832°F) and (b) at 1200°C (2192°F) in Air in 4-Point Bend.

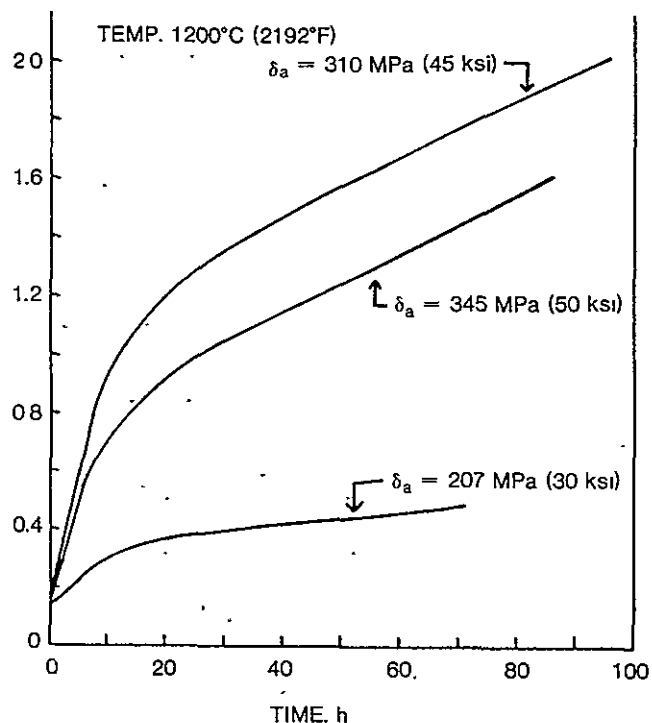


Figure 144 — Creep Curves at 1200°C (2192°F) for Fine Grain Reaction Sintered SiC in Air in 4-Point Bend

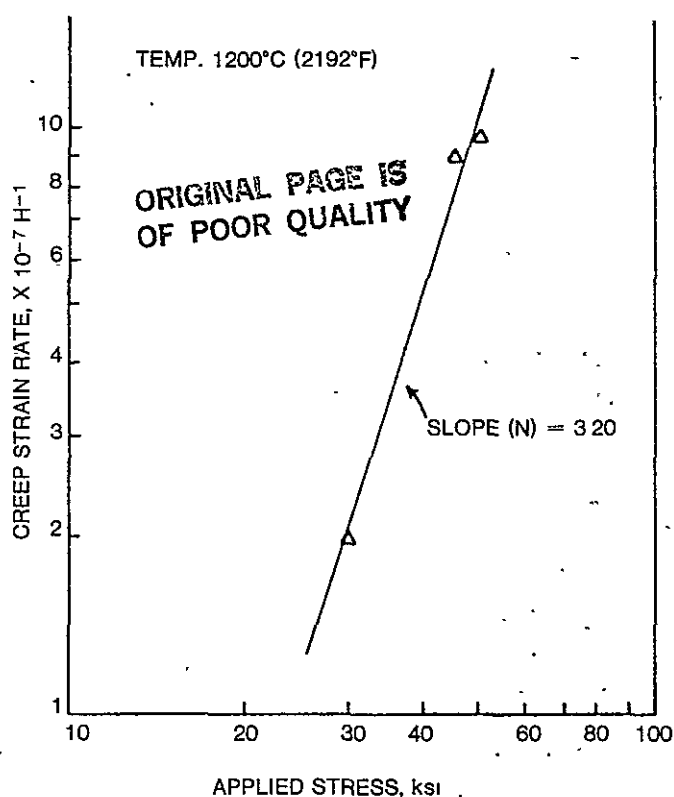
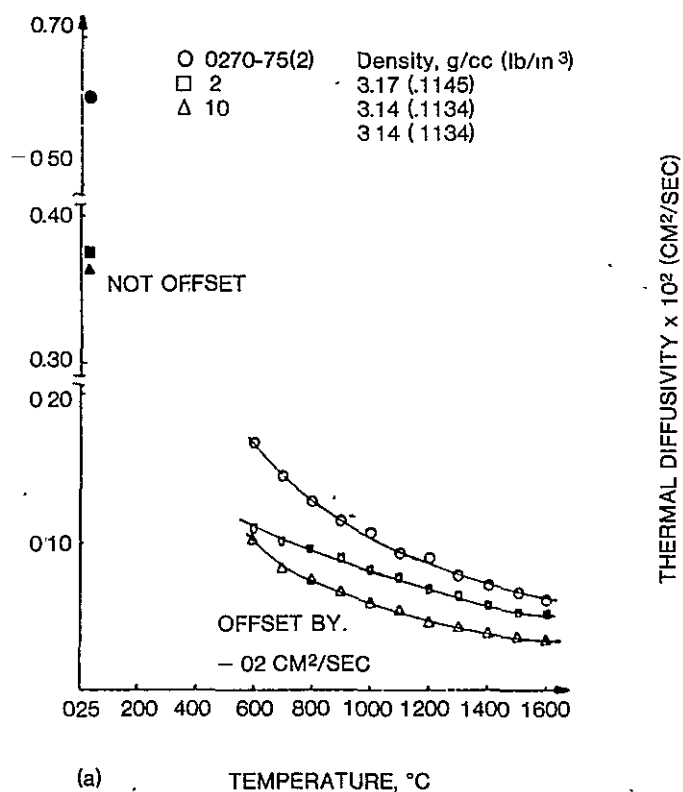


Figure 145 — Creep Rate Data at 1200°C (2192°F) for Fine Grain Reaction Sintered SiC



(a) TEMPERATURE, °C

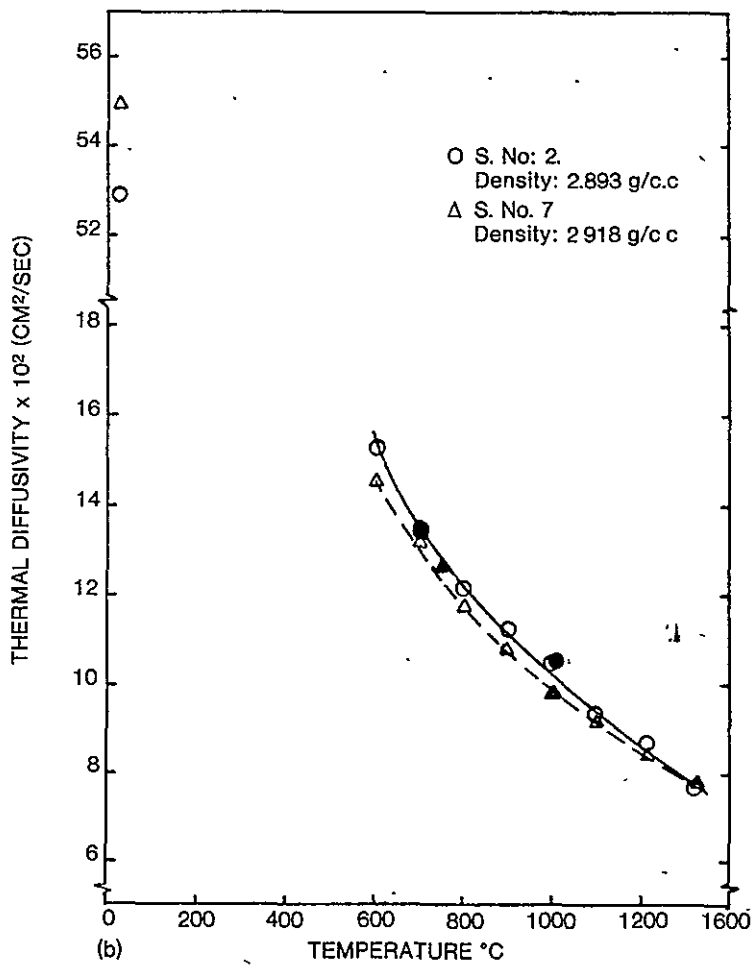


Figure 146 — Thermal Diffusivity Measurements for (a) Sintered Alpha SiC and (b) Reaction Bonded Silicon Carbide

1 Report No. CR 165346	2 Government Accession No	3 Recipient's Catalog No	
4 Title and Subtitle ADVANCED GAS TURBINE (AGT) POWERTRAIN SYSTEM SECOND SEMI-ANNUAL TECHNICAL SUMMARY REPORT		5 Report Date January 1981	6. Performing Organization Code
7 Author(s) H E Helms (DDA), J Kaufeld (PMD), R Kordes (DE)		8 Performing Organization Report No EDR 10578	10 Work Unit No
9 Performing Organization Name and Address Detroit Diesel Allison Div General Motors Corporation Box 894 Indianapolis, IN 46206		11 Contract or Grant No DEN 3-168	13 Type of Report and Period Covered Contractor Report
12 Sponsoring Agency Name and Address US Department of Energy Office of Transportation Programs Washington, DC 20545		14 Sponsoring Agency Code DOE/NASA	
15. Supplementary Notes Semiannual report Project Manager P T Kerwin, Transportation Propulsion Division, NASA Lewis Research Center, Cleveland, OH 44135			
16 Abstract Technical work on the design of a 745 kW (100 hp) advanced automotive gas turbine engine is described for the period July through December 1980. This is the second semi-annual report. Work this period was directed toward refining the engine design and starting component rig tests. A design iteration to improve the weight and production cost associated with the original concept is discussed. Major rig tests included 15 hours of compressor testing to 80% design speed and the results are presented. Approximately 150 hours of cold flow testing showed duct loss to be less than the design goal. Combustor test results are presented for initial checkout tests. Turbine design and rig fabrication is discussed. From a materials study of six methods to fabricate rotors, two have been selected for further effort. A discussion of all six methods is given.			
17 Key Words (Suggested by Author(s)) Automotive gas turbine Ceramic components Alternate propulsion systems Improved fuel economy		18 Distribution Statement Unclassified—unlimited	
19 Security Classif (of this report) Unclassified	20 Security Classif (of this page) Unclassified	21. No of Pages	22 Price*

*For sale by the National Technical Information Service, Springfield, Virginia 22161